Microhabitats save mammals, but not birds, from warming pp. 553 & 633

Gut microbiota modulate immunotherapy pp. 573, 595, & 602

Physically distanced quantum gates pp. 576 & 614

Science

$15
5 FEBRUARY 2021
sciencemag.org

AAAS

SPECIAL ISSUE

HUMAN GENOME AT

The heart of the matter.

The NEBNext® Ultra™ II workflow lies at the heart of NEB's portfolio for next gen sequencing library preparation. With specially formulated master mixes and simplified workflows, high quality libraries can be generated with low inputs and reduced hands-on time.

As sequencing technologies improve and applications expand, the need for compatibility with ever-decreasing input amounts and sub-optimal sample quality grows. Scientists must balance reliability and performance with faster turnaround, higher throughput and automation compatibility.

NEBNext Ultra II modules and kits for Illumina® are the perfect combination of reagents, optimized formulations and simplified workflows, enabling you to create DNA or RNA libraries of highest quality and yield, even when starting from extremely low input amounts.

The Ultra II workflow is central to many of our NEBNext products, including:

- Ultra II DNA & FS DNA Library Prep
- Enzymatic Methyl-seq
- Ultra II RNA & Directional RNA Library Prep
- Single Cell/Low Input RNA Library Prep
- Module products for each step in the workflow

The Ultra II workflow is available in convenient kit formats or as separate modules – it is easily scalable and automated on a range of liquid handling instruments.

End Repair/ dA-Tailing	Adaptor Ligation	Clean Up/ Size Selection	PCR Enrichment	Clean Up
Module NEB #E7546	Module NEB #E7595	Component of NEB #E7103	Module NEB #M0544	Component of NEB #E7103
NEBNext Ultra II DNA Library Prep Kit for Illumina (NEB #E7645)				
NEBNext Ultra II Library Prep with Sample Purification Beads (NEB #E7103)				

The NEBNext Ultra II workflow has been cited in thousands of publications, as well as a growing number of preprints and protocols related to COVID-19. Citation information and extensive performance data for each product is available on neb.com.

To learn more about why NEBNext is the choice for you, visit **NEBNext.com**.

One or more of these products are covered by patents, trademarks and/or copyrights owned or controlled by New England Biolabs, Inc. For more information, please email us at gbd@neb.com. The use of these products may require you to obtain additional third party intellectual property rights for certain applications. Illumina® is a registered trademark of Illumina, Inc.
© Copyright 2020, New England Biolabs, Inc.; all rights reserved.

NEW ENGLAND BioLabs® Inc.

be INSPIRED
drive DISCOVERY
stay GENUINE

CONTENTS

5 FEBRUARY 2021 • VOLUME 371 • ISSUE 6529

553 & 633

Small mammals, like this desert woodrat, are able to use habitat features, such as burrows, to escape desert warming related to climate change.

PHOTO: JACK DAYNES

NEWS

IN BRIEF

546 News at a glance

IN DEPTH

548 **Two new vaccines deliver good and bad news for the pandemic**
Novavax and J&J data underscore challenge of viral variants
By J. Cohen

549 **Danish scientists see tough times ahead as variant rises**
Some say the country should reopen—even if it causes cases to surge—once vulnerable populations are vaccinated
By K. Kupferschmidt

550 **Speedy robots gather spectra for sky surveys**
Telescopes retrofitted with hundreds of optical fibers dissect the light of stars and galaxies *By D. Clery*

552 **NIH's 'precision nutrition' bet aims for individualized diets**
Effort will piggyback on giant genomics and health program *By J. Kaiser*

553 **Study shows winners, losers as desert warms**
In 100-year record, small mammals burrow to beat the heat, but birds either fly away or die
By E. Pennisi
REPORT p. 633

554 **Science bill rankles Mexican research community**
Scientists feel ignored in debate over law that would reshape governance and funding *By I. Gutiérrez Jaber*

555 **Species? Climate? Cost? Ambitious goal means trade-offs**
Biden aims to protect 30% of U.S. land and water by 2030
By E. Stokstad

INSIGHTS

PERSPECTIVES

572 **Ultrafast generation of optical hyperbolicity**
A new strategy actively controls the trapping and manipulation of light
By S. Deng and H. Chen
REPORT p. 617

573 **Modulating gut microbiota to treat cancer**
Fecal microbiota transplantation is evaluated in melanoma patients resistant to immunotherapy
By C. H. Woelk and A. Snyder
RESEARCH ARTICLE p. 595; REPORT p. 602

574 **Superspreading genomes**
Virus mutations help to unravel key epidemiological events *By S. Alizon*
RESEARCH ARTICLE p. 588

576 **Quantum logic at a distance**
A quantum gate is realized by optically coupling trapped atoms separated by 60 meters
By D. Hunger
REPORT p. 614

577 **Designing the right protection**
A new iron-based catalyst helps avoid common pitfalls for making olefins
By J. Xie
REPORT p. 610

BOOKS *ET AL.*

579 **The origins of 'Oumuamua**
A high-profile astronomer argues that the strange interstellar object may be an alien signal
By D. Greenbaum

RESEARCH

IN BRIEF

580 From *Science* and other journals

REVIEW

583 **Noise pollution**
The soundscape of the Anthropocene ocean
C. M. Duarte et al.
REVIEW SUMMARY; FOR FULL TEXT: DOI.ORG/10.1126/SCIENCE.ABA4658

Apply for our exciting research Prize!

SCIENCE-PINS PRIZE FOR NEUROMODULATION

SCIENCE-PINS

$25, 000 Grand Prize!
Get published in *Science*!

The *Science*-PINS Prize is a highly competitive international prize that honors scientists for their excellent contributions to neuromodulation research. For purposes of the Prize, neuromodulation is any form of alteration of nerve activity through the delivery of physical (electrical, magnetic, or optical) stimulation to targeted sites of the nervous system with impications for translational medicine.

For full details, judging criteria and eligibility requirements, visit:

www.sciencemag.org/prizes/pins

Submission Deadline: 15 March 2021

Science AAAS

PINS 品驰

Science Translational Medicine AAAS

SPECIAL ISSUE

HUMAN GENOME AT 20

545 Editorial
A genome to celebrate *By Claire M. Fraser*

FEATURES

556 Genomes arising
Africans have begun to study their continent's rich human diversity—but what comes after current grants end? *By E. Pennisi*

LETTERS

560 Nextgen voices: Human genome anniversary

POLICY FORUM

564 Complicated legacies: The human genome at 20
PODCAST

PERSPECTIVES

570 For better drugs, diversify clinical trials
Genetic variation in drug metabolism can affect drug outcomes *By N. N. Bumpus*

BOOKS *ET AL.*

578 Genomics and genre
A scholar probes subtle shifts in stories told through genes *By L. A. Campos*

ON THE COVER

Twenty years after two groups published the first draft sequences of the human genome in *Science* and *Nature*, the intricate code embedded in human chromosomes has transformed research, medicine, and our concept of ourselves. This special issue explores the achievement's complex legacy. See pages 545, 556, 560, 564, 570, and 578. *Illustration: Charis Tsevis*

ILLUSTRATIONS (FROM LEFT): CHARIS TSEVIS; ROBERT NEUBECKER

RESEARCH ARTICLES

584 RNA stability
RNA stabilization by a poly(A) tail 3′-end binding pocket and other modes of poly(A)-RNA interaction *S.-F. Torabi* et al.
RESEARCH ARTICLE SUMMARY; FOR FULL TEXT: DOI.ORG/10.1126/SCIENCE.ABE6523

585 Cell biology
HSP70 chaperones RNA-free TDP-43 into anisotropic intranuclear liquid spherical shells *H. Yu* et al.
RESEARCH ARTICLE SUMMARY; FOR FULL TEXT: DOI.ORG/10.1126/SCIENCE.ABB4309

586 Developmental biology
Reactivation of the pluripotency program precedes formation of the cranial neural crest *A. Zalc* et al.
RESEARCH ARTICLE SUMMARY; FOR FULL TEXT: DOI.ORG/10.1126/SCIENCE.ABB4776

587 Coronavirus
Immunological memory to SARS-CoV-2 assessed for up to 8 months after infection *J. M. Dan* et al.
RESEARCH ARTICLE SUMMARY; FOR FULL TEXT: DOI.ORG/10.1126/SCIENCE.ABF4063

588 Coronavirus
Phylogenetic analysis of SARS-CoV-2 in Boston highlights the impact of superspreading events *J. E. Lemieux* et al.
RESEARCH ARTICLE SUMMARY; FOR FULL TEXT: DOI.ORG/10.1126/SCIENCE.ABE3261
PERSPECTIVE p. 574

589 Aerosol formation
Role of iodine oxoacids in atmospheric aerosol nucleation *X.-C. He* et al.

595 Clinical trials
Fecal microbiota transplant overcomes resistance to anti–PD-1 therapy in melanoma patients *D. Davar* et al.
PERSPECTIVE p. 573; REPORT p. 602

REPORTS

602 Clinical trials
Fecal microbiota transplant promotes response in immunotherapy-refractory melanoma patients *E. N. Baruch* et al.
PERSPECTIVE p. 573; RESEARCH ARTICLE p. 595

610 Catalysis
A hydrophobic FeMn@Si catalyst increases olefins from syngas by suppressing C1 by-products *Y. Xu* et al.
PERSPECTIVE p. 577

614 Quantum systems
A quantum-logic gate between distant quantum-network modules *S. Daiss* et al.
PERSPECTIVE p. 576

617 Quantum materials
Programmable hyperbolic polaritons in van der Waals semiconductors *A. J. Sternbach* et al.
PERSPECTIVE p. 572

620 Organic chemistry
Electrophotocatalytic diamination of vicinal C–H bonds *T. Shen and T. H. Lambert*

626 Surface chemistry
Solvent molecules form surface redox mediators in situ and cocatalyze O_2 reduction on Pd *J. S. Adams* et al.

633 Climate change
Exposure to climate change drives stability or collapse of desert mammal and bird communities *E. A. Riddell* et al.
NEWS STORY p. 553

636 Solar cells
Reconfiguring the band-edge states of photovoltaic perovskites by conjugated organic cations *J. Xue* et al.

DEPARTMENTS

646 Working Life
Tracing contacts, finding ourselves
By Nawar Naseer and Katherine Strelau

Science Staff 542
New Products 641
Science Careers 642

SCIENCE (ISSN 0036-8075) is published weekly on Friday, except last week in December, by the American Association for the Advancement of Science, 1200 New York Avenue, NW, Washington, DC 20005. Periodicals mail postage (publication No. 484460) paid at Washington, DC, and additional mailing offices.

Copyright © 2021 by the American Association for the Advancement of Science. The title SCIENCE is a registered trademark of the AAAS.

Domestic individual membership, including subscription (12 months): $165 ($74 allocated to subscription). Domestic institutional subscription (51 issues): $2148; Foreign postage extra: Air assist delivery: $98. First class, airmail, student, and emeritus rates on request. Canadian rates with GST available upon request, GST #125488122. Publications Mail Agreement Number 1069624. **Printed in the U.S.A.**
Change of address: Allow 4 weeks, giving old and new addresses and 8-digit account number. **Postmaster:** Send change of address to AAAS, P.O. Box 96178, Washington, DC 20090–6178. **Single-copy sales:** $15 each plus shipping and handling available from backissues.sciencemag.org; bulk rate on request. **Authorization to reproduce** material for internal or personal use under circumstances not falling within the fair use provisions of the Copyright Act can be obtained through the Copyright Clearance Center (CCC), www.copyright.com. The identification code for *Science* is 0036-8075. *Science* is indexed in the *Reader's Guide to Periodical Literature* and in several specialized indexes.

Science AAAS

Editor-in-Chief Holden Thorp, hthorp@aaas.org

Executive Editor Monica M. Bradford

Editors, Research Valda Vinson, Jake S. Yeston **Editor, Insights** Lisa D. Chong

DEPUTY EDITORS Julia Fahrenkamp-Uppenbrink (UK), Stella M. Hurtley (UK), Phillip D. Szuromi, Sacha Vignieri **SR. EDITORIAL FELLOW** Andrew M. Sugden (UK) **SR. EDITORS** Gemma Alderton (UK), Caroline Ash (UK), Brent Grocholski, Pamela J. Hines, Di Jiang, Marc S. Lavine (Canada), Yevgeniya Nusinovich, Ian S. Osborne (UK), Beverly A. Purnell, L. Bryan Ray, H. Jesse Smith, Keith T. Smith (UK), Jelena Stajic, Peter Stern (UK), Valerie B. Thompson, Brad Wible, Laura M. Zahn **ASSOCIATE EDITORS** Michael A. Funk, Priscilla N. Kelly, Tage S. Rai, Seth Thomas Scanlon (UK), Yury V. Suleymanov **LETTERS EDITOR** Jennifer Sills **LEAD CONTENT PRODUCTION EDITORS** Harry Jach, Lauren Kmec **CONTENT PRODUCTION EDITORS** Amelia Beyna, Jeffrey E. Cook, Chris Filiatreau, Julia Katris, Nida Masiulis, Suzanne M. White **SR. EDITORIAL COORDINATORS** Carolyn Kyle, Beverly Shields **EDITORIAL COORDINATORS** Aneera Dobbins, Joi S. Granger, Jeffrey Hearn, Lisa Johnson, Maryrose Madrid, Ope Martins, Shannon McMahon, Jerry Richardson, Hilary Stewart (UK), Alana Warnke, Alice Whaley (UK), Anita Wynn **PUBLICATIONS ASSISTANTS** Jeremy Dow, Alexander Kief, Ronmel Navas, Brian White **EXECUTIVE ASSISTANT** Jessica Slater **ASI DIRECTOR, OPERATIONS** Janet Clements (UK) **ASI SR. OFFICE ADMINISTRATOR** Jessica Waldock (UK)

News Editor Tim Appenzeller

NEWS MANAGING EDITOR John Travis **INTERNATIONAL EDITOR** Martin Enserink **DEPUTY NEWS EDITORS** Elizabeth Culotta, Lila Guterman, David Grimm, Eric Hand (Europe), David Malakoff **SR. CORRESPONDENTS** Daniel Clery (UK), Jon Cohen, Jeffrey Mervis, Elizabeth Pennisi **ASSOCIATE EDITORS** Jeffrey Brainard, Catherine Matacic **NEWS REPORTERS** Adrian Cho, Jennifer Couzin-Frankel, Jocelyn Kaiser, Kelly Servick, Robert F. Service, Erik Stokstad, Paul Voosen, Meredith Wadman **INTERNS** Lucy Hicks, Cathleen O'Grady **CONTRIBUTING CORRESPONDENTS** Warren Cornwall, Andrew Curry (Berlin), Ann Gibbons, Sam Kean, Eli Kintisch, Kai Kupferschmidt (Berlin), Andrew Lawler, Mitch Leslie, Eliot Marshall, Virginia Morell, Dennis Normile (Shanghai), Elisabeth Pain (Careers), Charles Piller, Michael Price, Tania Rabesandratana (Barcelona), Joshua Sokol, Emily Underwood, Gretchen Vogel (Berlin), Lizzie Wade (Mexico City) **CAREERS** Donisha Adams, Rachel Bernstein (Editor), Katie Langin (Associate Editor) **COPY EDITORS** Julia Cole (Senior Copy Editor), Cyra Master (Copy Chief) **ADMINISTRATIVE SUPPORT** Meagan Weiland

Creative Director Beth Rakouskas

DESIGN MANAGING EDITOR Marcy Atarod **GRAPHICS MANAGING EDITOR** Alberto Cuadra **PHOTOGRAPHY MANAGING EDITOR** William Douthitt **WEB CONTENT STRATEGY MANAGER** Kara Estelle-Powers **DESIGN EDITOR** Chrystal Smith **DESIGNER** Christina Aycock **GRAPHICS EDITOR** Nirja Desai **INTERACTIVE GRAPHICS EDITOR** Kelly Franklin **SENIOR SCIENTIFIC ILLUSTRATORS** Valerie Altounian, Chris Bickel **SCIENTIFIC ILLUSTRATOR** Alice Kitterman **SENIOR GRAPHICS SPECIALISTS** Holly Bishop, Nathalie Cary **SENIOR PHOTO EDITOR** Emily Petersen **PHOTO EDITOR** Kaitlyn Dolan **WEB DESIGNER** Jennie Pajerowski

Chief Executive Officer and Executive Publisher Sudip Parikh

Publisher, Science Family of Journals Bill Moran

DIRECTOR, BUSINESS SYSTEMS AND FINANCIAL ANALYSIS Randy Yi **DIRECTOR, BUSINESS OPERATIONS & ANALYSIS** Eric Knott **DIRECTOR OF ANALYTICS** Enrique Gonzales **MANAGER, BUSINESS OPERATIONS** Jessica Tierney **SENIOR BUSINESS ANALYST** Cory Lipman, Meron Kebede **FINANCIAL ANALYST** Alexander Lee **ADVERTISING SYSTEM ADMINISTRATOR** Tina Burks **SENIOR SALES COORDINATOR** Shirley Young **DIGITAL/PRINT STRATEGY MANAGER** Jason Hillman **QUALITY TECHNICAL MANAGER** Marcus Spiegler **ASSISTANT MANAGER DIGITAL/PRINT** Rebecca Doshi **SENIOR CONTENT SPECIALISTS** Steve Forrester, Jacob Hedrick, Antoinette Hodal, Lori Murphy **PRODUCTION SPECIALIST** Kristin Wowk **DIGITAL PRODUCTION MANAGER** Lisa Stanford **CONTENT SPECIALIST** Kimberley Oster **ADVERTISING PRODUCTION OPERATIONS MANAGER** Deborah Tompkins **DESIGNER, CUSTOM PUBLISHING** Jeremy Huntsinger **SR. TRAFFIC ASSOCIATE** Christine Hall **SPECIAL PROJECTS ASSOCIATE** Sarah Dhere

ASSOCIATE DIRECTOR, BUSINESS DEVELOPMENT Justin Sawyers **GLOBAL MARKETING MANAGER** Allison Pritchard **DIGITAL MARKETING MANAGER** Aimee Aponte **JOURNALS MARKETING MANAGER** Shawana Arnold **MARKETING ASSOCIATES** Tori Velasquez, Mike Romano, Ashley Hylton **DIGITAL MARKETING SPECIALIST** Asleigh Rojanavongse **SENIOR DESIGNER** Kim Huynh

DIRECTOR AND SENIOR EDITOR, CUSTOM PUBLISHING Sean Sanders **ASSISTANT EDITOR, CUSTOM PUBLISHING** Jackie Oberst

DIRECTOR, PRODUCT & PUBLISHING DEVELOPMENT Chris Reid **DIRECTOR, BUSINESS STRATEGY AND PORTFOLIO MANAGEMENT** Sarah Whalen **ASSOCIATE DIRECTOR, PRODUCT MANAGMENT** Kris Bishop **PRODUCT DEVELOPMENT MANAGER** Scott Chernoff **PUBLISHING TECHNOLOGY MANAGER** Michael Di Natale **SR. PRODUCT ASSOCIATE** Robert Koepke **SPJ ASSOCIATE** Samantha Bruno Fuller

DIRECTOR, INSTITUTIONAL LICENSING Iquo Edim **ASSOCIATE DIRECTOR, RESEARCH & DEVELOPMENT** Elisabeth Leonard **MARKETING MANAGER** Kess Knight **SENIOR INSTITUTIONAL LICENSING MANAGER** Ryan Rexroth **INSTITUTIONAL LICENSING MANAGER** Marco Castellan **MANAGER, AGENT RELATIONS & CUSTOMER SUCCESS** Judy Lillibridge **SENIOR OPERATIONS ANALYST** Lana Guz **FULFILLMENT COORDINATOR** Melody Stringer **SALES COORDINATOR** Josh Haverlock

DIRECTOR, GLOBAL SALES Tracy Holmes **US EAST COAST AND MID WEST SALES** Stephanie O'Connor **US WEST COAST SALES** Lynne Stickrod **US SALES MANAGER, SCIENCE CAREERS** Claudia Paulsen-Young **US SALES REP, SCIENCE CAREERS** Tracy Anderson **ASSOCIATE DIRECTOR, ROW** Roger Goncalves **SALES REP, ROW** Sarah Lelarge **SALES ADMIN ASSISTANT, ROW** Bryony Cousins **DIRECTOR OF GLOBAL COLLABORATION AND ACADEMIC PUBLISHING RELATIONS, ASIA** Xiaoying Chu **ASSOCIATE DIRECTOR, INTERNATIONAL COLLABORATION** Grace Yao **SALES MANAGER** Danny Zhao **MARKETING MANAGER** Kilo Lan **ASCA CORPORATION, JAPAN** Kaoru Sasaki (Tokyo), Miyuki Tani (Osaka) **COLLABORATION/ CUSTOM PUBLICATIONS/JAPAN** Adarsh Sandhu

DIRECTOR, COPYRIGHT, LICENSING AND SPECIAL PROJECTS Emilie David **RIGHTS AND LICENSING COORDINATOR** Jessica Adams **RIGHTS AND PERMISSIONS ASSOCIATE** Elizabeth Sandler **CONTRACTS AND LICENSING ASSOCIATE** Lili Catlett

---

MAIN HEADQUARTERS
Science/AAAS
1200 New York Ave. NW
Washington, DC 20005

SCIENCE INTERNATIONAL
Clarendon House
Clarendon Road
Cambridge, CB2 8FH, UK

SCIENCE CHINA
Room 1004, Culture Square
No. 59 Zhongguancun St.
Haidian District, Beijing, 100872

SCIENCE JAPAN
ASCA Corporation
Sibaura TY Bldg. 4F, 1-14-5
Shibaura Minato-ku
Tokyo, 108-0073 Japan

EDITORIAL
science_editors@aaas.org

NEWS
science_news@aaas.org

INFORMATION FOR AUTHORS
sciencemag.org/authors/science-information-authors

REPRINTS AND PERMISSIONS
sciencemag.org/help/reprints-and-permissions

MEDIA CONTACTS
scipak@aaas.org

MULTIMEDIA CONTACTS
SciencePodcast@aaas.org
ScienceVideo@aaas.org

INSTITUTIONAL SALES AND SITE LICENSES
sciencemag.org/librarian

PRODUCT ADVERTISING & CUSTOM PUBLISHING
advertising.sciencemag.org/products-services
science_advertising@aaas.org

CLASSIFIED ADVERTISING
advertising.sciencemag.org/science-careers
advertise@sciencecareers.org

JOB POSTING CUSTOMER SERVICE
employers.sciencecareers.org
support@sciencecareers.org

MEMBERSHIP AND INDIVIDUAL SUBSCRIPTIONS
sciencemag.org/subscriptions

MEMBER BENEFITS
aaas.org/membercentral

AAAS BOARD OF DIRECTORS
CHAIR Steven Chu
PRESIDENT Claire M. Fraser
PRESIDENT-ELECT Susan G. Amara
TREASURER Carolyn N. Ainslie
CHIEF EXECUTIVE OFFICER
Sudip Parikh
BOARD Cynthia M. Beall
Rosina M. Bierbaum
Ann Bostrom
Stephen P.A. Fodor
S. James Gates, Jr.
Laura H. Greene
Kaye Husbands Fealing
Maria M. Klawe
Robert B. Millard
Alondra Nelson
William D. Provine

Science serves as a forum for discussion of important issues related to the advancement of science by publishing material on which a consensus has been reached as well as including the presentation of minority or conflicting points of view. Accordingly, all articles published in *Science*—including editorials, news and comment, and book reviews—are signed and reflect the individual views of the authors and not official points of view adopted by AAAS or the institutions with which the authors are affiliated.

BOARD OF REVIEWING EDITORS (Statistics board members indicated with **(S)**)

Takuzo Aida, *U. of Tokyo*
Leslie Aiello, *Wenner-Gren Foundation*
Deji Akinwande, *UT Austin*
Judith Allen, *U. of Manchester*
Marcella Alsan, *Harvard U.*
Sebastian Amigorena, *Institut Curie*
James Analytis, *UC Berkeley*
Trevor Archer, *NIEHS, NIH*
Paola Arlotta, *Harvard U.*
David Awschalom, *U. of Chicago*
Clare Baker, *U. of Cambridge*
Delia Baldassarri, *NYU*
Nenad Ban, *ETH Zürich*
Franz Bauer, *Pontificia U. Católica de Chile*
Ray H. Baughman, *UT Dallas*
Carlo Beenakker, *Leiden U.*
Yasmine Belkaid, *NIAID, NIH*
Philip Benfey, *Duke U.*
Kiros T. Berhane, *Columbia U.*
Bradley Bernstein, *Mass. General Hospital*
Joseph J. Berry, *NREL*
Alessandra Biffi, *Harvard Med.*
Chris Bowler, *École Normale Supérieure*
Ian Boyd, *U. of St. Andrews*
Emily Brodsky, *UC Santa Cruz*
Ron Brookmeyer, *UCLA* **(S)**
Christian Büchel, *UKE Hamburg*
Dennis Burton, *Scripps Res.*
Carter Tribley Butts, *UC Irvine*
György Buzsáki, *NYU School of Med.*
Mariana Byndloss, *Vanderbilt U. Med. Ctr*
Annmarie Carlton, *UC Irvine*
Nick Chater, *U. of Warwick*
Ling-Ling Chen, *SIBCB, CAS*
M. Keith Chen, *UCLA*
Zhijian Chen, *UT Southwestern Med. Ctr.*
Ib Chorkendorff, *Denmark TU*
James J. Collins, *MIT*
Robert Cook-Deegan, *Arizona State U.*
Virginia Cornish *Columbia U.*
Carolyn Coyne, *U. of Pitt.*
Roberta Croce, *VU Amsterdam*
Ismaila Dabo, *Penn State U.*
Jeff L. Dangl, *UNC*
Chiara Daraio, *Caltech*
Nicolas Dauphas, *U. of Chicago*
Christian Davenport, *U. of Michigan*
Frans de Waal, *Emory U.*
Claude Desplan, *NYU*
Sandra Díaz, *U. Nacional de Córdoba*
Ulrike Diebold, *TU Wien*
Stefanie Dimmeler, *Goethe-U. Frankfurt*
Hong Ding, *Inst. of Physics, CAS*
Dennis Discher, *UPenn*
Jennifer A. Doudna, *UC Berkeley*
Raissa M. D'Souza, *UC Davis*
Bruce Dunn, *UCLA*
William Dunphy, *Caltech*
Scott Edwards, *Harvard U.*
Todd Ehlers, *U. of Tübingen*
Jennifer Elisseeff, *Johns Hopkins U.*
Andrea Encalada, *U. San Francisco de Quito*
Nader Engheta, *U. of Penn.*
Karen Ersche, *U. of Cambridge*
Beate Escher, *UFZ & U. of Tübingen*
Barry Everitt, *U. of Cambridge*
Vanessa Ezenwa, *U. of Georgia*
Michael Feuer, *GWU*
Toren Finkel, *U. of Pitt. Med. Ctr.*
Gwenn Flowers, *Simon Fraser U.*
Peter Fratzl, *Max Planck Inst. Potsdam*
Elaine Fuchs, *Rockefeller U.*
Jay Gallagher, *U. of Wisconsin*
Daniel Geschwind, *UCLA*
Ramon Gonzalez, *U. of South Florida*
Sandra González-Bailón, *UPenn*
Elizabeth Grove, *U. of Chicago*
Nicolas Gruber, *ETH Zürich*
Hua Guo, *U. of New Mexico*
Taekjip Ha, *Johns Hopkins U.*
Sharon Hammes-Schiffer, *Yale U.*
Wolf-Dietrich Hardt, *ETH Zürich*
Louise Harra, *U. Coll. London*
Jian He, *Clemson U.*
Carl-Philipp Heisenberg, *IST Austria*
Ykä Helariutta, *U. of Cambridge*
Janet G. Hering, *Eawag*
Heather Hickman, *NIAID, NIH*
Hans Hilgenkamp, *U. of Twente*
Kai-Uwe Hinrichs, *U. of Bremen*
Deirdre Hollingsworth, *U. of Oxford*
Randall Hulet, *Rice U.*
Auke Ijspeert, *EPFL*
Akiko Iwasaki, *Yale U.*
Stephen Jackson, *USGS & U. of Arizona*
Erich Jarvis, *Rockefeller U.*
Peter Jonas, *IST Austria*
Matt Kaeberlein, *U. of Wash.*
William Kaelin Jr., *Dana-Farber Cancer Inst.*
Daniel Kammen, *UC Berkeley*
V. Narry Kim, *Seoul Nat. U.*
Robert Kingston, *Harvard Med.*
Nancy Knowlton, *Smithsonian Institution*
Etienne Koechlin, *École Normale Supérieure*
Alex L. Kolodkin, *Johns Hopkins U.*
Julija Krupic, *U. of Cambridge*
Gabriel Lander, *Scripps Res.* **(S)**
Mitchell A. Lazar, *UPenn*
Wendell Lim, *UCSF*
Luis Liz-Marzán, *CIC biomaGUNE*
Omar Lizardo, *UCLA*
Jonathan Losos, *Wash. U. in St. Louis*
Ke Lu, *Inst. of Metal Res., CAS*
Christian Lüscher, *U. of Geneva*
Jean Lynch-Stieglitz, *Georgia Inst. of Tech.*
David Lyons, *U. of Edinburgh*
Fabienne Mackay, *QIMR Berghofer*
Anne Magurran, *U. of St. Andrews*
Asifa Majid, *U. of York*
Oscar Marín, *King's Coll. London*
Charles Marshall, *UC Berkeley*
Christopher Marx, *U. of Idaho*
David Masopust, *U. of Minnesota*
Geraldine Masson, *CNRS*
Jason Matheny, *Georgetown U.*
Heidi McBride, *McGill U.*
C. Robertson McClung, *Dartmouth*
Rodrigo Medellín, *U. Nacional Autónoma de México*
Jane Memmott, *U. of Bristol*
C. Jessica Metcalf, *Princeton U.*
Baoxia Mi, *UC Berkeley*
Tom Misteli, *NCI, NIH*
Alison Motsinger-Reif, *NIEHS, NIH* **(S)**
Danielle Navarro, *U. of New South Wales*
Daniel Nettle, *Newcastle U.*
Daniel Neumark, *UC Berkeley*
Beatriz Noheda, *U. of Groningen*
Helga Nowotny, *Vienna Sci., Res. & Tech. Fund*
Rachel O'Reilly, *U. of Birmingham*
Pilar Ossorio, *U. of Wisconsin*
Andrew Oswald, *U. of Warwick*
Isabella Pagano, *Istituto Nazionale di Astrofisica*
Elizabeth Levy Paluck, *Princeton U.*
Jane Parker, *Max Planck Inst. Cologne*
Giovanni Parmigiani, *Dana-Farber Cancer Inst.* **(S)**
Daniel Pauly, *U. of British Columbia*
Samuel Pfaff, *Salk Inst.*
Julie Pfeiffer, *UT Southwestern Med. Ctr.*
Philip Phillips, *UIUC*
Matthieu Piel, *Institut Curie*
Kathrin Plath, *UCLA*
Martin Plenio, *Ulm U.*
Katherine Pollard, *UCSF*
Elvira Poloczanska, *Alfred-Wegener-Inst.*
Julia Pongratz, *Ludwig Maximilians U.*
Philippe Poulin, *CNRS*
Jonathan Pritchard, *Stanford U.*
Lei Stanley Qi, *Stanford U.*
Trevor Robbins, *U. of Cambridge*
Joeri Rogelj, *Imperial Coll. London*
Amy Rosenzweig, *Northwestern U.*
Mike Ryan, *UT Austin*
Miquel Salmeron, *Lawrence Berkeley Nat. Lab*
Nitin Samarth, *Penn State U.*
Erica Ollmann Saphire, *La Jolla Inst.*
Joachim Saur, *U. zu Köln*
Alexander Schier, *Harvard U.*
Wolfram Schlenker, *Columbia U.*
Susannah Scott, *UC Santa Barbara*
Anuj Shah, *U. of Chicago*
Vladimir Shalaev, *Purdue U.*
Jie Shan, *Cornell U.*
Beth Shapiro, *UC Santa Cruz*
Jay Shendure, *U. of Wash.*
Steve Sherwood, *U. of New South Wales*
Brian Shoichet, *UCSF*
Robert Siliciano, *JHU School of Med.*
Lucia Sivilotti, *U. Coll. London*
Alison Smith, *John Innes Centre*
Richard Smith, *UNC* **(S)**
Mark Smyth, *QIMR Berghofer*
John Speakman, *U. of Aberdeen*
Tara Spires-Jones, *U. of Edinburgh*
Allan C. Spradling, *Carnegie Institution for Sci.*
V. S. Subrahmanian, *Dartmouth*
Ira Tabas, *Columbia U.*
Eriko Takano, *U. of Manchester*
Patrick Tan, *Duke-NUS Med. School*
Sarah Teichmann, *Wellcome Sanger Inst.*
Rocio Titiunik, *Princeton U.*
Shubha Tole, *Tata Inst. of Fundamental Res.*
Kimani Toussaint, *Brown U.*
Wim van der Putten, *Netherlands Inst. of Ecology*
Reinhilde Veugelers, *KU Leuven*
Bert Vogelstein, *Johns Hopkins U.*
David Wallach, *Weizmann Inst.*
Jane-Ling Wang, *UC Davis* **(S)**
Jessica Ware, *Amer. Mus. of Natural Hist.*
David Waxman, *Fudan U.*
Chris Wikle, *U. of Missouri* **(S)**
Terrie Williams, *UC Santa Cruz*
Ian A. Wilson, *Scripps Res.* **(S)**
Yu Xie, *Princeton U.*
Jan Zaanen, *Leiden U.*
Kenneth Zaret, *UPenn School of Med.*
Bing Zhu, *Inst. of Biophysics, CAS*
Xiaowei Zhuang, *Harvard U.*
Maria Zuber, *MIT*

Announcing the 2020
Swanson and META award winners

Partners in Science
A MURDOCK TRUST PROGRAM

College Science Research
A MURDOCK TRUST PROGRAM

The M.J. Murdock Charitable Trust congratulates **Dr. Daniel Burgard**, Professor of Chemistry, University of Puget Sound, winner of the 2020 Lynwood W. Swanson Scientific Research Award, and **Dr. Anna Ritz**, Associate Professor of Biology, Reed College, winner of the 2020 Lynwood W. Swanson Promise for Scientific Research Award, as well as **Ms. Emily Lindstrum Carson**, Earth Science Teacher, Olympia High School, winner of the 2020 Murdock Exemplary Teacher-Researcher Award.


Dr. Dan Burgard


Dr. Anna Ritz


Ms. Emily Carson

For more information on these awards and how scientific collaboration and partnership is helping to inspire the next generation of researchers and teachers, visit **murdocktrust.org**

M.J. Murdock
CHARITABLE TRUST

Where Science Gets Social.
AAAS.ORG/COMMUNITY


Member
COMMUNITY
AAAS

AMERICAN ASSOCIATION FOR THE ADVANCEMENT OF SCIENCE

ScienceSignaling.org

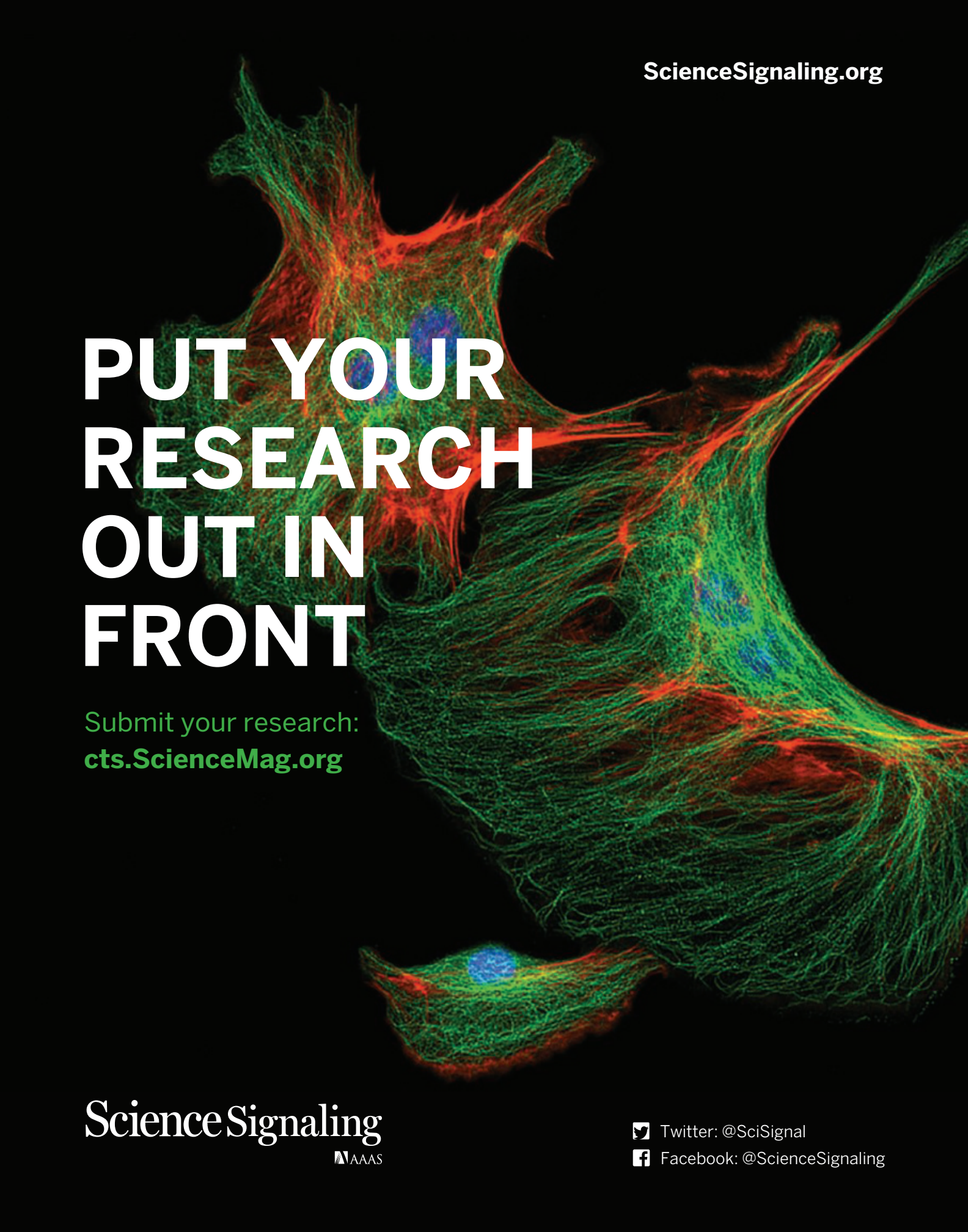

PUT YOUR RESEARCH OUT IN FRONT

Submit your research:
cts.ScienceMag.org

Science Signaling
AAAS

Twitter: @SciSignal
Facebook: @ScienceSignaling

EDITORIAL

A genome to celebrate

This week, *Science* celebrates the impending 20th anniversary of the publication of the draft human genome sequence—a landmark achievement by any measure. The American Association for the Advancement of Science (AAAS, the publisher of *Science*) also looks forward to next week's annual meeting, whose theme is "Understanding Dynamic Ecosystems." At first glance, these two events may seem unrelated. But the successful completion of the human genome sequence ushered in biology's era of "big science" and created a research ecosystem for tackling complex, technology-driven, and data-intensive multidisciplinary projects that continue to improve our understanding of cancer, the microbiome, the brain, and other areas of biology.

The Human Genome Project (HGP) was an internationally supported public project (Celera Genomics was the private effort that simultaneously sequenced the human genome). When the endeavor was launched in 1990, collaboration among a diverse group of scientists was essential because the sequencing was distributed across a number of international research sites. High-throughput technologies for DNA sequencing were critical to the project's success, and the participation of biotech companies in the effort was instrumental in driving down the cost, speed, and throughput of generating DNA sequence. The ever-increasing amount of sequence data drove the development of mathematical and computational tools for assembling and annotating the data. Neither the laboratory scientists nor the computational scientists could have done this alone, and the convergence of these disciplines has been one of the most important legacies of the early genome efforts. There was also a commitment to train the next generation of genome scientists, and over the past 20 years, many colleges and universities have established new undergraduate and graduate programs in quantitative and systems biology. Life sciences students today graduate with a very different set of skills than they did in 2000.

The topic of ongoing data availability was addressed throughout the sequencing endeavor. The Bermuda accord in 1996 and the Fort Lauderdale agreement in 2003 were crafted with the idea that these types of large, data-intensive projects should be community resources and the data generated should be freely available to all. This notion ran counter to the tradition that scientific data were made available at the time of peer-reviewed publication, and the idea was initially met with some skepticism. Today, through U.S. National Center for Biotechnology Information and affiliated databases, users can query genome, epigenome, transcriptome, metagenome, and metatranscriptome datasets from thousands of species. Despite concerns that the HGP would divert scarce resources away from individual investigators, and a view that the work was monotonous and repetitive, the availability of genome sequences from hundreds of thousands of microbes, plants, and animals has transformed the biological sciences. These public resources provide a robust foundation for biomedical research and discovery, and scientists with internet access can participate in genome analysis work without having to generate sequence data themselves. Indeed, the more these large datasets are interrogated by investigators with diverse perspectives, the greater the number of insights that will emerge.

> "...the human genome sequence ushered in biology's era of 'big science'..."

At its inception, efforts to sequence the human genome effort raised questions about the potential ethical, legal, and social issues that would arise as we deciphered our own genetic blueprint. These concerns ranged from privacy, discrimination, and ownership of data to the concept of "self." Passage of the Genetic Information Nondiscrimination Act (GINA) by the U.S. Congress in 2008 ensured that genetic information would not be used in health insurance and employment decisions. Senator Edward Kennedy called GINA "the first major new civil rights bill of the new century."

The completion of the draft sequence laid the foundation for a new precision medicine paradigm that aims to use a person's unique genetic profile to guide decisions about the treatment and prevention of disease. We have already seen some signs that precision medicine is possible, and although off to a slow start, the promise of this approach may ultimately be realized.

Given the pace at which breakthroughs based on the human genome sequence are happening, when we next commemorate the publication of the draft human genome sequence, be it at 25, 30, or 50 years, we may look back again, realize that this accomplishment was a watershed for the biological sciences, and marvel at how far we have come in such a short period of time.

–Claire M. Fraser

PHOTO: TOM JEMSKI/UNIVERSITY OF MARYLAND SCHOOL OF MEDICINE

Claire M. Fraser is the Dean's Endowed Professor and director of the Institute for Genome Sciences, University of Maryland, Baltimore, MD, USA, and is president of the American Association for the Advancement of Science, Washington, DC, USA. cmfraser@som.umaryland.edu

10.1126/science.abg8615

NEWS

> “I don’t want to call somebody on the phone and say, ‘You know … I wrote the textbook on vaccines.’”
>
> **Stanley Plotkin,** 88, who pioneered the widely used rubella vaccine, in *The Washington Post*, about the many tries it took for him to obtain a COVID-19 vaccine.

IN BRIEF

Edited by **Jeffrey Brainard**

EYE ON BIDEN

Order calls for science integrity review

Federal government policies designed to protect scientists from political interference will get a sweeping review under a 27 January order from President Joe Biden. In an implicit swipe at former President Donald Trump’s administration, the memo asks U.S. agencies to document instances in which “improper political interference” led to the suppression or distortion of data. It also asks them to review dozens of technical advisory panels and determine whether to revive ones killed or overhauled by Trump. Gretchen Goldman of the Union of Concerned Scientists says the review offers “a huge chance to assess and learn from what went wrong under Trump.” Some science policy specialists say Congress should pass new laws to prevent interference.

Travel ban reversal raises hope

IMMIGRATION | Researchers last week praised President Joe Biden’s Inauguration Day decision to revoke former President Donald Trump’s so-called Muslim ban. Imposed in 2017, the policy barred citizens of Iran, Syria, and several other Muslim-majority nations from entering the United States, leaving thousands of students and scientists in limbo at home. Biden’s move could help others already in the United States on single-entry visas who did not dare to leave the country out of fear they could not return. Despite the change, the COVID-19 pandemic and U.S. sanctions on Iran, the most advanced scientifically of the countries blacklisted, will likely continue to limit travel. Still, Sara Mashhadi Nejad (below), an aspiring environmental engineer in Iran, hopes Biden’s action will help her accomplish her goal of pursuing doctoral studies at the University of Toledo, which accepted her in 2019. The travel ban forced her to wait and reapply for a visa and admission to the university. “I will persevere,” she said.

PHOTO: MOSTAFA MOHAMMAD REZAEE

Harris recalls NIH memories

LEADERSHIP | As U.S. Vice President Kamala Harris last week received the Moderna COVID-19 vaccine at the National Institutes of Health (NIH), she called it a “full circle” moment. Her late mother, breast cancer researcher Shyamala Gopalan, served on NIH peer-review panels, and, Harris recalled, “My first job was cleaning pipettes in my mother’s lab,” CNN reported. Harris, who had received her first vaccine dose in December 2020, told NIH employees that everyone should “take the vaccine when it is your turn.”

Court axes Trump’s EPA data rule

POLICY | Ending a long battle, a U.S. federal judge on 1 February killed a controversial regulation that would have limited the kinds of scientific evidence the Environmental Protection Agency (EPA) could use in rulemaking. Environmental groups had challenged the rule in a lawsuit, later backed by President Joe Biden’s administration, and Judge Brian Morris of the U.S. District Court of Montana sided with their argument that former President Donald Trump’s administration violated proper procedures in finalizing the rule on 5 January. EPA spent much of Trump’s term crafting the rule, which originated in an effort by Republicans in Congress to prevent EPA from using confidential patient data from large health studies to justify stiffer air pollution regulations. The rule was “a flagrantly unlawful attempt to restrict EPA from using important scientific studies,” said attorney Benjamin Levitan of the Environmental Defense Fund. “We’re glad the court … put a stop to it.”

Doomsday Clock stays dire

GLOBAL SECURITY | The Bulletin of the Atomic Scientists last week kept its iconic Doomsday Clock unchanged from 2020, set at 100 seconds from a catastrophic “midnight” that symbolizes society’s self-destruction from military conflict and global warming. The past year saw little progress on those fronts, said the group of scientists, which monitors global tensions. But it cited some cause for hope, such as the election of a U.S. president who acknowledges the human contribution to climate change and the United States and Russia’s intentions to extend for 5 years their New Strategic Arms Reduction Treaty, set to expire on 5 February. Rachel Bronson, president of the Bulletin, said the COVID-19 pandemic, though lethal and global, doesn’t have the power to obliterate humanity. But she said it was “a wake-up call,” showing that national governments and international organizations remain unprepared to handle the even greater threats posed by nuclear war, climate change, and other new diseases.

ECOLOGY

Lizards help suppress Lyme disease in U.S. southeast

Skinks and a warm climate help protect people from Lyme disease in the southeastern United States, a study has found. Scientists have long known the disease—which is caused by bacteria borne by black-legged ticks (*Ixodes scapularis*) and can cause serious illness in humans bitten by them—is more common in the north, even though the ticks are found throughout the U.S. East Coast. A research team studied eight sites in the north and south and found factors that help explain the regional difference in human infections. In the north, the ticks prefer mammals; but in the south, they prefer glomming onto skinks (above, with attached ticks) and other lizards. These animals tend to transmit the Lyme disease bacteria poorly, infecting fewer ticks. What's more, the south's warmer temperatures tend to drive ticks under leaves on the ground to avoid dehydration, where they are less likely to bite passing humans. In *PLOS Biology* last week, the team speculated that a warming climate may lessen the incidence of Lyme disease in mid-Atlantic states, as southern lizards move north and ticks take cover.

U.S. cities underreport emissions

CLIMATE CHANGE | Cities in the United States are underestimating their greenhouse gas emissions by an average of more than 18%, a study has found. U.S. and French scientists compared estimates by 48 cities with an independent model. In all but 11 cases, the cities' projections were lower. Undercounts resulted because, for example, some cities estimated local car emissions primarily by checking local gasoline sales but did not monitor all traffic, according to the study, published in N*ature Communications* on 2 February. Cities with the biggest underestimates included Dallas and Los Angeles. The authors said the inaccuracies make it difficult to mitigate emissions, but researchers are building better accounting systems. If all U.S. cities undercount by as much, they are missing emissions totaling more than all those released annually in California, the study estimates.

Pandemic slams essential workers

COVID-19 | Workers in food, agriculture, transportation, and other essential sectors have suffered some of the highest increases in mortality during the COVID-19 pandemic, according to an analysis of California death records. Many of the jobs with large increases cannot be done while sheltering at home. The study, described in a 22 January preprint on the medRxiv server, examined records from March to October 2020 to calculate "excess mortality" over the same months in 2018 and 2019. Yea-Hung Chen at the University of California, San Francisco, and colleagues noted that disproportionately high numbers of Black and Latino people and individuals with low educational attainment work in high-risk jobs; this could help explain the above-average excess mortality observed among those groups as a whole, they said. The authors suggest prioritizing the hardest hit occupations for vaccination and providing essential workers who cannot stay home with free protective gear, easily accessible testing, and generous sick leave policies.

Increase in observed versus expected deaths for selected occupations

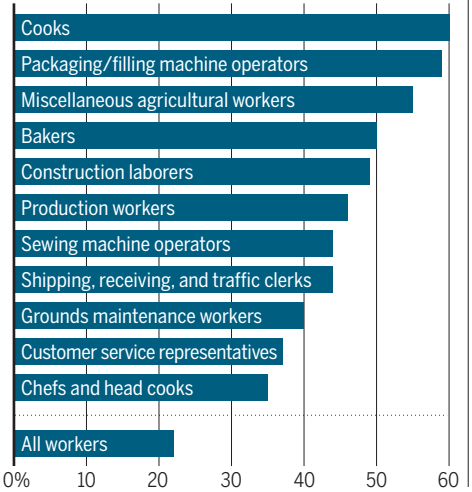

Football's risky practices

BIOMEDICINE | Almost three-quarters of concussions sustained by U.S. college football players occur during practice, a 1 February study in *JAMA Neurology* reports. Described as the largest of its kind, it evaluated 658 players in the National Collegiate Athletic Association from 2015 to 2019. The authors call for rules that reduce the number of practice sessions during which collisions are allowed; the National Football League and many high schools have already adopted them.

CREDITS: (PHOTO) GRAHAM HICKLING; (GRAPHIC) C. SMITH/*SCIENCE*; (DATA) Y. H. CHEN *ET AL.*, MEDRXIV, HTTPS://DOI.ORG/10.1101/2021.01.21.21250266

IN DEPTH

A volunteer in Soweto receives Novavax's COVID-19 vaccine in a South African trial that showed how a mutant virus reduces vaccine efficacy.

PHOTO: JOAO SILVA/THE NEW YORK TIMES/REDUX

COVID-19

Two new vaccines deliver good and bad news for the pandemic

Novavax and J&J data underscore challenge of viral variants

By **Jon Cohen**

Last week's efficacy results from two new COVID-19 vaccines bolstered confidence that more of the world will soon be protected from the worst of the pandemic disease, but simultaneously challenged the hopes that this first generation of vaccines will offer a sturdy shield against mild and moderate symptoms.

The COVID-19 vaccines made by Novavax and Johnson & Johnson (J&J) joined six others in showing extremely good protection against severe disease and death caused by SARS-CoV-2. But the multicountry trials conducted by each company found that in some places, the efficacy of their vaccines against mild disease fell far below the 90% to 95% range reported for other vaccines. The lowest efficacy against mild disease—49% and 57%, respectively, for Novavax and J&J—was in South Africa, where almost every case of symptomatic COVID-19 is caused by a mutant of SARS-CoV-2 that can dodge antibodies triggered by natural infection or vaccine-induced immunity.

"The euphoria over the vaccines has certainly been tempered by the recent data on the new variants," says Soumya Swaminathan, chief scientist for the World Health Organization. But she and others stress that the hope for perfection should not be the enemy of the good. Both of the new vaccines promise to prevent hospitalizations and deaths to the same degree as competitors, even against two of the most concerning viral variants.

In addition to increasing the world's paltry supply of COVID-19 vaccines, the new options might also speed mass immunization campaigns because of a key logistical advantage: Unlike the two messenger RNA (mRNA) vaccines authorized for use in the United States, which require subzero conditions during transport, they can be stored at 2°C to 8°C—refrigerator temperature. The J&J product offers another major plus: It is the first COVID-19 vaccine shown to work with one dose rather than two.

Company representatives and collaborating researchers revealed the new results within 16 hours of each other, in virtual press conferences and press releases that were often thin on data. First came Novavax, a small biotech firm once considered a dark horse in the COVID-19 vaccine race. In the mRNA vaccines that crossed the finish line first, a snippet of genetic code directs the recipient's cells to produce the SARS-CoV-2 surface protein, spike. In contrast, the Novavax candidate followed a more established strategy, mixing a labmade version of the viral protein with an immune-boosting adjuvant. A trial in the United Kingdom in more than 15,000 people found the vaccine was 89.3% efficacious against mild disease.

"These are spectacular results," says Clive Dix, chair of the U.K. Vaccine Taskforce. The vaccine also worked well against a highly transmissible SARS-CoV-2 variant, B.1.1.7, which accounted for more than half of the trial's COVID-19 cases. But interim results from a trial in South Africa were sobering. Among the 4400 participants, the efficacy of Novavax's vaccine plummeted to 49.4%—the first clinical evidence that a variant identified in South Africa can indeed sidestep vaccine-induced immunity to an extent, as lab evidence had suggested.

The South African trial also revealed that the variant readily evades natural immunity. Of the people in the placebo group who developed COVID-19, 30% had recovered from an earlier infection—a "really concerning" figure, says Shabir Madhi, dean of the medical school at the University of the Witwatersrand and the study's lead investigator. "We would have expected a large percentage of the population to have developed immunity from that first exposure."

Still, the trial results put to rest fears that South Africa's widespread variant might completely thwart the vaccine. "While there definitely is an impact, it's perhaps not as bad as we all thought it might be," says Lynn Morris, a virologist at the University of the Witwatersrand. And no one who was vaccinated died or was hospitalized, although there were only two cases of severe disease in the small trial's placebo group. Novavax says it is now developing "bivalent" vaccines

Science's COVID-19 reporting is supported by the Heising-Simons Foundation.

containing both the original spike and spikes altered to mimic variants of concern.

J&J reported similar bottom lines from a far larger study of its vaccine, made by its Janssen Pharmaceuticals division. The candidate, which like several two-dose COVID-19 vaccines uses a harmless adenovirus to deliver the gene for spike, was tested in 44,000 people in the United States, Latin America, and South Africa. The single-dose vaccine had an overall efficacy of 66% against symptomatic disease, rising to 85% against severe symptoms, regardless of a person's age or underlying medical conditions, the firm said.

The vaccine's efficacy against mild disease was 72% in the United States and 66% in Latin America, dropping to 57% in South Africa. But no one who received it anywhere required hospitalization for COVID-19 or died. "This represents a dream vaccine for a doctor," says Glenda Gray, a co-chair of the J&J study and head of the South African Medical Research Council. In South Africa, COVID-19 now is the No. 1 cause of death, eclipsing HIV/AIDS and tuberculosis.

J&J plans to file for emergency use authorization from the U.S. Food and Drug Administration (FDA) this week and projects it can produce 1 billion doses this year at about $10 per dose—one-sixth or less of the price of two doses of the mRNA vaccines. Novavax is discussing with FDA whether to wait for a readout from a larger efficacy trial underway in the United States, but says it can make 150 million doses per month as soon as May. It has not announced a price.

Gray and other researchers say the mRNA vaccines' spectacular efficacy against any COVID-19 symptoms may have become a misleading benchmark for a successful vaccine given SARS-CoV-2's evolution. Faced with mutant strains like the one in South Africa, those vaccines might not do much better than Novavax's and J&J's products did, they suspect. To many, solidly preventing severe disease, regardless of strain, is a significant win. "Do you want a vaccine that prevents coughs or do you want a vaccine that prevents death?" asks Lawrence Corey of the University of Washington, Seattle, who co-leads a trials network testing the J&J, Novavax, and other vaccines bankrolled by the U.S. government's Operation Warp Speed.

And as the emerging variants show, delivering COVID-19 vaccines into more arms is urgent, and the more options, the better. "What I take away from this week," says Nahid Bhadelia, an infectious disease physician at Boston Medical Center, "is that we have two more tools in our toolbox at a very precarious time." ■

With reporting by Meredith Wadman.

COVID-19

Danish scientists see tough times ahead as variant rises

Some say the country should reopen—even if it causes cases to surge—once vulnerable populations are vaccinated

By **Kai Kupferschmidt**

On its face, the curve of COVID-19 infections in Denmark looks reassuring enough. A nationwide lockdown has led numbers to plummet from more than 3000 daily cases in mid-December 2020 to just a few hundred now. But don't be fooled. "Sure, the numbers look nice," says Camilla Holten Møller of the Statens Serum Institute, who heads a group of experts modeling the epidemic. "But if we look at our models, this is the calm before the storm."

That's because the graph really reflects two epidemics: one, shrinking fast, that's caused by older variants of SARS-CoV-2, and a smaller, slowly growing outbreak of B.1.1.7, the variant first recognized in England and now driving a big third wave of the pandemic there. If B.1.1.7 keeps spreading at the same pace in Denmark, it will become the dominant variant later this month and cause the overall number of cases to rise again, despite the lockdown, Holten Møller says. "It is a complete game changer."

The same is likely happening in many countries without being noticed. But a massive virus-sequencing effort has allowed Denmark, a country of 5.8 million, to track the rise of the new COVID-19 variant more closely than any other country. "All eyes are on Denmark right now," says Kristian Andersen, an infectious diseases researcher at Scripps Research who is advising the Danish government. "When it comes to B.1.1.7, is there a way in which … we can prevent the kind of calamity that we have seen in the U.K. and Ireland, for example?" he asks.

The data aren't reassuring. Danish scientists' best guess is that B.1.1.7 spreads 1.55 times faster than previous variants, Holten Møller says. To keep it from spiraling out of control, the country will have to remain in lockdown—or even add new control measures—until a large part of the population has been vaccinated. That prospect is so unappealing that some epidemiologists say Denmark should consider an alternative: Reopen once the most vulnerable people are vaccinated, even if that means a big new surge in cases.

Denmark reported B.1.1.7 within its borders in December 2020, soon after the United Kingdom put the world on notice, and has since stepped up an already impressive virus-sequencing operation. Mads Albertsen, a bacterial genome researcher at Aalborg University, leads a team that has sequenced virus genomes from more than half of all COVID-19 patients so far this year and hopes to reach 70% soon.

It was clear by early January that B.1.1.7 was roughly doubling in frequency every week, says Lone Simonsen, an epidemiologist at Roskilde University. At that point, Denmark had already closed schools and restaurants; to combat the new threat, the lockdown was tightened by cutting the number of people allowed to gather from 10 to five, for example, and doubling the recommended distance between people from 1 to 2 meters. That helped bring the overall reproductive number (R) to a healthy 0.78, according to the most recent estimate. But B.1.1.7 still has an estimated R of 1.07; in

A new virus gathers steam

Previous SARS-CoV-2 variants are rapidly declining in Denmark (top), but B.1.1.7 is on the rise (bottom).

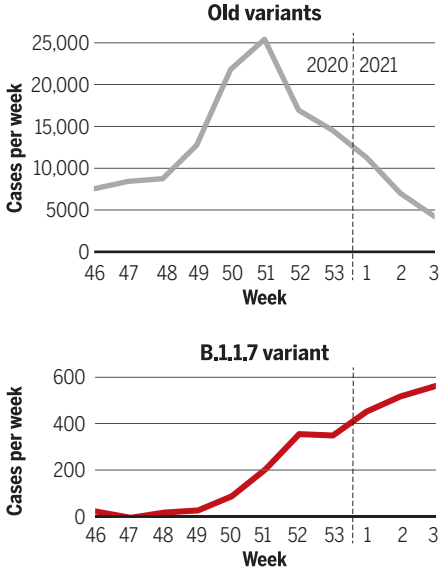

CREDITS: (GRAPHIC) V. ALTOUNIAN/*SCIENCE*; (DATA) STATENS SERUM INSTITUTE

other words, it's growing exponentially.

The country could take further steps such as requiring people to work from home when possible and improving contact tracing, which becomes easier as the numbers dwindle. Rolling out rapid tests could also help, and more can be done to encourage patients to isolate, says Michael Bang Petersen, a political scientist at Aarhus University; currently, half of those who receive a positive test do not self-isolate.

By doing more, Denmark can still rid itself of B.1.1.7 and avert a third wave, says Andersen, who points out that case numbers are falling in the United Kingdom, where B.1.1.7 now dominates: "It can be done, but it requires a tremendous amount of effort." (He says Denmark should attempt to end its epidemic altogether, New Zealand style, through aggressive measures and border closures.)

Others are not convinced the tide can be turned. The drop in the United Kingdom may partly be due to the fact that so many have been infected already and are no longer susceptible, says Viggo Andreasen, a modeler at Roskilde. At best, Denmark could push R for the variant just below 1, he says, leading to a very slow decline—although better weather by April could help.

So far, the public has accepted the government's message that the lockdown needs to remain in place despite the declining cases, says Petersen, who coordinates a project to study how the government and the public are reacting to the pandemic: "What has been amazing during January is that the numbers have substantially dropped, but at the same time, people have reduced their contacts even further." But that will be hard to sustain as time goes on, he says. "There's a huge pressure on the government to reopen the country," adds Thea Kølsen Fischer, a virologist at the University of Copenhagen. In a small first step, the government is reopening schools for children in first to fourth grade on 8 February.

Simonsen says the cost of extending the lockdown for many more months may prove too high. Instead, Denmark should consider opening as soon as people over age 50 and other vulnerable groups have been vaccinated—an effort that is underway. Reopening might trigger a sharp increase of cases among the unvaccinated, but few would presumably die. At that point, society could start to think of SARS-CoV-2 more like influenza, which also occasionally kills healthy young people, she says: "We don't close down birthday parties for this."

Andreasen disagrees. Accepting a new surge might have been a good strategy before other countries saw variants emerge that appear to partially evade human immunity. More infections raise the risk of further viral evolution, he says. "It's a nasty mix to have a population where half of the population harbors the virus, and the other half is like a big experimental vessel for the virus to learn how to escape immunity."

Letting the virus go would have another downside, says Devi Sridhar, a global health scientist at the University of Edinburgh: More people with mild infections might develop long-lasting health problems. "Given what we know about long COVID and the associated morbidity we might see," Sridhar says, "I just think the risks are high with that." ■

A shopping street in Copenhagen, Denmark, during the lockdown in January. Keeping the B.1.1.7 variant of COVID-19 at bay may require additional control measures, scientists say.

PHOTO: EMIL HELMS/RITZAU SCANPIX/AFP/GETTY IMAGES

ASTRONOMY

Speedy robots gather spectra for sky surveys

Telescopes retrofitted with hundreds of optical fibers dissect the light of stars and galaxies

By **Daniel Clery**

It was one of the stranger and more monotonous jobs in astronomy: plugging optical fibers into hundreds of holes in aluminum plates. Every day, technicians with the Sloan Digital Sky Survey (SDSS) prepped up to 10 plates that would be placed that night at the focus of the survey's telescopes in Chile and New Mexico. The holes matched the exact positions of stars, galaxies, or other bright objects in the telescopes' view. Light from each object fell directly on a fiber and was whisked off to a spectrograph, which split the light into its component wavelengths, revealing key details such as what the object is made of and how it is moving.

Now, after 20 years, the SDSS is going robotic. For the project's upcoming fifth set of surveys, known as the SDSS-V, plug plates are being replaced by 500 tiny robot arms, each holding fiber tips that patrol a small area of the telescope's focal plane. They can be reconfigured for a new sky map in 2 minutes. Other sky surveys are also adopting the speedy robots. They will not only save valuable observation time, but also allow the surveys to keep up with Europe's Gaia satellite, the upcoming Vera C. Rubin Observatory in Chile, and other efforts that produce huge catalogs of objects needing spectroscopic study. "It's driven by the science of enormous imaging surveys," says astronomer Richard Ellis of University College London.

COVID-19 has delayed the SDSS's robotic makeover. The survey's northern telescope at Apache Point Observatory in New Mexico began to take SDSS-V data in October 2020 using plug plates. It aims to switch over to the robots by mid-2021. The southern scope at Las Campanas Observatory in Chile will follow later in the year. "It's bananas," says SDSS-V Director Juna Kollmeier of the Carnegie Observatories, "but we're seeing the end of the tunnel."

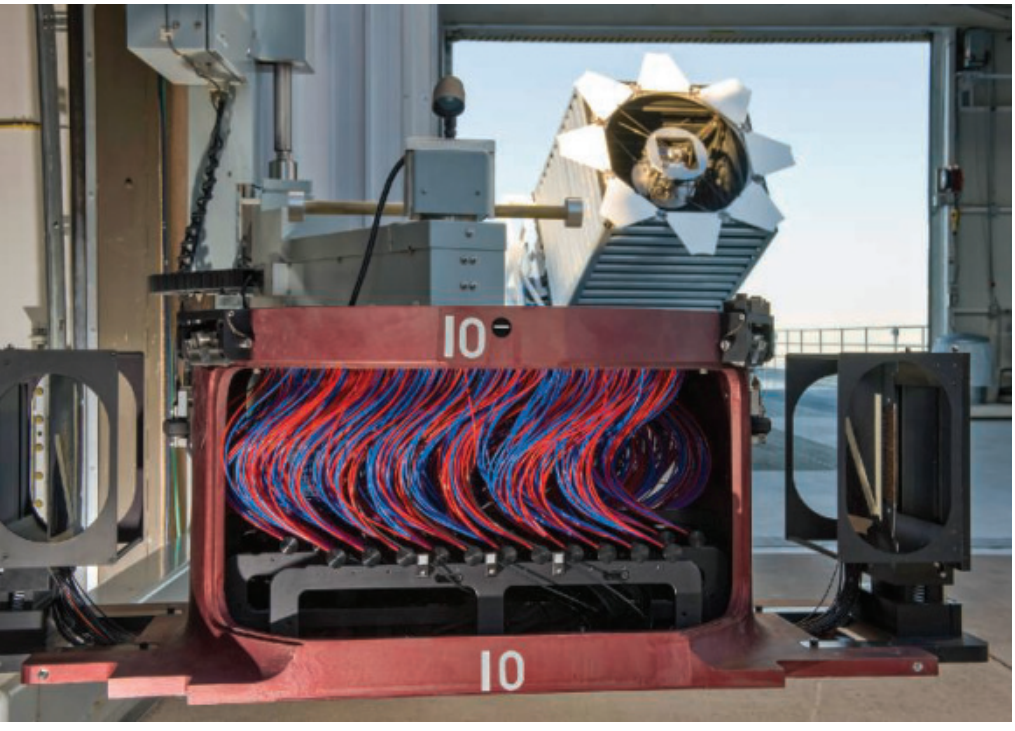

Hundreds of fibers, arranged by hand, capture light at the Sloan Digital Sky Survey's New Mexico telescope.

PHOTO: DAN LONG/APACHE POINT OBSERVATORY

The robots mark a new chapter for the SDSS. For 10 years much of its time went to the study of dark energy, the mysterious force that is accelerating the universe's expansion. The SDSS prised apart the light of millions of galaxies to determine their distance, via a redshift—a Doppler shift in their light due to the expansion of the universe, like the wail of a receding siren. Results from the galaxy survey, released in July 2020, traced the universe's expansion back through 80% of its history with 1% precision, confirming the effects of dark energy, perhaps the biggest mystery in cosmology. Cracking it will require looking further back in time to fainter galaxies, which is beyond the capabilities of the survey's 2.5-meter telescopes.

Instead, the scopes will carry out three new surveys. Milky Way Mapper will gather spectra from 6 million stars, probing their composition to find out how long they've been burning and forging heavy elements. "Stars are all clocks," Kollmeier explains. With age estimates, astronomers can work out when parts of the Milky Way formed. Subtle shifts in composition can also reveal whether a group of stars originated in another galaxy or star cluster that has been subsumed into ours—an unwinding of Milky Way history called galactic archaeology.

In a second survey, Black Hole Mapper, the optical fibers will gather light from bright galaxies to learn about the supermassive black holes they harbor. Doppler shifts in the spectra of glowing gases surrounding these black holes could reveal how fast they fling this material around—and thus how heavy they are. Shifts in the spectra could trace how they gobble up and spit out streams of this gas. By tracking the gases over time, Kollmeier says, astronomers may learn how the black holes grow, seemingly in concert with their galaxies.

The third survey, Local Volume Mapper, will bunch fibers together like a multipixel detector to get spectra from clouds of interstellar gas within nearby galaxies. "We're mapping a whole galaxy in exquisite detail at one time," Kollmeier says. By determining the motions and composition of the gas clouds, the SDSS team hopes to identify why some collapse into stars and others don't.

Meanwhile, the dark energy quest pioneered by the SDSS will move to the Dark Energy Spectroscopic Instrument, a 5000-fiber robotic spectrograph on a 4-meter telescope in Arizona. It will soon begin to track the distances to tens of millions of galaxies in the remote universe (*Science*, 13 September 2019, p. 1066).

In the coming months, the William Herschel Telescope, a 4.2-meter telescope in the Canary Islands, will join the robot revolution by sending light to a 1000-fiber spectrograph called the WHT Enhanced Area Velocity Explorer (WEAVE). Instead of using robots to hold fibers in place, WEAVE has two of them working offline, picking and placing magnetic fiber ends onto a metal plate—automating what the SDSS's plate pluggers did. One of WEAVE's goals is to gather Doppler shifts from the billion stars Gaia has mapped, nailing down their full 3D motions. Then, "We can run the clock backwards and see where they came from," says project scientist Scott Trager of the University of Groningen. It's another way to do galactic archeology.

Next year, the European Southern Observatory's (ESO's) 4-metre Multi-Object Spectroscopic Telescope in Chile will be fitted with yet another robotic technology. Its 2400 fibers will be fed through controllable "spines" that stick up into the telescope's focal plane and can be made to move, like wheat stalks in a breeze. Like WEAVE, it will follow up on sources identified by European spacecraft, including Gaia and Euclid, an upcoming dark energy mission.

It and other fiber spectrographs will also help with studies of fast-moving cosmic events such as supernovae or the violent collisions that produce gravitational waves. The Rubin Observatory will spot many of them. From 2023, it's expected to detect 10 million fast-changing objects every night. For the thousands that demand scrutiny, "spectra are really critical for understanding what a source is," says Eric Bellm of the University of Washington, Seattle, who is the science lead for Rubin's alert stream.

Even some of the world's largest scopes, in the 8-meter range, are adding robotic spectrographs. Japan's Subaru and ESO's Very Large Telescope are both developing systems that will vacuum up spectra from faint, distant objects. Ellis says a fiber spectrograph combined with Subaru's 8.2-meter mirror would be able to pick out spectra of individual stars in the Andromeda galaxy, the Milky Way's nearby twin. "With a big telescope, we can do galactic archaeology in our nearest neighbor," he says. ■

Robot revolution

To speed up the ability to split light from thousands of stars at once, sky surveys are turning to robot-controlled optical fibers.

INSTRUMENT	LOCATION	TELESCOPE DIAMETER	NO. OF FIBERS	FIRST LIGHT
LAMOST	China	4.9 meters	4000	2008
DESI	Arizona	4 meters	5000	2019
SDSS-V	New Mexico and Chile	2.5 meters	800	2021
WEAVE	Spain	4.2 meters	1000	2021
4MOST	Chile	4.1 meters	2400	2023
MOONS	Chile	8.2 meters	1000	2023
Prime Focus Spectrograph	Hawaii	8.2 meters	2400	2022

A massive new National Institutes of Health precision nutrition study will give some volunteers controlled meals, like this one being prepared by a dietician at the agency's metabolic research kitchen.

PHOTO: NATIONAL INSTITUTE OF DIABETES AND DIGESTIVE AND KIDNEY DISEASES

BIOMEDICINE

NIH's 'precision nutrition' bet aims for individualized diets

Effort will piggyback on giant genomics and health program

By **Jocelyn Kaiser**

There's no one-size-fits-all diet. If you want to avoid spiking your blood sugar with a snack, a banana may seem like a better choice than a sugary cookie. But some people in a 2015 study of 800 Israeli volunteers got their biggest blood sugar spike from bananas or bread instead of from sugar-laden baked goods. And as nutrition scientist Elizabeth Parks of the University of Missouri, Columbia, notes, "We all know people who lose weight easily, and others who don't."

Now, the U.S. National Institutes of Health (NIH) is making a major push to understand these individual differences. Last week, the agency announced what it calls the largest study yet to probe "precision nutrition," a $156 million, 5-year effort to examine how 10,000 Americans process foods by collecting data ranging from continuous blood glucose levels to microbes in a person's gut.

The study "has the potential to truly transform the field of nutrition science," generating new tools, methods, and "a wealth of data to fuel discovery science for years to come," Griffin Rodgers, director of the National Institute of Diabetes and Digestive and Kidney Diseases (NIDDK), said last year at an NIH board meeting where he introduced the project. Ultimately, it might enable nutritionists to tailor diets to an individual's genes and microbiome.

It is part of a broader push at NIH to boost nutrition science, a field sometimes viewed as "fuzzy" because "we are free-range eaters" and our diets are hard to control, notes Paul Coates, vice president of the American Society for Nutrition, who headed NIH's dietary supplements office until he retired in 2018.

In May 2020, NIH Director Francis Collins released the agency's first-ever 10-year strategic plan for nutrition science, acknowledging the importance of diet in chronic diseases such as heart disease and diabetes. The plan aims to fold in basic disciplines such as neurobiology, study the role of diet throughout life, consider how food can serve as medicine, and elevate precision nutrition. The concept recognizes that how the human body responds to food depends on factors from genetics to sleep habits, social environment, and gut microbes. For example, the Israeli study that found individual differences in the response to refined sugar versus fruit showed the microbiome was largely responsible.

Now comes NIH's Nutrition for Precision Health, which will piggyback on All of Us, the agency's huge genomics and health study, which has fully enrolled 272,000 of a planned 1 million participants, more than 50% from minority groups. "We realized it would be a really great fit" to take advantage of the All of Us data and infrastructure, says Holly Nicastro, a study coordinator and program director at NIH's nutrition office.

Some 10,000 All of Us participants who join the nutrition study will wear various monitors to track physical activity, blood sugar, and more; record what they eat; and visit a clinic to consume a specific meal and undergo clinical tests. A subset of up to 1500 will also follow three different diets at home or in the clinic, and then have the same tests. And 500 to 1000 volunteers will live at a clinical center for three 2-week stretches while eating three tightly prescribed diets. Such "controlled feeding" studies are the field's gold standard, but their high cost usually keeps them small. NIH has recently conducted some in its clinical center to explore, for example, the effects of ultraprocessed foods, but they involved only 20 people.

By collecting a wide range of personal data, from participants' DNA makeup to their ZIP code, "we are removing a lot of that 'noise' that we had for years, created by the factors that we were not measuring before," says Tufts University nutrition scientist José Ordovás who, with Parks, co-chaired a workshop last month to discuss the study. Artificial intelligence researchers will then use the collected data to create models that predict the best diet for an individual—an effort pioneered by the Israeli study, which spun off a company that developed an algorithm to tailor diets for people who are diabetic or trying to lose weight. A second, 5-year phase could test those models in clinical trials.

NIH is now inviting proposals for study components such as a data center, clinical centers, and a microbiome center. The aim is to begin enrolling volunteers by January 2023. "There's so much excitement" about the study, Parks says.

She and other nutritionists also welcome other signals of NIH's new focus. Its Office of Nutrition Research, once part of the NIH director's office, was demoted years ago to NIDDK. Last month, Collins announced it has been restored. Coates hopes that will mean a larger staff—the office now has just six people—and a modest budget to cofund studies with NIH institutes. "A lot [of nutrition science] falls between the cracks," he says—gaps he now hopes will close. ■

BIODIVERSITY

Study shows winners, losers as desert warms

In 100-year record, small mammals burrow to beat the heat, but birds either fly away or die

By **Elizabeth Pennisi**

In the early 1900s, Joseph Grinnell traversed the wilds of California in his Ford Model T truck, meticulously surveying its fauna. Along the Californian coast, he trapped pocket mice and watched condors soar; in the Mojave Desert, his team chronicled American kestrels swooping for insects and caught cactus mice hiding among rocks.

Now, by comparing Grinnell's data with modern surveys, ecologists have shown that climate change has not been an equal opportunity stressor. As the Mojave warmed by about 2°C over the past century, bird numbers and diversity declined dramatically, but small mammals like little pocket mice are holding their own. The survivors' secret seems to be a nocturnal lifestyle and an ability to escape the heat by burrowing, the team reports on p. 633.

Until now, researchers have often assumed climate change challenges mammals and birds in similar ways, because both need to maintain their body temperature. But, "There are clearly winners and losers," says Elise Zipkin, a quantitative ecologist at Michigan State University.

The pineapple heiress who established the Museum of Vertebrate Zoology at the University of California, Berkeley, in 1908 wanted it to do research, and Grinnell, the founding director, took that mandate to heart. Loaded with binoculars, clunky cameras, snap traps, and shotguns, his team drove through mountains and deserts, camping and collecting along the way. When flat tires halted the convoy, Grinnell hired prospectors and mules. Mindful of future researchers, he had his teams take copious notes and photos and map study sites. "He was draconian about it," says Steven Beissinger, an ecologist at the museum and a co-author of the new study.

"The Grinnell-era field notes are so detailed, I know I put my boots on the same talus slope they did," adds co-author James Patton, a retired museum ecologist.

The animals Grinnell studied now live in a markedly hotter, drier climate. Resurveys published in 2018 and 2019 in the *Proceedings of the National Academy of Sciences* showed "the bird community has collapsed to a new, lower number of species found per site," Beissinger says. On average, every spot surveyed had lost more than 40% of its desert bird species, such as American kestrels or mountain quail. At most sites, even the remaining species were scarcer.

But the new study, led by Iowa State University physiological ecologist Eric Riddell, tells a more hopeful story for rats, mice, chipmunks, and other small mammals. Since Grinnell's survey, three species have declined, 27 have remained stable, and four have increased in number. "This paper is really big news for small mammals," says Rebecca Rowe, an ecologist at the University of New Hampshire, Durham.

A cactus mouse hides in the rocks, a strategy that helps many small desert mammals stay cool.

PHOTO: JACK DAYNES

To find out why birds are so much more vulnerable, Riddell spent 2 years measuring heat transfer and light absorption in the fur and feathers of museum specimens of 50 desert bird species and 24 small mammals. He then fed those numbers and data on the species' behavior and habitat into a computer program that modeled how much heat stress an animal would be exposed to, and how well it could cool itself, under different temperature conditions. To keep cool, birds must expend energy, for example by dilating blood vessels to evaporate moisture from their legs or mouths. The energetic costs of cooling in birds were more than three times higher than in mammals.

That's because most small mammals take refuge underground during the hottest parts of the day. Such behaviors even helped mammals such as woodrats, which are not specially adapted for desert life. Only mammals that find themselves in soil too shallow to provide much cooling, such as the cactus mouse, suffered from the heat.

In contrast, many birds, such as the American kestrel and the prairie falcon, are exposed "to the full brunt of global heating," explains Andrew McKechnie, a physiological ecologist at the University of Pretoria who was not part of the study. "The models establish a convincing biological mechanism to explain why birds and mammals responded differently to climate change," says Lauren Buckley, an ecologist at the University of Washington, Seattle.

Other studies have shown declines in biodiversity as the climate warms, but this one is "impressive … because they provide the why," says Robert Cooke, an ecological modeler at the UK Centre for Ecology & Hydrology. "This hints at a worrying scenario that may be replicated for deserts across the globe as temperature rises." To ecologist Marlène Gamelon of the French national research agency CNRS in Lyon, the results suggest climate change poses as big a threat to desert ecosystems as it does to those in the fast-warming Arctic.

Mammals, too, may be at risk in the future. Thin soils cover just 2% of deserts today, but such areas are expected to grow as deserts get more arid. That's why "this paper shows the importance of preserving large areas with a diversity of microhabitats," says Linda Deegan, an ecologist at the Woodwell Climate Research Center.

Modeling studies like this one will also help conservationists make hard choices, says Mark Urban, an ecologist at the University of Connecticut, Storrs. "Understanding how species differ in their vulnerability to climate change will help us save money and time by ignoring those species that are doing just fine." ■

LATIN AMERICA

Science bill rankles Mexican research community

Scientists feel ignored in debate over law that would reshape governance and funding

By **Inés Gutiérrez Jaber**

Relations between Mexico's scientific community and the government of Andrés Manuel López Obrador, a left-wing populist, have never been warm. But the debate over a new bill governing Mexican science and technology has brought the acrimony to a boiling point.

The government says the new law, which may soon be sent to Mexico's parliament for a vote, would improve science and technology policymaking and help guarantee sufficient funding and support for research. But a draft presented in December 2020 by María Elena Álvarez-Buylla Roces, head of the National Council of Science and Technology (Conacyt), has met with a barrage of criticism from scientists. They say it would increase Conacyt's power, deprive the scientific community of a say in future science policy, and limit academic freedom.

Mexican researchers hope the bill can still be amended. But Conacyt, a funding agency that acts as a science ministry of sorts, is no longer speaking with the bill's critics, they say. "They have canceled all communication channels with us," says Maria Brenda Valderrama Blanco, a biotechnology researcher at the National Autonomous University of Mexico (UNAM), Cuernavaca, and one of the founding members of ProCienciaMX, a network of scientists seeking to influence science policy. Conacyt and Álvarez-Buylla Roces did not respond to questions from *Science*.

López Obrador has made several disparaging comments about scientists since he came to power in 2018, describing them as elitists and suggesting they are corrupt. His science policy has been marked by a series of dustups. Conacyt has suspended many scholarships for master's, Ph.D., and postdoc students in Mexico and abroad, for example, creating widespread discontent.

In September 2020, Conacyt removed biotechnology as one of the nine categories in new bylaws of the National System of Researchers (SNI), a mechanism to identify and fund the most important researchers. Some saw the move as an attempt by Álvarez-Buylla Roces, a plant scientist and vocal critic of genetically modified organisms, to control biotechnology research and deprive it of resources. "They removed biotechnology just because she doesn't like it," says María de la Luz Jimena de Teresa, a mathematician at UNAM, University City. But Conacyt says biotechnology researchers can seek SNI recognition through other disciplines.

Scientists were also upset at Álvarez-Buylla Roces's October 2020 decision to no longer cover Mexico's annual fees to international scientific groups, including the International Mathematical Union and the International Union of Pure and Applied Physics. The government says the cut was necessary to save money and help cope with the COVID-19 pandemic, but researchers say it will isolate Mexican scientists and deprive them of opportunities. Also in October, the government decided to terminate 109 trust funds run by public research centers and government institutes, one-third of them devoted to science and technology, and use the money for the pandemic response. Álvarez-Buylla Roces, who supported that decision, "is not doing her part in communicating the needs of Mexican science to our president," Jimena de Teresa says.

A previous science reform bill, proposed by a senator from López Obrador's political party in 2019, died after protests from scientists. In its wake, Conacyt invited input from the research community in March 2020. Many scientific organizations and universities sent in ideas for the bill; ProCienciaMX argued it should dedicate at least 2% of the federal budget to science and technology, set up a transparent allocation system in which scientists can play a role, and ensure academic freedom. "In theory, this new law could give us a clarity and strength that we don't have at the moment," Valderrama Blanco says.

But after reading Álvarez-Buylla Roces's draft in December, scientists said she had ignored their comments. The bill prioritizes research that addresses national problems "according to the state agenda," a phrase scientists say invites political interference. It also centralizes decisions about science in one council in Mexico City at the expense of the states, and provides few opportunities for scientists to participate in policymaking. Meanwhile, the bill makes no concrete promises about the future science budget. "This is serious," Valderrama Blanco says. "We're not paranoid."

In an opinion piece in *La Jornada*, Álvarez-Buylla Roces defended the proposal and said the opinions of the scientific community, including ProCienciaMX, had been taken on board. "This is a lie," the organization tweeted in response. "None of our proposals are reflected in the draft presented by Conacyt."

The draft has already been approved by the General Council for Scientific Research, Technological Development, and Innovation, chaired by López Obrador himself, and may soon head to parliament, where his party has a majority. Scientists hope it's not too late to come up with a new proposal. "We ask [the parliament] not to unilaterally approve a law where the feeling of the scientific community is not heard," says ProCienciaMX member Alma Maldonado-Maldonado, an education scientist who specializes in public policy. But Valderrama Blanco isn't hopeful. "I think they are going to surprise us with a document introduced through the back door that will be approved by the majority," she says. ■

María Elena Álvarez-Buylla Roces, head of Mexico's National Council of Science and Technology, has come under heavy fire from scientists.

PHOTO: LUCÍA GODINEZ/NEWSCOM

Inés Gutiérrez Jaber is a science journalist based in Mexico City.

Species-rich vernal pools, such as these in California, could be one target for greater protection.

PHOTO: ANTHONY AREND/ALAMY STOCK PHOTO

CONSERVATION SCIENCE

Species? Climate? Cost? Ambitious goal means trade-offs

Biden aims to protect 30% of U.S. land and water by 2030

By **Erik Stokstad**

President Joe Biden last week unveiled an ambitious conservation goal, unprecedented for the United States: conserving 30% of the country's lands and waters by 2030, which would require more than doubling the area of public and private holdings under heightened protections.

Conservation scientists welcomed the so-called 30-by-30 goal, announced in an executive order released 27 January. "The ambition is fantastic," says ecologist Joshua Tewksbury, interim executive director of the nonprofit Future Earth.

But Biden's order also raises a thorny practical question: Which swaths of land and sea should be the top targets for enhanced protection or management? The order says the effort should aim for a number of outcomes, including preserving biodiversity, curbing climate change, and even creating jobs and promoting environmental justice. But researchers warn that difficult trade-offs lie ahead, because few chunks of territory can provide all of the desired benefits. "The balancing act [will be] the hardest part of this work," Tewksbury says.

Reaching the 30% goal could require extending protection to vast expanses of land and sea, depending on how officials define "protected." Only about 12% of U.S. land is already in wilderness areas, wildlife refuges, national parks, and other reserves with strong protection, according to the U.S. Geological Survey. Much is in Alaska; just 7.5% of the lower 48 states is highly protected. (An additional 18% of all U.S. land has weaker protection that allows certain uses, such as logging or mining.) At sea, the country is much closer to the goal: Some 26% of coastal waters is protected to some degree within sanctuaries, national marine monuments, or other entities.

Last week, researchers at Boston University and the Nature Conservancy released a paper that maps and compares scenarios for reaching the 30% goal in the coterminous United States (which excludes Hawaii and Alaska). The scenarios examine trade-offs among four goals: minimizing cost, protecting climate-resilient landscapes, protecting species, and curbing carbon emissions.

Making cost the top priority led to expansive new protection in the western plains, where land is cheaper. But because most of the added land supports relatively few threatened species, the scheme would fall short on that measure. The least cost scenario also protected relatively little land that absorbs or stores climate warming gases such as carbon dioxide or methane.

Another scenario, which emphasized protecting resilient and connected landscapes, cost twice as much. It preserved areas across most of the country except deserts and the corn belt. A third vision, focused on preventing the loss of grasslands and forests that store carbon, delivered the most climate benefit, but cost three times as much. It also produced a patchwork of protected forests in the southeast that lacked connections, reducing their value for preserving biodiversity. A final scenario, which protected species across the country but especially in the south, covered the greatest range of ecosystems. It cost four times as much and provided fewer climate benefits. Overall, the analysis found that just 2% of lands scored highly on all four measures.

Observers say Biden could make rapid progress and contain costs by focusing on territory already owned by the federal government. "We can make really huge gains on Forest Service and Bureau of Land Management lands," says Jacob Malcom, a conservation biologist with Defenders of Wildlife. That could mean reducing logging, mining, drilling, and grazing. "There will be vested interests who are not happy about that," Malcom notes. "So I don't want to make it seem like it's going to be easy." Fishing associations, for example, have already criticized proposals to ban commercial fishing in 30% of U.S. waters. "Thirty-by-thirty is a campaign slogan, not a scientific proposal," Robert Vanasse, executive director of Saving Seafood, wrote last year.

Rebecca Shaw, chief scientist of the World Wildlife Fund, notes the Biden order does not exclude human uses of natural resources. "It's not protect, it's conserve," she says. "And that means getting creative." Ending subsidy programs for fossil fuel extraction, for example, and boosting programs that pay farmers to conserve lands could help reach the goal. Other assistance could come from a recent federal law that more than doubles spending—to some $900 million per year—on the Land and Water Conservation Fund, which can help states and local governments buy land.

The Biden administration's plans should become clearer by May, when federal agencies must outline their strategies for reaching the 30-by-30 goal. Other nations will be watching, notes Charles Barber, a senior biodiversity adviser at the World Resources Institute. He notes that many countries are pushing for the United Nations to adopt a global 30-by-30 goal, and "the credibility of the U.S. as an international leader will depend a lot on what people see the United States doing at home." ■

GENOMES ARISING

Africans have begun to study their continent's rich human diversity—but what comes after current grants end?

By **Elizabeth Pennisi**

In 1987, 10-year-old Segun Fatumo was on the streets of Lagos, Nigeria, hawking palm oil, yams, and pepper each day after school to help put food on the table. In the evenings, he and his family crowded into a two-room dwelling without running water or electricity. He knew nothing of the plan being hatched by U.S. and U.K. geneticists to sequence the human genome.

Thirteen years later, when researchers completed the draft sequence of the human genome, Fatumo—then an undergraduate studying computer science—heard all about it. "I knew the project would change our world," he recalls. What he didn't realize at the time was how it would change his life.

Fast forward more than 2 decades. Fatumo is now a computational geneticist in Entebbe, Uganda, with the Medical Research Council/Uganda Virus Research Institute and the London School of Hygiene & Tropical Medicine. Genome data by the terabytes flow through his seven-person lab, which is working to pinpoint genes involved in heart, kidney, and other diseases. All members of his team are African, the data come from African donors, and the ultimate goal is to improve the health of the people of Africa.

Until recently, genetic research in Africa was scanty, and most was done by researchers swooping in from afar to gather samples, then leaving to do analyses in well-equipped labs in the United States or Europe. "African genomic study was characterized by ethical dumping, helicopter science, and exploitation," Fatumo says. Researchers gathered samples with little regard for informed consent and without giving back to the communities they studied, he says.

Today, Fatumo and scores of other young Africans are doing a substantial and growing share of this research. "African genomics is a story that's going to be told more and more by Africans," says Charles Rotimi, a genetic epidemiologist at the U.S. National Human Genome Research Institute (NHGRI).

Bolstered by the internationally funded Human Heredity & Health in Africa (H3Africa) Initiative, which sponsored Fatumo as a postdoc, these researchers hope to one day use their data to bring genetically tailored medicine to people who

PHOTO: GEORGIAN MURPHY

Volunteers in rural Uganda provided blood samples and health information for the biggest genomics effort in Africa, the Uganda Genome Resource.

in some places still struggle to get electricity and basic health care. The work is beginning to close a wide gap in who benefits from the human genome revolution. "There's this genomics expansion across the world," says Neil Hanchard, molecular geneticist at Baylor College of Medicine. "Why should Africa be left behind?"

Including African populations is also paving the way for a better understanding of the links between disease and genes in everyone, everywhere, because Africa holds more genomic diversity than any other continent. "The African genome should be used as the reference genome for the entire world," says Tesfaye Mersha, a geneticist at the University of Cincinnati.

But genomic research in Africa has a long way to go. Researchers have only studied between 5000 and 10,000 whole genomes from Africans, compared with as many as 1 million worldwide. Africa has received less than 1% of the global investment in genomics research and clinical studies, Mersha says.

What's more, funding for all current projects in H3Africa, a $176 million program supported by the U.S. National Institutes of Health (NIH) and the Wellcome Trust that has jump-started African genomics, is set to end in 2022. Fatumo has corralled another prestigious fellowship, but researchers across the continent are scrambling to make sure the nascent genomics community can survive—and grow.

FATUMO DECIDED he wanted to study genetics as a youngster, after a doctor explained sickle cell disease to him. His brother suffered weeklong bouts of pain from the condition. Fatumo learned that his brother had two copies of the responsible gene—and that he himself would be spared because he had just one copy. "The role genes play in disease got me thinking," he recalls.

Sickle cell, which is now being treated through gene therapy, is a classic example of how genetic knowledge can inform medical practice (*Science*, 11 December 2020, p. 1254). And it primarily affects people of African descent. Yet most sickle cell studies and medical advances have happened in rich countries. Fatumo wants more Africans doing such research in the future.

One of six children, whose father worked as an unskilled tailor and later as a subsistence farmer and bush hunter, Fatumo moved with his family to the outskirts of Lagos when he was 9 years old. He hiked 2 kilometers early every morning to retrieve water from a river, wielded hoe and cutlass to tend crops, trekked to Lagos for school, then topped off the day hawking.

He and his parents managed to pay the 105 Nigerian naira (about $1) per year for school, thanks, in part, to Fatumo's hawking profits. Fatumo says poverty fueled in him a fierce determination to do better. "The story of my upbringing is the one that propels anger for success."

Later, he earned a B.S. in computer science at the African University of Science and Technology in Abuja, Nigeria. Because little genetics was being done at African universities, he pursued graduate degrees in computer science at Covenant University in Ota, Nigeria. "I was lucky to study at Covenant where they had some key resources and constant electricity," he recalls. Even so, his bioinformatics analyses kept crashing the school's computer system. He spent 1 year studying in Heidelberg, Germany, where "the same analysis was completed in less than 30 minutes" with high-performance computers.

But he was working his way through school at the right time, in the right place. In 2009, the founders of the 6-year-old African Society of Human Genetics met in Cameroon to discuss their vision for an African genome project. "It was a dream we had, but … we didn't know where the funding would come from," Rotimi says. Francis Collins, who had coordinated the Human Genome Project but was then between jobs, was invited to give the opening talk.

He and other participants knew how much genomics studies in Africa could contribute to research worldwide. Trace any human's family tree back far enough and the roots wind up in Africa, where our species was born some 300,000 years ago. When some groups left the continent over the past 80,000 years or so and spread across the globe, they carried only a subset of human genomic diversity. As a result, the people of Africa today carry more genetic diversity than those of any other continent. "There are parts of our genome that we cannot study any place beside Africa," says Rotimi, who directs NHGRI's Center for Research on Genomics and Global Health.

Those at the 2009 meeting also recognized that Africans needed to lead the way. "The idea that people outside of Africa are going to be able to decide the priorities … just doesn't work," Collins says. Local investigators are more likely to understand the culture and constraints and to be trusted by the community, Mersha adds.

Some researchers were skeptical about funding African-based research. "People said the money would just disappear," Collins recalls. But "I was pretty convinced we could step away from the colonial perspective where developed nations make the decisions." Collins became NIH director in 2009 and helped launch H3Africa in 2011. NIH has committed $150 million to the initiative through 2022, and Wellcome, a U.K. biomedical philanthropy giant, has kicked in another $26 million.

The initiative aimed to set up a network of laboratories across the continent to explore the relative roles of environment and genes in diseases that plague Africans, such as HIV/AIDS, trypanosome infections, stroke, diabetes, and heart disease. It also established biorepository and bioinformatics networks. To ensure a lasting legacy, it supports training as well as research.

IN 2013, with H3Africa funding, Fatumo traveled to the Wellcome Sanger Institute in Hinxton, U.K., and the University of Cambridge as a postdoc in genetic epidemiology. At Sanger, he took part in the largest African genomics project to date, a multimillion-dollar effort to analyze genomic data from 14,126 people from five African countries, including newly collected whole genomes from nearly 2000 Ugandans. The international team of researchers found 9.5 million gene variants not previously spotted, underscoring the diversity of African populations and laying the groundwork for future genomic studies.

The results, published in *Cell* in 2019, also included specific variants related to cardiovascular diseases in Africans, such as one previously linked to an inherited blood disorder called alpha thalassemia. That single variant could also shape the diagnosis of a third condition: It alters how sugars bind to red blood cells and so affects the results of the blood glucose test often used to track diabetes.

Africans overlooked

Genomewide association studies (GWAS) scan genome data for links to diseases. But the DNA in such studies mostly comes from white people.

GWAS by population

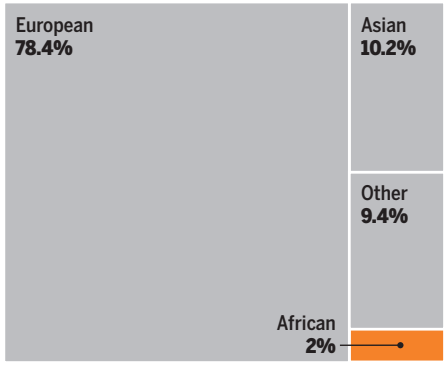

CREDITS: (GRAPHIC) K. FRANKLIN/*SCIENCE*; (DATA) G. SIRUGO *ET AL.*, *CELL*, 177, 1, 26 (2019)

One year later, H3Africa's milestone genome paper came out in *Nature*. Human geneticist Zané Lombard and bioinformaticist Ananyo Choudhury from the University of the Witwatersrand, along with other African and international colleagues, analyzed 426 genomes, many newly sampled, from 50 populations in 13 countries. They described more than 3 million new human DNA variants, most from previously unsampled populations. The analysis also confirmed the continent's complex migration patterns, tracing the path of Bantu-speaking people as they expanded southward and eastward more than 3000 years ago. That was just one of nearly 300 papers published so far by H3Africa teams, describing results as well as providing curated data sets of African genomes.

Genome researchers work with Cameroonian volunteers to ensure informed consent.

Those databases will illuminate studies of human variation worldwide, in part because the great genomic diversity in Africans can uncover spurious links to medical conditions, explains Concepcion Nierras, an NIH Common Fund geneticist. For example, in Europeans a rare variant of a gene for a low-density lipoprotein that contributes to high cholesterol seemed to raise the risk of heart disease. But Fatumo and his colleagues found that among Africans, the variant was common even in those who did not have heart disease, suggesting it may not have clinical relevance. The *Nature* paper uncovered 54 such variants that now need re-evaluation.

Scientists say H3Africa has been thoughtful about ethics, vital in a continent with a long history of colonial exploitation and where such concerns remain a flashpoint. For example, until 2019 Sanger was working to develop a DNA chip for scanning African genomes quickly. But whistleblowers said study participants hadn't granted the institute permission to use their DNA in this way. That chip is now not used, although one developed by H3Africa has become a mainstay (*Science*, 1 November 2019, p. 555).

Computational geneticist Segun Fatumo studies the genomics of kidney, heart, and other diseases.

To guard against exploitation, the project brought on bioethicists to discuss the research with local communities and figure out equitable partnerships, addressing concerns from populations worried about misuse of their data. They are also working to establish standards for effective, ethical informed consent. At Makerere University, orthopedic surgeon and bioethicist Erisa Mwaka Sabakaki and colleagues have reviewed hundreds of informed consent and other documents. Projects sometimes came up with unexpected solutions: For a study involving HIV-infected children, comic books proved a great way to communicate to both adults and children.

"There are ongoing and important questions about informed consent, how best to engage communities, benefit sharing, stigma, and many other issues," says Jantina De Vries, a bioethicist at the University of Cape Town who helped set up H3Africa's policies. "But we've started on a really good trajectory."

H3Africa's biggest achievement may be growing a generation of African genomicists, says Harvard University global public health expert Barry Bloom. The project has trained 137 Ph.D.s and 49 postdocs including Fatumo, as well as hundreds of master's students and undergraduates, and gives an incentive for scientists trained abroad to return to Africa. "If not for H3Africa, maybe I wouldn't be a group leader and principal investigator today," Fatumo says.

These efforts have had spillover effects beyond human genetics. For example, the project helped train Christian Happi, a molecular biologist at Redeemer's University in Ede, Nigeria, who runs the African Center of Excellence for Genomics of Infectious Diseases. His team quickly sequenced Nigeria's first Ebola case, identified Lassa fever strains in a 2018 outbreak and—in just 3 days in March 2020—sequenced the first coronavirus genome from an African, showing SARS-CoV-2 had arrived from Europe.

"The program's resources have enabled many African countries to respond to other health challenges," says Clement Adebamowo, a surgical oncologist at the University of Maryland School of Medicine who has been active in African genetics.

BUT H3AFRICA'S successes highlight how much more work is needed. Most of the project's genomes are from people of Southern, Central, and West African ancestry (see map, p. 559), and many populations haven't been sampled at all, including those in North Africa. "Our studies combined are just the tip of the iceberg," says Sarah Tishkoff, a human geneticist at the University of Pennsylvania who has led the way in sampling remote populations.

Individual studies highlight how much more researchers need to know to understand the intersection of genes and disease. For example, an H3Africa project called the Collaborative African Genomics Network (CAfGEN) aims to come up with a blood test for HIV-positive newborns to show how quickly their infection could progress to AIDS. Researchers scrutinized the genomes of infected children, hoping to find genetic variants associated with slow HIV progression. Children with such variants could postpone treatment and reduce and delay long-term side effects.

But so far, the team has found just one piece of DNA, involved in the immune system, that varies significantly among the children. And candidate variants that popped up in a study of Botswanan children failed to appear in Ugandan children, underscoring the diversity of African genomes. "The African genome is much more complex than we anticipated," says CAfGEN trainee Lesedi Williams,

PHOTOS: (TOP TO BOTTOM) ALESSIA RANCIARO; WELLCOME SANGER INSTITUTE/PHILIP MYNOTT

now a genomicist at the University of Botswana, Gaborone.

"The sad reality is that genomics data from Africa [are] still too few," says geneticist Aimé Lumaka of the University of Liège and the University of Kinshasa. So the medical significance of many variants in people of African descent is unknown.

Tishkoff and others are broadening their samples; this year she hopes to publish on 180 more African genomes, while Choudhury and his H3Africa colleagues are coming up with new places to sample, including Mauritius, Réunion, and other islands.

More mundane challenges also loom. "Our supply chains, financial systems, and infrastructure need strengthening," says Iruka Okeke, who studies pathogen genomes at the University of Ibadan. The continent is short of both sequencing capacity and computers powerful enough to analyze giant data sets. These impediments can lead H3Africa investigators to delay making data publicly available in order to do their own analyses, a practice that can create its own problems, says Steven Salzberg, a computational biologist at Johns Hopkins University. "As long as each group keeps its data private, the next group that wants to study these populations has to start over and sequence a new cohort," he says.

With funding scarce, some H3Africa trainees are leaving human genetics for fields where research is cheaper. One CAfGEN trainee, Gerald Mboowa at Makerere University, has shifted away from human genomes—which cost $1000 per sequence—to those of bacteria, which are a mere $90. He recently received a $100,000 Grand Challenges Africa grant funded by the Bill & Melinda Gates Foundation to track drug-resistant bacteria in hospitals.

Others, noting that direct health benefits from genes are often a long way off, wonder whether H3Africa money would be better spent on more immediate public health needs such as antismoking and healthy eating campaigns. "In 2011 we didn't know" whether H3Africa was the best way to spend international resources in Africa, says Richard Cooper, an emeritus epidemiologist at Loyola University Chicago who helped get the project off the ground. "Unfortunately I [now] think the answer is in the negative," because genomics has yet to lead to many concrete boosts in health.

Fatumo is satisfied that his own work is of immediate benefit. As his organization gathered blood samples in rural Uganda, it discovered and treated diseases participants hadn't been aware of, including hepatitis and hypertension.

But a big challenge looms in 2022, when NIH Common Fund support ends. That loss could "be a major blow to everything that's been built up," says Stefan Jansen, a psychologist at the University of Rwanda involved with an H3Africa project on posttraumatic stress disorder. Some support will come from another NIH program, Harnessing Data Science for Health Discovery and Innovation in Africa (DS-I Africa), which is slated to spend $62 million over the next 6 years. And an African genomics startup called 54Gene has gotten $15 million in international backing for a multimillion-dollar facility in Nigeria. But most H3Africa-supported researchers have had little luck finding funding within Africa. It's "really, really challenging getting African funding from private companies or African governments," Rotimi says.

Some of Africa's genomics researchers will manage to win new support from abroad, as Mboowa has done. Fatumo was recently awarded a highly competitive Wellcome International Intermediate Fellowship and now has $1.2 million over the next 5 years plus other support to explore genomic variants linked to chronic kidney disease; he hopes to develop risk scores based on patients' genetic makeup.

He has also teamed up with a South African colleague and applied to become a DS-I Africa research hub. If successful, they will get $1.3 million per year for 5 years to use existing African genetic data to find and validate new drug targets.

Fatumo and others hope their generation's accomplishments will lay the foundation for an even stronger research network. "It is a great time for all of us doing genomics in Africa," Okeke says. "The discovery potential is very high, and the impact that our work could have on health could be huge." ■

Tallying African genomes

Researchers have only just begun to sample the genomes of Africa's 2000 ethnic groups and populations. A handful of whole-genome sequences in 2010 has grown to thousands from multiple projects, many of which are captured on the map below. Their distribution reveals huge gaps in genomic sampling across the continent.

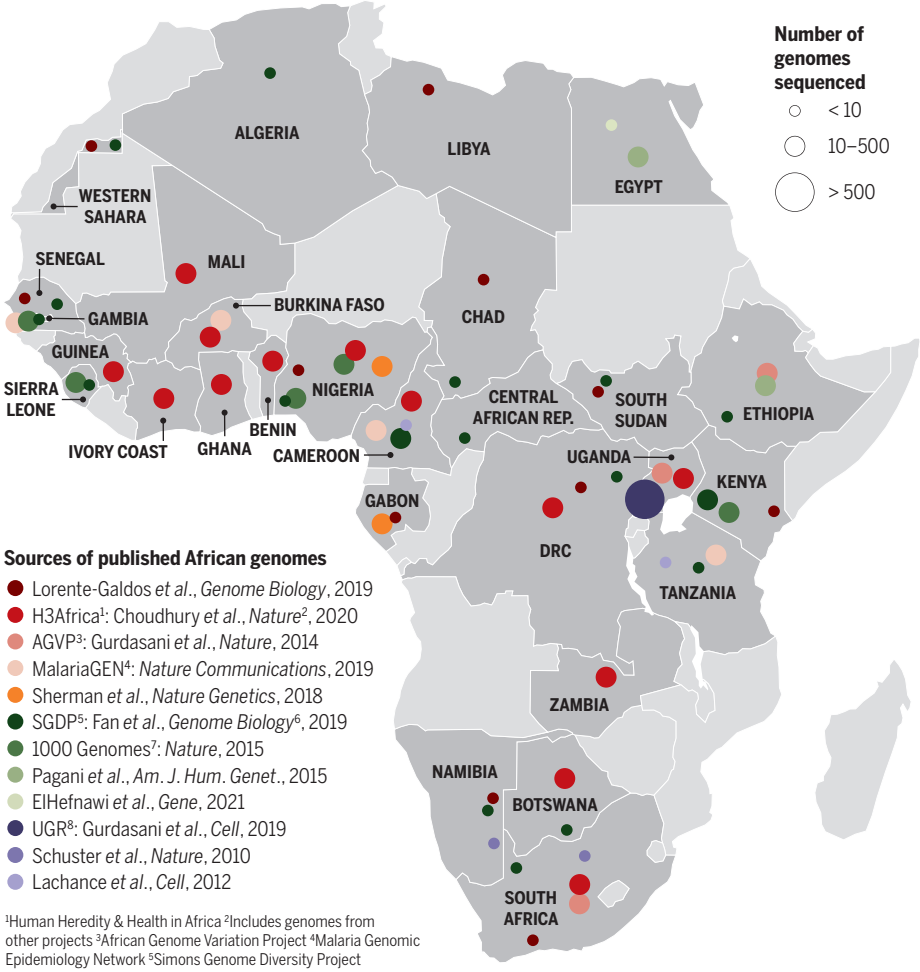

Sources of published African genomes

- Lorente-Galdos *et al*., *Genome Biology*, 2019
- H3Africa[1]: Choudhury *et al*., *Nature*[2], 2020
- AGVP[3]: Gurdasani *et al*., *Nature*, 2014
- MalariaGEN[4]: *Nature Communications*, 2019
- Sherman *et al*., *Nature Genetics*, 2018
- SGDP[5]: Fan *et al*., *Genome Biology*[6], 2019
- 1000 Genomes[7]: *Nature*, 2015
- Pagani *et al*., *Am. J. Hum. Genet*., 2015
- ElHefnawi *et al*., *Gene*, 2021
- UGR[8]: Gurdasani *et al*., *Cell*, 2019
- Schuster *et al*., *Nature*, 2010
- Lachance *et al*., *Cell*, 2012

[1]Human Heredity & Health in Africa [2]Includes genomes from other projects [3]African Genome Variation Project [4]Malaria Genomic Epidemiology Network [5]Simons Genome Diversity Project [6]Some data first reported in Mallick *et al*., *Nature*, 2016 [7]1000 Genomes Project Consortium [8]Uganda Genome Resource

GRAPHIC: K. FRANKLIN/*SCIENCE*

INSIGHTS

LETTERS

NEXTGEN VOICES: HUMAN GENOME ANNIVERSARY

Beyond DNA: The rest of the story

The availability of a fully sequenced human genome and genome-wide analyses of genetic variation have made DNA-based ancestry tests possible. These consumer DNA tests are now widely marketed as a way to discover or confirm family history. But what do they really tell us about our past, and what do they leave out? We asked young scientists to tell us about their family traditions, stories, and culture, and how they understood their DNA test results in the context of their lived experiences. Their stories are below. To read more reflections by young scientists, find past NextGen Voices pieces at https://science.sciencemag.org/collection/nextgen-voices. Follow NextGen Voices on Twitter with hashtag #NextGenSci. **—Jennifer Sills**

A taste of Caribbean Christmas

My family comes from Jamaica and the Virgin Islands. There is no meal I would rather have than my mom's home-cooked traditional Jamaican food. Now living in Florida, my mom grows many fruits and vegetables native to Jamaica in a garden that occupies her entire yard. When I visit, we spend most of our time together outside picking fresh mangoes, ackee (a tropical fruit grown in Jamaica), or whatever else happens to be in season. On Christmas, she makes oxtail (a kind of beef stew, my personal favorite), fried dumplings, and ackee with saltfish (its traditional complement of salted cod). These foods are well-spiced—although not always spicy—and flavorful.

Where my family originated is mostly hearsay, and the full history beyond a few generations is hard to trace. My DNA test results confirmed that we have some background in Europe and likely moved to the Caribbean through the slave trade. The

ILLUSTRATION: MICHELLE KONDRICH

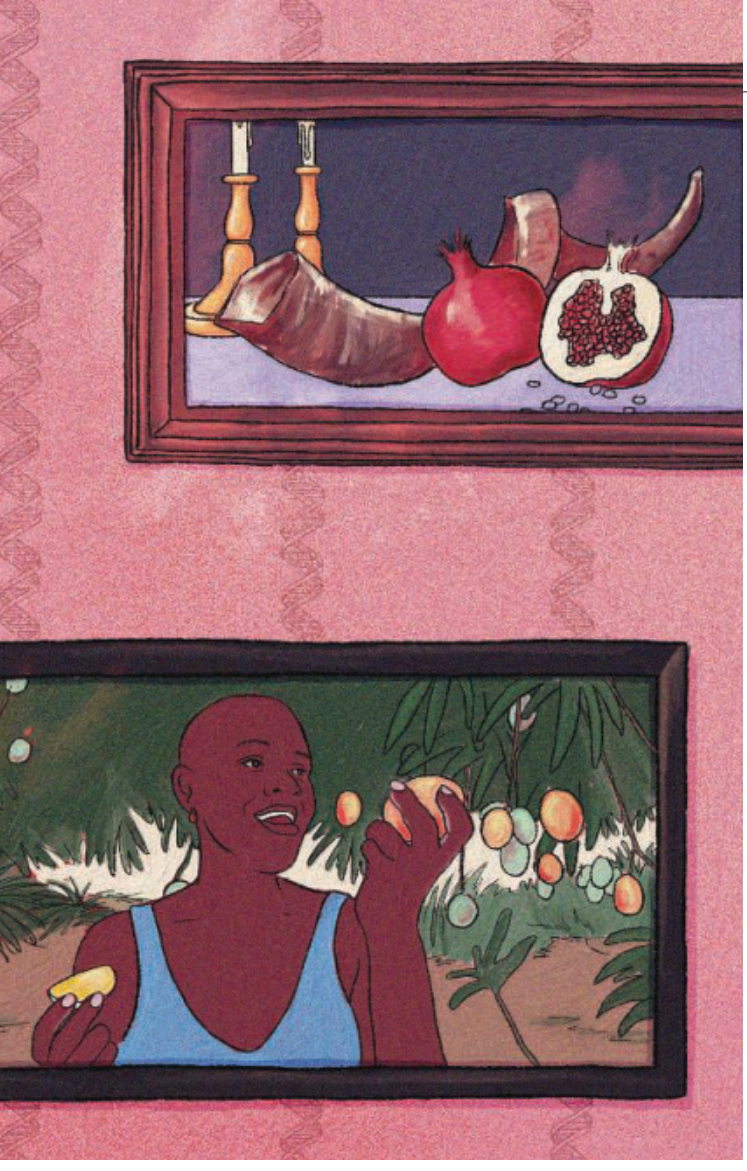

details echoed a story on my mom's side of the family that one of our ancestors was the child of an Irish slave master and a woman he enslaved.

I have mixed feelings about the business model of consumer DNA test companies, which make their profit based on the use of others' genetic information—in my mind, the most personal information one can share. However, my mom really wanted me or my dad to do the test to see how that side of our ancestry looked. I chose a company that gives users more control over who can access the results. Of course, these tests are not as accurate for those of us from non-European backgrounds, but the results were roughly what I expected, and it is humbling to think about where our family began compared with where it is now.

Gregg Duncan
Fischell Department of Bioengineering, University of Maryland, College Park, MD 20742, USA. E-mail: gaduncan@umd.edu

A poetic Han Spring Festival

My family is Han, the largest nationality of China. Like most families in China, we celebrate the Spring Festival (Chinese New Year) by gathering together to make and eat *jiaozi* (dumplings filled with vegetables and meat), which are shaped like ancient Chinese gold ingots to symbolize wealth. We hang festival couplets (two lines of poetry with the same number of words) that are painted along with intricate designs on red paper, and we put red lanterns and red candles on display throughout the house; the decorations symbolize happiness and protect us from the mythical monster named Nian, who is said to be afraid of the color red. While we wait for the New Year to arrive, we listen to Hebei Bangzi, the local opera, which sounds similar to the Beijing opera but is more difficult for people outside Hebei province to understand because the singers use pronunciations unique to the region. In my hometown (Shijiazhuang, Hebei), people of the same surname gather together to extend best wishes to their elders before the first sunrise of the new year.

Such traditions are a reminder that my surname (Ji) is not common in China. I hoped that finding out more about my family's origins would help to explain my unusual name. My DNA test results told me that 46.34% of my genome came from North China (Han), 20.13% from South China (Han), and 12.21% from Northeast Asia (Japan). I was disappointed that the results contained no detailed information that I found useful. I do not know how many Chinese people have a genetic pattern similar to mine, and—unlike scientific research—the company did not give me the raw data of my genome. Without more information about how the company analyzed my genomic data, I don't know what conclusions I can draw or even whether I should believe the test results.

Yongsheng Ji
Division of Life Science and Medicine, University of Science and Technology of China, Hefei, Anhui, 230026, China. Email: jiys2020@ustc.edu.cn

A scary Kiwi Mardi Gras

Fifteen years ago, I probably would have said that my family didn't have a French cultural identity, despite being raised in France. Today, after having been expatriated 10 years in New Zealand, I can confirm that we have a strong French cultural identity, especially when it comes to food. Yet, after we returned to France 3 years ago, our attachment to our home country and its culture and traditions did not feel quite the same. I believe that we unintentionally took bits of New Zealand back to France with us.

Our ever-evolving celebration of Mardi Gras encapsulates our cultural journey. Before our move, we had always celebrated the French holiday in its traditional (if less religious) form. Around the end of February, we would make and eat loads of French crêpes, and kids would dress up in festive costumes and attend the carnival. After our move, we discovered that New Zealanders do not observe Mardi Gras, so we adopted a different yet similar tradition, which was brought to the country from overseas and stuck: Halloween. Every year on the 31st of October, my eldest boy dressed up in a scary costume. But because good food is so deeply rooted in our culture, Halloween candy didn't feel sufficient. To supplement the prepackaged treats, we created our own tradition of the Halloween "scary lunch." Each year, I would prepare a lunch box filled with funny and scary little monsters, skeletons, and ghosts made of pancakes, carved fruits, and (for the mummies) baked sausages in pastry strings.

Now back in France, we have resumed our celebration of Mardi Gras in February. The kids dress up for school and for carnivals, just like Halloween, but with an emphasis on festive instead of scary, and we make crêpes, as we've done in the past. We've also kept our own multicultural family traditions. To adapt our New Zealand Halloween lunches, we now have a Halloween-themed French dinner in October. We've also updated the tradition of hiding a *fève* (trinket) in our *galette des rois* (king cake) by using a *koru* necklace (a traditional kiwi artifact) instead.

Our unique and changing traditions showed me that we could be open to incorporating new values and ideas when we learned the results of our DNA tests. My husband and I are both researchers in ecology and environmental genetics, manipulating DNA data daily and studying insect population genetics. It seemed only natural that we would want to see our own DNA test results. We originally thought that the genetic admixture might be quite high within our family home given that we were born 12,000 km apart—I grew up in northern France, and he was raised on the French island of La Réunion in the Indian Ocean. We were quite surprised by the results. For instance, I learned that I had ancestors from Italy and Scandinavia but very little French or Western European lineage, whereas my husband, despite being born in the Southern Hemisphere, has more Western European lineage than I do. (His results could perhaps be explained by the fact that half of the first settlers in La Réunion were from Brittany.) Although my husband has ancestors in many parts of the world where I do not (such as India, Africa, and Indonesia), we share an unexpectedly high rate of ancestry from the Iberian Peninsula (Spain and Portugal). The results have not changed our lives, but it is interesting to know that, genetically, we are more an Iberian family than a French one! We now want to travel to and discover more about the culture of these southwestern parts of Europe and pass on this heritage to our children. As ecologists, we are curious about the natural and geological histories of the Iberian region, but we would make food an important part of the trip as well. They may not have French crêpes in Portugal, but I have heard that the delicious *bolo lêvedo* (Portuguese muffins) are not to be missed.

Marie-Caroline Lefort
Cellule de Valorisation Pédagogique, Université de Tours, Tours, France.
Email: marie-caroline.lefort@univ-tours.fr

A Persian Israelite's new year

As a Jewish woman born in Iran and living in Israel, I feel connected to the ancient history of my people. Because it is rare to find an Iranian woman in science who keeps Jewish traditions, I feel a responsibility to manifest all the good that is in each part of my background.

My family celebrates the traditional holiday of Rosh Hashanah (the Jewish New Year). Wearing white clothing to symbolize purity, we light candles and look into the flames as we give thanks and ask for blessings in the coming year. We celebrate this contemplative holiday with a festive meal steeped in symbolism and tradition. We eat apples dipped in honey and pomegranates to symbolize our hopes for a sweet, peaceful, happy new year that is full of good deeds. The honey represents sweetness, and the apple tree is the only tree that has more fruit than leaves, reminding us that we should maximize our purpose in this world. The numerous seeds in pomegranates, a native fruit of ancient Persia, symbolize the many good deeds we should carry out during the coming year. We also make a traditional Iranian-Jewish stew out of quince, a native fruit of west Asia (including Iran and Israel) that looks like an apple. The sweet smell fills the entire house with a magical floral and fresh perfume. During Rosh Hashanah, the shofar (an ancient musical instrument typically made of a ram's horn) is blown 100 times. The sound marks the time to make our wishes for the new year, which we read in Hebrew.

My DNA test results show that I am mostly Persian, with a very small percentage (0.8%) of Egyptian in my ancestry. The data echo the Biblical and rabbinical stories that I consider my roots. Our cultural history tells us that our ancestors were in ancient Egypt for hundreds of years before moving to Israel with Moses. In 722 BCE, the Jews were exiled from Israel to other regions, including Iran. My father was born in a city that was first settled by the exiled Jewish people from Israel, and my mom is from a city that is well known in Iran as the site of the story of Esther and Mordechai, traditionally told during the holiday of Purim. My family moved to Israel after the revolution in Iran in 1979. My DNA results mirror both these ancient tales and my own family's story.

Ruty Mehrian-Shai
Pediatric Hemato-Oncology, Brain Cancer Molecular Medicine, Sheba Medical Center, Ramat Gan, 52621, Israel. Email: ruty.shai@sheba.health.gov.il

A Bengali Thanksgiving

I've always struggled with being identified as simply "Indian." My name reflects my Indian heritage better than I do, as a Montreal-born, New York City native living in Louisiana. No DNA test could reflect the mix of American and Indian cultural practices that my family has created. Take, for example, American Thanksgiving, which my family co-opted when I was young and combined with a traditional West Bengali feast. At our table, we served the turkey alongside traditional Indian *luchi* (oil-fried puffed dough) and fusion dishes such as vegetarian shepherd's pie with Indian spices. Because my birthday falls near Thanksgiving, the meal was often followed by a turkey-shaped ice cream cake, Indian sweets like *jalebi* (a bright orange pretzel of fried sweet dough), *gulab jamun* (fried syrupy-sweet milk balls), and a spiced tea. We did adhere to the American tradition of overstuffing ourselves with food.

During the holiday, we listened to Bollywood pop, with high-pitched Indian women singing in Hindi or Bengali. Later in the season, my father would mix in some Nat King Cole or Frank Sinatra, or we would play an album from jazz pianist Vince Guaraldi. Being in Queens, I would always play "Christmas in Hollis" by the Queens-native hip-hop group Run DMC. My parents enjoyed it about as much as I did their Bollywood music, which is to say, not much.

In December, the large extended family of cousins, uncles, and aunts (all with a different honorific based on their birth position relative to my parents) would come over, each removing their shoes at the door out of respect. The men, in sweaters and ties, played bridge cross-legged in a corner on the floor. The women, in saris and their finest gold necklaces and earrings (gaudier than any of the jewelry worn by the hip-hip artists I worshiped), congregated in the dining area, where they teased each other, told stories in Bengali, and prepared meals. Food was served constantly from the moment the first guests arrived until they left. The smell of food cooking, mostly oil and spices, radiated and permeated through every fabric of the house. Chatter, the sounds of food frying, and playful arguing filled every room with noise. Our home was festively decorated; Santa Claus had equal billing with Durga, Kali, and Ganesh.

The kids watched American football or challenged each other to an Indian game called *carrom*, which is similar to billiards but played on a flat smooth table on the floor. Players use their fingers to flick flat wooden discs into different corner pockets. We would play different tournament styles and use a mix of Bengali and English to taunt and tease each other over missed shots or "lucky" wins.

Before our current chapter as Americans, my family's Indian past stretches back to time immemorial, but India has a complicated history of invasions and rule. I hoped a DNA test would help clarify some ancestry questions. I wanted the results to say 25% Genghis Khan, 25% Gandhi, 25% Alexander the Great, and 25% unknown. What I got was 64% Central Asian, 30% South Asian, 3% Eastern European, 2% Southeast Asian, and 1% Siberian. So, I could claim Genghis, Gandhi, and Alexander! But of course, not really. I wondered when and where the mingling

of my different geographic ancestors took place and if the results were more a reflection of the current genetic reference populations in those areas. The DNA results didn't make me feel differently about my identity, and they were not as interesting as the results I received from a genetic profile that revealed an inversion in one of my chromosomes. That genetic result made me realize how hardy our genomes are and how similar we are as humans; even the 1% or so that makes each of us unique is almost meaningless when considering the bigger picture.

Prosanta Chakrabarty
Louisiana State University Museum of Natural Science, Baton Rouge, LA 70803–3216, USA. Email: prosanta@lsu.edu

A musical Colombian Novena

Born in South America, I identify as Latina and have always been aware of my mixed ethnicity. My family's celebration of Christmas and Novena (the previous 9 days, an important observance in Colombia) exemplifies our love of food, music, and dance. During the first 8 days, family and friends meet at different houses to share deep-fried cheesy dough and sweets. On Christmas day and the morning after, we eat homemade Colombian tamales wrapped in plantain leaves and boiled for hours, and we drink hot chocolate—first adding salty cheese to the mugs and eating it with a spoon once it has melted (a delicacy unique to Bogotá, Colombia's capital). Sometimes we also eat cheese arepas (flat corn bread) and *almojabánas* (cheese bread of Spanish-Arab origin). Meanwhile, my mum prepares about 20 liters of her famous *ajiaco*, a traditional soup from the Bogota plateau. She uses three kinds of potatoes (one of them endemic to the Northern Andes), *guascas* (*Galinsoga parviflora*), corn, chicken, capers, and cream. Toward the end of the day, the whole family gathers for a bowl of *ajiaco*. We admire our araucaria tree, decorated with lights and ornaments, and the creatively assembled nativity scene (often including llamas, lions, jaguars, and the occasional dinosaur) while waiting for midnight to come.

My family seems to carry music in our blood. There is always a moment when my uncle plays the guitar and everyone else joins in with percussion and voices, singing the melodies of cumbia, vallenato, and bambuco—musical styles incorporating strings and accordions from Europe, wind instruments from Indigenous communities, and African drums. The upbeat tunes belie the bittersweet themes in the Spanish lyrics. Soon, everyone is dancing to the energetic, fast-moving rhythms of cumbia, salsa, and merengue. Salsa originated with the Latin and Afro-Latin son cubano and jazz musicians from the Bronx in the United States. The music later made its way to Colombia, where it developed into something new, incorporating cumbia and vallenato elements and a faster dancing style.

I took a DNA test because I work in the fields of population genomics and phylogenomics and thought it would be fun to see my own genome sequences. Half of the sites sequenced on my genome were assigned to populations in Spain, Morocco, and West Africa; the other half to Native American populations. The results were not a surprise, but they encouraged me to dig deeper into my family's history. I wish I could learn about and celebrate the Native American traditions of my ancestors, but most were never documented and are now lost. Important traditions are kept in the Amazon regions, such as "*chontaduro* dancing," where communities share the *chontaduro* fruit (from the *Bactris gasipaes* palm) and drinks to celebrate abundance and usher in a good fishing season. Traditions around the cassava, plant growing seasons, and hunting also still take place, but because I grew up in the city, I don't feel personally connected to them. I do take pride in using the words from Quechua, Muisca, and even Arabic languages that have been assimilated into Colombian Spanish.

We knew my grandfather was "Indigenous from the south" (as the government labeled him back in the day), but the DNA test results suggest that our Indigenous ancestry could have been more recent and likely than we thought. I found the test interesting; I received a set of raw data that I can analyze myself, and the results brought my father and me together in a quest for the documents and stories surrounding my family.

Maria Fernanda Torres Jimenez
Gothenburg Global Biodiversity Centre, University of Gothenburg, Gothenburg, Sweden. Email: mftorres27@gmail.com

10.1126/science.abg5843

ILLUSTRATION: MICHELLE KONDRICH

POLICY FORUM

ILLUSTRATION: MICROSTOCKHUB/ISTOCK.COM

HUMAN GENOME ANNIVERSARY

Complicated legacies: The human genome at 20

Millions of people today have access to their personal genomic information. Direct-to-consumer services and integration with other "big data" increasingly commoditize what was rightly celebrated as a singular achievement in February 2001 when the first draft human genomes were published. But such remarkable technical and scientific progress has not been without its share of missteps and growing pains. *Science* invited the experts below to help explore how we got here and where we should (or ought not) be going. **—Brad Wible**

An ethos of rapid data sharing, more relevant than ever

By **Kathryn Maxson Jones**[1,2] *and* **Robert Cook-Deegan**[3]

Sharing data can save lives. The "Bermuda Principles" for public data disclosure are a fundamental legacy of producing the first human reference DNA sequence during the Human Genome Project (HGP) (*1*). Since the 1990s, these principles have become a touchstone for open science.

In February 1996, the leaders of the HGP gathered in Bermuda to discuss how to scale up production for a human reference DNA sequence. With some caveats, the consortium agreed that all sequencing centers would release their data online within 24 hours. Other examples of sharing data before publication existed, but most—such as the Protein Data Bank—restricted sharing of prepublication data to a small community of users, sometimes withholding data even after the related papers were published (*2*). At the time, the Bermuda Principles were distinctive in their aspiration that all HGP-funded sequences be released to anyone online within a day. Yet implementing this policy was hardly simple; the challenges that the HGP faced inform data sharing today (*3*).

The Bermuda Principles required advocacy. This came from John Sulston and Robert Waterston, whose experiences with data sharing in *Caenorhabditis elegans* biology were the practical precedent for a radical idea. Context also mattered, and data release within 24 hours remained an aspirational ethos rather than a strict requirement. Flexibility allowed smaller centers to participate while also allowing the project to accommodate then-incompatible policies in Germany, France, Japan, and the United States.

Finally, the policy required enforcement. Administrators from the HGP's largest patrons sent stern letters intended to make funders' policies conform to the Bermuda Principles, threatening expulsion from the international sequencing consortium.

The Bermuda Principles have since been adapted to different communities and have served as an inspiration for many others (*4*). For example, rapid data sharing has been crucial in the current coronavirus crisis. The severe acute respiratory syndrome coronavirus 2 (SARS-CoV-2) genome was identified quickly and its sequence released on 10 January 2020, starting the clock on the development of vaccines and diagnostic tests. The COVID-19 Host Genetics Initiative disseminated data rapidly and openly, building on precedents such as the Global Initiative on Sharing All Influenza Data (*5*, *6*).

Of course, unfettered data sharing is not, and should not be, universal. Identifiable individual medical data, for instance, cannot be treated the same way as samples contributed to build a reference genome sequence. Many communities have adopted prepublication sharing strategies with considerable success, such as the various consortia for Alzheimer's research, the "open science" experiments at the Montreal Neurological Institute and the Mario Negri Institute, and the advances enabled by the Structural Genomics Consortium.

The HGP set a high bar. Its core values of open science and rapid data flow persist, fomented by the urgency of rapid data sharing in biomedicine.

Lack of diversity hinders the promise of genome science

By **Charles N. Rotimi[4], Shawneequa L. Callier[4,5], Amy R. Bentley[4]**

The long-term global impact of human genomics will be compromised, and our understanding of human history and biology hindered, if we continue to focus predominantly on individuals of European ancestry (*7*). Although we all share a recent common origin in Africa, and the genetic difference between any two individuals is small (0.1%), this translates to about 3 million points where individual genomes can vary, and the distribution of these human genetic variants (HGVs) is not random. It has long been understood that genomes (and exposures to key nongenetic factors) differ across ancestral and geographical backgrounds; nonetheless, genomics has largely focused on European-ancestry genomes. Presumably this is attributable to the availability of large, well-characterized datasets of European-ancestry individuals, academic and research networks that exclude and disadvantage underrepresented scholars (*8*), and the absence of publishing or funding motivation for large-scale genomics of diverse individuals. But diversity and representation are now being elevated from the purview of specialized research to a broad awareness across genomics.

As this awareness develops, the field must grapple with understanding and communicating the implications: (i) Any two sub-Saharan Africans are more likely to be genetically different from each other than from an individual of European or Asian ancestry; (ii) a subset of HGVs can only be found in Africans because the small number of humans that left Africa about 100,000 years ago to populate the rest of the world carried a fraction of the variation that existed then; (iii) the African ecological environment has left its mark on human genomes (e.g., gene variants found to increase vulnerability to kidney failure) that are seen worldwide only in persons with ancestry from specific regions of Africa (*9*).

Similarly, there are HGVs of health and historical importance that are rare or absent in African populations. For example, genomic regions harboring ancient DNA—the result of interbreeding with archaic human relatives (such as Neanderthals) in Asia, Europe, and the Americas—have biological functions, such as susceptibility to diabetes and viruses (*10*). For genomics-driven technologies and clinical and public health approaches to be deployed globally without exacerbating health inequalities, we must include individuals from diverse ancestral and geographical backgrounds.

Growing prioritization of diverse populations in genomics research has begun to respond to these gaps. Programs such as TOPMed, All of Us, International Common Disease Alliance, Human Heredity and Health in Africa (H3Africa), Million Veteran Program, GenomeAsia, and the COVID global consortium contribute to advances in diversity and inclusion among research participants. The diversity of genomics researchers also merits continuing attention. The H3Africa initiative, for example, includes investments in training and infrastructure in each project, providing a blueprint for prioritizing capacity-building. The genomics community needs to value diverse samples in analyses and conclusions, as well as to focus resources on capacity-building and removing barriers to create a diverse workforce (*11*).

Algorithmic biology unleashed

By **Hallam Stevens[6]**

Over a few frenzied weeks in the middle of 2000, icing his wrists between coding sessions, Jim Kent, a graduate student at the University of California, Santa Cruz, created the first genome assembler software. GigAssembler pieced together the millions of fragments of DNA sequence generated at labs around the globe, literally making the human genome. At almost the same time, Celera Genomics acquired Paracel, a company that primarily designed software for intelligence gathering. Paracel owned specially designed text-matching hardware and software (the TRW Fast Data Finder) that was rapidly adapted for sniffing out genes within the vast spaces of the genome.

Untangling the jumble of genomic letters required rapidly and accurately searching for a specified sequence within a very large space. This demanded new forms of training and disciplinary expertise. Physicists, mathematicians, and computer scientists brought methods such as linear programming, hashing, and hidden Markov models into biology. Since 2005, the Moore's Law–like growth of next-generation sequencing has generated ever-increasing troves of data and required even faster algorithms for indexing and searching. Biology has borrowed "big data" methods from industry (e.g., Hadoop) but has also contributed to pushing the frontiers of computer science research (e.g., the Burrows-Wheeler transform) (*12*).

The coalescence of bioinformatics and computational biology around algorithms has also given rise to new institutional forms and new markets for biomedicine. Statistically powered "data-driven biology" has configured an emerging medical-industrial complex that promises personalized and "precision" forms of diagnosis and treatment. Algorithmic pipelines that compare an individual's genotype to reference data generate a range of predictions about future health and risk. Direct-to-consumer genomics companies such as 23andMe now promise us healthier, happier, and longer ways of living via algorithms.

This presents substantial challenges for privacy, data ownership, and algorithmic bias (*13*–*15*) that must be addressed if genomics is to avoid becoming a handmaiden of "surveillance capitalism" (*16*). Many tech companies have begun to look toward

using machine learning to combine more and more biological data with other forms of personal data—where we go, what we buy, whom we associate with, what we like. The hopes for genomics have long been tempered by fears that the genome could reveal too much about ourselves, exposing us to new forms of discrimination, social division, or control. Algorithmic biology is depicting and predicting our bodies with growing accuracy, but it is also drawing biomedicine more closely into the orbits of corporate tech giants that are aggregating and attempting to monetize data.

Value and affordability in precision medicine

By **Kathryn A. Phillips[7,8,9], Jeroen P. Jansen[7,9], Christopher F. Weyant[7]**

Debates about precision medicine (PM), which uses genetic information to target interventions, commonly focus on whether we can "afford" PM (*17*), but focusing only on affordability, not also value, risks rejecting technologies that might make health care more efficient. Affordability is a question of whether we can pay for an intervention given its impact on budgets, whereas value can be measured by the health outcomes achieved per dollar spent for an intervention. Ideally, a PM intervention both saves money and improves outcomes; however, most health care interventions produce better outcomes at higher cost, and PM is no exception. By better distinguishing affordability and value, and by considering how we can address both, we can further the agenda of achieving affordable and valuable PM.

The literature has generally not shown that PM is unaffordable or of low value; however, it has also not shown that PM is a panacea for reducing health care expenditures or always results in high-value care (*17*). Understanding PM affordability and value requires evidence on total costs and outcomes as well as potential cost offsets, but these data are difficult to capture because costs often occur up front while beneficial outcomes accrue over time (*18*). Also, PM could result in substantial downstream implications because of follow-up interventions, not only for patients but also for family members who may have inherited the same genetic condition. Emerging PM tests could be used for screening large populations and could include genome sequencing of all newborns, liquid biopsy testing to screen for cancers in routine primary care visits, and predictive testing for Alzheimer's disease in adults. These interventions may provide large benefits, but they are likely to require large up-front expenditures. Another complication is that many PM interventions measure multiple genes relevant to multiple conditions and provide myriad types of value, such as the personal value of this information to patients (*19*).

Various methods have been developed for integrating affordability and value, but cost-effectiveness analyses often do not examine the budget impact, which can result in incomplete or contradictory conclusions (*20*). However, assessments that consider affordability and value simultaneously, such as those by the Institute for Clinical and Economic Review, are becoming more accepted by decision-makers (*21*). The growing consideration of both affordability and value is less a result of methodological advances than of an increased focus on how to ensure sustainable and efficient health care (and the corresponding political will to do so). A positive consequence of this is an increase in research on how to best define and quantify affordability and value given the available data.

PM is here to stay. However, it can only achieve its potential if it is both affordable and of high value.

End the entanglement of race and genetics

By **Dorothy E. Roberts[10]**

In the aftermath of the first publication of the human genome, researchers confirmed what many scholars had recognized for decades: that race is a social construct, not a natural division of human beings written in our genes (*22*, *23*). Yet rather than hammer the final nail in the coffin, the human genome map sparked renewed interest in race-based genetic difference. The posting of recent genetic studies on white supremacist websites led the American Society of Human Genetics in 2018 to issue yet another statement denouncing genetics-based claims of racial purity as "scientifically meaningless," while many geneticists failed to see how the biological concept of race was itself invented to support racism. None of this history has restrained the search for genetic differences between races and genetic explanations for various racial disparities (e.g., in COVID-19 outcomes), which in turn generates persistent public confusion about race and genetics.

It is time to end the entanglement of race and genetics and to work toward a radically new understanding of human unity and diversity. There are two general approaches that can help guide innovative research questions and methods that no longer rely on invented racial classifications as if they were biological. First, genetic researchers should stop using race as a biological variable that can explain differences in health, disease, or responses to therapies (*24*). Treating race as a biological risk factor obscures how structural racism has biological effects and produces health disparities in racialized populations. Epigenetics offers promising models to investigate one pathway through which unequal social conditions get "embodied" or "under the skin" to generate disparate health outcomes. Still, researchers must use caution to avoid making deleterious epigenetic processes seem self-perpetuating and inevitable, taking attention away from structural inequities that caused the problem in the first place (*25*).

Second, genetic researchers should stop using a white, European standard for human genetics and instead study a fuller range of human genetic variation. Projects dedicated to expanding genetic databases with DNA from groups on the African continent, for example, have shown that these populations are the most genetically diverse on Earth and refute the myth that there is a genetically distinguishable Black race (*26*). The aim of diversifying biomedical research should not be to find innate genetic differences between racial groups; rather, it should be to give persons from racialized populations equal access to the benefits of participating in high-quality and ethical research (including clinical trials) and to give scientists a richer resource to understand human biology. In this way, genetic research can contribute to more individualized diagnoses and therapies that no longer rely on crude medical decisions based categorically on a patient's race.

Genetic privacy in the post-COVID world

By **Dina Zielinski[11,12]** *and* **Yaniv Erlich[13]**

In 2007, only two individuals had their full genome sequenced: Craig Venter and Jim Watson. Today, more than 30 million individuals have access to their detailed genomic datasets. This democratization of genomic data has helped to reunite families,

fight racism, and promote genetic literacy (*27*, *28*), but it has also enabled surveillance on a massive scale. The correlation of DNA variants between distant relatives means that relatively small databases can identify large parts of the population, including people who are not in the database (*29*). The high dimensionality of DNA data and linkage disequilibrium mean that efforts to obscure individual-level data, by pooling genomes or censoring parts of the genome, can fail unexpectedly (*30*). And with the advent of consumer genomics and third-party websites that allow participants to upload their genome data, it is increasingly easy to collect and access DNA data (*31*).

We envision that the COVID-19 pandemic will accelerate genetic surveillance. People will likely see infectious disease surveillance, swabbing upon arrival, at border crossings, including airports. Governments can harness pandemic control infrastructure to build a DNA database of all arrivals. Such databases can identify a substantial portion of the visitor's home-country population because genetic re-identification is magnified through familial connections. But massive surveillance will not be restricted to government efforts. With the growing size of third-party genetic databases, essentially everyone with the right technical skills will be able to identify individuals.

What are the implications of ubiquitous genetic surveillance? On the plus side, law enforcement agencies will be able to solve virtually all sexual assault cases. Screening at airports can help to reveal fraudulent identities, which is central in fighting human trafficking and espionage. However, the same technology can be used to target minorities or political opponents.

The convergence of these applications underscores the importance of treading lightly with these new forensic superpowers. On the technical side, one theoretical mitigation option to limit such re-identification could include creating a trail that leads a genealogical tracing attempt to a fake identity. But this and other methods have yet to be investigated in a principled approach. Beyond technological countermeasures, the field needs guidelines concerning the use of genetic surveillance technologies. An important step is the interim policy laid out by the U.S. Department of Justice restricting forensic investigators' usage of third-party genetic databases to investigations of violent crimes, and only with sites that receive informed consent from users for such searches (*32*). Open public discussion is vital to further shape policies and expectations so as to harness the power of the genomic revolution for the benefit of the public.

PHOTO: RENE BEGAY

Dr. Jessica Elm watches Alison Watson hold the pipette for a DNA extraction exercise during the Summer Internship for Indigenous Peoples in Genomics (SING) workshop in 2019.

Emerging ethics in Indigenous genomics

By **Nanibaa' A. Garrison**[14,15,16] *and* **Stephanie Russo Carroll**[17,18]

Despite considerable advances in genomics research over the past two decades, Indigenous Peoples are incredibly underrepresented. Biological materials from Indigenous Peoples have been collected to study diseases, medical traits, and the origins of human populations, yet many studies have not benefited the participants or their communities. Some research has even created harms such as exacerbation of derogatory and detrimental stereotypes or challenges to cultural beliefs. Without productive relationships, Indigenous communities may not benefit from research in areas such as precision medicine and pharmacogenomics, and health disparities may remain unaddressed. Thus, many Indigenous Peoples are hesitant to participate in genomics research without extensive discussions and agreements to ensure that the results have individual and collective benefits, as well as to learn what happens to samples and how they are used (*33*). Indigenous scholars are developing guidance to address concerns and pave pathways for more equitable and beneficial research that aligns with the rights and interests of Indigenous Peoples (*34*).

Culturally aligned research can increase Indigenous Peoples' participation in genomics research. The Summer Internship for Indigenous Peoples in Genomics (SING) trains and builds capacity for scientists and community members to shape research priorities of interest in their communities, and it has prompted the SING Consortium to develop a framework for ethical research engagement (*35*). The Center for the Ethics of Indigenous Genomic Research supports Indigenous-led research in biobanking and precision medicine that integrates sovereignty rights and Indigenous communities' ethical and cultural preferences. In Canada, Silent Genomes is creating an Indigenous Background Variant Library through close engagement with community and cultural advisors. Finally, in New Zealand, the Māori-developed Te Ara Tika framework integrates relationships, research design, cultural and social responsibility, justice, and equity as core interests for ethical genomic research with Māori people (*36*).

Recognizing the need to foster self-determination and collective rights within open science and secondary use, the Global

Indigenous Data Alliance's CARE Principles for Indigenous Data Governance (Collective Benefit, Authority to Control, Responsibility, and Ethics) complement the FAIR principles (Findability, Accessibility, Interoperability, and Reusability) that make data machine-readable and usable in multiple contexts (*37*, *38*). When operationalized together, CARE and FAIR enhance Indigenous leadership and innovation, leading to participatory governance and enabling opportunities for trust-building and accountability by incorporating Indigenous values and rights. For example, the creation of data standards and the use of Indigenous community-defined metadata can protect data while allowing them to be useful. The metadata become durable and persistent components of genomic information that provide guidance on future use, such as who has the authority to sanction that use, for what purposes, and to benefit whom (*34*, *37*).

An increased focus on rights and interests combined with enhanced engagement and capacity has the potential to reduce bias and produce more relevant and beneficial research for all.

N.A.G. is Diné, a citizen of the Navajo Nation. S.R.C. is Ahtna, a citizen of the Native Village of Kluti-Kaah.

Polygenic risk in a diverse world

By **Pilar N. Ossorio**[19]

Polygenic risk scores (PRSs) are a rapidly emerging technology for aggregating the small effects of multiple polymorphisms across a person's genome into a single score. A PRS can be calculated for any phenotype for which genome-wide association data are available, usually by summing the weighted effect sizes of alleles (*39*). In medicine and public health, PRSs could be used for selecting therapies, initiating additional risk screening, or motivating behavior change. Whether they will be used in medicine depends on factors such as the degree to which they provide actionable risk information beyond that provided by clinical algorithms, the availability of information technology for calculating PRSs in clinical settings, and the availability of decision support tools. To date, PRSs have demonstrated moderate utility for complex medical phenotypes, including blood pressure, obesity, diabetes, depression, schizophrenia, and coronary heart disease.

PRSs also highlight the complex intersection of race and ancestry in genomics. Substantiating and extending earlier work, a recent analysis showed that in 26 previous studies, PRSs performed significantly worse for people with predominantly African or South Asian ancestry than for people with predominantly European ancestry (*40*, *41*). There was not enough data to assess performance for many groups (e.g., South East Asians, Pacific Islanders). Researchers have attributed this result to underrepresentation of non-European individuals and racial/ethnic minorities in datasets used to develop PRSs. Relative to people who are included in most genomic datasets, racial/ethnic minorities tend to have a greater portion of recent ancestry from places other than Europe.

In response to the differential predictive power of PRSs, researchers have developed some PRSs specifically for people of predominantly African ancestry, and genome scientists are considering whether "ancestry-specific PRS are needed for every ethnic group…" (*42*). These developments occur as scholars of race call for an end to many uses of "race correction" in medicine (*43*). Appropriate attention to genetic ancestry's effects on PRSs can easily collapse into an ill-informed focus on race, without considering how social inequalities shape health and how race is an imperfect proxy for ancestry. Society needs a multidisciplinary approach for developing and implementing PRSs for diverse communities. Otherwise, ancestry-specific PRSs could reinvigorate people's misconceptions about human races as genetically distinct groups and encourage mistaken views that trait distribution between racial/ethnic groups is primarily caused by genetics (*39*). Such beliefs are central to white supremacy and racist medical practices. Injustice in science can occur because some groups of people are not included (*44*), but injustice can also result from inappropriate inclusion.

Risks of genomic surveillance and how to stop it

By **Yves Moreau**[20] *and* **Maya Wang**[21]

The use of DNA profiling for individual cases of law enforcement has helped to identify suspects and to exonerate the innocent. But retaining genetic materials in the form of national DNA databases, which have proliferated globally in the past two decades, raises important human rights questions. Landmark court decisions in Europe and in the United States set some limits on data collection and retention in DNA databases, such as restricting long-term retention of DNA profiles to people arrested for or convicted of a crime.

But these decisions are far from the comprehensive regulations we need. Privacy rights are fundamental human rights. Around the world, the unregulated collection, use, and retention of DNA has become a form of genomic surveillance. Kuwait passed a now-repealed law mandating the DNA profiling of the entire population. In China, the police systematically collected blood samples from the Xinjiang population under the guise of a health program, and the authorities are working to establish a Y-chromosome DNA database covering the country's male population. Thailand authorities are establishing a targeted genetic database of Muslim minorities (*45*). Under policies set by the previous administration, the U.S. government has been indiscriminately collecting the genetic materials of migrants, including refugees, at the Mexican border.

As the technology gets cheaper, and as the adoption of surveillance gets ever broader, there is an acute risk of pervasive genomic surveil-

[1]School of Life Sciences, Arizona State University, Tempe, AZ, USA. [2]Center for Medical Ethics and Health Policy, Baylor College of Medicine, Houston, TX, USA; kmaxson@alumni.princeton.edu. [3]School for the Future of Innovation in Society and Consortium for Science, Policy and Outcomes, Arizona State University, Washington, DC, USA. [4]Center for Research on Genomics and Global Health, National Human Genome Research Institute, Bethesda, MD, USA; rotimic@mail.nih.gov. [5]Department of Clinical Research and Leadership, George Washington University School of Medicine and Health Sciences, Washington, DC, USA. [6]School of Humanities, Nanyang Technological University, Singapore; hstevens@ntu.edu.sg. [7]Center for Translational and Policy Research on Personalized Medicine (TRANSPERS), Department of Clinical Pharmacy, University of California, San Francisco, CA, USA. [8]Philip R. Lee Institute for Health Policy Studies, University of California, San Francisco, CA, USA. [9]Helen Diller Family Comprehensive Cancer Center, University of California, San Francisco, CA, USA; kathryn.phillips@ucsf.edu. [10]Department of Africana Studies, Department of Sociology, and Law School, University of Pennsylvania, Philadelphia, PA, USA; dorothyroberts@law.upenn.edu. [11]Université de Paris, INSERM 970, Paris Translational Research Centre for Organ Transplantation, Paris, France. [12]Doctoral School 515, Sorbonne Université, Paris, France. [13]Efi Arazi School of Computer Science, IDC Herzliya, Herzliya, Israel; erlichya@gmail.com. [14]Institute for Society & Genetics, University of California, Los Angeles, CA 90095, USA. [15]Institute for Precision Health, David Geffen School of Medicine, University of California, Los Angeles, CA 90095, USA. [16]Division of General Internal Medicine & Health Services Research, David Geffen School of Medicine, University of California, Los Angeles, CA 90095, USA; nanibaa@socgen.ucla.edu. [17]Native Nations Institute, Udall Center for Studies in Public Policy, University of Arizona, Tucson, AZ 85724, USA. [18]Mel and Enid Zuckerman College of Public Health, University of Arizona, Tucson, AZ 85724, USA. [19]Morgridge Institute for Research and University of Wisconsin Law School, Madison, WI, USA; pnossorio@wisc.edu. [20]University of Leuven (KU Leuven), Leuven, Belgium; yves.moreau@kuleuven.be. [21]Human Rights Watch, New York, NY, USA; wangm@hrw.org.

A police officer holds a DNA test swab of blood found at a crime scene in Kansas City, Missouri, 24 July 2008. DNA tests and genetic databases have been increasingly used, with some success, by law enforcement, but this also raises concerns about how to prevent potential overreach in the form of ubiquitous genomic surveillance.

PHOTO: FRED BLOCHER/KANSAS CITY STAR/TRIBUNE NEWS SERVICE/GETTY IMAGES

lance, not only by authoritarian regimes but also in democracies with weakening rights. But such a loss of autonomy and freedom is not inevitable. Governments should reform surveillance laws and draft comprehensive privacy protections that tightly regulate the collection, use, and retention of DNA and other biometric identifiers (*46*). They should ban such activities when they do not meet international human rights standards of lawfulness, proportionality, and necessity. They should develop a coordinated global regime of export control legislation, as well as sanctions akin to the U.S. Magnitsky Act, to hold businesses accountable that recklessly supply or market this technology for genomic surveillance.

Journal editors and publishers should reassess hundreds of ethically suspect DNA-profiling publications—for example, publications co-authored by police forces involved in the persecution of the minorities studied (*47*) or lacking proper consent or ethical approval (*48*). Although there have been a few retractions (*47*, *48*), such assessments should not be limited to the bureaucratic verification of informed consent and ethical approval documents; they also need to consider the basic ethical principles of beneficence, nonmaleficence, autonomy, justice, and faithfulness. The scientific community should also refuse to cooperate with law enforcement anywhere in the world that is proven to be violating human rights standards, in particular the Chinese police and military.

REFERENCES AND NOTES

1. E. S. Lander *et al.*, *Nature* **409**, 860 (2001).
2. B. J. Strasser, *Isis* **102**, 60 (2011).
3. K. M. Jones, R. A. Ankeny, R. Cook-Deegan, *J. Hist. Biol.* **51**, 693 (2018).
4. National Human Genome Research Institute, *NHGRI Genomic Data Sharing (GDS) Policy: Data Standards* (2020).
5. N. L. Yozwiak, S. F. Schaffner, P. C. Sabeti, *Nature* **518**, 477 (2015).
6. "Benefits of sharing" [editorial], *Nature* **530**, 129 (2016).
7. A. R. Bentley, S. Callier, C. N. Rotimi, *J. Community Genet.* **8**, 255 (2017).
8. T. A. Hoppe *et al.*, *Sci. Adv.* **5**, eaaw7238 (2019).
9. G. N. Nadkarni *et al.*, *N. Engl. J. Med.* **379**, 2571 (2018).
10. Y. Luo, *Nature* **587**, 552 (2020).
11. E. D. Green *et al.*, *Nature* **586**, 683 (2020).
12. H. Stevens, *Biosocieties* **11**, 352 (2016).
13. D. Grishin, K. Obbad, G. M. Church, *Nat. Biotechnol.* **37**, 1115 (2019).
14. L. Bonomi, Y. Huang, L. Ohno-Machado, *Nat. Genet.* **52**, 646 (2020).
15. K. Ferryman, M. Pitcan, *Fairness in Precision Medicine* (Data & Society, 2019).
16. S. Zuboff, *The Age of Surveillance Capitalism: The Fight for a Human Future at the New Frontier* (Profile, 2019).
17. D. M. Cutler, *JAMA* **323**, 109 (2020).
18. K. A. Phillips, M. P. Douglas, D. A. Marshall, *JAMA* **324**, 2029 (2020).
19. E. Faulkner *et al.*, *Value Health* **23**, 529 (2020).
20. A. Towse, J. A. Mauskopf, *Value Health* **21**, 249 (2018).
21. S. D. Pearson, *Value Health* **21**, 258 (2018).
22. J. L. Graves Jr., *The Emperor's New Clothes: Biological Theories of Race at the Millennium* (Rutgers Univ. Press, 2001).
23. D. Roberts, *Fatal Invention: How Science, Politics, and Big Business Re-Create Race in the Twenty-First Century* (New Press, 2012).
24. M. Yudell, D. Roberts, R. DeSalle, S. Tishkoff, *Science* **351**, 564 (2016).
25. D. E. Roberts, O. Rollins, *Annu. Rev. Sociol.* **46**, 195 (2020).
26. M. C. Campbell, S. A. Tishkoff, *Annu. Rev. Genomics Hum. Genet.* **9**, 403 (2008).
27. A. Panofsky, J. Donovan, *Soc. Stud. Sci.* **49**, 653 (2019).
28. J. S. Roberts *et al.*, *Publ. Health Genomics* **20**, 36 (2017).
29. Y. Erlich, T. Shor, I. Pe'er, S. Carmi, *Science* **362**, 690 (2018).
30. D. R. Nyholt, C.-E. Yu, P. M. Visscher, *Eur. J. Hum. Genet.* **17**, 147 (2009).
31. S. C. Nelson, D. J. Bowen, S. M. Fullerton, *Am. J. Hum. Genet.* **105**, 122 (2019).
32. J. Kaiser, *Science* 10.1126/science.aaz6336 (25 September 2019).
33. R. Taitingfong *et al.*, *J. Am. Med. Inform. Assoc.* **27**, 1987 (2020).
34. M. Hudson *et al.*, *Nat. Rev. Genet.* **21**, 377 (2020).
35. K. G. Claw *et al.*, *Nat. Commun.* **9**, 2957 (2018).
36. M. Hudson *et al.*, *He Tangata Kei Tua—Guidelines for Biobanking with Māori* (Te Mata Hautū Taketake—Māori & Indigenous Governance Centre, Univ. of Waikato, 2016).
37. S. R. Carroll *et al.*, *Data Sci. J.* **19**, 43 (2020).
38. M. D. Wilkinson *et al.*, *Sci. Data* **3**, 160018 (2016).
39. N. A. Rosenberg *et al.*, *Evol. Med. Public Health* **2019**, 26 (2019).
40. L. Duncan *et al.*, *Nat. Commun.* **10**, 3328 (2019).
41. A. R. Martin *et al.*, *Am. J. Hum. Genet.* **100**, 635 (2017).
42. National Human Genome Research Institute, *Genomic Medicine XII: Genomics and Risk Prediction*, Executive Summary (2019); www.genome.gov/sites/default/files/media/files/2019-07/GMXII_Executive_Summary.pdf.
43. D. E. Roberts, *Lancet* **397**, 17 (2021).
44. A. R. Martin *et al.*, *Nat. Genet.* **51**, 584 (2019).
45. UN Committee on the Elimination of Racial Discrimination, Letter to the Permanent Representative of Thailand to the United Nations Office (15 May 2015); https://bit.ly/39VxGJe.
46. Forensic Genetics Policy Initiative, *Establishing Best Practices for Forensic DNA Databases* (2017); https://bit.ly/3iasJzL.
47. D. Zhang *et al.*, *Int. J. Legal Med.* 10.1007/s00414-019-02049-6 [retracted] (2019).
48. X. Pan *et al.*, *Int. J. Legal Med.* **134**, 2079 [retracted] (2020).

ACKNOWLEDGMENTS

K.M.J. and R.C.-D. were funded by National Cancer Institute (NCI) grant R01 CA237118. C.N.R., S.L.C., and A.R.B. were supported in part by the Intramural Research Program of NIH through the Center for Research on Genomics and Global Health (CRGGH) at the National Human Genome Research Institute (NHGRI). The CRGGH is also supported by the National Institute of Diabetes and Digestive and Kidney Diseases. K.A.P. is a consultant to Illumina Inc. and was funded by NCI grant R01 CA221870 and NHGRI grant U01 HG009599. J.P.J. is a part-time salaried employee of the Precision Medicine Group. D.Z. and Y.E. hold equity in DNA.Land, a third-party genetic service. D.Z. is an employee of Cibiltech; Y.E. is an employee of Eleven Therapeutics, MyHeritage, and consultant to ArcBio. The views and opinions expressed in this article are those of the authors and do not necessarily reflect the official policies or positions of any of their employers.

10.1126/science.abg5266

PERSPECTIVES

HUMAN GENOME ANNIVERSARY

For better drugs, diversify clinical trials

Genetic variation in drug metabolism can affect drug outcomes

By **Namandjé N. Bumpus**

COVID-19 has highlighted the devastating disparities that exist for Black, Latinx, and Indigenous people in health care and medicine in the United States and other parts of the world. As a result, the importance of ethnic diversity in clinical trials has entered public discourse. This moral issue is enough to warrant elevation. But there are also scientific considerations because a lack of diversity in clinical trials hinders the ability to fully understand variation and predict drug outcomes across populations, including those most hard-hit by a disease.

A key aspect of clinical testing is to assess a drug's safety, evaluate side effects, determine a safe dosage range, and determine effectiveness. However, for decades, most clinical trials in the United States have been carried out primarily in individuals of European descent. As a result, dosing recommendations are largely based on data obtained in trials mainly comprising individuals with European ancestry (*1*). A study analyzing cancer trials that led to the approval of oncology drugs by the U.S. Food and Drug Administration (FDA) between 2008 and 2018 found that of 230 clinical trials, only 88 (38%) reported the number of Black participants in the study and only 23 (10%) reported on Hispanics (*2*). Overall, Black people and Hispanic people were found to represent only 3.1% and 6.1% of oncology trial participants, respectively. Furthermore, when accounting for the proportion of U.S. cancer incidence, the numbers of Black people in oncology trials were only 22% of what would be expected from proportional representation. Hispanics were similarly underrepresented; their participation was 44% of what would be expected based on the proportion of U.S. cancer incidence. By contrast, the representation according to cancer incidence was 98% for white people in oncology trials.

Humans are more similar than they are different, and genetic differences are small. But genetic variation in processes that control drug exposure and response, such as drug metabolism, can result in interindividual variability in outcomes. Thus, a lack of diversity in trials can skew safety, dosing, and efficacy results. When drugs are taken orally, they pass through the liver, which contains an abundance of drug-metabolizing enzymes, before entering systemic circulation. Once in the liver, these enzymes biochemically modify a drug, usually resulting in the conversion of the drug (which tends to be fat-soluble) into a "metabolite" that is more water-soluble and therefore more readily excreted from the body (for example, through urine or bile). The metabolites may be pharmacologically active, inactive, or toxic. As such, for a majority of currently marketed oral drugs, this process controls the amount of drug that ultimately reaches the target site, and thus drug metabolism influences the magnitude and the duration of pharmacological action.

Owing to genetics, people can be categorized as poor, intermediate, extensive, or ultrarapid metabolizers of certain drugs. For example, in the case of a drug that is pharmacologically active and its metabolites inactive, a drug may accumulate in the body of a poor metabolizer and toxicity could occur as a result. By contrast, someone who is an ultrarapid metabolizer of the same drug may not achieve concentrations of the drug in their blood that are high enough to be effective. For prodrugs, where the parent drug is inactive or substantially less active than its metabolite, genetically encoded variation in drug metabolism could affect the ability of a person to activate the drug.

Although genetic variation in drug metabolism does not influence all drugs in this way, diversification of clinical trials allows for enhanced understanding of when it does. Certain gene variants that encode drug-metabolizing enzymes are often more prevalent in specific ethnic groups and can have relevance in the context of dosing, therapeutic efficacy, and the likelihood of side effects and hypersensitivity reactions. Indeed, about one-fifth of new drugs approved by the U.S. Food and Drug Administration (FDA) between 2008 and 2013 exhibit differences in exposure and/or outcomes across ethnic groups (*3*). Pharmacogenetics is the science of understanding drug-gene interactions and how genetic variability governs therapeutic outcomes. However, even studies focused on understanding individual drug responses (in terms of either drug efficacy or toxicity) have mostly been performed in individuals of European ancestry. This is problematic because, for example, African Americans have been shown to have greater genetic variation than people of European descent (*4*). Thus, underrepresentation of African Americans and other individuals of non-European descent impedes the ability to integrate pharmacogenomics findings into clinical care and to fully leverage pharmacogenetics to predict drug outcomes (*5*–*7*).

The cytochromes P450 are a family of heme-containing monooxygenases that metabolize ~75% of clinically used drugs (*8*). The expression and activities of these enzymes are influenced by a range of factors, including genetic polymorphisms; as a result, they are a primary source of variability in drug response. A notable example of this is cytochrome P450 3A5 (CYP3A5), an enzyme that is not functionally expressed in most people of European descent because of genetic variation, including a 6986A>G single-nucleotide polymorphism that results in a splicing defect and consequently a truncated protein. This *CYP3A5*3* variant has an allele frequency of ~90% in individuals of European descent. By contrast, most people of African descent are CYP3A5 expressors because they carry one or two *CYP3A5*1* alleles (*9*). This means that most people of African ancestry have functional CYP3A5, whereas those of European ancestry do not.

The clinical implications of *CYP3A5* variation have been best described for tacrolimus, an immunosuppressive agent that is one of the most widely used drugs to prevent solid organ transplant rejection. Blood concentrations of tacrolimus have been linked to the *CYP3A5* genotype in several studies: People with *CYP3A5*1* exhibit greater rates of tacrolimus clearance and thus have lower drug concentrations than individuals with the *CYP3A5*3* genotype. Furthermore, a study conducted in African Americans demonstrated that the *CYP3A5*1* allele is associated with subtherapeutic con-

Department of Pharmacology and Molecular Sciences, Johns Hopkins University School of Medicine, Baltimore, MD 21205, USA. Email: nbumpus1@jhmi.edu

PHOTO: NATAGOLUBNYCHA/ISTOCK.COM

centrations of tacrolimus, and thus higher dose requirements than for patients with a *CYP3A5*3/*3* genotype (*10*).

African Americans are at 58% higher risk of major bleeding from warfarin, a widely prescribed anticoagulant used to treat or prevent blood clots in veins and arteries, compared to European Americans (*11*). Marked interindividual variability in warfarin dose requirements is observed clinically, and in general, African Americans require higher warfarin doses to achieve efficacy as compared to individuals of European or Asian descent. Warfarin acts by inhibiting vitamin K epoxide reductase complex subunit 1 (VKORC1) and thereby interferes with clotting factor activation. *VKORC1* and cytochrome P450 2C9 (*CYP2C9*) variants have been established as modulators of the warfarin dose that is required for an efficacious response. Regarding alleles associated with decreased CYP2C9 enzymatic function, *CYP2C9*2* and *CYP2C9*3* are the most common in people of European descent (*12*). These alleles are less prevalent in people of African descent. As a result of the reduction in warfarin metabolism, carriers of one or two copies of *CYP2C9*2* or *CYP2C9*3* have reduced warfarin clearance leading to significantly lower dosing requirements. In African Americans, the *CYP2C9*5*, **6*, **8*, and **11* alleles are important contributors to warfarin metabolism.

A large, multicenter, double-blind, randomized controlled trial [called Clarification of Optimal Anticoagulation through Genetics (COAG)] investigated the impact of incorporating genetic data into a warfarin dosing algorithm (*13*). The cohort was ethnically diverse and 27% of participants were of African descent. However, for *CYP2C9*, the genotyping panel in this study was limited to *CYP2C9*2* and *CYP2C9*3*, and therefore did not include variants that influence warfarin metabolism in people of African descent specifically (i.e., *CYP2C9*5*, **6*, **8*, and **11*). This resulted in potential overdosing in individuals carrying the *CYP2C9*5*, **6*, **8*, and **11* alleles and, ultimately, guidance by the Clinical Pharmacogenetics Implementation Consortium that pharmacogenetic dosing of warfarin should not be used in people of African ancestry when only *CYP2C9*2* and *CYP2C9*3* genotyping data are available (*14*).

Beyond those explained by genetic differences in drug metabolism, several other therapies have shown ethnic associations. African Americans are more likely to experience angioedema after treatment with angiotensin-converting enzyme inhibitors (*15*). Angioedema is a rapid swelling that involves the skin and subcutaneous tissue or submucosa, and severe cases can result in respiratory distress by affecting the upper airway and larynx. The mechanism(s) underlying the frequency of this adverse outcome in African Americans remain to be understood; however, it may be related to genetic differences in the kallikrein-kinin system, which is a metabolic cascade connected to vasodilation.

Additionally, ~10% of African American males are glucose-6-phosphate dehydrogenase–deficient, which can result in hemolytic anemia in response to certain drugs such as chloroquine and primaquine that are used to treat malaria. This is attributed to the finding that intracellular concentrations of reduced nicotinamide adenine dinucleotide phosphate (NADPH) are depleted in these individuals under conditions of oxidative stress, thereby increasing the risk of intravascular hemolysis in response to oxidative agents, including chloroquine and primaquine.

Collectively, these examples underscore the importance of investigating drug outcomes and genetic variation in a diverse range of populations. Well-designed trials, including those for COVID-19 therapeutics, need to be powered in such a way that they can characterize potential genetic differences in clinical outcomes that may be specific to certain ethnic groups. This means that clinical trials must reflect the population, and in diseases where ethnic disparities in incidence and/or mortality have been established, consideration should be given to making commensurate adjustments in clinical trial demographics. Historic mistrust regarding clinical trials must be acknowledged, and scientists and medical professionals must fully engage in the work of trust building.

As part of this work, it is necessary to dismantle barriers to clinical trial participation, including through careful consideration of participant eligibility criteria. For example, participant exclusion based on HIV-positive status can have a disproportionate impact on the ability of people from certain populations to participate in a study, and this may not always be necessary from a scientific or safety perspective. Key to addressing these issues is a diverse and inclusive scientific workforce, as it will enhance the likelihood that there will be equity in the selection of genes, models, study design, and outcomes investigated. Funding agencies also have a role to play in ensuring accountability for representation in clinical trials, enabling the development of model systems to better understand the mechanisms underlying ethnic disparities in drug outcomes, as well as safeguarding the vitality of basic sciences (such as pharmacology) so that the foundation upon which drug trials are built can be continuously strengthened. Finally, reporting of ethnicity data in published reports of clinical trials should be required to ensure transparency regarding study demographics. Recognizing and acting on the need to diversify clinical trials is an important way to ensure that treatments are most likely to work for all people and that existing health disparities and the costs they bring are not further exacerbated. ■

REFERENCES AND NOTES

1. J. A. Johnson, *J. Pharm. Sci.* **86**, 1328 (1997).
2. J. M. Loree *et al.*, *JAMA Oncol.* **5**, e191870 (2019).
3. A. Ramamoorthy, M. A. Pacanowski, J. Bull, L. Zhang, *Clin. Pharmacol. Ther.* **97**, 263 (2015).
4. M. A. Perera, L. H. Cavallari, J. A. Johnson, *Clin. Pharmacol. Ther.* **95**, 242 (2014).
5. V. A. Johnson, Y. M. Powell-Young, E. R. Torres, I. J. Spruill, *ABNF J.* **22**, 84 (2011).
6. W. Hernandez *et al.*, *Pharmacogenomics J.* **20**, 126 (2020).
7. C. L. Scherr, S. Ramesh, C. Marshall-Fricker, M. A. Perera, *Front. Genet.* **10**, 548 (2019).
8. F. P. Guengerich, M. R. Waterman, M. Egli, *Trends Pharmacol. Sci.* **37**, 625 (2016).
9. J. K. Lamba, Y. S. Lin, E. G. Schuetz, K. E. Thummel, *Adv. Drug Deliv. Rev.* **54**, 1271 (2002).
10. D. J. Taber *et al.*, *Transplantation* **101**, 2931 (2017).
11. N. A. Limdi *et al.*, *Pharmacogenet. Genomics* **27**, 347 (2017).
12. C. R. Lee, J. A. Goldstein, J. A. Pieper, *Pharmacogenetics* **12**, 251 (2002).
13. S. E. Kimmel *et al.*, *N. Engl. J. Med.* **369**, 2283 (2013).
14. J. A. Johnson *et al.*, *Clin. Pharmacol. Ther.* **102**, 397 (2017).
15. D. R. Miller *et al.*, *Hypertension* **51**, 1624 (2008).

ACKNOWLEDGMENTS

The author has received consulting fees, honoraria, or funding from Amgen, Merck, and Genentech.

10.1126/science.abe2565

PHOTONICS

Ultrafast generation of optical hyperbolicity

A new strategy actively controls the trapping and manipulation of light

By **Shaozhi Deng** and **Huanjun Chen**

The propagation of light through a material is governed by an isofrequency surface related to the crystal structure. This surface is spherical for an isotropic crystal and an ellipsoid for many anisotropic crystals. An extreme, unusual, and intriguing surface is a hyperboloid. Hyperbolic media are able to support electromagnetic waves with ultrashort wavelengths. This makes them attractive for subwavelength light trapping and manipulation. Particularly, hyperbolicity in the mid-infrared to terahertz range can find applications in controlling thermal radiation and heat transfer (*1*). Although hyperbolicity has been realized in artificial metamaterials (*2*) and recently discovered in natural materials (*3*–*5*), generating and actively controlling the hyperbolicity in materials that are inherently nonhyperbolic is difficult. On page 617 of this issue, Sternbach *et al.* (*6*) propose a strategy for creating hyperbolicity in tungsten diselenide (WSe_2) by means of femtosecond carrier photoinjection.

WSe_2 is a van der Waals (vdW) semiconductor. The high-density electron-hole pairs from photoinjection result in transient hyperbolic polaritons—electromagnetic modes attributable to the coupling of incident light with collective electric or magnetic dipole oscillations. The operation wavelengths can be dynamically controlled in the mid-infrared regime by tuning the photoexcitation density. The authors further visualize the conical polariton wavefront using a nano-imaging technique.

Hyperbolicity essentially requires that the in-plane and out-of-plane dielectric permittivities exhibit opposite signs. Traditionally, this is realized with artificial metamaterials composed of repeating metallic patterns (*2*). Yet, the feature size of the patterns (tens of nanometers to hundreds of micrometers) seriously impedes the ability to confine light to nanoscale dimensions. This issue can be alleviated by resorting to natural materials with atomic-scale unit cells (*3*). Among them, vdW crystals and their heterostructures that consist of atomic planes bonded by vdW force exhibit highly orientation-dependent dielectric responses, which are inherited from their anisotropic electronic structures or lattice vibrations. In particular, vdW crystals sustaining polaritons can be endowed with hyperbolicity in the spectral range from ultraviolet to terahertz (*4*, *5*). Since 2014, hyperbolic polaritons have been experimentally identified in a few vdW crystals, including plasmon polaritons in tungsten ditelluride (WTe_2) (*7*) and phonon polaritons in hexagonal boron nitride (h-BN) (*8*), molybdenum trioxide (α-MoO_3) (*9*, *10*), and vanadium pentoxide (α-V_2O_5) (*11*). Moreover, the polaritonic properties of the vdW crystals can be actively controlled through chemical doping, electrical gating, and photoinjection, making them highly attractive for tunable photonic and optoelectronic applications.

Compared with other approaches, photoinjection is an effective method for modulating the polariton properties of vdW crystals, in terms of its high speed, all optical control, and high on/off ratios. However, preparation of hyperbolicity in vdW crystal without intrinsic polaritons remains challenging. Sternbach *et al.* demonstrate that the injection of high-density electron-hole pairs generates hyperbolic polaritons. Because of its anisotropic electronic structure, the optical isofrequency surface of pristine WSe_2 is an ellipsoid, and correspondingly, the permittivities in the basal plane are different from that along a perpendicular direction (see the figure). The photoinjected electron-hole pairs can form series of discrete excitonic states. Polaritons can thereafter be formed because of exciton transitions between different states coupling to photons. Accordingly, the topology of the isofrequency surface will transform from a closed ellipsoid to an open hyperboloid. Because the transition energies are tens of milli–electron volts, the hyperbolic responses locate in the mid-infrared range (~750 to 1000 cm^{-1}). The evidence for hyperbolicity is the directional light rays that propagate inside the crystal. Furthermore, because of the short lifetime of the excitonic states, the hyperbolicity is a transient process of the subpicosecond time scale.

Sternbach *et al.* also show that the hyperbolicity can be dynamically controlled by tuning the photoexcitation density. This control is possible because the exciton transitions, which determine the magnitude and sign of the permittivities, are strongly dependent on the photoinjected carrier density (n_x). The n_x monotonically increases with increasing excitation power. The polaritonic bands can therefore span a very broad elec-

Transient hyperbolicity

The optical properties of WSe_2 can be quickly changed by photoinjection from a normal state to an exotic hyperboloid. The hyperboloid state allows light to be trapped and manipulated.

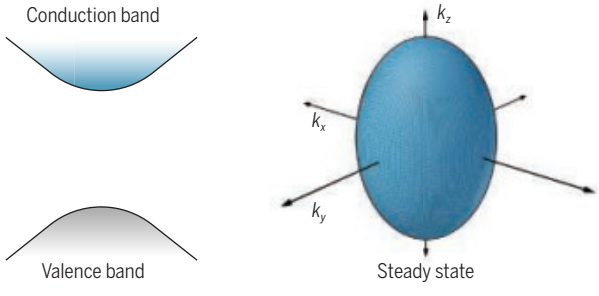

Normal state
In the steady state, WSe_2 is a typical semiconductor with a moderate bandgap. The permittivities are different in different directions because of the crystal structure.

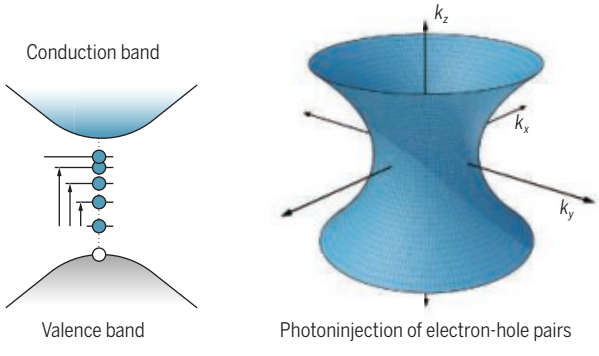

Pumped state
Photoinjection from femtosection laser illumination forms a series of exciton states because of high density electron-hole pairs. This changes the isofrequency surface from the normal closed ellipsoid to an open hyperboloid.

GRAPHIC: C. BICKEL/*SCIENCE*

State Key Laboratory of Optoelectronic Materials and Technologies, Guangdong Province Key Laboratory of Display Material and Technology, School of Electronics and Information Technology, Sun Yat-sen University, Guangzhou 510275, China. Email: stsdsz@mail.sysu.edu.cn

tromagnetic spectrum through adjustment of the excitation power. This virtue can address the issue that most of the hyperbolicity in vdW crystals can only be tuned in a narrow spectral width. Potential applications could be envisioned, for example, to enhance the performance of biological and chemical sensing by tuning the hyperbolic band to overlap with and enhance the molecular vibrational and rotational fingerprints in the mid-infrared to terahertz spectral regime.

The transient hyperbolic polaritons offer an opportunity for on-demand control of light flow at the nanoscale, in the subpicosecond time scale, and over a broad spectral range. The ultrafast and strongly confined infrared polaritonic fields can also add subpicosecond temporal resolution and nanometer spatial resolution to the study of various physical and chemical processes, which cannot be accessed by using conventional spectroscopic techniques. For example, relaxation of the polaritons created could be used to probe the decay dynamics of the energetic carriers inside the materials and crossing over the barrier of heterostructure interfaces. Coupling of the transient polaritonic fields with quantum materials would allow investigations of the various quantum phase transitions in condensed-matter physics, which can be activated by the mid-infrared or terahertz wave. More broadly, a variety of interesting phenomena and relevant applications can be inspired by coupling the ultrafast hyperbolic polaritons with electronic and photonic processes within the materials. For example, ultrafast electron sources with simultaneous high spatial and temporal resolutions are anticipated by harnessing the electron field emission assisted by the strong and transient localized polaritonic fields (*12*). The rationale established here can be applied to other types of polaritons by coupling the photoinjected carriers to the collective polarized charge oscillations, rendering it a new paradigm for effective subdiffractional modulation of a light field. ■

REFERENCES AND NOTES

1. K.-J. Tielrooij *et al.*, *Nat. Nanotechnol.* **13**, 41 (2018).
2. A. Poddubny *et al.*, *Nat. Photonics* **7**, 948 (2013).
3. K. Korzeb *et al.*, *Opt. Express* **23**, 25406 (2015).
4. D. N. Basov *et al.*, *Science* **354**, aag1992 (2016).
5. T. Low *et al.*, *Nat. Mater.* **16**, 182 (2017).
6. A. J. Sternbach *et al.*, *Science* **371**, 617 (2020).
7. C. Wang *et al.*, *Nat. Commun.* **11**, 1158 (2020).
8. S. Dai *et al.*, *Science* **343**, 1125 (2014).
9. Z. B. Zheng *et al.*, *Adv. Mater.* **30**, 1705318 (2018).
10. W. Ma *et al.*, *Nature* **562**, 557 (2018).
11. J. Taboada-Gutiérrez *et al.*, *Nat. Mater.* **19**, 964 (2020).
12. Y. Shen *et al.*, *ACS Nano* **13**, 1977 (2019).

ACKNOWLEDGMENTS

S.D. and H.C. thank the National Key R&D Program of China (nos. 2019YFA0210201 and 2019YFA0210203) and the National Natural Science Foundation of China (no. 91963205).

10.1126/science.abf7933

CANCER IMMUNOTHERAPY

Modulating gut microbiota to treat cancer

Fecal microbiota transplantation is evaluated in melanoma patients resistant to immunotherapy

By **Christopher H. Woelk**[1] *and* **Alexandra Snyder**[2]

In the fourth century, a Chinese practitioner reportedly used the stool of healthy subjects to treat patients with diarrhea (*1*). In 1958, fecal microbiota transplantation (FMT) was reported as a treatment for *Clostridium difficile* infection that was resistant to antibiotics (*2*). FMT became an option for routine treatment for such infections in 2013, after a clinical trial demonstrated a higher response rate in *C. difficile*–infected patients treated with FMT (81%) compared to those treated with an antibiotic (31%) (*3*). Since then, interest in FMT has evolved in diverse clinical settings. In cancer, studies on hematopoietic stem cell transplantation, arguably the first immunotherapy of the modern cancer era, have suggested a role for the gut microbiota in clinical outcomes (*4*). On pages 602 and 595 of this issue, Baruch *et al.* (*5*) and Davar *et al.* (*6*), respectively, report that manipulating the gut microbiota may allow cancer patients to overcome resistance to immunotherapy.

"The regulatory reality for this combination therapy is linked to the scientific challenges of this field..."

Cancer immunotherapy for solid tumors experienced a rebirth in the 2010s with the approval of checkpoint inhibitors (CPIs) that block cytotoxic T lymphocyte–associated protein-4 (CTLA-4), programmed cell death protein 1 (PD-1), and programmed death-ligand 1 (PD-L1). These proteins act as cellular "brakes" to control immune responses; thus, CPIs release this restraint. Biomarkers of response and resistance to CPIs include tumor-specific attributes (such as PD-L1 expression and mutation burden). Earlier studies reported that mice subjected to FMT or oral gavage with specific bacteria showed greater sensitivity to CPIs (*7, 8*). Subsequent studies described associations between the gut microbiota and outcomes in cancer patients treated with CPIs (*9, 10*).

Baruch *et al.* and Davar *et al.* attempt to bridge association to causation, suggesting that altering the gut microbiota may restore sensitivity to CPIs in patients with advanced cancer. Baruch *et al.* treated 10 melanoma patients with FMT from two donors who had exhibited a complete response (disappearance of cancer as determined by imaging) to CPIs. Eligible transplant recipients had to have shown progressive disease during or after prior CPI therapy. These patients were then treated with antibiotics to deplete their existing gut microbiota, a process thought to aid subsequent microbiota engraftment. This was followed by FMT administered by colonoscopy every 14 days, together with standard dosing of a CPI targeting PD-1 (nivolumab). Three of the 10 patients showed a radiographic response (shrinking of tumor size as determined by imaging). Of the three patients, one (who had no prior response to CPIs) showed a complete response to FMT when it was given 66 days after the last dose of a previous CPI treatment. This suggests a true *de novo* response. However, the other two patients showed only a partial response to FMT. They exhibited some response to immunotherapy early on but over time eventually showed disease progression and were therefore considered immunotherapy nonresponsive. Yet, after 119 and 204 days had passed, they then responded to CPI-FMT therapy. Thus, responses to a CPI-FMT combination may have been due to retreatment with CPI alone rather than from a new effect of added FMT, although a role for FMT cannot be excluded. Notably, two of these three responding patients experienced pseudoprogression (when imaging suggests an apparent worsening of a cancer that is followed by subsequent improvement) at a rate much higher than typically seen in patients with melanoma (*11*). The three responding patients also showed increased expression of immune-related genes in the lamina propria (part of the lining of the gastrointestinal tract) and in their

[1]Exploratory Science Center, Merck & Co., Inc., Cambridge, MA, USA. [2]Global Clinical Development, Merck & Co., Inc., Rahway, NJ, USA. Email: alex.snyder@merck.com

tumors. These changes may reflect biological processes associated with clinical response.

The melanoma patients treated by Davar *et al.* met a stricter definition of resistance to immunotherapy, as they were required to demonstrate no response to prior CPI treatment as well as progressive disease. Stool was collected from seven patients with partial or complete response to CPIs. Patients who were previously refractory to CPIs were initially treated with FMT (stool selected from any one of the seven donors) in combination with a CPI (pembrolizumab), followed by CPI alone every 3 weeks until cancer progression was observed. Three of 15 FMT-treated patients demonstrated a partial response (as determined by imaging of tumor burden), and a further three patients showed stable disease for more than 12 months.

The observations of Baruch *et al.* and Davar *et al.* suggest a possible therapeutic effect of FMT in CPI-treated patients. However, several clinical, regulatory, and scientific questions need to be addressed for this approach to become an approved treatment. Notably, a subset of patients who are treated beyond progression with CPIs may experience benefit (*12*), and larger studies in a defined post-CPI population are needed to show FMT efficacy. In addition, across all the patients studied, neither study reported PD-L1 expression or tumor mutation burden, two biomarkers of CPI response. This information is important to determine whether patients require a preexisting adaptive immune response to respond to microbiota-modulating therapy. The studies of Baruch *et al.* and Davar *et al.* were each conducted at a single facility, where patients are more likely to have a similar diet and microbiota profiles than at the diverse sites accrued during a phase 2 or 3 clinical trial. Future work is needed to better understand which response profiles for sourcing donor FMT, engraftment procedures, and recipient phenotypes are required for successful CPI-FMT combination therapy.

From a regulatory perspective, challenges in the post-CPI setting include defining the proportion of activity attributable to each part of a combination therapy, defining a CPI-refractory population, and positioning FMT intervention in the context of cancer therapies. Furthermore, because FMT is considered a live biological product and a drug by the U.S. Food and Drug Administration (*13*), FMT combinations with CPIs are likely to encounter regulatory challenges similar to those experienced by FMT for *C. difficile* infection, which has no clinical approval to date. The regulatory reality for this combination therapy is linked to the scientific challenges of this field; unlike other anticancer therapies being developed for post-CPI use, the "active ingredient" in FMT and its mechanism(s) are unknown. Recent advances in treating *C. difficile* infection may overcome regulatory hurdles, as illustrated by ECOSPOR III, a phase 3 clinical trial in which capsules containing purified bacterial spores were administered to patients (thought to be potentially safer and more consistent than FMT) (*14*). Different cancer studies have used different DNA sequencing and bioinformatic strategies, attribute the salutary effects of FMT to different bacteria (*7*–*10*), and have not resolved whether general diversity of the microbiota, particular bacterial species, a specific bacterial metabolite, or some other interaction between the host and donor microbiota is the dominant factor in patient response to FMT. Although Baruch *et al.* and Davar *et al.* agree that bacteria belonging to the phylum Firmicutes may be associated with response to CPI-FMT therapy, well-powered studies need to robustly show a clear association between specific taxa and clinical response. Shifting from comparisons of bacterial taxonomy to comparisons of functional metabolic profiles, as performed by Baruch *et al.*, may provide better mechanistic insights.

Future studies should consider integrating microbiota-related data with tumor- and patient-intrinsic factors that affect outcomes to CPI. Baruch *et al.* and Davar *et al.* indicate an acceptable safety profile and potential efficacy for CPI-FMT therapy in advanced melanoma patients. In addition, several companies have live biological products in clinical trials with CPIs in patients with solid tumors (e.g., NCT03817125, NCT04208958, NCT03637803). Large-scale studies should better define efficacy and answer outstanding regulatory and scientific questions. ■

REFERENCES AND NOTES

1. J. Stripling, M. Rodriguez, *Am. J. Med. Sci.* **356**, 424 (2018).
2. B. Eiseman *et al.*, *Surgery* **44**, 854 (1958).
3. E. van Nood *et al.*, *N. Engl. J. Med.* **368**, 407 (2013).
4. J. U. Peled *et al.*, *J. Clin. Oncol.* **35**, 1650 (2017).
5. E. N. Baruch *et al.*, *Science* **371**, 602 (2021).
6. D. Davar *et al.*, *Science* **371**, 595 (2021).
7. M. Vétizou *et al.*, *Science* **350**, 1079 (2015).
8. A. Sivan *et al.*, *Science* **350**, 1084 (2015).
9. V. Gopalakrishnan *et al.*, *Science* **359**, 97 (2018).
10. B. Routy *et al.*, *Science* **359**, 91 (2018).
11. F. S. Hodi *et al.*, *J. Clin. Oncol.* **34**, 1510 (2016).
12. J. A. Beaver *et al.*, *Lancet Oncol.* **19**, 229 (2018).
13. FDA, *Fed. Reg.* **84**, 47911 (2011); http://bit.ly/3qAKtqY.
14. Seres Therapeutics, "Seres Therapeutics Announces Positive Topline Results from SER-109 Phase 3 ECOSPOR III Study in Recurrent C. difficile Infection," press release, 10 August 2020; http://bit.ly/3617EmC.

ACKNOWLEDGMENTS

The authors acknowledge the support and input of E.Rubin and D. Hazuda (both at Merck & Co.). The authors are employees of Merck Sharp & Dohme Corp. (of Merck & Co.) and own stock in Merck & Co. A research group within Merck & Co., separate from the authors', provided funding and drug supply for NCT03341143, a trial described in (*6*). Merck & Co. collaborates with 4D Pharma to evaluate live biotherapeutics in conjunction with pembrolizumab.

10.1126/science.abg2904

CORONAVIRUS

Superspreading genomes

Virus mutations help to unravel key epidemiological events

By **Samuel Alizon**

Individual contributions to epidemic spread vary. Although some infections may not cause any secondary cases, others are associated with so-called "superspreading" events in which numerous infections result from the same case. These events can shape the course of an epidemic, but their detection remains challenging. On page 588 of this issue, Lemieux *et al.* (*1*) show that phylogenetic analyses of severe acute respiratory syndrome coronavirus 2 (SARS-CoV-2) genome sequence data help quantify the prevalence and impact of superspreading events on COVID-19 outbreaks.

Superspreading gained attention during the 2002–2004 SARS epidemic, and mathematical models highlighted its contrasting effects, by which the phenomenon is predicted to increase the probability that an outbreak will go extinct by chance but also to fuel the growth of outbreaks that evade extinction (*2*). Superspreading could also be involved in the adaptation of emerging infectious diseases to new hosts (*3*). Such events have since been identified in measles (*2*), Middle East respiratory syndrome (*4*), and Ebola (*5*) outbreaks. Their presence can be detected from cluster sizes (*4*) or spatial incidence data (*5*), but they appear most clearly in contact tracing data. However, studies to generate these data are expensive, invasive, and time consuming. Their quality is also limited because many people are unreliable respondents and list no or multiple potential sources of infection. Digital tracking could increase data quality but comes with substantial privacy risks. Most of these limitations are minimal for virus genome analyses.

A common motivation to monitor the diversity of circulating viral strains is that some genetic variations may threaten treatment or long-term vaccine efficiencies

Maladies Infectieuses et Vecteurs: Écologie, Génétique, Évolution et Contrôle, UMR CNRS 5290, Institut pour la Recherche et le Développement 224, Montpellier, France. Email: samuel.alizon@cnrs.fr

(*6*). But genetic evolution can also be harnessed to track infections as they spread, informing public health decisions. Assuming a constant mutation rate, viruses originating from infections that are close in the transmission chain should be more alike, from a genetic standpoint, than viruses from infections that are temporally or geographically distant. Using sequence data, it is possible to infer phylogenetic trees, which bear many similarities with dated genealogies of infections.

Phylogenetic analyses readily provide insights regarding epidemic structure, including the presence of superspreading events, but also temporal aspects such as the date of origin of an epidemic wave (*7*) (see the figure). The Ebola virus (EBOV) epidemic in West Africa in 2013–2016 marked a shift in the production and sharing of virus genomic sequence data (*8*). This allowed monitoring of a potentially important role of superspreading events (*9*), which was later confirmed with spatial incidence data (*5*). The large number of EBOV genome sequences that were published during that time now seems limited. Owing to technological progress, rapid and affordable full genome sequencing protocols (*10*), and the involvement of many teams across the world, more than 300,000 open-licensed SARS-CoV-2 genomes were shared in 2020 (*11*).

The impressive number of SARS-CoV-2 genomes should not mask the strong sampling heterogeneity. Half of the genomes are from the United Kingdom. Within the United States, more than half originate from only five states (California, Texas, Washington, Michigan, and New York). Timing also matters. For example, that the oldest SARS-CoV-2 genome dates from December 2019 limits our ability to accurately estimate the date of onset of the pandemic. The study by Lemieux *et al*. stands out because it uses dense and early sampling of the local epidemic in Boston, Massachusetts. This offers a detailed view of the structure and history of the epidemic in the city area. The study also confirms and analyzes two contrasting superspreading events. One of these occurred in a skilled nursing facility and had a substantial impact locally in terms of mortality. The second event was associated with a business conference. Thanks to their understanding of the local epidemics, the Global Initiative on Sharing All Influenza Data (GISAID) collaborative effort, and two key mutations in the virus genome, Lemieux *et al*. show that this event generated transmission chains all over the world that may account for hundreds of thousands of infections.

Phylogenetic analyses may interpret any type of heterogeneity not included in the underlying model, especially uneven sampling or spatial structure, as superspreading (*7*). A promising research avenue to address this issue is called "data integration." It hypothesizes that combining different types of data—for example, genome sequences and incidence data (*12*)—should contain more information. This could improve the detection of individual heterogeneity in transmission (*13*). It could also help answer a longstanding question: Are superspreading events due to individual biological (such as virus load) or behavioral (such as contact rate) properties, or to the environment (such as poorly ventilated meeting rooms)? This is illustrated in two ways in the study by Lemieux *et al*. They use their knowledge of the sampling location to distinguish superspreading events from clusters generated by uneven sampling. Also, they show that two virus introductions in the skilled nursing facility had opposite trajectories, with one leading to a handful of secondary cases and the other to a massive outbreak.

The unfolding of an epidemic depends on the underlying causes of superspreading events. If transmissibility is correlated with susceptibility and if natural immunity after recovery is strong, the effect of superspreaders should decrease as the epidemic unfolds, decreasing herd immunity thresholds (*14*). In terms of control, identifying risk factors associated with superspreading events—whether they relate to individuals, activities, or locations—opens the possibility for targeted interventions that can disproportionately hamper epidemic spread (*2*, *15*).

The evolutionary rate of SARS-CoV-2 has, so far, been relatively slow, making multiple sources of data particularly complementary. The ease with which virus genomes can now be generated and the importance of monitoring virus evolution are opportunities for phylodynamics to become a routine tool in outbreak management. ■

The effect of superspreading events

Virus genome sequences are arranged in a phylogeny to track transmission over time. Each node corresponds to a transmission event ("birth"), and each tip corresponds to the end of an infection ("death"). Superspreading generates many secondary infections that cluster in the phylogenetic tree. In epidemics with superspreading, many infections do not cause any secondary case.

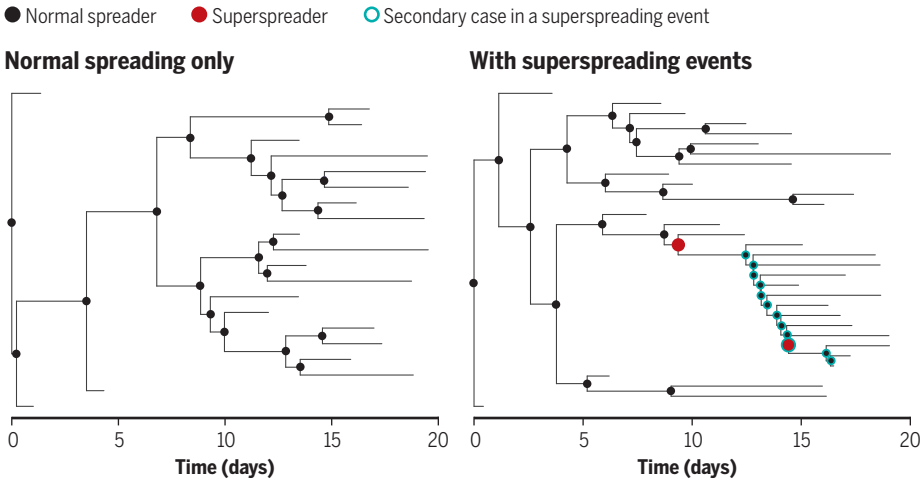

GRAPHIC: N. CARY/*SCIENCE*

REFERENCES AND NOTES

1. J. E. Lemieux *et al.*, *Science* **371**, eabe3261 (2021).
2. J. O. Lloyd-Smith, S. J. Schreiber, P. E. Kopp, W. M. Getz, *Nature* **438**, 355 (2005).
3. A. Yates, R. Antia, R. R. Regoes, *Proc. Biol. Sci.* **273**, 3075 (2006).
4. A. J. Kucharski, C. L. Althaus, *Euro Surveill.* **20**, 14 (2015).
5. M. S. Y. Lau *et al.*, *Proc. Natl. Acad. Sci. U.S.A.* **114**, 2337 (2017).
6. D. A. Kennedy, A. F. Read, *PLOS Biol.* **18**, e3001000 (2020).
7. E. M. Volz, K. Koelle, T. Bedford, *PLOS Comput. Biol.* **9**, e1002947 (2013).
8. S. K. Gire *et al.*, *Science* **345**, 1369 (2014).
9. T. Stadler, D. Kühnert, D. A. Rasmussen, L. du Plessis, *PLOS Curr.* ecurrents.outbreaks.02bc6d927ecee7bbd33532ec8ba6a25f (2014).
10. N. E. Freed, M. Vlková, M. B. Faisal, O. K. Silander, *Biol. Methods Protoc.* **5**, bpaa014 (2020).
11. The GISAID Initiative; www.gisaid.org.
12. X. Du, A. A. King, R. J. Woods, M. Pascual, *Sci. Transl. Med.* **9**, eaan5325 (2017).
13. L. M. Li, N. C. Grassly, C. Fraser, *Mol. Biol. Evol.* **34**, 2982 (2017).
14. T. Britton, F. Ball, P. Trapman, *Science* **369**, 846 (2020).
15. M. E. J. Woolhouse *et al.*, *Proc. Natl. Acad. Sci. U.S.A.* **94**, 338 (1997).

ACKNOWLEDGMENTS

I thank CNRS, Institut pour la Recherche et le Développement, and Région Occitanie for financial support and T. Kamiya, M. T. Sofonea, M. van Baalen, and the Experimental and Theoretical Evolution team for discussion.

10.1126/science.abg0100

QUANTUM SYSTEMS

Quantum logic at a distance

A quantum gate is realized by optically coupling trapped atoms separated by 60 meters

By **David Hunger**

Quantum computers could revolutionize how specific computational problems are solved that remain untractable even for the world's best supercomputers. However, although the basic elements of a quantum computer—realizing a register of qubits that preserve superposition states, controlling and reading out qubits individually, and performing quantum gates between them—have been scaled to a few dozen qubits, millions are needed to attack problems such as integer factorization. One approach for scaling up quantum computers is to "divide and conquer"—keep individual processing units smaller and connect many of them together. This approach leaves local processing nodes tractable but requires generation of entanglement and performance of quantum gates on qubits located at distant nodes to keep the advantages of quantum processing. On page 614 of this issue, Daiss *et al.* (*1*) made substantial progress toward this goal by performing quantum-logic operations on two distant qubits in an elementary network.

Entangling distant qubits in quantum networks can enable distributed computing and secure data transmission. Basic quantum networks have been demonstrated with a few different systems such as ultracold atoms (*2*), trapped ions (*3*), color centers in diamond (*4*), and superconducting qubits (*5*). By using schemes to improve the quality of initially imperfect entanglement, e.g., by so-called entanglement distillation (*6*), it should be possible to build noise-resilient, error-corrected quantum networks that perform better than their individual components (*7*). The additional benefits of improved qubit addressability, reduced cross-talk, and improved connectivity between arbitrary qubits controlled through the network connections suggest that a distributed quantum computer could outperform one large computing core.

Daiss *et al.* realized a quantum gate between two separated qubits in independent setups connected by a 60-m-long optical fiber. The qubits are implemented by internal spin states of two atoms that are trapped inside optical cavities. The qubits become connected when a single photon sent through the two setups is successively reflected from the two cavities and then detected (*8*). The presence of an atom strongly coupled to a cavity changes the reflection phase of the photon. A photon reflected off an empty resonant cavity undergoes a π phase shift. However, an atom strongly coupled to a cavity causes a frequency shift of the cavity resonance. This shift prevents photon entry upon reflection, and the reflected-photon phase remains unchanged. One qubit state of the atom, but not the other, couples strongly to the cavity, so one state does not change the photon reflection phase, and the other adds a π phase shift. An atom in a superposition state of its qubit levels will produce a corresponding superposition of the photon phase and create an atom-photon entangled state. When such an entangled photon is bounced off a second cavity and undergoes another atom-photon entangling operation with the second atom, a final state can be produced that corresponds to a NOT-gate operation.

The full scheme is actually more complicated and requires encoding through polarization states, a measurement of the resulting combined atom-atom state based on the photon polarization, and a conditional change of the first atom's state that depends on the measurement result. Daiss *et al.* realized a controlled-NOT gate with <15% deviation from the ideal gate performance. Together with the simpler single-qubit gates, this result represents a complete toolbox to implement any kind of quantum logic operation. The scheme is heralded, meaning that it produces a measurable signal when the gate operation is successful and becomes immune against photon loss as an error source.

At a first glance, the scheme requires surprisingly few resources—only a single photon that is reflected successively by two atom-cavity devices. Indeed, strong atom-cavity coupling makes the scheme efficient as it increased the probability that the photon is reflected rather than lost through processes such as spontaneous emission. However, realizing such strongly coupled atom-cavity systems requires overcoming hurdles that include atom control, cavity performance, atomic coherence, and minimized photon loss. Also, the experiment was not yet operated with single photons but with attenuated laser pulses, which is easier to do but introduces errors caused by the presence of two-photon contributions and enforces low average photon numbers.

Although all of these issues limit the efficiency and fidelity of the gate demonstrated by Daiss *et al.*, none of them introduce fundamental limits and could be improved in the future. Thus, it should be possible to scale up the system (see the figure). For example, multiple atoms coupled to a single cavity could allow the reflection of a single photon to immediately produce an *N*-qubit Toffoli gate (*8*), an element of the Grover's search algorithm. Also, elegant ways for scaling multiple cavities in interferometer-type configurations have been proposed (*9*) in which a single photon can generate an entangling quantum gate between any selected qubits in a network. Although formidable challenges remain, it is intriguing to imagine the possibilities when distributed quantum computers form a quantum internet (*10*, *11*). ■

Large-scale quantum circuits

Daiss *et al.* created quantum processors with single photons guided by optical fibers that were reflected successively by two atom–cavity devices. Scaling to multiple qubits could be achieved with large-scale photonic networks connecting optical cavities containing multiple atomic spin qubits.

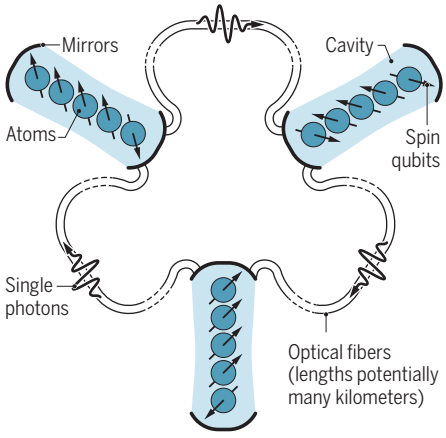

Physikalisches Institut, Institute for Quantum Materials and Technologies, Karlsruhe Institute of Technology (KIT), Wolfgang-Gaede Strasse 1 76131 Karlsruhe, Germany. Email: david.hunger@kit.edu

REFERENCES

1. S. Daiss *et al.*, *Science* **371**, 614 (2021).
2. S. Ritter *et al.*, *Nature* **484**, 195 (2012).
3. D. L. Moehring *et al.*, *Nature* **449**, 68 (2007).
4. P. C. Humphreys *et al.*, *Nature* **558**, 268 (2018).
5. N. Roch *et al.*, *Phys. Rev. Lett.* **112**, 170501 (2014).
6. N. Kalb *et al.*, *Science* **356**, 928 (2017).
7. N. H. Nickerson, J. F. Fitzsimons, S. C. Benjamin, *Phys. Rev. X* **4**, 041041 (2014).
8. L.M. Duan, B. Wang, H. J. Kimble, *Phys. Rev. A* **72**, 032333 (2005).
9. I. Cohen, K. Molmer, *Phys. Rev. A* **98**, 030302 (R) (2018).
10. H. J. Kimble, *Nature* **453**, 1023 (2008).
11. S. Wehner, D. Elkouss, R. Hanson, *Science* **362**, eaam9288 (2018).

10.1126/science.abg1536

GRAPHIC: V. ALTOUNIAN/*SCIENCE*

CATALYSIS

Designing the right protection

A new iron-based catalyst helps avoid common pitfalls for making olefins

By **Jingxiu Xie**

Olefins are used to manufacture our everyday essentials, including plastics, detergents, and hand sanitizers. Olefins are conventionally produced from crude oil cracking, but environmental concerns drive the urgent search for alternative, more sustainable carbon feedstocks. Carbon-containing waste streams ranging from biomass to industrial carbon dioxide (CO_2) to municipal waste are increasingly explored for the synthesis of chemicals and fuels (*1*, *2*). These waste streams may first be converted to carbon monoxide (CO) and hydrogen (H_2) called synthesis gas or syngas. The gas is further converted to olefins. Because the waste streams may be contaminated with impurities, catalysts with higher resistance to poisons would be advantageous for these processes. On page 610 of this issue, Xu *et al.* (*3*) report iron catalysts that are particularly suitable for this task owing to their robustness and the low selectivity toward CO_2 and methane (CH_4).

The current industrial process to produce lower olefins (ethylene, propylene, and butenes) from syngas is indirect and requires two steps, the first to synthesize methanol and the second to convert methanol to olefins (*4*, *5*). The process is mainly commercialized in China, by using syngas derived from coal gasification or by the import of methanol produced from natural gas. Direct processes, namely Fischer-Tropsch to olefins (FTO) (*6*) and oxide-zeolite (via oxygenate intermediates) (*7*, *8*), are more attractive owing to cost and material savings along with being able to avoid the thermodynamic constraints for methanol synthesis.

Several strategies suppress the formation of CO_2 and CH_4 in the FTO process. One approach is to use promoted metallic cobalt catalysts, which are not active for the water gas shift (WGS) reaction ($CO + H_2O \rightarrow CO_2 + H_2$), that gives rise to formation of CO_2 (*9*). The other approach is to use pure iron carbide catalysts and prevent the phase transitions to iron oxides, which are presumed to be more active for WGS (*10*, *11*). For these types of catalysts, high steam partial pressures are often detrimental to the catalytic performance because of oxidation or sintering of the active phase.

Xu *et al.* present a catalyst composed of iron carbide nanocrystals encapsulated in hydrophobic amorphous silica shells. This may be a viable solution to overcome the limitations brought about by high steam partial pressure. A high steam partial pressure in the reactor is inevitable at high conversion levels because H_2O is a by-product of FTO, but the hydrophobic silica shell is effective at suppressing the WGS reaction. Hence, the authors achieved a relatively high CO conversion of 56% and a low CO_2 selectivity of 13%.

Xu *et al.* used water-droplet contact angle and water vapor adsorption and desorption tests to support the claim on the catalyst hydrophobicity, which has two functions. It stabilizes the iron carbide phase and suppresses its phase transition to iron oxide. This decreases the primary CO_2 formation from FTO. Additionally, the authors suggest that the hydrophobicity may facilitate the timely desorption of H_2O and prevent its readsorption. This decreases the secondary CO_2 formation by the WGS reaction. A possible scenario to higher WGS activity is spillover of H_2O species from the hydrophilic silica shell to the active sites, which is absent with the hydrophobic silica shell (see the figure).

To reduce CH_4 production, Xu *et al.* added manganese to the iron carbide catalyst because it can promote carbon-carbon coupling to longer hydrocarbon products. Therefore, at the industrially relevant conditions of 320°C, 20 bar, and $H_2/CO = 2$, with a 56% CO conversion and 13% CO_2 selectivity, the selectivity of methane was less than 10% and the olefin selectivity reached more than 60%.

Conceptually, the use of a hydrophobic shell to reduce the coverage of the catalytic surface with H_2O is interesting and could very well be applicable to other reactions that are kinetically inhibited by H_2O adsorption. A common strategy to overcome this issue has been the addition of adsorbents in the reactor, but this requires a temperature and/or pressure swing to release the adsorbed steam, which drives up production costs. As such, the approach of Xu *et al.* could improve process efficiency, although the hypothetical mechanism still needs to be verified. The hydrophobicity tests were carried out with liquid H_2O, which means the surface species and coverages of the active sites with H_2O still need to be established.

Xu *et al.* demonstrate the feasibility of this catalyst in the coal-based FTO process with a techno-economic analysis. Despite the focus on a coal-based FTO process, the technological advancement should be transferable to other FTO processes that use more sustainable and renewable raw materials. Nonetheless, it remains to be shown if the unit product cost would be competitive when this catalyst and technology are used with more sustainable feedstocks from, for example, municipal waste and CO_2 with H_2 from water electrolysis. ■

Getting water out of the way

Olefins are used for making polymers and plastics. A catalyst on a support that adsorbs water may produce CO_2 from the water gas shift reaction (left), which reduces the efficiency for making olefins. Replacing the support with one that is hydrophobic (right) allows for a more effective Fischer-Tropsch reaction and olefin production.

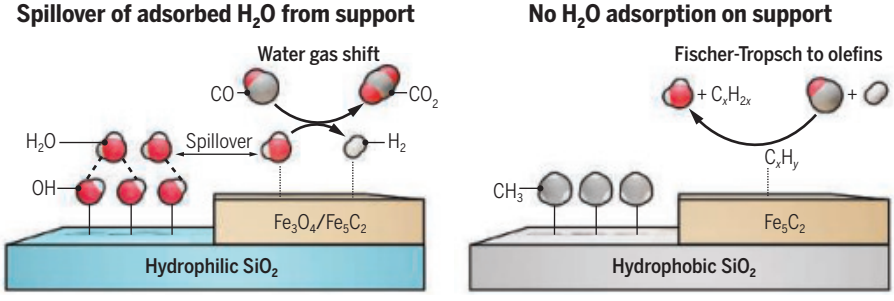

GRAPHIC: A. KITTERMAN/*SCIENCE*

Green Chemical Reaction Engineering, Engineering and Technology Institute Groningen, University of Groningen Nijenborgh 4, 9747 AG Groningen, Netherlands.
Email: jingxiu.xie@rug.nl

REFERENCES AND NOTES

1. B. Liu, D. Rajagopal, *Nat. Energy* **4**, 700 (2019).
2. C. Hepburn *et al.*, *Nature* **575**, 87 (2019).
3. Y. Xu *et al.*, *Science* **371**, 610 (2021).
4. U. Olsbye *et al.*, *Chem. Soc. Rev.* **44**, 7155 (2015).
5. I. Yarulina *et al.*, *Nat. Catal* **1**, 398 (2018).
6. H. M. Torres Galvis *et al.*, *Science* **335**, 835 (2012).
7. F. Jiao *et al.*, *Science* **351**, 1065 (2016).
8. K. Cheng *et al.*, *Angew. Chem. Int. Ed.* **128**, 4803 (2016).
9. J. Xie *et al.*, *Nat. Commun.* **10**, 167 (2019).
10. P. Wang *et al.*, *Sci. Adv.* **4**, eaau2947 (2018).
11. S. Lyu *et al.*, *Nat. Commun.* **11**, 6219 (2020).

10.1126/science.abg1750

BOOKS *et al.*

HUMAN GENOME ANNIVERSARY

Genomics and genre

A scholar probes subtle shifts in stories told through genes

By **Luis A. Campos**

Framed as a family history, *The Immortal Life of Henrietta Lacks* is actually a horror story, argues Choksey.

"If the double helix is an icon of the modern age, then the genome is one of the last grand narratives of modernity," writes Lara Choksey in her new book, *Narrative in the Age of the Genome*. Hybridizing literary criticism with a genre-spanning consideration of a dozen distinct literary works, and imbued throughout with deep concern for the peripheral, the possible, and the political, the book seeks to challenge the "whole imaginative apparatus for constructing the self into a coherent narrative, via the lexicon and syntax of the molecular."

To a reading of Richard Dawkins's *The Selfish Gene* (1976) as a repudiation of class struggle and E. O. Wilson's *Sociobiology* (1975) as a defense of warfare, Choksey juxtaposes another kind of ambiguous heterotopia in which genetic engineering is "a tool of neoliberal self-fashioning." In Samuel R. Delany's *Trouble on Triton* (1976), Bron, a transgender ex-gigolo turned informatics expert, is caught "between sociobiology and the selfish gene, between the liberal developmentalism of progressive evolution, and the neoliberal extraction and rearrangement of biological information." Even the "undulating interruptions" and parentheticals of Bron's thoughts "[mimic] the description of the activation and silencing of genes," she suggests, tying together gene and genre in a way that encapsulates neoliberal alienation.

Choksey next explores the ways in which collectivist fantasies of biological reinvention under Soviet Lysenkoism fused "code and cultivation" through a close reading of Arkady and Boris Strugatsky's *Roadside Picnic* (1972) in which cultivated utopian dreamworlds become contaminated by alien forces, resulting in fundamental ecological transformations beyond the promised reach of human control. The novel brings to light not forgotten Soviet utopias but literal zombies and mutations. In a world where planned cultivation fails entirely in the face of the unfamiliar, even as new biological weapons are being developed, Earth itself viscerally reflects a fractured reality of lost promises—a world in crisis with all meaning gone, and survival itself a chancy proposition.

As the promise of precision medicine emerged, so too did new forms of memoir. In Kazuo Ishiguro's *Never Let Me Go* (2005) and the film *Gattaca* (1997), for example, the traditional aspirational narrative of a pilgrim's progress is subverted: As the unitary subject disappears into data, algorithms, and commodities, "a new grammar of existence" emerges, albeit one in which the inherited problems of the past—racism, ableism, and the "fiction of heteronormativity"—remain ever-present.

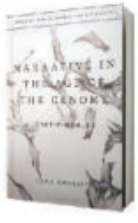

Narrative in the Age of the Genome: Genetic Worlds
Lara Choksey
Bloomsbury Academic, 2021. 232 pp.

In Saidiya Hartman's *Lose Your Mother* (2006) and Yaa Gyasi's *Homegoing* (2016), Choksey sees a "reorientation" of genomics away from the "reduction of self to code" and toward new forms of kinship and belonging that offer a "reckoning with the histories of brutalization and displacement upon which liberal humanism is founded." Even as genomics seeks to locate "the trauma of enslavement at the level of the molecular," communities seeking reunion and reparation know that technology alone "cannot do the cultural work of caring for history" that narrative can offer.

Reading Rebecca Skloot's *The Immortal Life of Henrietta Lacks* (2010) as "a biography of Black horror which tries, time and again, to resolve itself as family romance," Choksey identifies the perils of narratives unable to recognize their own genre. She argues that by blurring the lines not between fact and fiction but between "horror and family history," the dehumanization of Black lives as "experimental biomatter" echoes inescapably with larger histories of "the extraction of Black flesh for the expansion of colonial-capitalist production."

What emerges as most compelling out of this entire tapestry of readings is the author's interpretation of the limits and failures of the extraordinary "cultural power of the genome." Concluding that genomics has "privileged a particular conception of the human that is in the process of being reconfigured," Choksey ventures that the uncomplicated subject, the Vitruvian Man of the Human Genome Project, has reached its end. What is left is neither dust, stardust, nor a face erased in the sand (as Foucault would have it) but rather whatever might emerge next from the "unwieldy kaleidoscope of possible meanings." ■

10.1126/science.abf6096

The reviewer is secretary of the History of Science Society and regents' lecturer in the Department of History, University of New Mexico, Albuquerque, NM 87131, USA. Email: luiscampos@unm.edu

PHOTO: SMITHSONIAN INSTITUTION NATIONAL PORTRAIT GALLERY

ASTRONOMY

The origins of ‘Oumuamua

A high-profile astronomer argues that the strange interstellar object may be an alien signal

By **Dov Greenbaum**

Extraterrestrial: The First Sign of Intelligent Life Beyond Earth
Avi Loeb
Houghton Mifflin Harcourt, 2021. 240 pp.

In the introduction of his sixth book, *Extraterrestrial: The First Sign of Intelligent Life Beyond Earth*, Avi Loeb, chair of the Harvard Department of Astronomy, acknowledges the elephant in the room: “In the spirit of transparency, know that some scientists find my hypothesis unfashionable, outside of mainstream science, even dangerously ill conceived. But the most egregious error we can make, I believe, is not to take this possibility seriously enough.” The provocative possibility he refers to is that an interstellar object known as ‘Oumuamua (Hawaiian for “scout”), which passed through the Solar System in 2017, is an artificial object created by intelligent extraterrestrials.

Scanning the skies for extraterrestrial signatures is one of the Allen Telescope Array’s intended uses.

PHOTO: DR. SETH SHOSTAK/SCIENCE SOURCE

Loeb, a prolific academic author, meticulously walks the reader through his reasoning, describing how, after accounting for ‘Oumuamua’s various anomalies—its orbit, size, shape, and density; its origin in velocity-position space; and its lack of an icy tail, among other properties—he calculates that its chance of arising naturally is less than one in a trillion. With the odds seemingly stacked against the scientific consensus that the object is a naturally occurring space rock, he wonders why so many researchers refuse to consider what he believes is an equally likely scenario, that the object is artificial, especially given the long-appreciated probability that life exists beyond Earth.

Loeb uses ‘Oumuamua to criticize what he perceives to be a long-standing trend in science toward falling in step with conventional positions rather than staking out contrarian concepts. While he holds science fiction and modern entertainment partially responsible for sensationalizing extraterrestrial life, he also claims that the astrophysics community has been derisive of and hostile toward research that engages with the possibility of extraterrestrial life.

The search for alien life is worth the cost, argues Loeb, especially given the resources dedicated to more-traditional fields that similarly lack tangible proof. “Despite the absence of experimental evidence,” he notes, “the mathematical ideas of supersymmetry, extra-spatial dimensions, string theory, Hawking radiation, and the multiverse are considered irrefutable and self-evident by the mainstream of theoretical physics.”

Loeb argues that we are not prepared to respond should alien life eventually contact us. He suggests that new disciplines should be developed to address this discrepancy, including the emerging field of space archaeology, which he believes would be well suited to search for techno- and biosignatures of extinct civilizations.

Regardless of the ultimate origins of ‘Oumuamua, our cognitive dissonance with regard to alien life must be acknowledged. We added gold-plated disks to the Voyager probes and plaques to the Pioneer probes to introduce ourselves to potentially intelligent extraterrestrials, we have provided government funding to organizations such as the SETI Institute, and we continue to spend billions of dollars looking for life beyond Earth, yet no official protocols have been established for how to send out signals or how to respond to extraterrestrial communication that we may encounter as a result of, or in spite of, those efforts. “Even a nascent treaty agreed to by all terrestrial signatories would provide a framework for how we, as a species, respond to an encounter with a mature intelligence,” Loeb argues.

Throughout the book, Loeb frames his nonconformist position on ‘Oumuamua as a teaching opportunity for students. He implores young scientists to seek out data-driven areas of investigation that go beyond popular paradigms, describing a number of instances in which leading scientists of the past failed to think beyond convention and by doing so, potentially delayed or even impeded fertile areas of research. He writes, for example, of Charles Townes, who in 1954 was discouraged by Nobel laureates Isidor Isaac Rabi and Polykarp Kusch from continuing his line of research on masers (the forerunner of lasers), who insisted that the technology would never work. Fortunately, he ignored them and persevered. Masers are an integral component of some global navigation satellite systems.

At the same time, Loeb entreats his peers to help foster research environments that encourage budding scientists to indulge their curiosity and seek out scientific truths. “If the flame of inquiry is to continue,” he writes, “it is incumbent on senior scholars to not only gather to themselves promising young scholars but to cultivate an environment within which the next generations of scientists can nurture discoveries despite their inherently unpredictable nature.” ■

10.1126/science.abg5218

The reviewer is at the Zvi Meitar Institute for Legal Implications of Emerging Technologies, Harry Radzyner Law School, Interdisciplinary Center, Herzliya, Israel, and the Department of Molecular Biophysics and Biochemistry, Yale University, New Haven, CT, USA. Email: dov.greenbaum@aya.yale.edu

RESEARCH

IN *SCIENCE* JOURNALS

Edited by **Michael Funk**

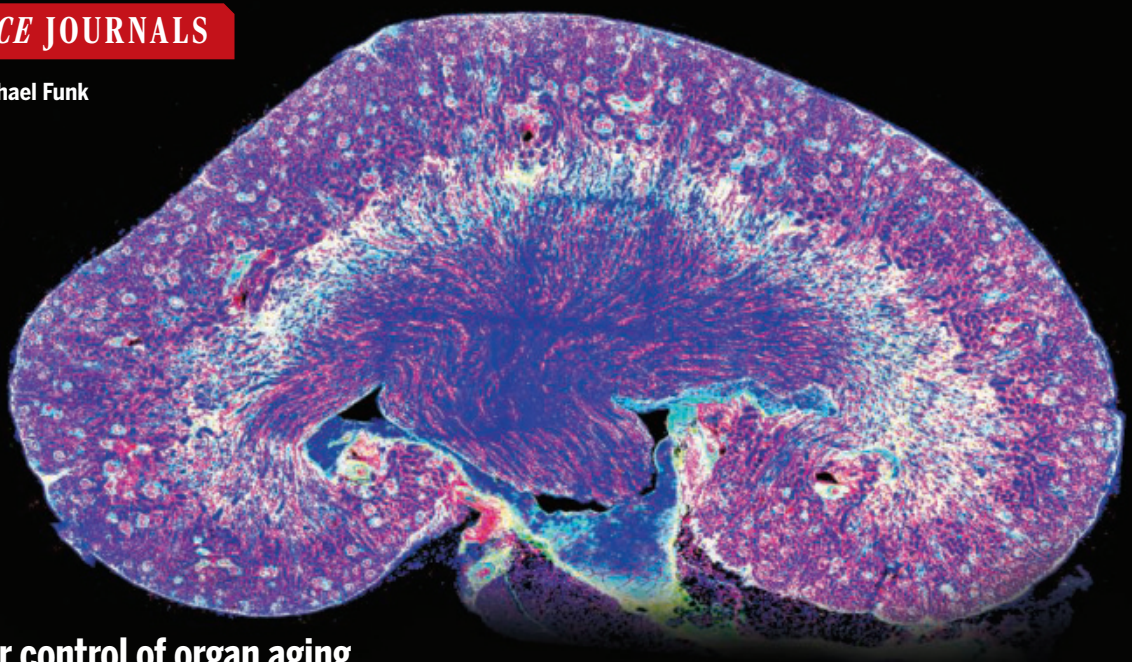

IMAGING

Vascular control of organ aging

Blood vessels provide nutrients and oxygen to organs, and changes to the vasculature during aging are expected to contribute to organ function decline. Chen *et al.* performed a comprehensive analysis of tissue-specific vasculature of young and aging mice using high-resolution three-dimensional (3D) imaging of organ-specific vascular beds, with validation in human samples. They found evidence of capillary and artery loss in the early stages of aging, preceding senescence, in a tissue-specific manner. Vascular alterations precede cellular aging hallmarks, suggesting that vessel loss is a primary trigger for aging. These high-quality 3D maps of vascular microenvironments will be a crucial resource for the scientific community. —GO

Sci. Adv. 10.1126/sciadv.abd7819 (2021).

A representative slice from a three-dimensional imaging project reveals immunostained proteins and nuclei in the kidney of a young mouse.

IMAGE: JACK DAYNES

SURFACE CHEMISTRY

Solvents forming redox mediators

The role of solvents participating directly in thermal catalytic reactions is clearer for homogeneous catalysis than for heterogeneous catalysis. Adams *et al*. studied the formation of hydrogen peroxide from hydrogen and oxygen on palladium nanoparticles by measuring the kinetic isotope effect and performing density functional theory simulations in aqueous and organic solvents. Methanol formed chemisorbed hydroxymethyl intermediates. These surface redox mediators transferred electrons and protons to adsorbed oxygen species and were regenerated by oxidizing chemisorbed hydrogen atoms. However, water molecules heterolytically oxidized hydrogen to generate solvated protons and surface electrons that reduced oxygen. —PDS

Science, this issue p. 626

AEROSOL FORMATION

Faster than expected

Iodine species are one of only a handful of atmospheric vapors known to make new aerosol particles, which play a central role in controlling the radiative forcing of climate. He *et al.* report experimental evidence from the CERN Cosmics Leaving Outdoor Droplets, or CLOUD, chamber demonstrating that iodic acid and iodous acid rapidly form new particles and can compete with sulfuric acid in pristine regions. —HJS

Science, this issue p. 589

ORGANIC CHEMISTRY

Double C–H amination

The conversion of C–H bonds into C–N bonds is broadly useful in producing pharmaceutically important compounds from simple, readily available feedstocks. Shen and Lambert report a method to induce this reaction twice in a row at benzylic and neighboring alkyl carbon centers, using acetonitrile solvent as a convenient source of nitrogen. The method relies on successive electrochemical and photochemical activation of a cyclopropenium catalyst and yields hydrogen gas as a clean co-product. —JSY

Science, this issue p. 620

CLINICAL TRIALS

New fecal microbiota for cancer patients

The composition of the gut microbiome influences the response of cancer patients to immunotherapies. Baruch *et al.* and Davar *et al.* report

first-in-human clinical trials to test whether fecal microbiota transplantation (FMT) can affect how metastatic melanoma patients respond to anti–PD-1 immunotherapy (see the Perspective by Woelk and Snyder). Both studies observed evidence of clinical benefit in a subset of treated patients. This included increased abundance of taxa previously shown to be associated with response to anti–PD-1, increased $CD8^+$ T cell activation, and decreased frequency of interleukin-8–expressing myeloid cells, which are involved in immunosuppression. These studies provide proof-of-concept evidence for the ability of FMT to affect immunotherapy response in cancer patients. —PNK

Science, this issue p. 602, p. 595; see also p. 573

ASTHMA

Defiant ILC2s resist steroids

Group 2 innate lymphoid cells (ILC2s) contribute to the inflammation associated with human allergic airway diseases, including asthma and chronic rhinosinusitis. Corticosteroid drugs are used to manage type 2 respiratory diseases, but steroid resistance may arise in the course of therapy. By comparing ILC2s from inflamed nasal polyps with blood ILC2s from healthy controls, van der Ploeg *et al.* observed that enhanced cytokine expression by nasal polyp ILC2s and loss of steroid responsiveness were both associated with surface expression of the receptor isoform CD45RO rather than CD45RA, which is found on most resting ILC2s. Expression of the CD45RO isoform by inflammatory ILC2s in blood was increased in patients with asthma and correlated with more severe airway disease. CD45RO is a candidate biomarker for human inflammatory ILC2s that correlates with the acquisition of steroid resistance. —IRW

Sci. Immunol. **6**, eabd3489 (2021).

QUANTUM SYSTEMS

Quantum gating at a distance

The processing of quantum information is reliant on the encoding and manipulation of quantum states of a qubit. Superconducting circuits are the most advanced platform at present, but there is an issue with cross-talk between the qubits and the challenge of error correction as the systems are scaled up. Another approach being pursued is a modular platform in which the qubits are spatially separated. Daiss *et al.* demonstrate the operation of a quantum gate in which one qubit conditionally controls the state of another qubit spatially separated by 60 meters (see the Perspective by Hunger). Because the approach is platform independent, it could be extended from the demonstrated neutral atoms to ions, impurity vacancy centers, or even a combination of these qubits. —ISO

Science, this issue p. 614; see also p. 576

CLIMATE CHANGE

Microhabitat matters

Understanding how our warming climate affects vulnerable species is of paramount importance. However, predicting responses is complicated because species are complex and may adapt or respond in distinct ways. Riddell *et al.* compared a century-old dataset on species richness in the Mojave against modern surveys to measure climate-related changes in bird and small mammal communities. They found little change in mammal richness or occupancy but large declines across birds. They attribute these differences to differences in microclimate opportunities: Specifically, mammals can mitigate temperature impacts through burrowing, whereas birds are generally more exposed. —SNV

Science, this issue p. 633

IN OTHER JOURNALS

Edited by **Caroline Ash** *and* **Jesse Smith**

Surface melting in Greenland may soon outpace snow accumulation there.

ICE SHEETS

Too hot for our own good

Climate is warming faster in the Arctic than in any other large region, and the Greenland Ice Sheet is melting faster as a result. Noël *et al.* project that the rate of summertime surface melting will surpass that of winter snow accumulation in Greenland when the average air temperature there rises to 4.5°C above preindustrial values, which corresponds to a global warming threshold of 2.7°C. Without strong CO_2 emission mitigation measures, net surface mass loss could occur as soon as the middle of the 21st century. —HJS

Geophys. Res. Lett. 10.1029/2020GL090471 (2021).

SIGNAL TRANSDUCTION

How adiponectin fights diabetes

Adiponectin, a hormone produced in adipose tissue, may provide a useful therapeutic lead for type 2 diabetes because it improves glucose homeostasis and tissue sensitivity to insulin. But how it does so is unclear. Li *et al.* show that in mice with insulin resistance caused by a high-fat diet, treatment with adiponectin reduced the amount of triglyceride in the liver and in skeletal muscle. It did so by increasing lipoprotein lipase

PHOTO: GLOBAL WARMING IMAGES/ALAMY STOCK PHOTO

GENETICS

Not such identical twins

Monozygotic twins that originate in the fertilization of one egg that splits into two are classically considered genetically identical. As a result, twin studies are an important aspect of research to unpick questions of nature versus nurture. To verify this assumption, Eriksson *et al.* sequenced the genomes of 381 monozygotic twin pairs and two sets of triplets and mapped mutations. The authors found that some twin pairs showed no differences, whereas 15% showed substantial differences in the number of mutations. In some twin pairs, the mutated lineages occurred in most cell lineages sampled, suggesting that they had occurred early in development. Phenotypic differences between twins are usually attributed to environmental effects, but this study suggests that this might not always be the case. —GKA *Nat. Genet.* **53**, 27 (2021).

Some identical twin pairs, such as the former cricketers Eric Bedser (left) and Sir Alec Bedser, who were born on 4 July 1918, may have substantial mutational differences.

activity and triglyceride uptake into epididymal white adipose tissue and increasing fatty acid oxidation in muscle. These effects decreased the amount of diacylglycerol in the plasma membrane of liver and muscle cells, thus decreasing the activity of protein kinase C family members that impair signaling by the insulin receptor. —LBR

Proc. Natl. Acad. Sci. U.S.A. **117**, 32584 (2020).

RNA BIOLOGY

RNA fold into life

In addition to their well-known roles serving as messengers of genetic material from DNA to proteins, RNAs also regulate a myriad of cellular processes. Regulatory functions require proper folding of RNA by processes that remain challenging to understand. In a recent study, Yu *et al.* tackled this problem by developing a method that combined experimental RNA structure data with computational structure predication. They focused on a bacterial noncoding RNA called SRP RNA and found that internal structural fluctuation was required to lead this newly synthesized RNA through a folding pathway called toehold-mediated strand displacement. Their results corroborated a prior study by Fukuda *et al.*, which used optical tweezers to follow in real time the cotranscriptional folding of SRP RNA. —DJ

Mol. Cell **81**, 1 (2021); *Mol. Cell* **77**, 241 (2020).

MATERIALS DISCOVERY

First Mo–Bi intermetallic material

Despite ordered structure and well-defined stoichiometry, stable intermetallic compounds are challenging to predict even in binary systems because of the numbers of structures that depend on chemical composition and need to be considered. Incorporation of Bi is of particular interest because of the potentially distinctive properties that it could introduce into intermetallic materials. Using a density functional theory–based random structure searching approach, Altman *et al.* explored the high-pressure phase space of the Mo–Bi system and predicted stability of the stoichiometric compound $MoBi_2$ of the $CuAl_2$ structure type, the first group 6-Bi binary intermetallic structure confirmed experimentally. Additional electronic structure calculations revealed important correlations that could be useful in directing the synthesis of analogous intermetallic compounds of transition metals with Bi. —YS

J. Am. Chem. Soc. **143**, 214 (2021).

COOLING TECHNOLOGY

A cooler paint

Passive radiative cooling relies on materials that emit infrared radiation through an atmospheric window of low energy absorption, thereby using outer space as a cold sink. Li *et al.* found a paint-like material that allowed for daytime, subambient daytime cooling. Calcium carbonate particles with a wide size distribution were mixed with acrylic and the resulting paint was field tested to demonstrate the cooling capabilities. Passively providing cooling may help mitigate the need for air conditioning and easy application is a key incentive for adopting the technology. —BG

Cell Rep. Phys. Sci. **1**, 100221 (2020).

CANCER GENOMICS

Lineage trajectories differ by mutation

Mutations in the essential RUNX1 gene are associated with several diseases of the blood, including leukemias, familial platelet disorder, and other malignancies. How these mutations underly each phenotype is unknown. Using embryonic stem cells, Kellaway *et al.* examined the genomic effects of four different mutant RUNX1 transcription factor proteins. The mutations affect binding of RUNX1 to DNA or its transactivation domains in differentiated hematopoietic stem cells. Each mutation altered RUNX1 function by a different mechanism, leading to divergent trajectories for stem cell development for each disease phenotype. Thus, each malignancy will need a different therapeutic approach. —LMZ

Life Sci. Alliance **4**, e202000864 (2021).

PHOTO: POPPERFOTO VIA GETTY IMAGES/GETTY IMAGES

REVIEW SUMMARY

NOISE POLLUTION

The soundscape of the Anthropocene ocean

Carlos M. Duarte*, Lucille Chapuis, Shaun P. Collin, Daniel P. Costa, Reny P. Devassy, Victor M. Eguiluz, Christine Erbe, Timothy A. C. Gordon, Benjamin S. Halpern, Harry R. Harding, Michelle N. Havlik, Mark Meekan, Nathan D. Merchant, Jennifer L. Miksis-Olds, Miles Parsons, Milica Predragovic, Andrew N. Radford, Craig A. Radford, Stephen D. Simpson, Hans Slabbekoorn, Erica Staaterman, Ilse C. Van Opzeeland, Jana Winderen, Xiangliang Zhang, Francis Juanes

BACKGROUND: Sound is the sensory cue that travels farthest through the ocean and is used by marine animals, ranging from invertebrates to great whales, to interpret and explore the marine environment and to interact within and among species. Ocean soundscapes are rapidly changing because of massive declines in the abundance of sound-producing animals, increases in anthropogenic noise, and altered contributions of geophysical sources, such as sea ice and storms, owing to climate change. As a result, the soundscape of the Anthropocene ocean is fundamentally different from that of preindustrial times, with anthropogenic noise negatively impacting marine life.

ADVANCES: We find evidence that anthropogenic noise negatively affects marine animals. Strong evidence for such impacts is available for marine mammals, and some studies also find impacts for fishes and invertebrates, marine birds, and reptiles. Noise from vessels, active sonar, synthetic sounds (artificial tones and white noise), and acoustic deterrent devices are all found to affect marine animals, as are noise from energy and construction infrastructure and seismic surveys. Although there is clear evidence that noise compromises hearing ability and induces physiological and behavioral changes in marine animals, there is lower confidence that anthropogenic noise increases the mortality of marine animals and the settlement of their larvae.

OUTLOOK: Anthropogenic noise is a stressor for marine animals. Thus, we call for it to be included in assessments of cumulative pressures on marine ecosystems. Compared with other stressors that are persistent in the environment, such as carbon dioxide emitted to the atmosphere or persistent organic pollutants delivered to marine ecosystems, anthropogenic noise is typically a point-source pollutant, the effects of which decline swiftly once sources are removed. The evidence summarized here encourages national and international policies to become more ambitious in regulating and deploying existing technological solutions to mitigate marine noise and improve the human stewardship of ocean soundscapes to maintain a healthy ocean. We provide a range of solutions that may help, supported by appropriate managerial and policy frameworks that may help to mitigate impacts on marine animals derived from anthropogenic noise and perturbations of soundscapes. ■

The list of author affiliations is available in the full article online.

*Corresponding author. Email: carlos.duarte@kaust.edu.sa

Cite this article as C. M. Duarte *et al.*, *Science* **371**, eaba4658 (2021). DOI: 10.1126/science.aba4658

READ THE FULL ARTICLE AT
https://doi.org/10.1126/science.aba4658

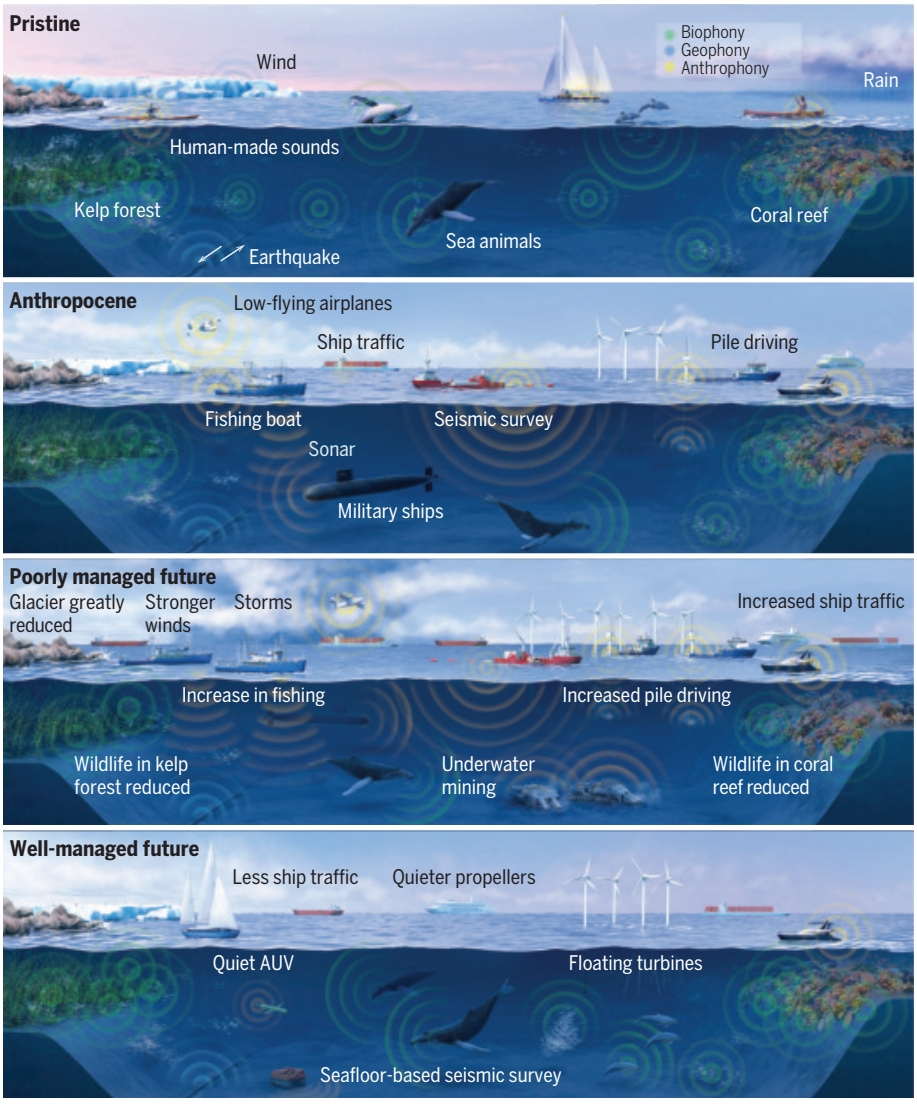

ILLUSTRATION: XAVIER PITA/KAUST

Changing ocean soundscapes. The illustrations from top to bottom show ocean soundscapes from before the industrial revolution that were largely composed of sounds from geological (geophony) and biological sources (biophony), with minor contributions from human sources (anthrophony), to the present Anthropocene oceans, where anthropogenic noise and reduced biophony owing to the depleted abundance of marine animals and healthy habitats have led to impacts on marine animals. These impacts range from behavioral and physiological to, in extreme cases, death. As human activities in the ocean continue to increase, management options need be deployed to prevent these impacts from growing under a "business-as-usual" scenario and instead lead to well-managed soundscapes in a future, healthy ocean. AUV, autonomous underwater vehicle.

RESEARCH ARTICLE SUMMARY

RNA STABILITY

RNA stabilization by a poly(A) tail 3′-end binding pocket and other modes of poly(A)-RNA interaction

Seyed-Fakhreddin Torabi, Anand T. Vaidya, Kazimierz T. Tycowski, Suzanne J. DeGregorio, Jimin Wang, Mei-Di Shu, Thomas A. Steitz, Joan A. Steitz*

INTRODUCTION: The polyadenylate [poly(A)] tail is one of the most conserved modifications of RNA molecules and is an important contributor to RNA function. In conjunction with other cis-acting RNA elements, the poly(A) tail plays a central role in RNA stabilization. The element for nuclear expression (ENE), which contains a U-rich internal loop (URIL) flanked by short double helices, stabilizes RNA by sequestration of the poly(A) tail via formation of a triple helix. ENE elements have been identified in evolutionarily diverse cellular and viral RNAs. Double-domain ENEs (dENEs), containing two URILs separated by a predicted double-helical region, appear in transcripts produced by plant and fungal transposons. All dENEs exhibit several distinguishing sequence features: three highly conserved adenosines (the adenosine triad) and a striking pyrimidine/purine (Y/R) bias in the composition of the URIL-flanking stems. The structural importance of these features in poly(A) tail protection has remained unknown.

RATIONALE: To understand the mechanism of poly(A) tail sequestration by dENEs, we solved the crystal structure of a rice transposase mRNA dENE, TWIFB1, complexed with a poly(A)$_{28}$. Complementary cellular and biochemical approaches then validated the contributions of the key structural elements to dENE function and provided mechanistic insights into poly(A) tail 3′-end protection.

RESULTS: The structure of the dENE+poly(A)$_{28}$ complex at 2.89 Å resolution revealed multiple modes of interaction between the dENE and poly(A), including (i) two predicted canonical major-groove triple helices, (ii) a previously unnamed subclass of A-minor interactions between poly(A) and RNA double helices, (iii) an unrecognized quintuple-base motif that transitions poly(A) from minor-groove interactions to the major-groove triplexes, and (iv) a novel poly(A) 3′-end binding pocket. The 5′ region of the poly(A) interacts with the upper dENE domain while its extreme 3′ end is buried in the pocket motif of the lower domain. Poly(A) adenosines are inserted into the minor groove of the upper Y/R-biased stem through their Watson-Crick and/or Hoogsteen edges, forming what we call a WC/H A-minor motif, followed by the quintuple-base transition motif and subsequently a major-groove triple helix composed of four U-A•U triples. Similar structural features engage the poly(A) in the lower dENE domain but, unlike the upper dENE domain in which the 3′ end of poly(A) can freely exit the upper major-groove triple helix, they are followed by interactions with the pocket motif. The pocket, which is formed through stacking of the bases of the adenosine triad (cyan in the figure) within the major groove of the lower dENE stem, engulfs the 3′-most adenosine of the poly(A) and poises its 3′-OH group to form a hydrogen bond with a phosphate in the backbone of the pocket-forming RNA residues. Cell-based and biochemical assays confirmed the contributions of these structural features to poly(A) binding and demonstrated that the pocket motif augments sequestration of the poly(A) tail by protecting its 3′-most adenosine through a steric mechanism. The WC/H A-minor and quintuple-base transition motifs are found in other RNA structures.

CONCLUSION: Structural features uncovered in the dENE+poly(A)$_{28}$ complex underscore the ability of the poly(A) tail to form extensive and underappreciated RNA-RNA interactions. Several consecutive adenosines can form a WC/H A-minor motif by interacting with a Y/R-biased stem, possibly contributing to the stabilization of polyadenylated RNAs. Moreover, a poly(A) 3′-end binding pocket composed solely of RNA provides insight into how polyadenylation can protect an RNA's extreme 3′ end. Our data raise the possibility that comparable RNA-poly(A) interactions exist in other RNAs and play more pervasive roles in RNA biology than are currently known. ■

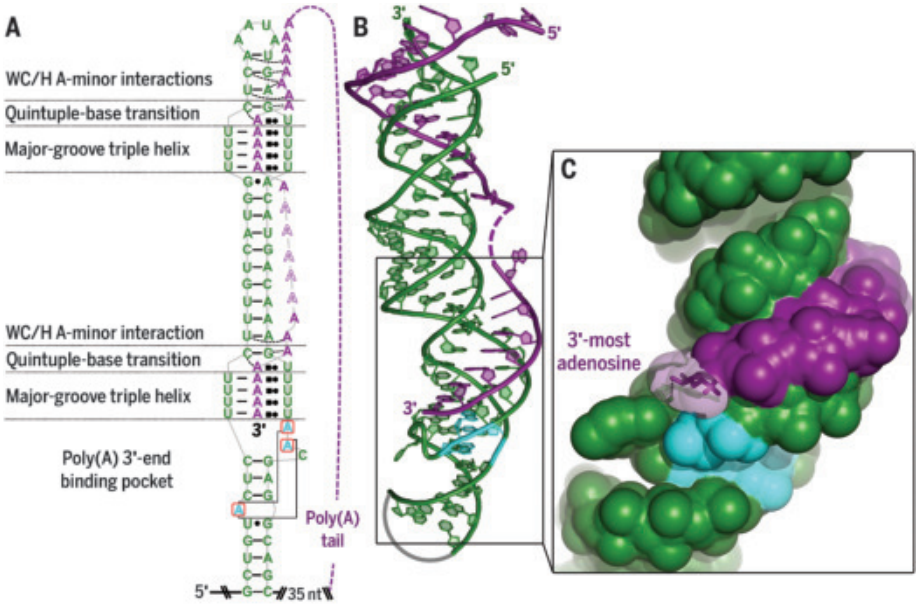

Structural overview of the TWIFB1 dENE+poly(A) complex. (**A** and **B**) Multiple modes of interaction between the dENE and poly(A) tail are shown in cartoon representation (A) based on the crystal structure of the dENE (green) + poly(A)$_{28}$ (purple) complex (B). The poly(A) 3′-end binding pocket formed by the stacked bases of the adenosine triad (cyan) lies in the major groove of the lower dENE stem. Non-native nucleotides in the crystallization construct are represented by a thick gray line. (**C**) Surface representation showing how the pocket motif engulfs the 3′-most adenosine of poly(A), as well as the hydrogen bond (dotted line) between the poly(A) 3′-OH group and a backbone phosphate of the pocket motif.

The list of author affiliations is available in the full article online.
*Corresponding author. Email: joan.steitz@yale.edu
Cite this article as S.-F. Torabi *et al.*, *Science* **371**, eabe6523 (2021). DOI: 10.1126/science.abe6523

READ THE FULL ARTICLE AT
https://doi.org/10.1126/science.abe6523

RESEARCH ARTICLE SUMMARY

CELL BIOLOGY

HSP70 chaperones RNA-free TDP-43 into anisotropic intranuclear liquid spherical shells

Haiyang Yu*, Shan Lu†, Kelsey Gasior†, Digvijay Singh, Sonia Vazquez-Sanchez, Olga Tapia, Divek Toprani, Melinda S. Beccari, John R. Yates III, Sandrine Da Cruz, Jay M. Newby, Miguel Lafarga, Amy S. Gladfelter, Elizabeth Villa, Don W. Cleveland*

INTRODUCTION: Aggregation of the RNA binding protein TDP-43 (TAR DNA-binding protein 43) is a common pathological hallmark shared by several age-related neurodegenerative diseases, including amyotrophic lateral sclerosis (ALS) and frontotemporal dementia (FTD). The predominantly nuclear TDP-43 normally undergoes liquid-liquid phase separation (LLPS), in which a homogeneous solution separates into two compartments resembling oil droplets in vinegar.

RATIONALE: Intranuclear TDP-43 can phase-separate under physiological conditions. Cellular stress can induce cytoplasmic TDP-43 liquid droplets, which can transition to a solid state, suggesting that TDP-43 aggregation observed in neurodegeneration could be initiated by LLPS. The mechanisms that drive phase separation and aggregation remain unclear.

RESULTS: We identified key regulatory mechanisms of TDP-43 phase separation in cultured cells and in neurons of the rodent nervous system. RNA binding–deficient TDP-43, produced by ALS- or FTD-causing mutations or posttranslational acetylation in its RNA recognition motifs, phase-separated into anisosomes (i.e., droplets with symmetrical liquid spherical shells and liquid cores). RNA-free TDP-43 was found to be enriched in anisosomal shells at concentrations 50 times those of the surrounding nucleoplasm. Acetylation promoted anisosomal formation by abolishing RNA interaction with TDP-43. Anisosomal shells exhibited birefringence (i.e., evidence of a liquid crystal compartment formed from proteins within living cells). Shells were densely packed, as determined with cryo–electron tomography, producing a membraneless, selective barrier to some nuclear proteins and RNAs.

Our mathematical modeling predicted that anisosomes were driven by a core component that self-interacted, weakly bound TDP-43, and did not bind RNA. Guided by these concepts, we used proximity labeling and quantitative proteomics to identify HSP70 chaperones as the primary anisosomal core components. HSP70 chaperones selectively bound to and stabilized RNA-unbound TDP-43. Inhibiting adenosine triphosphate (ATP)–dependent chaperone activity of the HSP70 family or reducing cellular ATP levels induced rapid conversion of TDP-43 anisosomes into uniform gels. Transient proteasome inhibition, mimicking the known reduction in proteasome activity during aging, provoked TDP-43 demixing into anisosomes in neurons in rodents. Postmortem ATP reduction was sufficient to convert anisosomes into aggregates similar to those found in neurodegenerative disease.

CONCLUSION: We identified how phase separation of the RNA-binding protein TDP-43 can be regulated through RNA binding, disease-causing mutation, posttranslational modification, or chaperone activity inside cells. RNA binding–deficient TDP-43 demixed into anisosomes with cores that could be characterized as a "liquid inside a liquid inside a liquid." Chaperone activity of the HSP70 family was required to maintain liquidity of anisosomal shells and cores. When ATP levels fell, anisosomes converted into protein aggregates, consistent with being precursors of the pathological aggregates found in patient brain tissues. These findings suggest an essential partnership between TDP-43 and HSP70 chaperones in driving RNA-unbound TDP-43 phase separation into anisosomes and preventing TDP-43 aggregation. ■

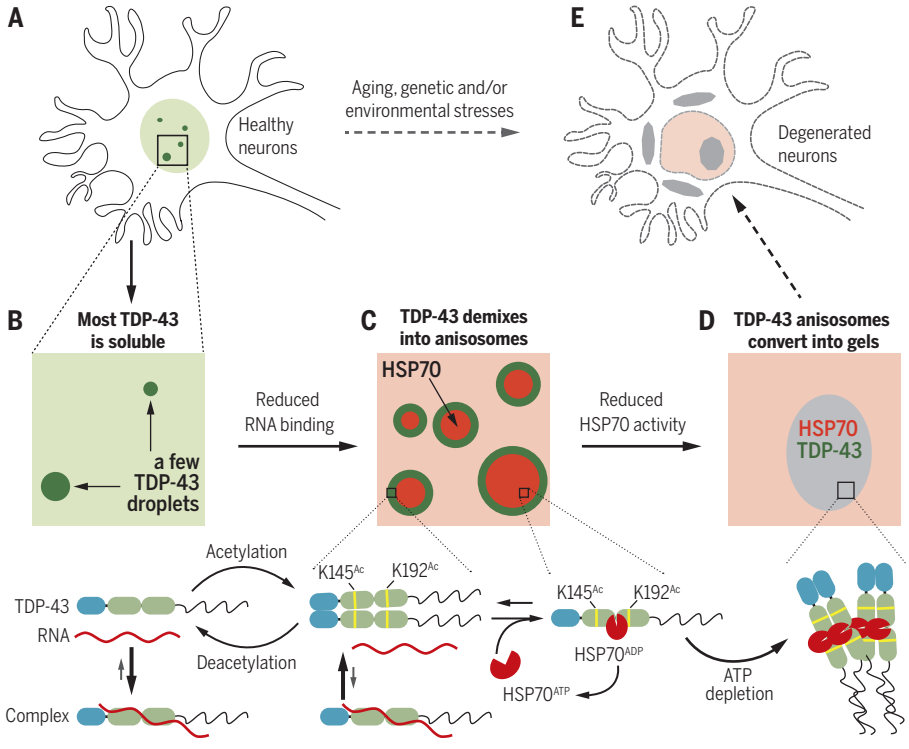

TDP-43 phase transition is regulated by its RNA affinity and HSP70 activity. RNA binding protein TDP-43 forms aggregates in degenerating neurons, a pathological feature associated with aging, genetic, and/or environmental factors. Although naturally demixed, RNA binding–proficient TDP-43 is largely soluble in the nucleus, with a small proportion demixed (**A** and **B**). Its RNA affinity is eliminated by acetylation, which drives most TDP-43 into anisosomes—intranuclear membraneless compartments with symmetrically aligned shells and cores in which RNA-free TDP-43 is enriched in the shells. HSP70 stabilizes RNA-free TDP-43 and is enriched in the anisosomal core (**C**). When ATP-dependent chaperone activity of HSP70 is reduced by ATP depletion, TDP-43 anisosomes collapse into gels (**D**), which may be precursors of intranuclear and cytoplasmic aggregates observed in degenerating neurons (**E**).

The list of author affiliations is available in the full article online.
*Corresponding author. Email: dcleveland@ucsd.edu (D.W.C.); haiyang-yu@ucsd.edu (H.Y.)
†These authors contributed equally to this work.
Cite this article as H. Yu *et al.*, *Science* **371**, eabb4309 (2021). DOI: 10.1126/science.abb4309

READ THE FULL ARTICLE AT
https://doi.org/10.1126/science.abb4309

RESEARCH ARTICLE SUMMARY

DEVELOPMENTAL BIOLOGY

Reactivation of the pluripotency program precedes formation of the cranial neural crest

Antoine Zalc*, Rahul Sinha*, Gunsagar S. Gulati, Daniel J. Wesche, Patrycja Daszczuk, Tomek Swigut, Irving L. Weissman, Joanna Wysocka†

INTRODUCTION: Cell differentiation is classically described as a unidirectional process that progresses through a series of lineage restriction events, with cellular potential being increasingly reduced as the embryo develops, a concept famously illustrated by Conrad Waddington in his epigenetic landscape. However, the vertebrate-specific transient cell population called cranial neural crest cells (CNCCs) challenges this paradigm. Although they originate in the ectoderm and are capable of differentiating into cell types typical of this germ layer, CNCCs can also give rise to mesenchymal cell types canonically associated with the mesoderm lineage, such as bone, cartilage, and smooth muscle. How CNCCs expand their differentiation potential beyond their germ layer of origin remains unresolved.

RATIONALE: We hypothesized that unbiased analysis of transcriptional heterogeneity during the early stages of mammalian CNCC development may identify a precursor population and provide clues as to how these specialized cells gain their extraordinary differentiation potential. To test this, we combined single-cell RNA-sequencing analysis of murine CNCCs from staged mouse embryos with follow-up lineage-tracing, loss-of-function, and epigenomic-profiling experiments.

RESULTS: We found that premigratory CNCCs are heterogeneous and carry positional information reflective of their origin in the neuroepithelium, but this early positional information is subsequently erased, with delaminating CNCCs showing a relatively uniform transcriptional signature that later rediversifies as CNCCs undergo first commitment events. We identify an early precursor population that expresses canonical pluripotency transcription factors and gives rise to CNCCs and craniofacial structures. Rather than being maintained from the epiblast, pluripotency factor Oct4 is transiently reactivated in the prospective CNCCs after headfold formation, and its expression shifts from the most anterior to the more posterior part of the cranial domain as development progresses. Oct4 is not required for the induction of CNCCs in the neuroepithelium, but instead is important for the specification and survival of facial mesenchyme, thus directly linking this pluripotency factor with the expansion of CNCC cellular potential. Open chromatin landscapes of Oct4$^+$ CNCC precursors are consistent with their neuroepithelial origin while also broadly resembling those of pluripotent epiblast stem cells. In addition, we saw priming of distal regulatory regions at a subset of loci associated with future neural crest migration and mesenchyme formation.

CONCLUSION: Our results show that premigratory CNCCs first form as a heterogeneous population that rapidly changes its transcriptional identity during delamination, resulting in the formation of a transcriptionally (and likely also functionally) equivalent cell group capable of adapting to future locations during and after migration. Such functional equivalency and plasticity of CNCCs is consistent with previous embryological studies. Furthermore, the demonstration that CNCC precursors transiently reactivate pluripotency factors suggests that these cells undergo a natural in vivo reprogramming event that allows them to climb uphill on Waddington's epigenetic landscape. Indeed, our results show that at least one of the pluripotency factors, Oct4, is required for the expansion of CNCC developmental potential to include formation of facial mesenchyme. Whether this mechanism is specific to CNCCs and if such expansion of cellular plasticity could be harnessed for regenerative medicine purposes remain interesting questions for future investigations. ■

The list of author affiliations is available in the full article online.
*These authors contributed equally to this work.
†Corresponding author. Email: wysocka@stanford.edu
Cite this article as: A. Zalc *et al.*, *Science* **371**, eabb4776 (2021). DOI: 10.1126/science.abb4776

READ THE FULL ARTICLE AT
https://doi.org/10.1126/science.abb4776

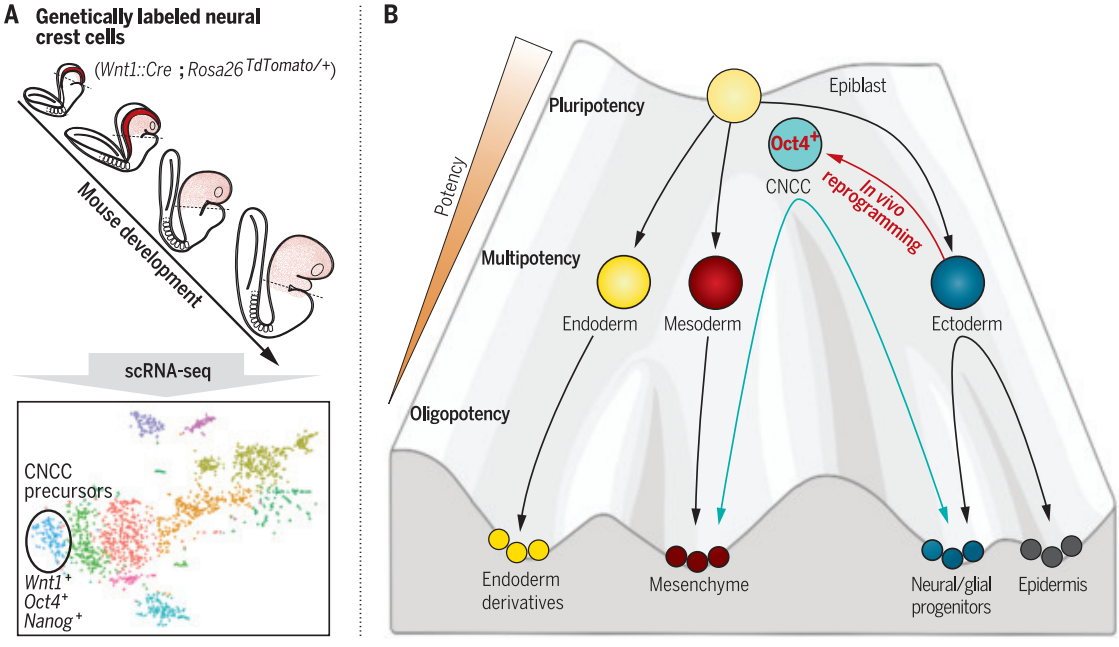

CNCCs expand their developmental potential through transient reactivation of a pluripotency program. (**A**) Single-cell RNA (scRNA) sequencing of genetically labeled murine CNCCs over 14 hours of development revealed rapid transcriptional changes and identified a precursor population expressing pluripotency factors. (**B**) Uphill on Waddington's epigenetic landscape, reactivation of Oct4 endows CNCC precursors with the ability to form derivatives typical of mesoderm, such as mesenchyme.

RESEARCH ARTICLE SUMMARY

CORONAVIRUS

Immunological memory to SARS-CoV-2 assessed for up to 8 months after infection

Jennifer M. Dan*, Jose Mateus*, Yu Kato*, Kathryn M. Hastie, Esther Dawen Yu, Caterina E. Faliti, Alba Grifoni, Sydney I. Ramirez, Sonya Haupt, April Frazier, Catherine Nakao, Vamseedhar Rayaprolu, Stephen A. Rawlings, Bjoern Peters, Florian Krammer, Viviana Simon, Erica Ollmann Saphire, Davey M. Smith, Daniela Weiskopf†, Alessandro Sette†, Shane Crotty†

INTRODUCTION: Immunological memory is the basis for durable protective immunity after infections or vaccinations. Duration of immunological memory after severe acute respiratory syndrome coronavirus 2 (SARS-CoV-2) infection and COVID-19 is unclear. Immunological memory can consist of memory B cells, antibodies, memory $CD4^+$ T cells, and/or memory $CD8^+$ T cells. Knowledge of the kinetics and interrelationships among those four types of memory in humans is limited. Understanding immune memory to SARS-CoV-2 has implications for understanding protective immunity against COVID-19 and assessing the likely future course of the COVID-19 pandemic.

RATIONALE: Assessing virus-specific immune memory over at least a 6-month period is likely necessary to ascertain the durability of immune memory to SARS-CoV-2. Given the evidence that antibodies, $CD4^+$ T cells, and $CD8^+$ T cells can all participate in protective immunity to SARS-CoV-2, we measured antigen-specific antibodies, memory B cells, $CD4^+$ T cells, and $CD8^+$ T cells in the blood from subjects who recovered from COVID-19, up to 8 months after infection.

RESULTS: The study involved 254 samples from 188 COVID-19 cases, including 43 samples at 6 to 8 months after infection. Fifty-one subjects in the study provided longitudinal blood samples, allowing for both cross-sectional and longitudinal analyses of SARS-CoV-2–specific immune memory. Antibodies against SARS-CoV-2 spike and receptor binding domain (RBD) declined moderately over 8 months, comparable to several other reports. Memory B cells against SARS-CoV-2 spike actually increased between 1 month and 8 months after infection. Memory $CD8^+$ T cells and memory $CD4^+$ T cells declined with an initial half-life of 3 to 5 months. This is the largest antigen-specific study to date of the four major types of immune memory for any viral infection.

Among the antibody responses, spike immunoglobulin G (IgG), RBD IgG, and neutralizing antibody titers exhibited similar kinetics. Spike IgA was still present in the large majority of subjects at 6 to 8 months after infection. Among the memory B cell responses, IgG was the dominant isotype, with a minor population of IgA memory B cells. IgM memory B cells appeared to be short-lived. $CD8^+$ T cell and $CD4^+$ T cell memory was measured for all SARS-CoV-2 proteins. Although ~70% of individuals possessed detectable $CD8^+$ T cell memory at 1 month after infection, that proportion declined to ~50% by 6 to 8 months after infection. For $CD4^+$ T cell memory, 93% of subjects had detectable SARS-CoV-2 memory at 1 month after infection, and the proportion of subjects positive for $CD4^+$ T cells (92%) remained high at 6 to 8 months after infection. SARS-CoV-2 spike-specific memory $CD4^+$ T cells with the specialized capacity to help B cells [T follicular helper (T_{FH}) cells] were also maintained.

The different types of immune memory each had distinct kinetics, resulting in complex interrelationships between the abundance of T cell, B cell, and antibody immune memory over time. Additionally, substantially heterogeneity in memory to SARS-CoV-2 was observed.

CONCLUSION: Substantial immune memory is generated after COVID-19, involving all four major types of immune memory. About 95% of subjects retained immune memory at ~6 months after infection. Circulating antibody titers were not predictive of T cell memory. Thus, simple serological tests for SARS-CoV-2 antibodies do not reflect the richness and durability of immune memory to SARS-CoV-2. This work expands our understanding of immune memory in humans. These results have implications for protective immunity against SARS-CoV-2 and recurrent COVID-19. ■

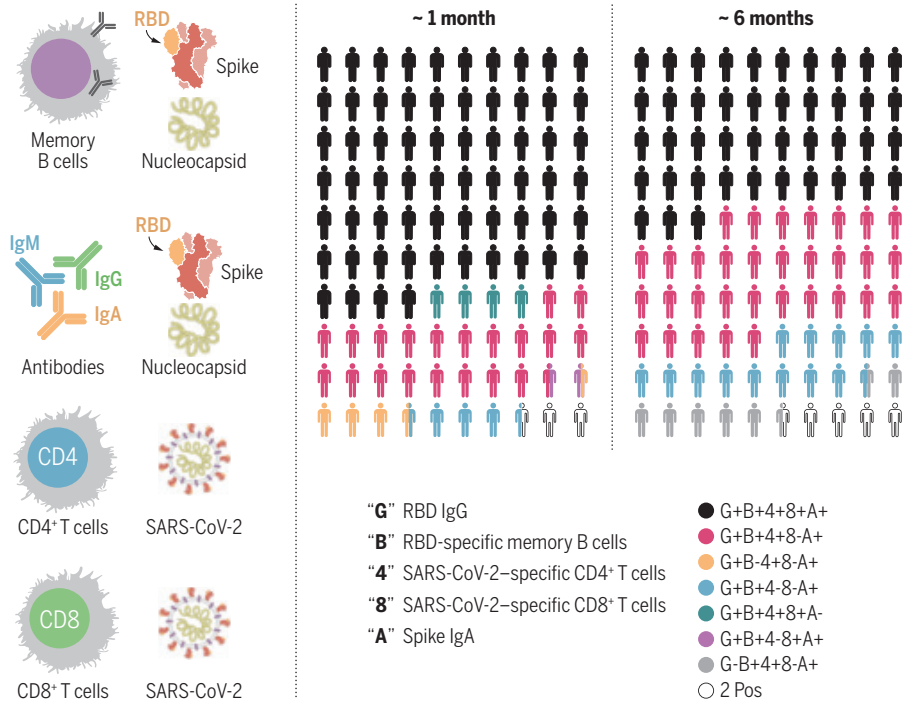

Immunological memory consists of antibodies, memory B cells, memory $CD8^+$ T cells, and memory $CD4^+$ T cells. This study examined all of the types of virus-specific immune memory against SARS-CoV-2 in COVID-19 subjects. Robust immune memory was observed in most individuals.

The list of author affiliations is available in the full article online.
*These authors contributed equally to this work.
†Corresponding author. Email: shane@lji.org (S.C.); alex@lji.org (A.S.); daniela@lji.org (D.W.)
This is an open-access article distributed under the terms of the Creative Commons Attribution license (https://creativecommons.org/licenses/by/4.0/), which permits unrestricted use, distribution, and reproduction in any medium, provided the original work is properly cited.
Cite this article as J. M. Dan *et al.*, *Science* 371, eabf4063 (2021). DOI: 10.1126/science.abf4063

READ THE FULL ARTICLE AT
https://doi.org/10.1126/science.abf4063

RESEARCH ARTICLE SUMMARY

CORONAVIRUS

Phylogenetic analysis of SARS-CoV-2 in Boston highlights the impact of superspreading events

Jacob E. Lemieux*†, Katherine J. Siddle*, Bennett M. Shaw, Christine Loreth, Stephen F. Schaffner, Adrianne Gladden-Young, Gordon Adams, Timelia Fink, Christopher H. Tomkins-Tinch, Lydia A. Krasilnikova, Katherine C. DeRuff, Melissa Rudy, Matthew R. Bauer, Kim A. Lagerborg, Erica Normandin, Sinéad B. Chapman, Steven K. Reilly, Melis N. Anahtar, Aaron E. Lin, Amber Carter, Cameron Myhrvold, Molly E. Kemball, Sushma Chaluvadi, Caroline Cusick, Katelyn Flowers, Anna Neumann, Felecia Cerrato, Maha Farhat, Damien Slater, Jason B. Harris, John A. Branda, David Hooper, Jessie M. Gaeta, Travis P. Baggett, James O'Connell, Andreas Gnirke, Tami D. Lieberman, Anthony Philippakis, Meagan Burns, Catherine M. Brown, Jeremy Luban, Edward T. Ryan, Sarah E. Turbett, Regina C. LaRocque, William P. Hanage, Glen R. Gallagher‡, Lawrence C. Madoff‡, Sandra Smole‡, Virginia M. Pierce‡, Eric Rosenberg‡, Pardis C. Sabeti†‡, Daniel J. Park‡, Bronwyn L. MacInnis†‡

INTRODUCTION: We used genomic epidemiology to investigate the introduction and spread of severe acute respiratory syndrome coronavirus 2 (SARS-CoV-2) in the Boston area across the first wave of the pandemic, from March through May 2020, including high-density sampling early in this period. Our analysis provides a window into the amplification of transmission in an urban setting, including the impact of superspreading events on local, national, and international spread.

RATIONALE: Superspreading is recognized as an important driver of SARS-CoV-2 transmission, but the determinants of superspreading—why apparently similar circumstances can lead to very different outcomes—are poorly understood. The broader impact of such events, both on local transmission and on the overall trajectory of the pandemic, can also be difficult to determine. Our dataset includes hundreds of cases that resulted from superspreading events with different epidemiological features, which allowed us to investigate the nature and effect of superspreading events in the first wave of the pandemic in the Boston area and to track their broader impact.

RESULTS: Our data suggest that there were more than 120 introductions of SARS-CoV-2 into the Boston area, but that only a few of these were responsible for most local transmission: 29% of the introductions accounted for 85% of the cases. At least some of this variation results from superspreading events amplifying some lineages and not others. Analysis of two superspreading events in our dataset illustrate how some introductions can be amplified by superspreading. One occurred in a skilled nursing facility, where multiple introductions of SARS-CoV-2 were detected in a short time period. Only one of these led to rapid and extensive spread within the facility, and significant mortality in this vulnerable population, but there was little onward transmission. A second superspreading event, at an international business conference, led to sustained community transmission, including outbreaks in homeless and other higher-risk communities, and was exported domestically and internationally, ultimately resulting in hundreds of thousands of cases. The two events also differed substantially in the genetic variation they generated, possibly suggesting varying transmission dynamics in superspreading events. Our results also show how genomic data can be used to support cluster investigations in real time—in this case, ruling out connections between contemporaneous cases at Massachusetts General Hospital, where nosocomial transmission was suspected.

CONCLUSION: Our results provide powerful evidence of the importance of superspreading events in shaping the course of this pandemic and illustrate how some introductions, when amplified under unfortunate circumstances, can have an outsized effect with devastating consequences that extend far beyond the initial events themselves. Our findings further highlight the close relationships between seemingly disconnected groups and populations during a pandemic: Viruses introduced at an international business conference seeded major outbreaks among individuals experiencing homelessness; spread throughout the Boston area, including to other higher-risk communities; and were exported extensively to other domestic and international sites. They also illustrate an important reality: Although superspreading among vulnerable populations has a larger immediate impact on mortality, the cost to society is greater for superspreading events that involve younger, healthier, and more mobile populations because of the increased risk of subsequent transmission. This is relevant to ongoing efforts to control the spread of SARS-CoV-2, particularly if vaccines prove to be more effective at preventing disease than blocking transmission. ■

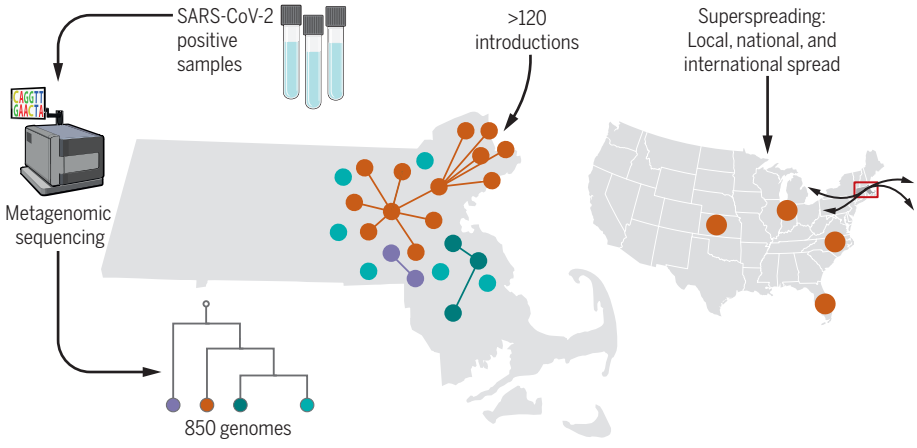

Schematic outline of this genomic epidemiology study. Illustrated are the numerous introductions of SARS-CoV-2 into the Boston area; the minimal spread of most introductions; and the local, national, and international impact of the amplification of one introduction by a large superspreading event.

The list of author affiliations is available in the full article online.
*These authors contributed equally to this work.
†Corresponding author. Email: lemieux@broadinstitute.org (J.E.L.); pardis@broadinstitute.org (P.C.S.); bronwyn@broadinstitute.org (B.L.M.)
‡These authors contributed equally to this work.
This is an open-access article distributed under the terms of the Creative Commons Attribution license (https://creativecommons.org/licenses/by/4.0/), which permits unrestricted use, distribution, and reproduction in any medium, provided the original work is properly cited.
Cite this article as J. E. Lemieux *et al.*, *Science* 371, eabe3261 (2021). DOI: 10.1126/science.abe3261

READ THE FULL ARTICLE AT
https://doi.org/10.1126/science.abe3261

RESEARCH ARTICLES

AEROSOL FORMATION

Role of iodine oxoacids in atmospheric aerosol nucleation

Xu-Cheng He[1]*, Yee Jun Tham[1], Lubna Dada[1], Mingyi Wang[2], Henning Finkenzeller[3], Dominik Stolzenburg[4,1], Siddharth Iyer[5], Mario Simon[6], Andreas Kürten[6], Jiali Shen[1], Birte Rörup[1], Matti Rissanen[5], Siegfried Schobesberger[7], Rima Baalbaki[1], Dongyu S. Wang[8], Theodore K. Koenig[3], Tuija Jokinen[1], Nina Sarnela[1], Lisa J. Beck[1], João Almeida[9], Stavros Amanatidis[10], António Amorim[11], Farnoush Ataei[12], Andrea Baccarini[8], Barbara Bertozzi[13], Federico Bianchi[1], Sophia Brilke[4], Lucía Caudillo[6], Dexian Chen[2], Randall Chiu[3], Biwu Chu[1], António Dias[11], Aijun Ding[14,15], Josef Dommen[8], Jonathan Duplissy[1,16], Imad El Haddad[8], Loïc Gonzalez Carracedo[4], Manuel Granzin[6], Armin Hansel[17,18], Martin Heinritzi[6], Victoria Hofbauer[2], Heikki Junninen[19,1], Juha Kangasluoma[1], Deniz Kemppainen[1], Changhyuk Kim[10,20], Weimeng Kong[10], Jordan E. Krechmer[21], Aleksander Kvashin[22], Totti Laitinen[1], Houssni Lamkaddam[8], Chuan Ping Lee[8], Katrianne Lehtipalo[1,23], Markus Leiminger[17,18], Zijun Li[7], Vladimir Makhmutov[22], Hanna E. Manninen[9], Guillaume Marie[6], Ruby Marten[8], Serge Mathot[9], Roy L. Mauldin[24], Bernhard Mentler[17], Ottmar Möhler[13], Tatjana Müller[6], Wei Nie[14,15], Antti Onnela[9], Tuukka Petäjä[1], Joschka Pfeifer[9], Maxim Philippov[22], Ananth Ranjithkumar[25], Alfonso Saiz-Lopez[26], Imre Salma[27], Wiebke Scholz[17,18], Simone Schuchmann[28], Benjamin Schulze[10], Gerhard Steiner[17], Yuri Stozhkov[22], Christian Tauber[4], António Tomé[29], Roseline C. Thakur[1], Olli Väisänen[7], Miguel Vazquez-Pufleau[4], Andrea C. Wagner[3,6], Yonghong Wang[1], Stefan K. Weber[9], Paul M. Winkler[4], Yusheng Wu[1], Mao Xiao[8], Chao Yan[1], Qing Ye[2], Arttu Ylisirniö[7], Marcel Zauner-Wieczorek[6], Qiaozhi Zha[1], Putian Zhou[1], Richard C. Flagan[10], Joachim Curtius[6], Urs Baltensperger[8], Markku Kulmala[1,14,16,30], Veli-Matti Kerminen[1], Theo Kurtén[31], Neil M. Donahue[2,32,33,34], Rainer Volkamer[3], Jasper Kirkby[9,6]*, Douglas R. Worsnop[1,21], Mikko Sipilä[1]*

Iodic acid (HIO_3) is known to form aerosol particles in coastal marine regions, but predicted nucleation and growth rates are lacking. Using the CERN CLOUD (Cosmics Leaving Outdoor Droplets) chamber, we find that the nucleation rates of HIO_3 particles are rapid, even exceeding sulfuric acid–ammonia rates under similar conditions. We also find that ion-induced nucleation involves IO_3^- and the sequential addition of HIO_3 and that it proceeds at the kinetic limit below +10°C. In contrast, neutral nucleation involves the repeated sequential addition of iodous acid (HIO_2) followed by HIO_3, showing that HIO_2 plays a key stabilizing role. Freshly formed particles are composed almost entirely of HIO_3, which drives rapid particle growth at the kinetic limit. Our measurements indicate that iodine oxoacid particle formation can compete with sulfuric acid in pristine regions of the atmosphere.

New particle formation plays an important role in radiative forcing of the climate. If particles survive to larger sizes, they influence climate directly, by scattering light, and indirectly, by producing more than half of all cloud condensation nuclei (CCN) (*1*). However, new particle formation and aerosol–cloud interactions remain relatively poorly understood and constitute major uncertainties in determining Earth's equilibrium climate sensitivity with climate models (*2*). So far, only a few vapors that can form new particles under atmospheric conditions have been identified: sulfuric acid (*3*–*7*), methanesulfonic acid (*3*, *8*), iodine species (*9*–*11*), highly oxygenated organic molecules (HOMs) (*12*), and, more recently, nitric acid (*13*). Under warm conditions or low vapor concentrations, acidic molecular clusters further require base vapors such as ammonia (*6*, *13*, *14*) or dimethylamine (*15*) to stabilize them against evaporation. Ions can play a comparable role in stabilizing nucleating acidic (*6*) or biogenic (*12*) particles.

Marine new particle formation is especially important, as the ocean is vast, and marine clouds are highly sensitive to CCN because their concentrations are low. Marine clouds are radiatively important because they have a high infrared emission and albedo in contrast with the dark ocean surface. Marine new particle formation has thus been a focus for aerosol–climate interactions and feedbacks for many years (*16*), mostly concerning dimethylsulfide and its oxidation products (*3*, *8*, *16*). Although nucleation of iodine oxides was first studied almost 20 years ago (*9*, *10*), iodine particle formation is presently considered to have limited global significance (*17*) and remains relatively poorly understood.

The ocean surface is a major source of atmospheric iodine; hypoiodous acid (HOI) and molecular iodine (I_2) are emitted by the reaction of gaseous ozone with aqueous iodide (I^-) (*18*). Typical daytime emissions from the tropical Atlantic Ocean are 7×10^7 HOI molecules cm^{-2} s^{-1} and 7×10^6 I_2 molecules cm^{-2} s^{-1} (*18*), leading to daytime mixing ratios in the marine boundary layer of ~1 part per trillion by volume (pptv) HOI and 0.1 pptv iodine atoms (*19*). Land surfaces (vegetation and soils) emit comparable iodine fluxes as iodomethane (CH_3I), producing boundary layer mixing ratios of ~0.5 pptv and free tropospheric levels of ~0.1 pptv (*20*). Iodine compounds have been found at a variety of sites, including coastal regions (*9*, *10*), Arctic sea ice (*11*, *21*), the marine boundary layer (*22*), the lower (*23*) and upper free troposphere (*24*), and the stratosphere (*25*).

More recently, iodic acid (HIO_3) has been shown to drive coastal marine new particle formation at Mace Head, Ireland (*11*), and

[1]Institute for Atmospheric and Earth System Research/Physics, Faculty of Science, University of Helsinki, 00014 Helsinki, Finland. [2]Center for Atmospheric Particle Studies, Carnegie Mellon University, Pittsburgh, PA 15213, USA. [3]Department of Chemistry and Cooperative Institute for Research in the Environmental Sciences, University of Colorado Boulder, Boulder, CO 80309, USA. [4]Faculty of Physics, University of Vienna, 1090 Vienna, Austria. [5]Aerosol Physics Laboratory, Physics Unit, Faculty of Engineering and Natural Sciences, Tampere University, 33014 Tampere, Finland. [6]Institute for Atmospheric and Environmental Sciences, Goethe University Frankfurt, 60438 Frankfurt am Main, Germany. [7]Department of Applied Physics, University of Eastern Finland, 70211 Kuopio, Finland. [8]Laboratory of Atmospheric Chemistry, Paul Scherrer Institute, CH-5232 Villigen, Switzerland. [9]CERN, the European Organization for Nuclear Research, CH-1211 Geneva 23, Switzerland. [10]Division of Chemistry and Chemical Engineering, California Institute of Technology, Pasadena, CA 91125, USA. [11]CENTRA and Faculdade de Ciências da Universidade de Lisboa, 1749-016 Lisboa, Portugal. [12]Leibniz Institute for Tropospheric Research, 04318 Leipzig, Germany. [13]Institute of Meteorology and Climate Research, Karlsruhe Institute of Technology, 76344 Eggenstein-Leopoldshafen, Germany. [14]Joint International Research Laboratory of Atmospheric and Earth System Sciences, School of Atmospheric Sciences, Nanjing University, Nanjing 210023, China. [15]Jiangsu Provincial Collaborative Innovation Center of Climate Change, Nanjing 210023, China. [16]Helsinki Institute of Physics, University of Helsinki, 00014 Helsinki, Finland. [17]Institute of Ion Physics and Applied Physics, University of Innsbruck, 6020 Innsbruck, Austria. [18]Ionicon Analytik Ges.m.b.H., 6020 Innsbruck, Austria. [19]Institute of Physics, University of Tartu, 50411 Tartu, Estonia. [20]School of Civil and Environmental Engineering, Pusan National University, Busan 46241, Republic of Korea. [21]Aerodyne Research, Inc., Billerica, MA 01821, USA. [22]P.N. Lebedev Physical Institute of the Russian Academy of Sciences, 119991 Moscow, Russia. [23]Finnish Meteorological Institute, 00560 Helsinki, Finland. [24]Department of Atmospheric and Oceanic Sciences, University of Colorado, Boulder, CO 80309, USA. [25]School of Earth and Environment, University of Leeds, Leeds LS2 9JT, UK. [26]Department of Atmospheric Chemistry and Climate, Institute of Physical Chemistry Rocasolano, CSIC, 28006 Madrid, Spain. [27]Institute of Chemistry, Eötvös University, H-1117 Budapest, Hungary. [28]Institue of Physics, Johannes Gutenberg University Mainz, 55128 Mainz, Germany. [29]Institute Infante Dom Luíz, University of Beira Interior, 6201-001 Covilhã, Portugal. [30]Aerosol and Haze Laboratory, Beijing Advanced Innovation Center for Soft Matter Science and Engineering, Beijing University of Chemical Technology, Beijing 100029, China. [31]Department of Chemistry, University of Helsinki, University of Helsinki, 00014 Helsinki, Finland. [32]Department of Chemistry, Carnegie Mellon University, Pittsburgh, PA 15213, USA. [33]Department of Chemical Engineering, Carnegie Mellon University, Pittsburgh, PA 15213, USA. [34]Department of Engineering and Public Policy, Carnegie Mellon University, Pittsburgh, PA 15213, USA.
*Corresponding author. Email: xucheng.he@helsinki.fi (X.-C.H.); jasper.kirkby@cern.ch (J.Ki.); mikko.sipila@helsinki.fi (M.Sip.)

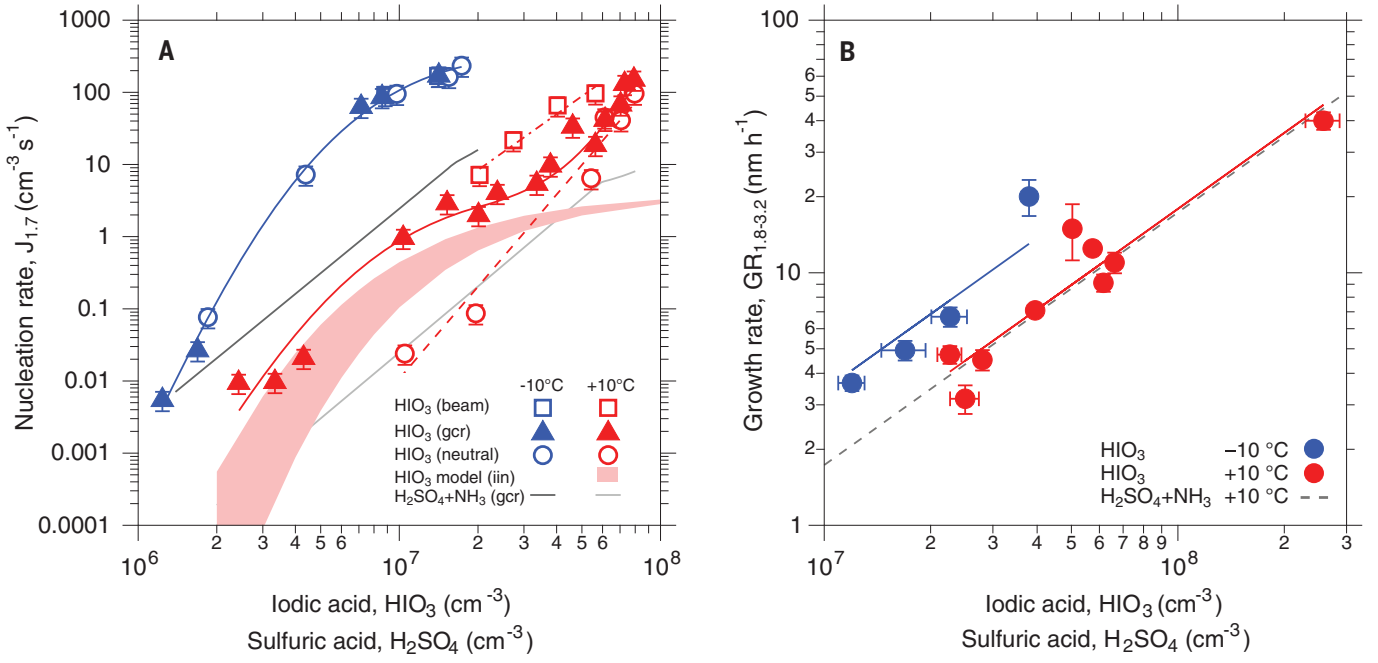

Fig. 1. Nucleation and growth rates versus iodic acid concentration. (**A**) Nucleation rates at 1.7 nm diameter versus iodic acid concentration at +10°C (red symbols and curves) and −10°C (blue symbols and curves). Hollow circles show the nucleation rates for neutral conditions, J_n; solid triangles for gcr conditions, J_{gcr}; and hollow squares for beam conditions, J_{beam}. To guide the eye, the measurements are connected by approximate curves. The red band shows a kinetic model prediction for HIO_3 ion-induced nucleation, J_{iin} (= J_{gcr} − J_n), at +10°C (see supplementary materials for further details). The lower and upper limits correspond, respectively, to zero and two H_2O molecules per iodine atom in the cluster. For comparison, the gcr nucleation rates measured for sulfuric acid with 100 pptv ammonia are shown at +10°C (light gray curve) and −10°C (dark gray curve) (*14*). (**B**) Mean growth rates of particles (neutral, gcr, and beam conditions) between 1.8 and 3.2 nm diameter versus HIO_3 concentration at +10°C (filled red circles) and −10°C (filled blue circles). For comparison, the dashed gray line shows the growth rates of H_2SO_4-NH_3 particles measured at +10°C (*30*). The bars in both panels represent ±1σ measurement errors. The experimental conditions are 36 to 44 ppbv O_3, 34 to 73% RH, 0.4 to 168 pptv I_2, and an I atom production rate of 4.4 × 10^4 to 1.5 × 10^7 cm^{-3} s^{-1}. An overall systematic scale error on the HIO_3 concentration of −33% or +50% is not shown on the data points.

intense iodine particle formation has been reported along China's coast (*26*). So far, however, controlled laboratory experiments under atmospheric conditions are lacking, and so atmospheric observations of HIO_3 cannot be connected with predicted particle formation and growth rates. A mechanism for HIO_3 nucleation has been identified (*11*), but the ion-induced (charged) and neutral (uncharged) clusters were unseparated and may involve different iodine compounds. Furthermore, iodine oxides (I_xO_y) are presently considered to be the major species responsible for the growth and composition of iodic particles (*9*, *10*, *27*), although, once again, experimental measurements under atmospheric conditions are lacking.

Nucleation and growth rates

Here we report iodine new particle formation experiments performed under marine boundary layer conditions in the CERN CLOUD (Cosmics Leaving Outdoor Droplets) chamber (see supplementary methods) between September 2017 and November 2019. The experiments were conducted at +10° and −10°C, at 34 to 73% relative humidity (RH), and 20 to 46 parts per billion by volume (ppbv) ozone. We introduced molecular iodine from an evaporator (0.4 to 168 pptv; median I_2 = 6.4 pptv) into the chamber.

The formation pathways of iodine oxoacids from iodine precursor vapors are not well understood, although computational studies assume that HO_x radicals are required to produce HIO_3 (*28*, *29*). We tested this hypothesis by using green light (528 nm) alone to photolyze I_2 into iodine atoms. At full intensity, CLOUD's green light source photolyzes iodine vapor at a rate of 7 × 10^{-3} s^{-1}, although most experiments were carried out at relative intensities of 10 to 20%. Because green light cannot photolyze O_3, it gives rise to negligible HO_x. Nevertheless, we found that iodine atoms are rapidly oxidized in the presence of water vapor and ozone to produce both HIO_3 and iodous acid (HIO_2) (fig. S1). Iodine oxoacids can form from hydrated iodine atoms and iodine oxide radicals reacting with ozone, and they can also form from hydrolysis of I_xO_y (*27*). Under our experimental conditions, photolysis of I_2 typically produces 2 × 10^5 I atoms cm^{-3} s^{-1} and ~1 pptv iodine monoxide (IO) radicals. The full range of conditions probed includes IO concentrations found in the open ocean marine boundary layer and remote free troposphere (*18*, *19*, *23*, *24*) (table S1). Notably, at constant actinic flux, HIO_3 increases linearly with iodine concentration, whereas HIO_2 increases as the square root (fig. S2). We speculate that iodine oxoacids form at CLOUD either from iodine radicals (e.g., I + H_2O + O_3 → HIO_3 + OH) or the initial I_xO_y intermediates (e.g., I_2O_2 + H_2O → HIO_2 + HOI). Because ozone and water vapor are found throughout the troposphere, our findings imply that molecular iodine will produce iodine oxoacids even under cloudy daylight conditions with negligible ultraviolet irradiation.

We show in Fig. 1A our measured nucleation rates at 1.7 nm, $J_{1.7}$, versus the HIO_3 concentration at +10° and −10°C and under three ionization conditions: neutral, J_n (ions eliminated from the chamber by a 20 kV m^{-1} electric field); galactic cosmic ray, J_{gcr} (boundary layer ion pair concentrations of ~700 cm^{-3}); and beam enhanced, J_{beam} (ion pair concentrations of ~2500 cm^{-3}, comparable to the upper free troposphere). The measurements were performed at contaminant ammonia levels near 3 pptv. The nucleation rates show a strong dependency on HIO_3 concentration, charge, and temperature. There is a large ion enhancement of the nucleation rate at +10°C,

whereas J_{gcr} and J_n are comparable at −10°C. The nucleation rate increases rapidly as the temperature falls from +10° to −10°C. For comparison, we include in Fig. 1A our previous measurements of J_{gcr} at 1.7 nm for sulfuric acid (H_2SO_4) with 100 pptv ammonia (NH_3) (*14*), which show that the nucleation rate of iodine oxoacids exceeds that of H_2SO_4·NH_3 at the same acid concentrations.

In Fig. 1B we show the dependence on HIO_3 concentration of the particle growth rates between 1.8 and 3.2 nm at +10° and −10°C. The growth rates of iodine oxoacid particles at +10°C are identical to our measurements for H_2SO_4·NH_3 particles between +5° and +20°C at the same acid concentrations (*30*). The close agreement implies that the iodine oxoacid particles are growing at the dipole-dipole enhanced kinetic limit for HIO_3, with negligible evaporation at +10°C or below. The measurements further indicate that HIO_3 dominates the growth of iodine particles in this size range and above (because the Kelvin barrier falls with increasing size). This behavior is in marked contrast with previous studies that considered iodine oxides to be responsible for growth (*10*, *27*). At −10°C, the growth rate of HIO_3 particles increases by a factor of 2. This faster growth exceeds the kinetic limit for the arrival rate of HIO_3 monomers onto the particles and is attributed to additional growth from HIO_3 molecular clusters—similar to the situation for sulfuric acid–dimethylamine particles (*31*)—which provide a large pool of condensable material that is "hidden" from the HIO_3 monomer measurement.

Our nucleation and growth rate measurements (Fig. 1) indicate that HIO_3 concentrations above ~3 × 10^6 cm^{-3} and 1 × 10^7 cm^{-3} lead to rapid new particle formation at −10° and +10°C, respectively. The survival probability of particles at low acid concentrations depends exponentially on the ratio of growth rate to condensation sink (in the atmosphere) or wall loss rate (in a chamber). For CLOUD, the wall loss rate of sulfuric acid vapor is 2.2 × 10^{-3} s^{-1} (*30*), which is comparable to the condensation sink in the pristine continental boundary layer. In clean marine regions of the boundary layer or in the upper free troposphere, the condensation sink is often as low as 10^{-4} to 10^{-5} s^{-1}. In such regions, even lower HIO_3 concentrations will lead to sustained new particle formation and subsequent growth rates of a few tenths of a nanometer per hour. Under such conditions of extremely low HIO_3 concentrations and condensation sinks, it is likely that ions will be important to stabilize the embryonic clusters against evaporation, i.e., ion-induced nucleation will be the dominant mechanism.

Particle formation mechanisms

In Fig. 2 we show mass defect plots of negatively charged clusters (Fig. 2A) and neutral clusters (Fig. 2B) containing up to five iodine atoms, measured during nucleation events. The event in Fig. 2A is continued in fig. S3, up to clusters containing 12 iodine atoms. Figure S4 shows all identified peaks of the event in Fig. 2B, before summing over water molecules and charger ions as displayed in Fig. 2B. Further details of the charged and neutral clusters and their signal strengths are provided in table S2.

For ion-induced nucleation (Fig. 2A), we observe a sequence of negatively charged iodine clusters of the form $(HIO_3)_{0-1}(I_2O_5)_n \cdot IO_3^-$, involving sequential addition of HIO_3 followed by rapid dehydration of HIO_3·HIO_3 pairs in the cluster to form I_2O_5, as previously observed at Mace Head (*11*). We find that no nucleation occurs for positively charged iodine clusters (fig. S5). This is clearly seen from the negative and positive charged particle spectra in fig. S6; nucleation and growth only take place for negative particles. Almost all the negative particles have been neutralized by charge recombination before they reach 3 nm, and they continue to grow as mainly neutral particles. A schematic representation of the mechanism for ion-induced iodic acid nucleation,

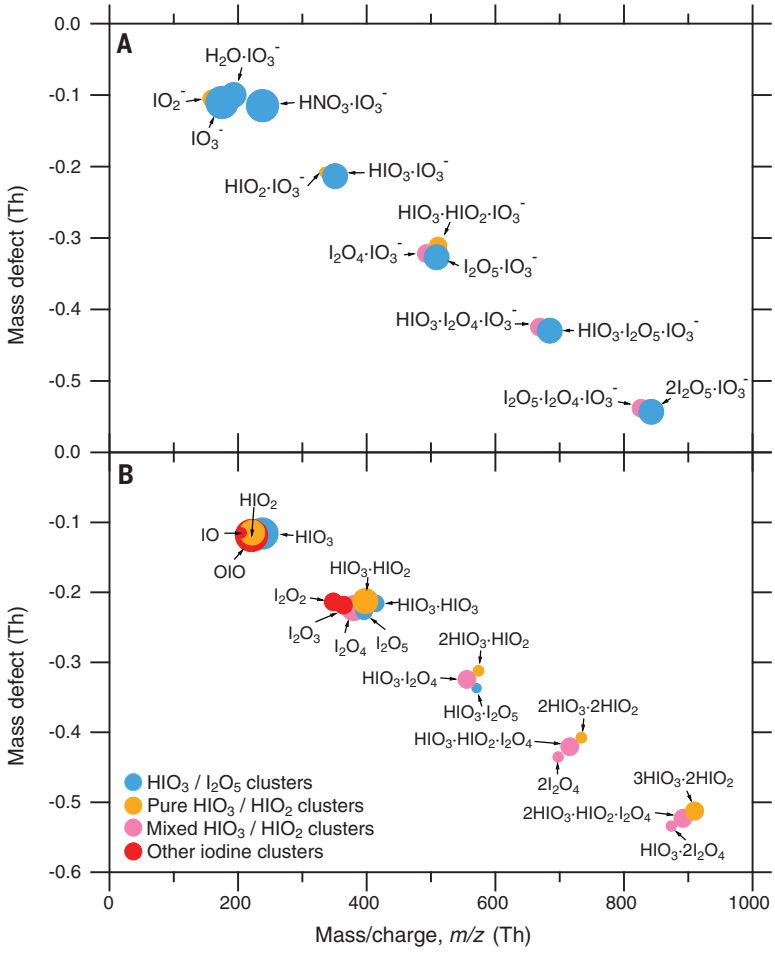

Fig. 2. Charged and neutral mass defect plots during nucleation events. Cluster mass defect (difference from integer mass) versus mass-to-charge ratio [*m/z*, in thomson (Th) units] of (**A**) negatively charged and (**B**) neutral clusters containing up to five iodine atoms, measured during nucleation events. The experimental conditions are (A) 36 ppbv O_3, 40% RH, +10°C, 168 pptv I_2, and 1.5 × 10^7 I atoms cm^{-3} s^{-1} and (B) 46 ppbv O_3, 43% RH, +10°C, 49 pptv I_2, and 2.4 × 10^5 I atoms cm^{-3} s^{-1}. The event shown in (A) is continued in fig. S3 up to clusters containing 12 iodine atoms. To simplify (B), water molecules and nitrate charger ions are ignored (fig. S4 shows the same event where they are included). Charged clusters are measured with the APi-TOF(−) (atmospheric pressure interface–time-of-flight mass spectrometer operating in negative ion mode) and neutral clusters with the nitrate-CIMS (chemical ionization mass spectrometer; preceded by an ion filter). We find that no nucleation takes place for positively charged clusters (figs. S5 and S6). Blue circles indicate clusters containing only HIO_3 and I_2O_5. Orange circles indicate clusters containing only HIO_3 and HIO_2. Pink circles indicate clusters containing HIO_3, HIO_2, I_2O_5, and I_2O_4. Red circles indicate other iodine-containing neutral clusters. The size of the circles indicates signal strength on a logarithmic scale. Further details of the clusters and their signal strengths are provided in table S2.

as interpreted from the mass defect plot (Fig. 2A), is provided in Fig. 3A.

Nucleation of neutral iodine oxoacid particles, however, proceeds by a different mechanism (Fig. 2B). We find that neutral $HIO_3 \cdot I_2O_5$ clusters are relatively weakly bound at these temperatures (no clusters of this type are seen above $HIO_3 \cdot I_2O_5$). During neutral nucleation, we observe repeated sequential addition of HIO_2 followed by HIO_3. The nucleating cluster sequences are shown schematically in Fig. 3B. A certain fraction of $HIO_3 \cdot HIO_2$ pairs in the cluster dehydrate to form iodine tetroxide (I_2O_4) (Fig. 3C). The comparable intensities of the three sequences shown in Fig. 3C indicate that the formation rate of I_2O_4 in the neutral clusters is comparable to the monomer collision rate (few 10^{-3} s^{-1}). In contrast, the strict conversion of $HIO_3 \cdot HIO_3$ pairs during ion-induced nucleation (Fig. 3A) shows that the formation rate of I_2O_5 in the charged clusters is much faster than the monomer collision rate (few 10^{-2} s^{-1}).

Our measurements show that HIO_2 plays a key role in stabilizing neutral HIO_3 clusters. To assess this observation, we used quantum chemistry calculations to compute the formation free energy of several molecular dimers involving HIO_3 (table S3 and fig. S7). The most strongly bound dimer is $HIO_3 \cdot HIO_2$ (−12.9 kcal mol^{-1}). On the other hand, the $HIO_3 \cdot HIO_3$ (−7.7 kcal mol^{-1}) and $HIO_3 \cdot HOI$ (−1.6 kcal mol^{-1}) dimers are both much less stable. These calculations argue in favor of the dominant $HIO_3 \cdot HIO_2$ dimer shown in the 1→2 iodine step in Fig. 3B and not $HIO_3 \cdot HIO_3$ at the current experimental conditions. Our measurements and quantum chemical calculations suggest that HIO_2 stabilizes neutral HIO_3 clusters with a 1:1 stoichiometry similar to that seen for ammonia stabilization of embryonic H_2SO_4 clusters (*6*). For completeness, we note that, for neutral nucleation, the direct addition of I_2O_4 molecules from gas phase I_2O_4, which we measure at concentrations of ~1% of HIO_3 (table S2), cannot be excluded. We also note that HIO_3 shows very weak affinity for pairing with a base ($HIO_3 \cdot NH_3$ is −5.0 kcal mol^{-1}). Once the neutral particles exceed a critical size, they can continue to grow by condensation of HIO_3 alone (most of the particles in Fig. 1B are neutralized), and so growth is no longer limited by the lower concentrations of HIO_2.

Ion-induced nucleation rate

To investigate ion-induced nucleation further, we measured the collision rate coefficients, k_{i+1}, for each step in the process, $N_i^- + HIO_3 \rightarrow N_{i+1}^-$, where N_i^- represents a negatively charged cluster containing i iodine atoms [see (*32*) and the supplementary materials for further details]. The rate coefficients measured between neutral HIO_3 monomers and charged clusters containing up to 11 iodine atoms are shown in Fig. 4A. Within measurement errors, we find the same HIO_3 rate coefficient for each charged iodic cluster from the dimer to 11-mer, with a mean value [1.72 ± 0.26 (stat.) +0.24/−0.21 (syst.)] × 10^{-9} cm^3 s^{-1} (1σ uncertainties). For comparison, we show the theoretical expectations for the rate coefficients for charged HIO_3 clusters from average dipole orientation theory (ADO, red curve) (*33*) and its extensions: hard-sphere average dipole orientation theory (HSA, green curve) and surface charge capture theory (SCC, blue curve) (*34*). The latter theory, SCC, agrees closely with our measurements. We show in Fig. 4B the enhancement factors for charged versus neutral rate coefficients (ratios of the CLOUD measurements divided by the neutral rate coefficients, ignoring dipole enhancement). The enhancement during ion-induced nucleation, which averages 6.3, rapidly shepherds newly formed particles through the smallest size range where they are highly mobile and most vulnerable to scavenging loss, and it contributes to the faster particle formation rate.

Our measurements of the individual collision rate coefficients for charged clusters containing up to 11 iodine atoms (Fig. 4A)—and their good agreement with theoretical expectations—show that ion-induced iodic acid nucleation proceeds at the kinetic limit and therefore is strictly a barrierless process rather than nucleation. Substantial evaporation of any cluster in this range would lead to a telltale higher apparent rate coefficient for the previous cluster. We have confirmed kinetic formation of charged clusters in two further ways. (i) We have used a kinetic model to calculate the ion-induced component of J_{gcr} (= J_{iin} + J_n) at +10°C (see supplementary materials for details) and find it is consistent with our experimental measurements (Fig. 1A). (ii) We have calculated the reaction free energies and evaporation rates for several molecular clusters containing an IO_3^- ion (table S4). Our calculations show that extremely low evaporation rates are expected for charged iodic acid clusters. They also indicate that the $HIO_3 \cdot HIO_3 \cdot IO_3^-$ cluster is much less stable than $I_2O_5 \cdot IO_3^-$, supporting the sequence observed experimentally in the first steps of Fig. 3A. The HIO_3 collision rate measurements in Fig. 4A confirm that ion-induced nucleation is indeed due to the sequential addition of HIO_3 monomers and not, for example, to mixed accretion of HIO_3 and I_2O_5 molecules.

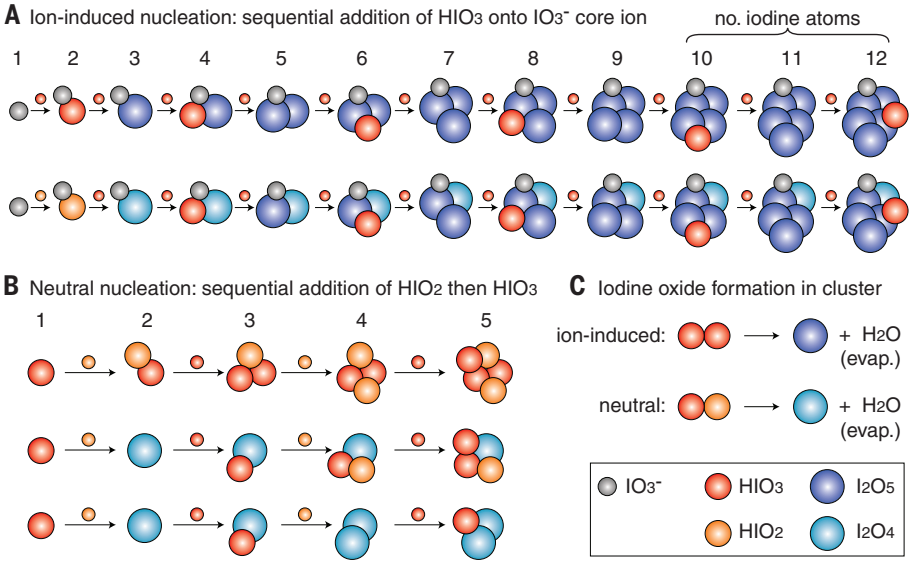

Fig. 3. Nucleation mechanisms for iodine oxoacid clusters. Schematic representations of the nucleation mechanisms for (**A**) ion-induced (charged) and (**B**) neutral (uncharged) iodine oxoacid clusters, interpreted from the mass defect plots. Ion-induced nucleation involves condensation of iodic acid (HIO_3) alone onto an IO_3^- ion, whereas neutral nucleation involves repeated stepwise condensation of iodous acid (HIO_2) followed by iodic acid. Iodine oxide formation takes place in the clusters, as shown in (**C**), involving evaporation (evap.) of a water molecule. Pairs of HIO_3 molecules always dehydrate to form I_2O_5 in charged clusters (A). However, HIO_3 molecules do not form I_2O_5 in neutral clusters, but some may combine with HIO_2 and dehydrate to form I_2O_4 (B). The relative intensities of the final neutral clusters in (B) are $(HIO_3)_3 \cdot (HIO_2)_2$:$(HIO_3)_2 \cdot HIO_2 \cdot I_2O_4$:$HIO_3 \cdot (I_2O_4)_2$ = 0.38:0.46:0.16, indicating that the formation rate of I_2O_4 in the neutral clusters is comparable to the monomer collision rate.

Particle composition

The measurements presented in Fig. 1B provide strong evidence that HIO_3 drives the growth of iodic particles above 1.8 nm. However, we have seen that additional iodine compounds play important roles during nucleation: HIO_2 for neutral nucleation, and the formation of iodine oxides—I_2O_5 and I_2O_4—in the charged and neutral clusters, respectively (Fig. 2).

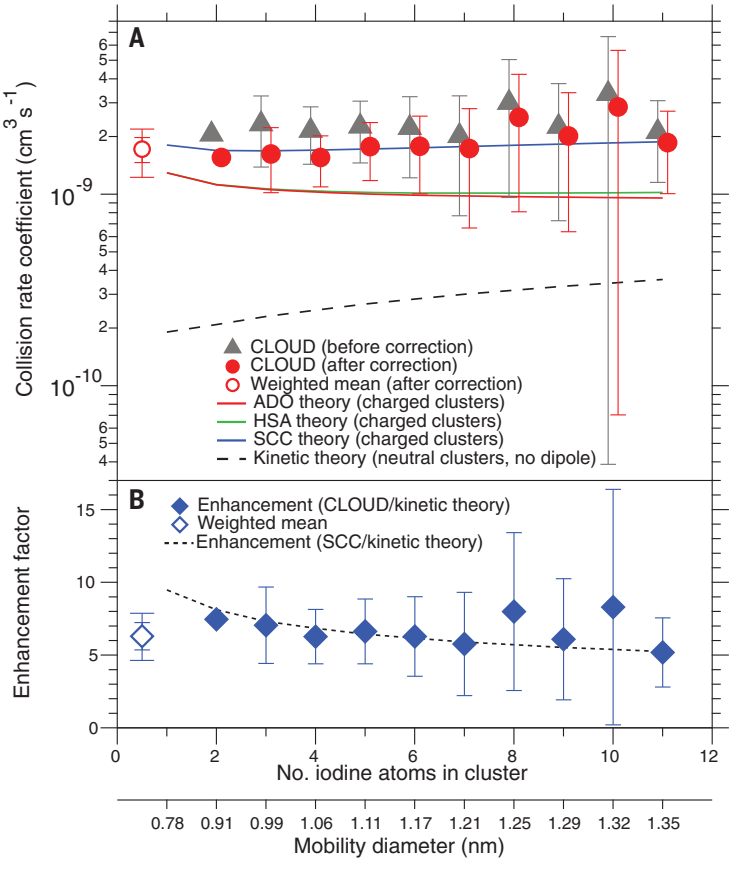

Fig. 4. Collision rate coefficients for ion-induced iodic acid nucleation. (**A**) Collision rate (reaction rate) coefficients measured between neutral HIO_3 monomers and charged clusters containing up to 11 iodine atoms. The experimental conditions are 20 to 41 ppbv O_3, 34 to 44% RH, +10°C, 0.4 to 3.5 pptv I_2, and 0.44×10^5 to 3.2×10^5 I atoms cm^{-3} s^{-1}. The gray triangles are calculated from the 50% appearance times of eight experiments with 0.76×10^7 to 2.0×10^7 cm^{-3} HIO_3. The red circles are the final experimental values after applying corrections from a kinetic model. The experimental points are horizontally shifted from integers to avoid overlaps. The solid curves show theoretical expectations for the charged collision rate coefficients from average dipole orientation theory (ADO, red curve) (*36*), hard-sphere average dipole orientation theory (HSA, green curve) (*37*), and surface charge capture theory (SCC, blue curve) (*37*). The expected collision rate coefficients between neutral monomers and neutral clusters, ignoring dipole-dipole interactions, are shown by the dashed black curve. (**B**) Measured enhancement factors for charged versus neutral collision rate coefficients (ratios of the corrected CLOUD measurements divided by the neutral collision rate coefficients). The black dotted line is the ratio of the SCC value to the neutral kinetic theory value. For both panels, the hollow markers show the weighted mean values from the trimer to 11-mer, with ±1σ errors indicating statistical without (inner caps) and with systematic errors (outer).

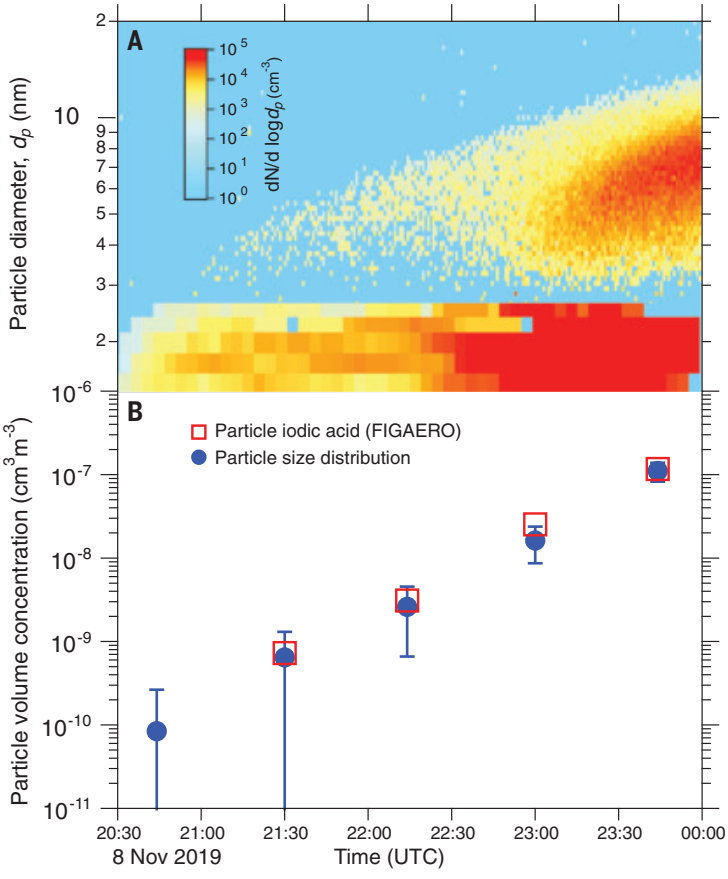

Fig. 5. Evolution of particle size and chemical composition during iodic oxoacids nucleation. (**A**) Evolution of the particle size distribution measured by the particle size magnifier (PSM; smaller than 2.5 nm) and nano–scanning mobility particle sizer (nano-SMPS; larger than ~4 nm). The experimental conditions are 40 ppbv O_3, 40% RH, +10°C, 8 pptv I_2, 2.9×10^5 to 5.3×10^5 I atoms cm^{-3} s^{-1}, and 3.1×10^7 to 7.1×10^7 cm^{-3} HIO_3. The event is started by switching on green illumination (528 nm), and HIO_3 is increased toward the end. (**B**) Evolution of the particle volume concentration derived from (i) the particle size distribution (blue circles) and (ii) the HIO_3 volume for particles collected and analyzed with the FIGAERO (hollow red squares). Particle concentrations in the size range between 2.5 and 4 nm are obtained by interpolation between the PSM and nano-SMPS distributions and are verified by measurements of the total number concentrations above a 2.5-nm threshold of the PSM. The FIGAERO collects particles on a Teflon filter for 30 min and then evaporates the sample with a controlled temperature ramp over the next 15 min at the inlet of the mass spectrometer. The FIGAERO data points are centered on the 30-min collection interval. The bars indicate ±1σ total errors. The FIGAERO mass spectrum shows that HIO_3 dominates the particle composition (80% mass fraction). This is independently confirmed by the close agreement between the volume concentrations measured by the particle sizers and by the FIGAERO.

To address the question of the extent to which these other iodine species contribute to particle growth at larger sizes, we have directly measured the composition of freshly nucleated iodic particles in the size range up to ~10 nm with a soft-ionization Br^--FIGAERO (filter inlet for gases and aerosols) mass spectrometer. The majority (90%) of particles between 3 and 10 nm are neutral (fig. S6). The FIGAERO collects particles on a Teflon filter for 30 min and then evaporates the sample with a controlled temperature ramp over the next 15 min at the inlet of a mass spectrometer. The mass spectrometer thereby measures the deposited mass of each chemical constituent of the particles and produces an individual thermogram of its volatility (evaporation temperature).

In Fig. 5A we show the evolution of particle size during a nucleation experiment. Particle sizes <2.5 nm are measured by a PSM (particle size magnifier), and those >4 nm are measured by a nano-SMPS (scanning mobility particle sizer). In Fig. 5B we show the evolution of total particle volume derived from these measurements (blue circles). We also show in Fig. 5B the evolution of total HIO_3 volume concentration in the particle phase, measured by the FIGAERO. The mass spectrum is dominated by the single channel, HIO_3 (78% of the total mass, excluding water), with the rest being primarily I_2. We found very little HIO_2 in the particle phase, owing to its low concentration. The mass spectrum shows that the freshly formed particles are composed almost entirely of HIO_3, and not I_2O_{4-5} as previously thought (*9*–*11*). This conclusion is independently confirmed by the close agreement seen in Fig. 5B between the volume concentrations measured by the particle sizers and by the direct measurements of particulate HIO_3 with the FIGAERO. We have confirmed, by conducting laboratory calibrations, that the evaporated HIO_3 resulted from iodic acid in the particle phase, and not by thermal decomposition of other iodine compounds. We nebulized iodic acid particles and then collected and analyzed them with the FIGAERO using the same procedures as for our experiments at CLOUD (see supplementary materials for details). The FIGAERO thermograms for the nebulized samples agree well with those obtained at CLOUD (fig. S8).

Climate implications

Sulfuric acid–ammonia nucleation is known to be important in relatively pristine environments such as the free troposphere (*14*) or the Antarctic coastal region (*35*). We show here that the nucleation rate of iodine oxoacids exceeds $H_2SO_4{\cdot}NH_3$ at the same acid concentrations. In pristine, cooler regions of the atmosphere, HIO_3 concentrations above ~10^6 cm^{-3} will lead to copious new particle formation and sustained growth at a few times 0.1 nanometer per hour. The question then arises: Are there pristine regions of the atmosphere where the concentrations of HIO_3 are comparable to or exceed sulfuric acid, or else ammonia is insufficient? For such regions, HIO_3 could be the dominant source of new particles.

Our global boundary layer measurements of HIO_3 at 10 sites are shown in figs. S9 and S10. The conditions for abundant iodine new particle formation and rapid growth are frequently reached at mid-latitude coastal sites with marine algae, such as Mace Head and Helsinki, and at coastal polar sites such as Villum and Ny-Ålesund in the Arctic, or Neumayer in the Antarctic. Although measurements over the remote ocean are sparse, frequent new particle formation over the high Arctic pack ice has recently been reported, driven by HIO_3 with little contribution from sulfuric acid (*36*).

The implications for the future are notable. Global iodine emissions have increased threefold over the past 70 years and may continue to increase in the future as sea ice becomes thinner (*37*) and surface ozone increases (*18*). Any resultant increase of iodic CCN in the Arctic region could increase longwave radiative forcing from clouds and provide a positive feedback mechanism that accelerates the loss of sea ice. Iodine is also widespread in the free troposphere (*23*, *24*), where low temperatures, low condensation sinks, and high ion production rates from galactic cosmic rays favor iodic particle formation. Indeed, particulate iodate (IO_3^-) has recently been observed near the tropopause at iodine mixing ratios of ~0.1 to 0.5 pptv, and IO_3^- is the main iodine reservoir in the stratosphere (*25*) (further discussion is provided in the supplementary materials).

Our study shows that iodic acid, HIO_3, is the major iodine species driving both nucleation and growth of iodine oxoacid particles in the boundary layer and remains as the dominant constituent in the particulate phase. We have further shown that iodous acid, HIO_2, plays a key role in neutral nucleation by stabilizing HIO_3 clusters against evaporation, but it is not important for particle growth at larger sizes. The efficacy of iodine oxoacids to form new particles exceeds that of the $H_2SO_4{\cdot}NH_3$ system at the same acid concentrations. Although atmospheric measurements remain limited, they are nevertheless sufficient to demonstrate the ubiquity of HIO_3 and its potential to compete with sulfuric acid(–ammonia) particle formation in pristine regions of the atmosphere such as marine coasts, the Arctic boundary layer, or the upper free troposphere.

REFERENCES AND NOTES

1. H. Gordon *et al.*, *J. Geophys. Res.* **122**, 8739–8760 (2017).
2. G. A. Meehl *et al.*, *Sci. Adv.* **6**, eaba1981 (2020).
3. S. M. Kreidenweis, J. H. Seinfeld, *Atmos. Environ.* **22**, 283–296 (1988).
4. P. H. McMurry *et al.*, *J. Geophys. Res.* **110**, D22S02 (2005).
5. C. Kuang, P. H. McMurry, A. V. McCormick, F. L. Eisele, *J. Geophys. Res.* **113**, D10209 (2008).
6. J. Kirkby *et al.*, *Nature* **476**, 429–433 (2011).
7. M. Kulmala *et al.*, *Science* **339**, 943–946 (2013).
8. M. L. Dawson *et al.*, *Proc. Natl. Acad. Sci. U.S.A.* **109**, 18719–18724 (2012).
9. T. Hoffmann, C. D. O'Dowd, J. H. Seinfeld, *Geophys. Res. Lett.* **28**, 1949–1952 (2001).
10. C. D. O'Dowd *et al.*, *Nature* **417**, 632–636 (2002).
11. M. Sipilä *et al.*, *Nature* **537**, 532–534 (2016).
12. J. Kirkby *et al.*, *Nature* **533**, 521–526 (2016).
13. M. Wang *et al.*, *Nature* **581**, 184–189 (2020).
14. E. M. Dunne *et al.*, *Science* **354**, 1119–1124 (2016).
15. J. Almeida *et al.*, *Nature* **502**, 359–363 (2013).
16. R. J. Charlson, J. E. Lovelock, M. O. Andreae, S. G. Warren, *Nature* **326**, 655–661 (1987).
17. T. M. Sherwen *et al.*, *Geophys. Res. Lett.* **43**, 10012–10019 (2016).
18. L. J. Carpenter *et al.*, *Nat. Geosci.* **6**, 108–111 (2013).
19. A. S. Mahajan *et al.*, *Atmos. Chem. Phys.* **10**, 4611–4624 (2010).
20. B. C. Sive *et al.*, *Geophys. Res. Lett.* **34**, L17808 (2007).
21. J. D. Allan *et al.*, *Atmos. Chem. Phys.* **15**, 5599–5609 (2015).
22. C. Prados-Roman *et al.*, *Atmos. Chem. Phys.* **15**, 583–593 (2015).
23. B. Dix *et al.*, *Proc. Natl. Acad. Sci. U.S.A.* **110**, 2035–2040 (2013).
24. R. Volkamer *et al.*, *Atmos. Meas. Tech.* **8**, 2121–2148 (2015).
25. T. K. Koenig *et al.*, *Proc. Natl. Acad. Sci. U.S.A.* **117**, 1860–1866 (2020).
26. H. Yu *et al.*, *Atmos. Chem. Phys.* **19**, 4025–4039 (2019).
27. J. C. Gómez Martín *et al.*, *Nat. Commun.* **11**, 4521 (2020).
28. E. Drougas, A. M. Kosmas, *J. Phys. Chem. A* **109**, 3887–3892 (2005).
29. J. M. C. Plane, D. M. Joseph, B. J. Allan, S. H. Ashworth, J. S. Francisco, *J. Phys. Chem. A* **110**, 93–100 (2006).
30. D. Stolzenburg *et al.*, *Atmos. Chem. Phys.* **20**, 7359–7372 (2020).
31. K. Lehtipalo *et al.*, *Nat. Commun.* **7**, 11594 (2016).
32. X.-C. He *et al.*, *Aerosol Sci. Technol.* **55**, 231–242 (2021).
33. T. Su, M. T. Bowers, *J. Chem. Phys.* **58**, 3027–3037 (1973).
34. G. Kummerlöwe, M. K. Beyer, *Int. J. Mass Spectrom.* **244**, 84–90 (2005).
35. T. Jokinen *et al.*, *Sci. Adv.* **4**, eaat9744 (2018).
36. A. Baccarini *et al.*, *Nat. Commun.* **11**, 4924 (2020).
37. C. A. Cuevas *et al.*, *Nat. Commun.* **9**, 1452 (2018).
38. X.-C. He *et al.*, Role of iodine oxoacids in atmospheric aerosol nucleation: data resources, Version 1, Zenodo (2021); http://doi.org/10.5281/zenodo.4299441.

ACKNOWLEDGMENTS

Funding: We thank the European Organization for Nuclear Research (CERN) for supporting CLOUD with important technical and financial resources and for providing a particle beam from the CERN Proton Synchrotron. This research has received support from the Academy of Finland (projects 316114, 307331, 310682, 266388, 3282290, 306853, 296628, 229574, 333397, 326948, and 1325656); the European Research Council (projects 692891, 616075, 764991, 316662, 742206, and 714621); CSC – Finnish IT center; the EC Seventh Framework Programme and the EU H2020 programme Marie Skłodowska Curie ITN "CLOUD-TRAIN" (316662) and "CLOUD-MOTION" (764991); Austrian Science Fund (FWF) (J3951-N36 and P27295-N20); the Swiss National Science Foundation (20FI20_159851, 200021_169090, 200020_172602, and 20FI20_172622); the U.S. National Science Foundation (grants AGS1447056, AGS1439551, AGS1801574, AGS1620530, AGS1801897, AGS153128, AGS1649147, AGS1801280, AGS1602086, and AGS1801329); MSCA H2020 COFUND-FP-CERN-2014 fellowship (665779); German Federal Ministry of Education and Research: CLOUD-16 (01LK1601A); Portuguese Foundation for Science and Technology (CERN/FIS-COM/0014/2017); Academy of Finland Centre of Excellence in Atmospheric Sciences (grant 272041); European Regional Development Fund (project MOBTT42); Jiangsu Collaborative Innovation Center for Climate Change; Yangtze River Delta Atmosphere and Earth System Science National Observation and Research Station; Estonian Research Council (project PRG714); Hungarian National Research, Development and Innovation Office (K116788 and K132254); NASA Graduate Fellowship (NASA-NNX16AP36H); and ACTRIS 2TNA H2020 OCTAVE (654109). We are also grateful for all the people who have contributed to the field measurements around the world.
Author contributions: X.-C.H., M.K., R.V., J.Ki., and M.Sip. planned the experiments. X.-C.H., Y.J.T., L.D., M.W., H.F., D.S., M.Sim., A.Kü., J.S., B.R., S.I., M.R., S.Scho., R.B., D.S.W., T.K.K., S.A., A.A., A.B., S.B., L.C., D.C., B.C., A.Dia., J.Du., I.E.H., R.C.F., L.G.C., M.G., M.H., V.H., H.J., J.Ka., D.K., C.K., W.K., J.E.K., A.Kv., T.L., H.L., C.P.L., K.L., M.L., Z.L., V.M., H.E.M., G.M., R.M., R.L.M., B.M., O.M., T.M., A.O., T.P., J.P., M.P., W.S., S.Schu., B.S., G.S., Y.S., A.T., M.V.-P., A.C.W., S.K.W., W.N., P.M.W., Y.Wu., A.Y., Y.Wang, M.Z.-W., Q.Z., J.C., M.K., U.B., R.V., J.Ki., and M.Sip. prepared the CLOUD

facility or measuring instruments. X.-C.H., Y.J.T., L.D., M.W., H.F., D.S., M.Sim., J.S., B.R., M.R., R.B., D.S.W., T.K.K., T.J., N.S., L.J.B., F.A., A.B., F.B., B.B., S.B., D.C., R.C., A.Din., J.Du., L.G.C., M.G., M.H., V.H., H.J., D.K., C.K., J.E.K., H.L., C.P.L., M.L., Z.L., H.E.M., G.M., R.M., R.L.M., B.M., T.M., J.P., A.R., I.S., S.Schu., B.S., G.S., C.T., A.T., R.C.T., O.V., M.V.-P., A.C.W., S.K.W., W.N., Y.Wu, M.X., C.Y., Q.Y., A.Y., Y.Wang, M.Z.-W., R.V., and J.Ki. collected the data. X.-C.H., Y.J.T., L.D., M.W., H.F., D.S., M.Sim., J.S., B.R., R.C.F., D.K., C.K., W.K., S.K.W., P.M.W., P.Z., T.K., R.V., J.Ki, and D.R.W. analyzed the data. J.Ki. and X.-C.H. wrote the manuscript with contributions from R.V., Y.J.T., M.W., H.F., T.K.K., M.K., T.K., N.M.D., D.R.W., and M.Sip. X.-C.H., Y.J.T., L.D., M.W., H.F., D.S., B.R., S.I., M.R., S.Scho., R.B., T.K.K., N.S., A.B., A.Din., J.Do., J.Du., I.E.H., A.H., H.J., J.Ka., J.E.K., H.L., C.P.L., K.L., R.L.M., B.M., O.M., T.P., A.S.-L., I.S., P.Z., J.C., U.B., M.K., V.-M.K., T.K., N.M.D., R.V., J.Ki., D.R.W., and M.Sip. commented on and edited the manuscript. **Competing interests:** The authors declare no competing interests. **Data and materials availability:** Data for all figures in the main text and supplementary materials are available at the Zenodo repository (*38*).

SUPPLEMENTARY MATERIALS

science.sciencemag.org/content/371/6529/589/suppl/DC1
Materials and Methods
Supplementary Text
Figs. S1 to S10
Tables S1 to S4
References (*39*–*81*)

27 July 2020; accepted 6 January 2021
10.1126/science.abe0298

CLINICAL TRIALS

Fecal microbiota transplant overcomes resistance to anti–PD-1 therapy in melanoma patients

Diwakar Davar[1]*, Amiran K. Dzutsev[2]*, John A. McCulloch[2], Richard R. Rodrigues[2,3], Joe-Marc Chauvin[1], Robert M. Morrison[1], Richelle N. Deblasio[1], Carmine Menna[1], Quanquan Ding[1], Ornella Pagliano[1], Bochra Zidi[1], Shuowen Zhang[1]†, Jonathan H. Badger[2], Marie Vetizou[2], Alicia M. Cole[2], Miriam R. Fernandes[2], Stephanie Prescott[2], Raquel G. F. Costa[2], Ascharya K. Balaji[2], Andrey Morgun[4], Ivan Vujkovic-Cvijin[5], Hong Wang[6], Amir A. Borhani[7], Marc B. Schwartz[8], Howard M. Dubner[8], Scarlett J. Ernst[1], Amy Rose[1], Yana G. Najjar[1], Yasmine Belkaid[5], John M. Kirkwood[1], Giorgio Trinchieri[2]‡§, Hassane M. Zarour[1,9]‡§

Anti–programmed cell death protein 1 (PD-1) therapy provides long-term clinical benefits to patients with advanced melanoma. The composition of the gut microbiota correlates with anti–PD-1 efficacy in preclinical models and cancer patients. To investigate whether resistance to anti–PD-1 can be overcome by changing the gut microbiota, this clinical trial evaluated the safety and efficacy of responder-derived fecal microbiota transplantation (FMT) together with anti–PD-1 in patients with PD-1–refractory melanoma. This combination was well tolerated, provided clinical benefit in 6 of 15 patients, and induced rapid and durable microbiota perturbation. Responders exhibited increased abundance of taxa that were previously shown to be associated with response to anti–PD-1, increased $CD8^+$ T cell activation, and decreased frequency of interleukin-8–expressing myeloid cells. Responders had distinct proteomic and metabolomic signatures, and transkingdom network analyses confirmed that the gut microbiome regulated these changes. Collectively, our findings show that FMT and anti–PD-1 changed the gut microbiome and reprogrammed the tumor microenvironment to overcome resistance to anti–PD-1 in a subset of PD-1 advanced melanoma.

Immune checkpoint blockade with monoclonal antibodies (mAbs) targeting programmed cell death protein 1 (PD-1) provides long-term clinical benefits to nearly 40% of patients with advanced melanoma (*1*–*5*). In addition to tumor-intrinsic mechanisms supporting resistance to anti–PD-1 mAbs (anti–PD-1), the gut microbiome is a major tumor-extrinsic regulator of responses to anti–PD-1 (*6*–*9*). In mice, composition of the gut microbiome modulates therapeutic activity of anti–PD-1 and anti–programmed death-ligand 1 (PD-L1), and administration of certain gut commensals or fecal microbiota transplantation (FMT) promotes anti–PD-1 efficacy in melanoma-bearing mice (*10*–*12*). Although multiple studies have reported that a favorable gut microbiome is associated with response to anti–PD-1 in cancer patients, its precise composition is not yet fully understood (*10*–*12*). Specifically in melanoma, key bacterial species belonging to various phyla, including Actinobacteria (*Bifidobacteriaceae* spp. and *Coriobacteriaceae* spp.) and Firmicutes (*Ruminococcaceae* spp. and *Lachnospiraceae* spp.), are associated with favorable response to mAbs targeting PD-1 in cancer patients, although limited concordance among the identified species has been reported in different studies (*10*–*14*). Whether microbiome-based therapy can overcome resistance to anti–PD-1 in patients with advanced melanoma has not been evaluated. To address this question, we designed a single-arm clinical trial to evaluate the safety and efficacy of FMT obtained from individual long-term responder (R) melanoma patients together with anti–PD-1 in PD-1–refractory metastatic melanoma patients (NCT03341143; fig. S1).

A subset of PD-1–refractory melanoma patients respond to fecal microbiota transplant and anti–PD-1 therapy

Sixteen melanoma patients were enrolled between June 2018 and January 2020 (table S1), and the results presented here reflect a data cutoff of 1 September 2020. All melanoma patients were primary refractory to anti–PD-1 therapy, defined as patients who had no prior response to anti–PD-1 alone or in combination with anticytotoxic T lymphocyte–associated protein 4 or investigational agents (table S1) and had confirmed primary progressive disease (PD), as assessed by an independent radiologist using response evaluation criteria in solid tumors (RECIST v1.1) (*15*, *16*). Among PD-1–refractory patients included in the trial, only one had a best response of short-term stable disease (SD) before radiographically confirmed PD. All enrolled patients and candidate donors underwent serial stool sampling and extensive infectious studies to eliminate the possibility of transmitting infectious agents (fig. S2). Seven donors, including four with complete response (CR) and three with partial response (PR), with median progression-free survival (PFS) of 56 months (range: 45 to 70 months) were used to treat 16 patients (table S2). Blood and stool specimens were obtained serially and screened for 32 viral, bacterial, fungal, and protozoan agents before FMT (fig. S2). A single donor–derived FMT was administered along with pembrolizumab (fig. S1), followed by additional pembrolizumab therapy every 3 weeks until disease progression or intolerable toxicity. Radiographic assessments were conducted every 12 weeks (four cycles), and response was classified by using RECIST v1.1. Of the 16 patients enrolled, 15 received FMT and pembrolizumab and had at least one restaging computed tomography (CT) scan and thus were deemed evaluable

[1]Department of Medicine and UPMC Hillman Cancer Center, University of Pittsburgh, Pittsburgh, PA 15213, USA. [2]Laboratory of Integrative Cancer Immunology, Center for Cancer Research, National Cancer Institute, Bethesda, MD 20892, USA. [3]Genetics and Microbiome Core, Basic Science Program, Frederick National Laboratory for Cancer Research, Frederick, MD 21702, USA. [4]College of Pharmacy, Oregon State University, Corvallis, OR 97331, USA. [5]Laboratory of Immune System Biology, National Institute of Allergy and Infectious Diseases (NIAID), National Institutes of Health, Bethesda, MD 20892, USA. [6]Biostatistics Facility, UPMC Hillman Cancer Center, University of Pittsburgh, Pittsburgh, PA 15213, USA. [7]Division of Abdominal Imaging, Department of Radiology, University of Pittsburgh, Pittsburgh, PA 15213, USA. [8]Division of Gastroenterology, Hepatology and Nutrition, University of Pittsburgh, Pittsburgh, PA 15213, USA. [9]Department of Immunology, University of Pittsburgh, Pittsburgh, PA 15213, USA.
*These authors contributed equally to this work. †Present address: School of Medicine, Tsinghua University, No. 1 Tsinghua Yuan, Haidian District, Beijing 100084, China. ‡These authors contributed equally to this work.
§Corresponding author. Email: zarourhm@upmc.edu (H.M.Z.); trinchig@mail.nih.gov (G.T.)

for response. One patient who had a rapid clinical decline after FMT that was deemed secondary to rapid disease progression was evaluable for safety but not response. Objective responses (ORs) were noted in 3 (PT-18-0032, CR; PT-18-0007 and PT-19-0024, PR) out of 15 patients [OR rate (ORR): 20%], whereas 3 (PT-18-0018, PT-19-0002, and PT-19-0010) out of 15 patients (20%) had durable SD lasting >12 months (Fig. 1, A and B). Representative radiographic examples from all three R patients with ORR are provided (Fig. 1C and figs. S3 and S4). Median PFS and overall survival (OS) in all patients were 3.0 and 7.0 months, respectively, at a median follow-up of 7 months.

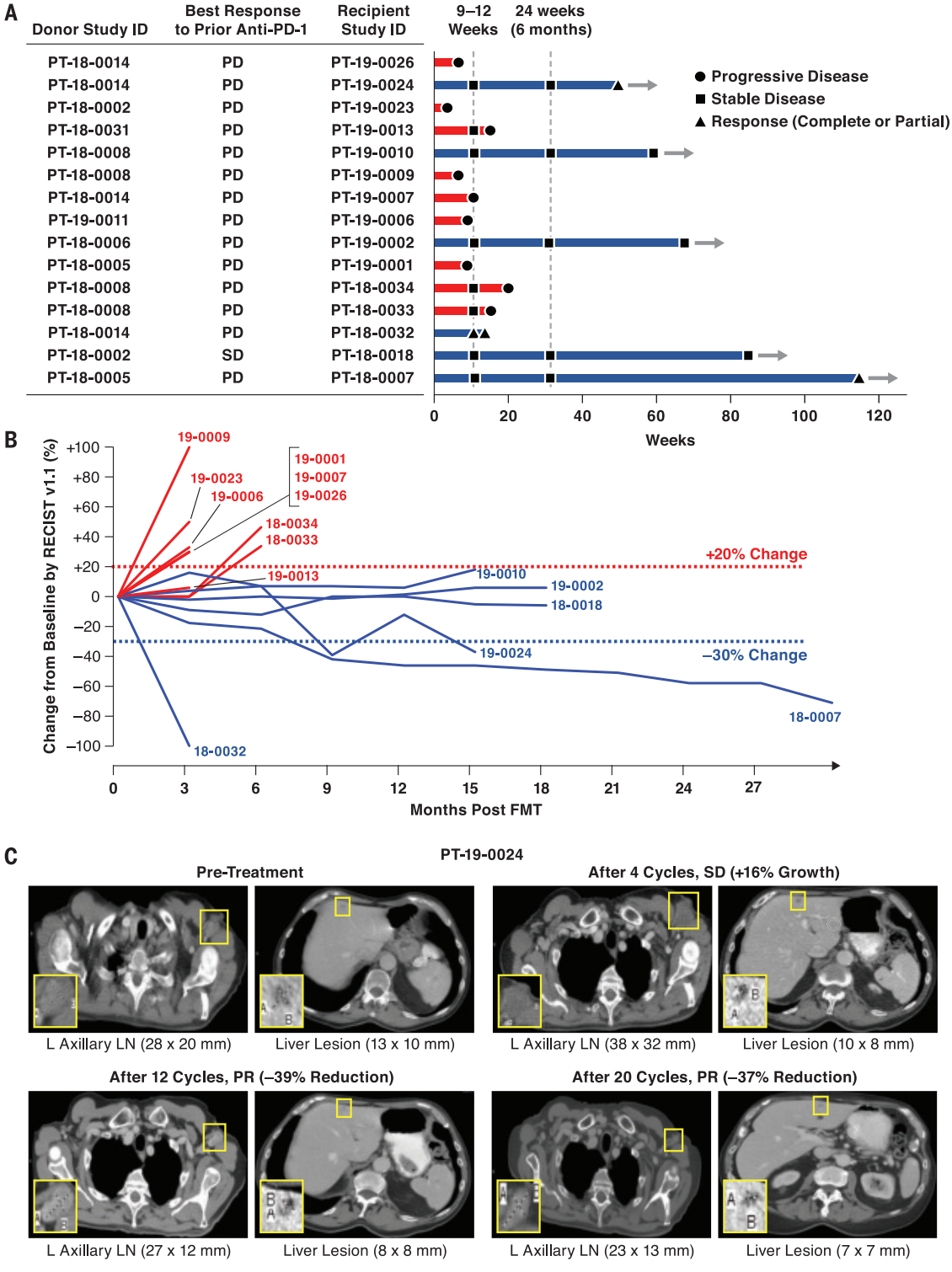

Fig. 1. Radiographic responses from a phase 2 study of anti–PD-1 responder–derived FMT and pembrolizumab in PD-1–refractory melanoma. Melanoma patients who had primary refractory disease to anti–PD-1 therapy received FMT derived from individual melanoma patients with durable OR to anti–PD-1 therapy. FMT was administered colonoscopically on day 0 along with pembrolizumab (200 mg). Pembrolizumab was repeated every 3 weeks. Restaging scans were performed at weeks 9 to 12 and repeated every 9 to 12 weeks while in the study. Patients remained in the study until intolerable toxicity, RECIST v1.1–confirmed disease progression, or completion of 35 cycles of pembrolizumab. (**A** and **B**) Treatment exposure and response duration by RECIST v1.1 (investigator assessed; *n* = 15). (A) FMT donor and best response to prior line(s) of anti–PD-(L)1 therapy singly or in combination are shown for each FMT-recipient patient. The length of each bar corresponds to the duration of time that patients received treatment (in weeks). Response status is color coded (R, blue; NR, red). Response symbols represent status at first restaging scan (9 to 12 weeks) and at most recent review. Patients with ongoing response in the study are depicted with horizontal arrows. (B) Radiographic change of tumor burden from baseline (investigator assessed per RECIST v1.1; *n* = 15). One patient (PT-18-0018) had initial disease stability with subsequent progression after antibiotic therapy and was offered a retransplant with the same donor, with subsequent disease stabilization. (**C**) Representative CT scans from one responding patient. CT scans from patient PT-19-0024 at four separate time points depict initial tumor growth after FMT followed by eventual PR. L, left; LN, lymph node.

In six patients with disease control (i.e., OR and SD), median PFS and OS were 14.0 and 14.0 months, respectively (Fig. 1B). Among these patients, one patient (PT-18-0007) exhibited ongoing PR after >2 years and is currently on surveillance, whereas four patients (PT-18-0018, PT-19-0002, PT-19-0010, and PT-19-0024) remain on treatment. One patient (PT-18-0032) with radiographic CR underwent an elective surgical procedure for spinal stenosis but suffered a spinal infarct unrelated to therapy and subsequently passed away. Our study shows that FMT together with anti–PD-1 overcame resistance to anti–PD-1 in a subset of PD-1–refractory melanoma patients. Although these preliminary findings warrant further evaluation in a larger randomized clinical trial, the observed ORR was superior to ORRs reported in melanoma patients primary refractory to anti–PD-1 therapy treated beyond progression (*17*). Treatment-related adverse events (AEs) were minimal (table S3). Although all patients experienced at least one AE, these were mostly low grade (grade 1, 72.9%; grade 2, 20.0%). Endocrinologic AEs, mostly hypothyroidism, occurred in 17.6% of patients and were easily managed with hormone replacement. Grade 3 AEs occurred in three patients: two instances of fatigue, in which underlying endocrinological issues were excluded and resolved, and one case of peripheral motor neuropathy (PT-19-0024) that required hospitalization, intravenous immunoglobulin, and corticosteroids and resolved with no further sequelae upon reinstitution of pembrolizumab.

Fecal microbiota transplant induces persistent perturbation of recipients' gut microbiome

To evaluate the effects of FMT on gut microbiota composition in recipients and the relationship with clinical response, defined as OR or SD >12 months after FMT and anti–PD-1 on the basis of RECIST 1.1 criteria, we performed shotgun metagenomic sequencing of 223 fecal samples obtained from recipients (n = 15) and donors (n = 7). For each recipient, we sequenced one pre-FMT sample (obtained 7 to 21 days before FMT) and all available post-FMT samples (obtained weekly for 12 weeks and then every 3 weeks for as long as the patient remained on trial) (Fig. 2A). For each corresponding FMT, we sequenced the distinctive donor-specific "FMT infusate" obtained from specific FMT donors (table S2 and fig. S5A). Uniform manifold approximation and projection (UMAP) analyses depicted distinct gut microbiota composition in recipients (Fig. 2A) and donors (fig. S5A). No significant difference in response after FMT was observed in patients that received infusates from donors that had either a CR or PR to anti–PD-1 (fig. S5B). The microbiota in CR donors exhibited higher alpha diversity than in PR donors, but no significant differences were observed between donors and recipients before FMT (fig. S5C). In recipients, gut microbiota composition changed after a single FMT in Rs and nonresponders (NRs) (Fig. 2A), an alteration that persisted unless a significant perturbation occurred (e.g., antibiotic use in PT-18-0032 before day 22 and PT-18-0018 before day 84). Of note, all separately collected infusates produced from individual donors were highly similar to each other (fig. S5, A and D). To evaluate intrapatient variability in both donors and recipients, we computed sample variance across all time points and all taxa in all available samples from recipients and donors (only those with at least three samples) (Fig. 2B). Variance was significantly greater in all recipients after FMT compared with that in donors (Fig. 2B), although Rs had a trend toward greater variance compared with NRs (fig. S6). We quantified differences and rate of change in microbiome communities in recipients using multidimensional Euclidean distance. Specifically, the speed of traversion, as inferred from the Euclidean distance traversed per day, trended higher in Rs than NRs (Fig. 2C). Although this parameter did not reach statistical significance (likely because of the limited sample size), the Euclidean distance still notably separated patients who achieved disease control from those who did not.

To investigate the degree of donor microbial implantation and its relationship to response in patients over time, we evaluated the acquired similarity of the recipient microbiota to the donor microbiota by measuring the Euclidian distance between donor microbial composition and every available time point of the corresponding recipients, starting from the pretreatment sample (Fig. 2D). We observed that the gut microbiota composition shifted significantly toward donor microbiota in Rs but not in NRs (Fig. 2D and fig. S7, left). FMT implantation was clearly heterogeneous in the NR group (n = 9), in which about half of the recipients had samples that were similar and the other half had samples that were dissimilar to corresponding donors (Fig. 2D, top). By contrast, the gut microbiota in Rs (n = 6) uniformly shifted toward donor samples (Fig. 2D, bottom). We also evaluated the humoral immune response to donor bacteria using recipient serum and donor feces and observed that FMT administration induced donor bacteria–specific immunoglobulin G (IgG) to a greater extent in Rs compared with NRs (Fig. 2E and fig. S8), suggesting that successful implantation and mucosal translocation of the transplanted bacteria, known to induce an IgG response against commensal bacteria, may preferentially occur in Rs (*18*).

The use of systemic antibiotics was prohibited on study; however, PT-18-0018 developed a soft-tissue infection that required antibiotics (fig. S9). During this period, pembrolizumab was withheld, although stool samples and imaging were obtained at protocol-specified intervals. Initial microbiome after FMT shifted toward the donor's microbiome with SD. After antibiotics, metagenomic data revealed pronounced changes in microbial community composition (loss of *Faecalibacterium prausnitzii*, *Alistipes* spp., and *Ruminococcaceae* spp.), which correlated with clinical progression. A second transplant from the same donor was performed nearly 1 year after initial FMT and resulted in rapid gut colonization associated with ongoing SD (fig. S9). Overall, although successful colonization after FMT did not always resensitize PD-1–refractory melanoma patients to anti–PD-1, clinical response was associated with FMT implantation and donor microbiota–specific IgG response. Furthermore, the changes of microbiome composition after FMT were rapidly disturbed by use of antibiotics, which depleted beneficial taxa (i.e., *F. prausnitzii*, *Alistipes* spp., and *Ruminococcaceae* spp.), in accordance with previously reported deleterious effects of antibiotic use with regards to anti–PD-1 in cancer patients (*12*, *19*).

To analyze the bacterial species most commonly associated with clinical benefit to FMT, we first performed statistical analyses between pre- and post-FMT samples in Rs, followed by a meta-analysis using Fisher's method to identify common features among all samples (Fig. 2G and fig. S10). Several bacterial species associated with clinical response have been previously reported (*Bifidobacterium longum*, *Colinsella aerofaciens*, and *F. prausnitzii*) (*10*, *11*). Most of the significantly enriched taxa in Rs belonged to the phyla Firmicutes (Lachnospiraceae and Ruminococcaceae families) and Actinobacteria (Bifidobacteriaceae and Coriobacteriaceae families), whereas most of the bacteria decreased in Rs belonged to phylum Bacteroidetes.

Fecal microbiota transplant and anti–PD-1 modulate immune responses peripherally and intratumorally

To evaluate the immunological effects of FMT and anti–PD-1 in treated patients, we performed multiparameter flow cytometry and single-cell RNA sequencing (scRNA-seq) analysis from peripheral blood mononuclear cells (PBMCs) and tumor samples, respectively, collected before and after treatment. Unsupervised single-cell analysis on spectral flow cytometry of PBMCs was performed at three consecutive time points before and after treatment (Fig. 3, A and B, and fig. S11, A and B) (*20*, *21*). Compared with NRs, Rs displayed higher percentages of $CD56^+CD8^+$ T cells after treatment (day 42), which represent a subset of activated $CD8^+$ T cells with higher cytolytic functions (Fig. 3B) (*22*–*24*). $CD8^+CD56^+$ T cells expressed high

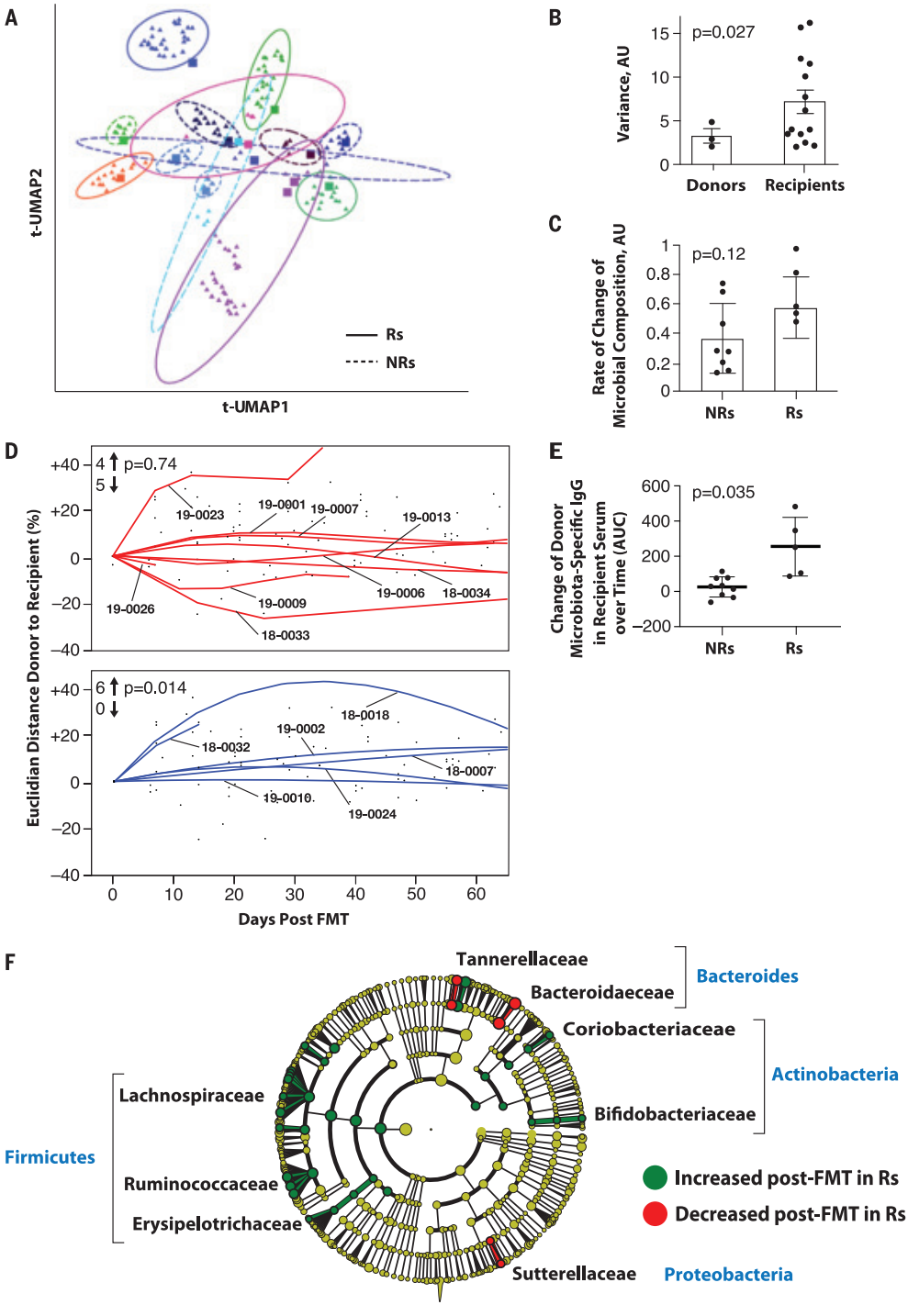

Fig. 2. Microbiome analyses before and after FMT in melanoma patients. (**A**) Dimensionality reduction using t-distributed UMAP (t-UMAP) plot of microbial taxa abundances by last known taxon of FMT recipients at different time points. Each color corresponds to a different FMT-treated patient. Pre-FMT stool samples are depicted as squares and post-FMT stool samples as triangles. Ellipses encapsulate each recipient's pre- and post-FMT samples, and the size of the ellipse spans two standard deviations from the centroid. Rs and NRs are distinguished by solid and dashed lines, respectively. PT-19-0026 (PD) is not depicted because the patient had a single post-FMT sample. (**B**) Intrapatient variance of stool samples from donors and recipients after standardization and dimensionality reduction. Donors (n = 3) and recipients (n = 15) who contributed at least three fecal samples are depicted. Data were standardized, PCA was performed, PC loading was computed, and variances of patients for every PC loading were calculated as the squared standard deviation divided by the mean and were multiplied by the PC variance contribution. Resultant values were added together to produce a combined variance number, which was compared between donors (n = 3) and recipients (n = 15) by using the nonparametric t test. AU, arbitrary units. (**C**) Rate of taxonomic change of stool samples sequentially obtained from treated patients. The rate of taxonomic change for each sample sequentially obtained from each patient was calculated by using speed of traversion (Euclidean distances traversed per day), which was calculated by dividing total Euclidean distance traveled by days. Euclidean distance was calculated by using log-transformed normalized taxonomic data from shotgun sequencing between Rs (n = 6) and NRs (n = 9) by using the nonparametric t test. (**D**) Plot of Euclidean distance over time from patients' gut microbiota to corresponding FMT donor's microbiota. To assess the efficiency of FMT engraftment, Euclidean fitted curves were generated by using points on the graph in both NRs (red, above) and Rs (blue, below). A positive percentage of each curve indicates similarity to the corresponding donor, whereas a negative percentage indicates changes in the recipient microbiota even further from the donor microbiota. Graphs were normalized by truncating at 60 days in both Rs and NRs. The chi-square test was calculated by using an even distribution as null hypothesis. (**E**) Recipient IgG response against donor microbiota induced by FMT. Donor fecal bacteria were incubated with recipient sera at 1:200 dilutions, washed and stained with phycoerythrin-labeled antihuman IgG, and fixed and analyzed on a flow cytometer. Change in IgG positivity of donor fecal bacteria for each FMT recipient was calculated in relation to the first FMT recipient serum sample available compared with the subsequent two time points up to 50 days later. Percent IgG-positive donor fecal bacteria was assessed, and area under the curve (AUC) for percent IgG-positive donor bacteria was calculated, adjusting all recipient time points relative to the baseline time point set to zero. Difference in reactivity between sera from Rs and NRs was evaluated by Student's t test. (**F**) Cladogram visualization of phylogenetic distribution of differentially abundant taxa before and after FMT in responding patients. Fisher's method for meta-analyses was used to validate statistical significance and calculate effect size of the differential abundances of taxa in Rs (fig. S10). Differentially abundant taxa are color coded on the basis of relative abundance in post- compared with pretransplant samples (green, higher; yellow, unchanged; red, lower). The most significantly associated taxa are highlighted at the family level.

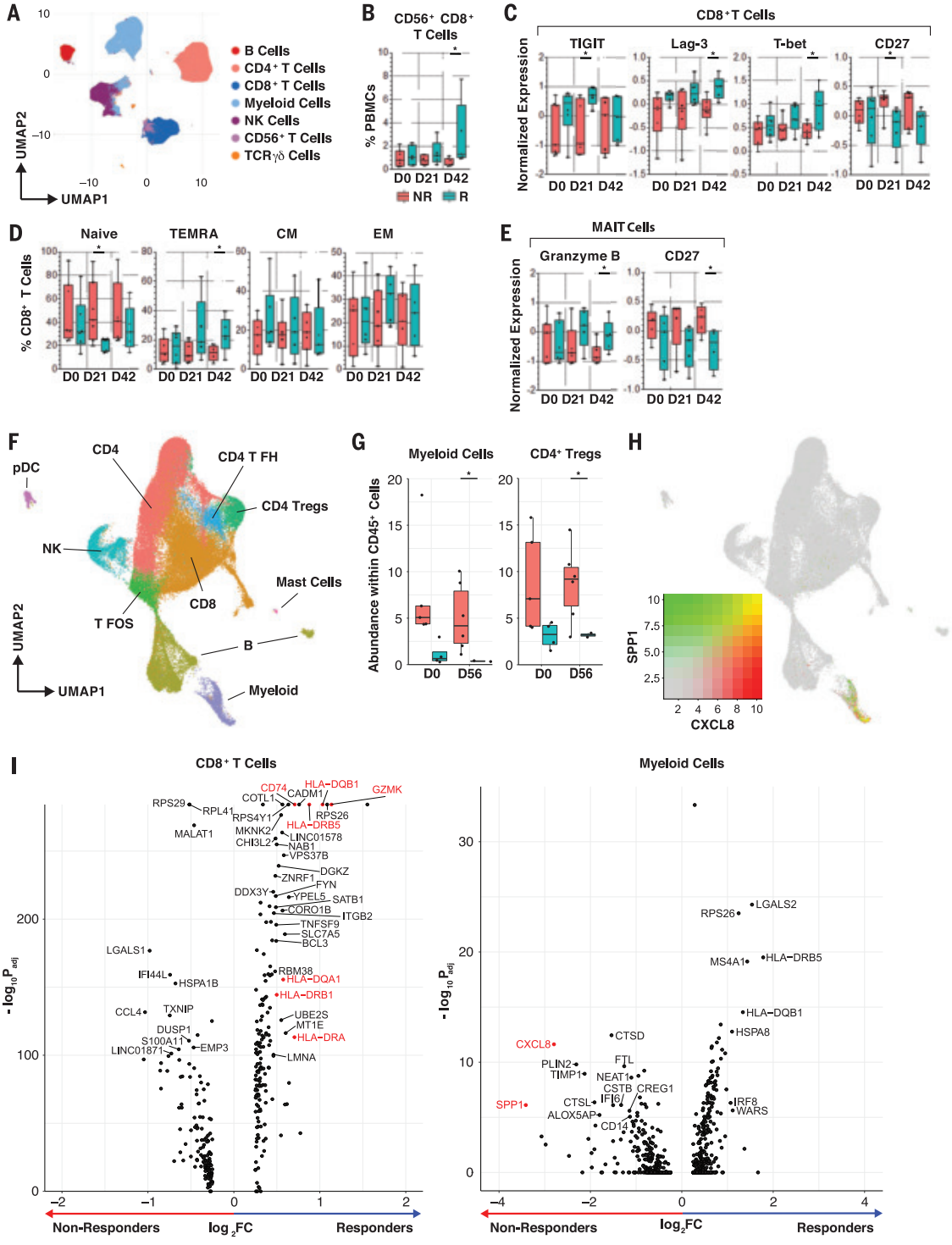

Fig. 3. Single-cell analyses of circulating and tumor-infiltrating immune cells. (**A**) Unsupervised multiparameter flow cytometry analysis of circulating immune cells. UMAP visualization of 100,000 live single cells from Rs and NRs at three time points—pretreatment (D0), day 21 (D21), and D42—from 30-parameter flow panel analysis (n = 14) after merging clusters on the basis of expression of CD3, CD4, CD8, CD19, CD14, CD56, Tγδ1, and Tγδ2. Myeloid cells were identified as lineage-negative cell clusters on the basis of presence or absence of CD14$^+$ cells. (**B**) Frequency of CD56$^+$CD8$^+$ clustered T cells in PBMCs of patients. Whisker boxes show frequencies of CD56$^+$CD8$^+$ clustered T cells in PBMCs between Rs and NRs at D0, D21, and D42. We observed a significant increase of CD56$^+$CD8$^+$ T cells in Rs at D42 using the unpaired t test. *p < 0.05. (**C** and **D**) Phenotypic analysis of circulating CD8$^+$ T cells. Whisker boxes show markers that are significantly differentially expressed (normalized mean fluorescence intensity) in CD8$^+$ T cells (C) and CCR7$^+$CD45RA$^+$-naïve, TEMRA, CCR7$^+$CD45RA$^-$ effector memory (EM), and CCR7$^-$CD45RA$^-$ central memory (CM) cells (D) between Rs (n = 5 to 6) and NRs (n = 5 to 7) at the three time points. Analysis was performed on live single CD3$^+$ and TCRgd$^-$ T cells. In Rs, we observed up-regulation of TIGIT, Lag-3, and T-bet after treatment and down-regulation of CD27 in CD8$^+$ T cells using the unpaired t test. *p < 0.05. (**E**) Phenotypic analysis of circulating MAIT cells. Whisker boxes comparing MAIT cells between Rs (n = 5 to 6) and NRs (n = 5 to 7) at the three time points. Analysis was performed on live single CD3$^+$ and TCRgd$^-$ T cells. In Rs, MAIT cells up-regulated granzyme B expression and down-regulated CD27 after treatment using the unpaired t test. *p < 0.05. (**F**) scRNA-seq analysis of tumor-infiltrating immune cells. UMAP projection of 64,000 CD45$^+$ cells that were clustered and manually identified on the basis of their expression profile. NK, natural killer; pDC, plasmacytoid dendritic cell; T FH, T follicular helper; T FOS, T cells expressing FOS; Tregs, T regulatory cells. (**G**) Whisker boxes showing the abundance of myeloid cells and CD4$^+$ Tregs in CD45$^+$ tumor-infiltrating cells. We observed decreased abundance of myeloid cells and CD4$^+$ Tregs in Rs compared with NRs using the unpaired t test. *p < 0.05. (**H**) Cell-associated expression of two markers (*CXCL8* and *SPP1*) in UMAP projection. These markers are predominantly expressed in suppressive myeloid cells. (**I**) Volcano plots showing the differences in phenotype of CD8$^+$ T cells and myeloid cells between Rs and NRs after FMT. Rs show a CD8$^+$ T phenotype with increased activation markers (*GZMK*, class II *HLA* genes, *CD74*), whereas NRs show a myeloid phenotype with an increased suppressive signature (*CXCL8* and *SPP1*) at day 56 after treatment. Adjusted p values were obtained by Wilcoxon rank sum test.

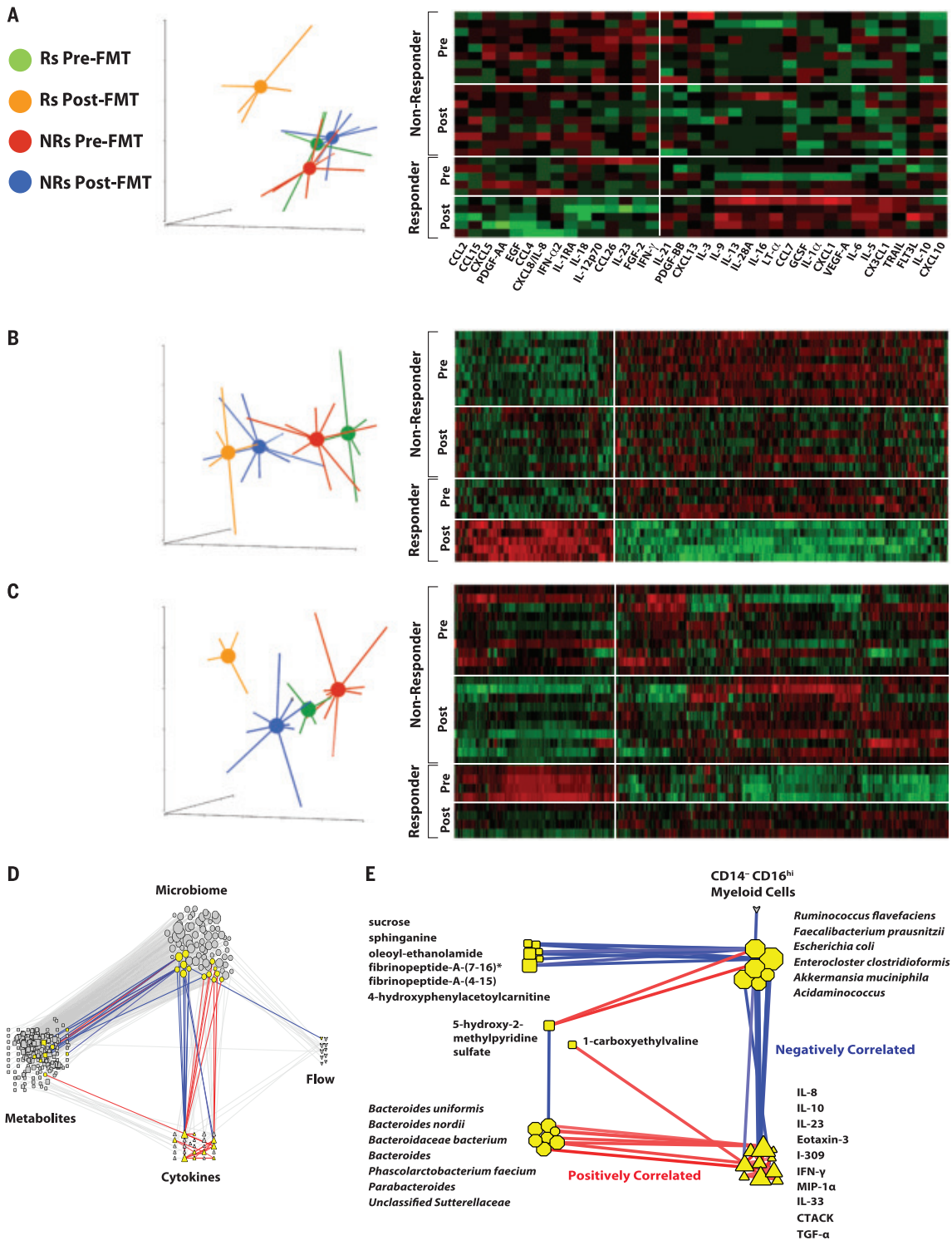

Fig. 4. Serum proteomics, metabolomics, and lipidomics signatures before and after FMT. (**A**) PCA and heatmap of serum cytokines of Rs and NRs before and after FMT. Data show that Rs after treatment (orange) separate from Rs before treatment (green), along with NRs before (red) and after (blue) treatment, as assessed by two-way analysis of variance (ANOVA; $*p < 0.05$). (**B**) PCA and heatmap of serum metabolites of Rs and NRs before and after FMT. Data show that Rs after treatment (orange) separate from Rs before treatment (green), along with NRs before (red) and after treatment (blue), as assessed by using two-way ANOVA ($q < 0.05$). (**C**) PCA and heatmap of serum lipidomics of Rs and NRs before and after FMT. Serum lipidomic analyses show that Rs after treatment (orange) distinctly clustered separately from Rs before treatment (green), along with NRs before (red) and after (blue) treatment, as assessed by using two-way ANOVA ($q < 0.05$). (**D**) Transkingdom network analysis of multi-omic data. Data for microbial (octagons), metabolites (squares), cytokines (triangles), and multiparameter flow cytometry (hearts) were analyzed to identify highly differentially abundant elements between Rs and NRs to FMT and pembrolizumab. To identify nodes (i.e., any of these four types of elements) and their groups with potential contribution to a regulatory activity, a "transkingdom" network integrating -omics data was constructed by using their correlations within the different groups (Rs or NRs, before or after FMT and pembrolizumab). Network interrogation revealed that "microbiome" and "metabolite" as well as "microbiome" and "cytokine" subnetworks were the most interconnected. We identified a dense subnetwork (module) containing the highest number of nodes from different -omics data (nodes highlighted in yellow, positively correlated edges in red, and negatively correlated edges in blue). (**E**) Subnetwork identified in (D). Network analyses established that CXCL8 (IL-8), IL-10, and CCL3 (MIP-1α) were positively correlated with organisms enriched in NRs before treatment (*Bacteroides uniformis*, *Bacteroides nordii*, *Phascolarctobacterium faecium*, etc.) and negatively correlated with organisms enriched in Rs after treatment (e.g., *Ruminococcus flavefaciens* and *F. prausnitzii*).

levels of TIGIT, CD57, 2B4, OX40, ICOS, 4-1BB, CD16, NKp46, NKp30, granzyme B, perforin, and CD103 compared with total $CD8^+$ T cells (fig. S11C). These findings are in line with previous reports in cancer patients responding to immunotherapy, including radioimmunotherapy (*25*) or PD-1 blockade (*26*). In Rs, $CD8^+$ T cells up-regulated TIGIT (day 21) as well as T-bet and LAG-3 (day 42) and down-regulated CD27 (day 21) compared with NRs at these time points (Fig. 3C). Rs exhibited lower percentages of naïve $CD8^+$ T cells (day 21) and higher percentages of terminally differentiated effector memory $CCR7^-CD45RA^+$ (TEMRA) cells (day 42) compared with NRs (Fig. 3D). These observations suggest that circulating $CD8^+$ T cells are more activated and differentiated in Rs, as previously shown in cancer patients who respond to PD-1 blockade (*27*, *28*). Mucosal-associated invariant T (MAIT) cells, which respond to bacterial antigens and inflammatory cytokines, expressed more granzyme B (day 42) and less CD27 (day 42) in Rs compared with NRs, suggesting a more differentiated phenotype (Fig. 3E). We observed no significant differences in the frequencies of circulating myeloid cell subsets before and after treatment (fig. S11, D and E). Our data show that FMT together with anti–PD-1 expanded activated $CD56^+CD8^+$ T cells and increased activation of $CD8^+$ T and MAIT cells in PBMCs of Rs.

$CD45^+$ cells were sorted from single-cell suspension obtained from tumor biopsies used for scRNA-seq analysis (10X Genomics Chromium). In total, 64,340 cells from 17 tumor samples were collected before (four Rs and five NRs) and after treatment (two Rs and six NRs). After normalization and batch-effect removal (*29*), cells were clustered into 26 groups. Each cluster was manually labeled by gene expression profile (table S4) to identify 10 distinct cell types (Fig. 3F). We observed a high frequency of myeloid cells ($p = 0.026$) and $CD4^+$ regulatory T cells ($P = 0.02$) among $CD45^+$ cells in NRs compared with Rs after treatment, whereas the other clusters did not exhibit significant changes (Fig. 3G and fig. S12). Myeloid cells expressed high levels of *CXCL8* [interleukin-8 (IL-8)] and *SPP1* (osteopontin), which increased after FMT in NRs compared with Rs, suggesting a myeloid gene signature previously associated with tumor progression (Fig. 3, H and I) (*30*, *31*). $CD8^+$ T cells up-regulated human leucocyte antigen (HLA) class II genes *CD74* and *GZMK* in Rs compared with NRs after treatment, supporting increased T cell activation at tumor sites (Fig. 3I, left). Together, our findings demonstrate that FMT and anti–PD-1 counteract myeloid-induced immunosuppression to augment $CD8^+$ T cell activation in the tumor microenvironment of Rs. Insufficient tumor tissue was available to evaluate the role of tumor mutation burden, PD-L1 expression, and interferon-γ (IFN-γ) gene expression signature in predicting clinical outcome.

Fecal microbiota transplant alters serum metabolome and cytokines in responders

To assess the impact of FMT on systemic parameters of the host and its relationship with response to therapy, we performed multi-omics analysis of serum samples, including analyses of serum cytokines and chemokines, as well as serum metabolomics and lipidomics analyses. Although Rs and NRs exhibited similar composition of serum cytokines and chemokines, Luminex multiparameter proteomics profiling showed a prominent shift in levels of circulating cytokines and chemokines in Rs, whereas NRs had little or no change [Fig. 4A, principal components analysis (PCA)]. Multiple circulating cytokines and chemokines decreased after FMT in Rs, including CCL2 (MCP1), CXCL8 (IL-8), and IL-18 that have been associated with negative outcomes to anti–PD-1 (*32*, *33*), and IL-12p70 and IFN-γ (Fig. 4A, heatmap). These latter two cytokines are usually associated with antitumor effector T cell responses. However, chronic activation of the IL-12–IFN-γ axis, as may occur in refractory patients treated with anti–PD-1, could induce a multigenic resistance program in tumor cells and could disrupt T cell response, differentiation, and exhaustion through production of nitric oxide and down-regulation of TCF1 (*34*–*36*). The cytokines and chemokines that were most prominently up-regulated are associated with follicular helper T and B cell signatures found in tertiary lymphoid structures, such as IL-21 and CXCL13 (BCP1). We also observed up-regulation of type II cytokines such as IL-5, IL-13, and IL-10; the tumor necrosis factor (TNF) family of cytokines such as TNF and TRAIL; and cytokines promoting monocyte cell migration (CX3CL1) and dendritic cell expansion (FLT3L). Altogether, our findings show that Rs down-regulated multiple circulating cytokines and chemokines associated with resistance to anti–PD-1 while up-regulating circulating biomarkers that are associated with favorable clinical outcome. In particular, Rs exhibited decreased circulating IL-8 and decreased frequencies of IL-8–producing myeloid cells in tumors. IL-8 is an immunosuppressive cytokine secreted by intratumoral and circulating myeloid cells, levels of which correlate adverse prognosis to anti–PD-1 in multiple cancers, including melanoma (*30*, *37*).

FMT and anti–PD-1 resulted in significant changes in the serum metabolomic profile of both Rs and NRs (Fig. 4B and fig. S13), although the most pronounced metabolomic shifts occurred in Rs (Fig. 4B, PCA plot). The most significant and pronounced changes after FMT affected metabolites that are usually associated with gut microbiota (*38*). Serum bile acids were increased after FMT with more efficient transformation of primary to secondary bile acids in Rs versus NRs (fig. S14). In addition, the levels of bacterial catabolism products of aromatic compounds through benzoate degradation were higher in Rs than in NRs. Some of these compounds, including hippurate, *p*-cresol sulfate, and hydrocinnamate, have been described as biomarkers of microbiome diversity and correlated with the presence of taxa associated with response to anti–PD-1 (figs. S13 and S14) (*39*). Whereas pre-FMT samples from Rs and NRs had very similar lipidomic profiles, significant changes were observed in post-FMT samples from Rs but not NRs (Fig. 4C and fig. S15), including higher levels of triacylglycerols and lower levels of monoacylglycerols and diacylglycerols, possibly reflecting microbiome-controlled differences in lipid absorption (*40*).

The gut microbiome regulates the biological signatures observed in responders

To identify causal relationships between host and microbes independent of a particular group or patient, we created a statistical model of robust interactions between the different players—"transkingdom network" analyses—using different types of -omics data (*41*, *42*). The transkingdom network consisted of 371 nodes and 819 edges, in which nodes represented individual elements of -omics datasets (metagenomic, metabolomic, lipidomic, flow cytometric, and proteomic) and edges represented positive and negative correlations between those elements (Fig. 4D). Most of the interomic edges belonged to the microbial metagenome dataset, which had a large number of positive (red) and negative (blue) network connections with the metabolomic and proteomic datasets. Microbial nodes were more densely connected to other -omics datasets than any other node, suggesting their central role in governing interomic changes after FMT and anti–PD-1. Some nodes in the transkingdom network analysis were highly interconnected, forming subnetworks. These subnetworks were identified by using the MCODE plugin of Cytoscape (*43*), and one subnetwork connected all four -omics datasets (Fig. 4E). In particular, we observed that gut bacterial commensals that were previously shown to increase (*F. prausnitzii* and *Akkermansia muciniphila*) and decrease (*Bacteroides* genus) responses to anti–PD-1 (*10*) were negatively and positively correlated with CXCL8 (IL-8), respectively.

Conclusion

Our findings show that a single FMT administered colonoscopically together with PD-1 blockade successfully colonized the gut of Rs and reprogrammed the tumor microenvironment to overcome primary resistance to anti–PD-1 in a subset of patients with advanced

melanoma. FMT shifted microbiome composition toward taxa favoring anti–PD-1 efficacy to induce clinical responses to anti–PD-1 in PD-1–refractory melanoma patients, who had an immunological ability to respond to the treatment but exhibited an unfavorable microbiota composition. Conversely, PD-1–refractory patients may not respond to FMT for various reasons, including (i) an inability to respond to the tumor regardless of microbiota composition because of the patient's immunodeficient status or lack of tumor immunogenicity, (ii) an absence of taxa needed for anti–PD-1 therapy effectiveness in the FMT, or (iii) failure of the FMT to successfully implant into the recipient and induce perturbations of host microbiota favoring anti–PD-1. Our findings warrant further investigation in larger clinical trials to better identify microbial, circulating, and intratumoral biomarkers to select patients most likely to benefit from microbiome-based therapy of melanoma. We expect that such studies will lead to the identification of a bacterial consortium capable of converting a subset of melanoma patients primary refractory to anti–PD-1 therapy into R patients.

REFERENCES AND NOTES

1. J. Larkin *et al.*, *JAMA Oncol.* **1**, 433–440 (2015).
2. A. Ribas *et al.*, *JAMA* **315**, 1600–1609 (2016).
3. C. Robert *et al.*, *N. Engl. J. Med.* **372**, 320–330 (2015).
4. C. Robert *et al.*, *Lancet Oncol.* **20**, 1239–1251 (2019).
5. C. Robert *et al.*, *N. Engl. J. Med.* **372**, 2521–2532 (2015).
6. A. Dzutsev, R. S. Goldszmid, S. Viaud, L. Zitvogel, G. Trinchieri, *Eur. J. Immunol.* **45**, 17–31 (2015).
7. B. B. Finlay *et al.*, *Nat. Rev. Immunol.* **20**, 522–528 (2020).
8. R. S. Goldszmid *et al.*, *Cancer Immunol. Res.* **3**, 103–109 (2015).
9. H. M. Zarour, *Clin. Cancer Res.* **22**, 1856–1864 (2016).
10. V. Gopalakrishnan *et al.*, *Science* **359**, 97–103 (2018).
11. V. Matson *et al.*, *Science* **359**, 104–108 (2018).
12. B. Routy *et al.*, *Science* **359**, 91–97 (2018).
13. A. E. Frankel *et al.*, *Neoplasia* **19**, 848–855 (2017).
14. B. A. Peters *et al.*, *Genome Med.* **11**, 61 (2019).
15. E. A. Eisenhauer *et al.*, *Eur. J. Cancer* **45**, 228–247 (2009).
16. H. M. Kluger *et al.*, *J. Immunother. Cancer* **8**, e000398 (2020).
17. A. Ribas, J. M. Kirkwood, K. T. Flaherty, *Lancet Oncol.* **19**, e219 (2018).
18. M. Y. Zeng *et al.*, *Immunity* **44**, 647–658 (2016).
19. D. J. Pinato *et al.*, *JAMA Oncol.* **5**, 1774–1778 (2019).
20. C. Krieg *et al.*, *Nat. Med.* **24**, 144–153 (2018).
21. M. Nowicka *et al.*, *F1000Res.* **6**, 748 (2017).
22. M. J. Pittet, D. E. Speiser, D. Valmori, J. C. Cerottini, P. Romero, *J. Immunol.* **164**, 1148–1152 (2000).
23. T. Ohkawa *et al.*, *Immunology* **103**, 281–290 (2001).
24. S. Guia *et al.*, *Blood* **111**, 5008–5016 (2008).
25. K. Hasumi, Y. Aoki, R. Wantanabe, D. L. Mann, *Oncolmmunology* **2**, e26381 (2013).
26. A. Ribas *et al.*, *Cancer Immunol. Res.* **4**, 194–203 (2016).
27. A. O. Kamphorst *et al.*, *Proc. Natl. Acad. Sci. U.S.A.* **114**, 4993–4998 (2017).
28. A. Kunert *et al.*, *J. Immunother. Cancer* **7**, 149 (2019).
29. T. Stuart *et al.*, *Cell* **177**, 1888–1902.e21 (2019).
30. K. A. Schalper *et al.*, *Nat. Med.* **26**, 688–692 (2020).
31. H. Alshetaiwi *et al.*, *Sci. Immunol.* **5**, eaay6017 (2020).
32. B. Gok Yavuz *et al.*, *Sci. Rep.* **9**, 3172 (2019).
33. M. Terme *et al.*, *Cancer Res.* **71**, 5393–5399 (2011).
34. J. L. Benci *et al.*, *Cell* **167**, 1540–1554.e12 (2016).
35. M. Danilo, V. Chennupati, J. G. Silva, S. Siegert, W. Held, *Cell Rep.* **22**, 2107–2117 (2018).
36. H. K. Koblish, C. A. Hunter, M. Wysocka, G. Trinchieri, W. M. Lee, *J. Exp. Med.* **188**, 1603–1610 (1998).
37. M. F. Sanmamed *et al.*, *Ann. Oncol.* **28**, 1988–1995 (2017).
38. P. Vernocchi, F. Del Chierico, L. Putignani, *Front. Microbiol.* **7**, 1144 (2016).
39. T. Pallister *et al.*, *Sci. Rep.* **7**, 13670 (2017).
40. K. Martinez-Guryn *et al.*, *Cell Host Microbe* **23**, 458–469.e5 (2018).
41. R. R. Rodrigues, N. Shulzhenko, A. Morgun, *Methods Mol. Biol.* **1849**, 227–242 (2018).
42. A. Yambartsev *et al.*, *Biol. Direct* **11**, 52 (2016).
43. P. Shannon *et al.*, *Genome Res.* **13**, 2498–2504 (2003).

ACKNOWLEDGMENTS

We acknowledge all patients and families affected by metastatic melanoma. We acknowledge the input of E. Chu for design and conduct of this study. **Funding:** The clinical trial (NCT03341143) was supported by a research contract from Merck MSD to D.D. D.D. is supported by the Melanoma Breakthrough Foundation Breakthrough Consortium. H.M.Z. is supported by the National Cancer Institute (NCI) of the National Institutes of Health (NIH) (award numbers R01 CA228181 and R01 CA222203) and the James W. and Frances G. McGlothlin Chair in Melanoma Immunotherapy Research. Work of the UPMC Hillman Cancer Center Microbiome Shared Facility and Cytometry Facility is supported by the NIH NCI Comprehensive Cancer Center Support CORE grant (P30 CA047904). This research was supported in part by the University of Pittsburgh Center for Research Computing and Unified Flow Cytometry Core of the University of Pittsburgh's Department of Immunology through the resources provided. This work was supported in part by the Intramural Research Program of the NIH, NIAID, and NCI Center for Cancer Research. **Author contributions:** Conception and design: D.D., A.K.D., G.T., and H.M.Z. Administrative support: O.P., S.J.E., and A.R. Provision of study materials or patients: D.D., Y.G.N., and J.M.K. Colonoscopic administration of FMT: M.B.S. and H.M.D. Independent radiographic review: A.A.B. Collection of data: D.D., A.K.D., J.A.M., R.N.D., C.M., Q.D., O.P., B.Z., S.Z., J.H.B., M.V., A.M.C., M.R.F., S.P., R.G.F.C., A.K.B., and I.V.-C. Assembly and interpretation of data: D.D., A.K.D., J.A.M., R.R.R., J.C., R.M.M., A.M., H.W., Y.B., G.T., and H.M.Z. Manuscript writing: D.D., A.K.D., J.A.M., R.R.R., J.C., R.M.M., G.T., and H.M.Z. Final approval of manuscript: All authors. Accountable for all aspects of the work: D.D., A.K.D., G.T., and H.M.Z. **Competing interests:** D.D. reports the following disclosures: Merck, Bristol-Myers Squibb, Checkmate Pharmaceuticals, CellSight Technologies, MedPacto, and GlaxoSmithKline (research support); Array Biopharma, Checkmate Pharmaceuticals, Incyte, Immunocore, and Merck; Shionogi (consulting); and Vedanta Biosciences (scientific advisory board). Y.G.N. reports the following disclosures: Merck, Pfizer, and Bristol-Myers Squibb (research support). J.M.K. reports the following disclosures: Amgen, Bristol-Myers Squibb, Castle Biosciences, Checkmate Pharmaceuticals, Immunocore LLC, Iovance, and Novartis (research support) and Amgen, Bristol-Myers Squibb, Checkmate Pharmaceuticals, and Novartis (consulting). H.M.Z. reports the following disclosures: Bristol-Myers Squibb, Checkmate Pharmaceuticals, and GlaxoSmithKline (research support) and Bristol-Myers Squibb, Checkmate Pharmaceuticals, GlaxoSmithKline, and Vedanta (consulting). The other authors declare no competing interests. **Data and materials availability:** The data reported in this paper are tabulated in the main text and supplementary materials. Sequencing data and metadata have been deposited with the BioProject database, ID PRJNA672867 (www.ncbi.nlm.nih.gov/bioproject/672867).

SUPPLEMENTARY MATERIALS

science.sciencemag.org/content/371/6529/595/suppl/DC1
Materials and Methods
Figs. S1 to S15
Tables S1 to S4
References (*44*–*51*)
MDAR Reproducibility Checklist

19 October 2020; accepted 30 November 2020
10.1126/science.abf3363

REPORTS

CLINICAL TRIALS

Fecal microbiota transplant promotes response in immunotherapy-refractory melanoma patients

Erez N. Baruch[1,2]*†, Ilan Youngster[3,4], Guy Ben-Betzalel[1], Rona Ortenberg[1], Adi Lahat[5], Lior Katz[6], Katerina Adler[7], Daniela Dick-Necula[8], Stephen Raskin[4,9], Naamah Bloch[10], Daniil Rotin[8], Liat Anafi[8], Camila Avivi[8], Jenny Melnichenko[1], Yael Steinberg-Silman[1], Ronac Mamtani[11], Hagit Harati[1], Nethanel Asher[1], Ronnie Shapira-Frommer[1], Tal Brosh-Nissimov[12], Yael Eshet[4,8,13], Shira Ben-Simon[10], Oren Ziv[10], Md Abdul Wadud Khan[14], Moran Amit[15], Nadim J. Ajami[14], Iris Barshack[4,8], Jacob Schachter[1,4], Jennifer A. Wargo[14,16], Omry Koren[10], Gal Markel[1,2,17]*‡, Ben Boursi[4,18,19]‡

The gut microbiome has been shown to influence the response of tumors to anti–PD-1 (programmed cell death–1) immunotherapy in preclinical mouse models and observational patient cohorts. However, modulation of gut microbiota in cancer patients has not been investigated in clinical trials. In this study, we performed a phase 1 clinical trial to assess the safety and feasibility of fecal microbiota transplantation (FMT) and reinduction of anti–PD-1 immunotherapy in 10 patients with anti–PD-1–refractory metastatic melanoma. We observed clinical responses in three patients, including two partial responses and one complete response. Notably, treatment with FMT was associated with favorable changes in immune cell infiltrates and gene expression profiles in both the gut lamina propria and the tumor microenvironment. These early findings have implications for modulating the gut microbiota in cancer treatment.

Immunotherapy to inhibit the programmed cell death–1 (PD-1) checkpoint protein in metastatic melanoma patients has demonstrated durable complete response (CR) rates of 10 to 20% (*1*). However, most of the patients do not respond to PD-1 blockade, and many of the partially responding patients eventually progress (*1*). Extensive research efforts have been undertaken to overcome the resistance to anti–PD-1 therapy. One of the most promising leads involves modulation of the gut microbiota (*2*–*4*), which has been

shown to have a profound effect on the development and function of the immune system (*5*). Although no specific bacterial taxa have been consistently associated with clinical response to immunotherapy (*6*), fecal microbiota transplantation (FMT)—which transfers the entire gut microbiota from one host to another—has demonstrated promising results in preclinical models (*2*–*4*). Compared with mice that received FMT from melanoma patients not responding to anti–PD-1 therapy, mice that received FMT from responders demonstrated increased intratumoral $CD8^+$ T cell infiltration and enhanced overall effectiveness of anti–PD-1 therapy (*2*, *3*). On the basis of these data, we designed a phase 1 clinical trial (NCT03353402) to assess the safety, feasibility, and immune cell impact of FMT and reinduction of anti–PD-1 immunotherapy in patients with refractory metastatic melanoma.

The trial included two FMT donors who had previously been treated with anti–PD-1 monotherapy for metastatic melanoma and had achieved a CR for at least 1 year (table S1 and materials and methods). Patients were considered eligible FMT recipients if they had a diagnosis of metastatic melanoma and had progressed on at least one line of anti–PD-1 therapy. Recipients harboring a BRAF-V600E mutation must have also progressed on BRAF-targeted therapy. As part of the trial's protocol, recipients underwent an initial native microbiota depletion phase in which they were administered with orally ingested antibiotics (vancomycin and neomycin) for 72 hours (Fig. 1A). FMT was then performed by means of both a colonoscopy (protocol day 0) and the administration of oral stool capsules followed by reinduction of anti–PD-1 therapy (nivolumab). Six combined treatment cycles composed of anti–PD-1 infusions (nivolumab at standard dose) and additional stool capsules (maintenance FMT) were administered every 14 days until day 90. Each recipient underwent positron emission tomography combined with computed tomography (PET-CT) imaging before the trial and on day 65. Response to treatment was defined as an objective tumor regression per imaging according to iRECIST criteria (response evaluation criteria in solid tumors, modified for immunotherapy) (*7*). Objective responders and recipients who demonstrated a clinical benefit to the treatment continued anti–PD-1 beyond day 90 as monotherapy and underwent consecutive PET-CTs in intervals of 6 to 8 weeks until disease progression.

Correlative studies included stool, gut, and tumor analyses (see materials and methods). 16*S* ribosomal RNA (rRNA) gene and metagenomics sequencing were conducted on stool samples that were collected from recipients up to 1 week before the native microbiota depletion phase (defined as pretreatment) and on stool samples collected on days 7, 31, and 65. Donor stool samples were collected during the fecal donation period. Gut and tumor biopsies were collected pretreatment and at days 31 and 70, respectively. Infiltration and activity of immune cells in the tissue samples were assessed using immunohistochemical (IHC) and bulk RNA sequencing (RNA-seq). In cases where no specific gene differed in a statistically significant manner, gene set testing was conducted using the Gene Ontology (GO) dataset. Recipient 2 refused to undergo posttreatment biopsies and withdrew consent immediately after the day-65 imaging assessment, leaving nine available recipients for gut and tumor tissue assessment.

Ten recipients with confirmed progression on anti–PD-1 therapy were enrolled and treated between June 2018 and March 2019 (Table 1 and table S2). Recipients were assigned to receive FMT from one of the two available donors, alternating between donor 1 and donor 2. The median recipient age was 66 years [interquartile range (IQR), 49 to 68 years], the majority were males (70%), and the median elapsed time from the last previous dose of anti–PD-1 to the first dose of the current trial was 113 days (IQR, 59 to 183 days). The most common PD-L1 expression category in pretreatment tumor biopsies was ≥5%. This expression category was noted in four recipients, whereas three recipients had no pretreatment PD-L1 expression (table S2). In terms of safety results, the only observed FMT-related adverse event (AE) was mild bloating between days 3 and 15 in one recipient. Several mild (grade 1) immune-related adverse events (irAEs) were observed, mainly arthralgia (table S3). No moderate-to-severe irAEs (grades 2 to 4) were observed, although five recipients had developed such irAEs during their previous anti–PD-1 treatment lines (table S4).

Objective responses to treatment were demonstrated by three recipients, all of them from the donor 1 group: Recipient 3 achieved a CR, and recipients 5 and 7 achieved partial responses (Fig. 1B, Table 1, and table S5). All responders crossed the progression-free survival milestone of 6 months. Both recipients 3 and 5 demonstrated an initial increase in their metastases size followed by regression (Fig. 1, B and C, and fig. S1). This phenomenon is known as pseudoprogression (*8*) because the increment in metastasis radiological volumes is not caused by tumor proliferation but rather by an influx of antitumoral immune cells into the tumor. Recipient 1 (donor 1 group) demonstrated an initial mixed response with regression of some of lesions, but, overall, the disease had progressed (fig. S2).

Stool 16*S* rRNA gene sequencing analysis demonstrated that posttreatment gut microbiota composition of all recipients significantly differed from their baseline [β-diversity, unweighted UniFrac, $P = 0.02$; false discovery rate (FDR) = 0.05; Fig. 2A and figs. S3 and S4]. There was no statistically significant difference between the pretreatment microbiota composition of recipients from the donor 1 group and those of the donor 2 group ($P = 0.36$; FDR = 0.45). However, posttreatment microbiota compositions of the donor 1–group recipients differed from those of the donor 2 group ($P = 0.001$; FDR = 0.003; Fig. 2A). Donor 2 had a higher microbiota richness (α-diversity, Faith's phylogenetic diversity) compared with donor 1. Accordingly, despite similar richness in the pretreatment compositions ($P = 0.60$; FDR = 0.77), posttreatment compositions of the donor 2 group demonstrated higher richness than those of the donor 1 group ($P < 0.001$; FDR = 0.001; fig. S5). Metagenomic sequencing was used to identify specific taxa and functional pathways that differed between the trial's groups. Overall comparison between recipient pre- and posttreatment microbiota compositions [analysis of composition of microbiomes (ANCOM) test] showed that posttreatment compositions had a higher relative abundance of the immunotherapy-favorable *Veillonellaceae* family (*3*) and a lower relative abundance of *Bifidobacterium bifidum*, which was reported

[1]The Ella Lemelbaum Institute for Immuno-Oncology, Sheba Medical Center, Tel-HaShomer, Israel. [2]Department of Clinical Immunology and Microbiology, Sackler Faculty of Medicine, Tel Aviv University, Tel Aviv, Israel. [3]Pediatric Division and the Microbiome Research Center, Shamir (Assaf Harofeh) Medical Center, Be'er Ya'akov, Israel. [4]School of Medicine, Sackler Faculty of Medicine, Tel Aviv University, Tel Aviv, Israel. [5]Department of Gastroenterology, Sheba Medical Center, Tel HaShomer, Israel. [6]Department of Gastroenterology, Hadassah Medical Center, Jerusalem, Israel. [7]Department of Mathematics, Bar Ilan University, Ramat Gan, Israel. [8]Institute of Pathology, Sheba Medical Center, Tel-HaShomer, Israel. [9]Radiological Institute, Sheba Medical Center, Tel HaShomer, Israel. [10]Azrieli Faculty of Medicine, Bar Ilan University, Safed, Israel. [11]Division of Hematology and Oncology, University of Pennsylvania, Philadelphia, PA, USA. [12]Infectious Diseases Unit, Assuta Ashdod University Hospital, Ashdod, Israel. [13]Department of Nuclear Medicine, Sheba Medical Center, Tel HaShomer, Israel. [14]Program for Innovative Microbiome and Translational Research, Department of Genomic Medicine, The University of Texas MD Anderson Cancer Center, Houston, TX, USA. [15]Department of Head and Neck Surgery, The University of Texas MD Anderson Cancer Center, Houston, TX, USA. [16]Department of Surgical Oncology, The University of Texas MD Anderson Cancer Center, Houston, TX, USA. [17]Talpiot Medical Leadership Program, Sheba Medical Center, Tel HaShomer, Israel. [18]Center for Clinical Epidemiology and Biostatistics, University of Pennsylvania, Philadelphia, PA, USA. [19]Department of Oncology, Sheba Medical Center, Tel HaShomer, Israel.

***Corresponding author. Email: erezbaruch@mail.tau.ac.il (E.N.B.); gal.markel@sheba.health.gov.il (G.M.)** †Present addresses: Program for Innovative Microbiome and Translational Research, Department of Genomic Medicine, The University of Texas MD Anderson Cancer Center, Houston, TX, USA, and Department of Internal Medicine, McGovern Medical School at The University of Texas Health Science Center, Houston, TX, USA. ‡These authors contributed equally to this work.

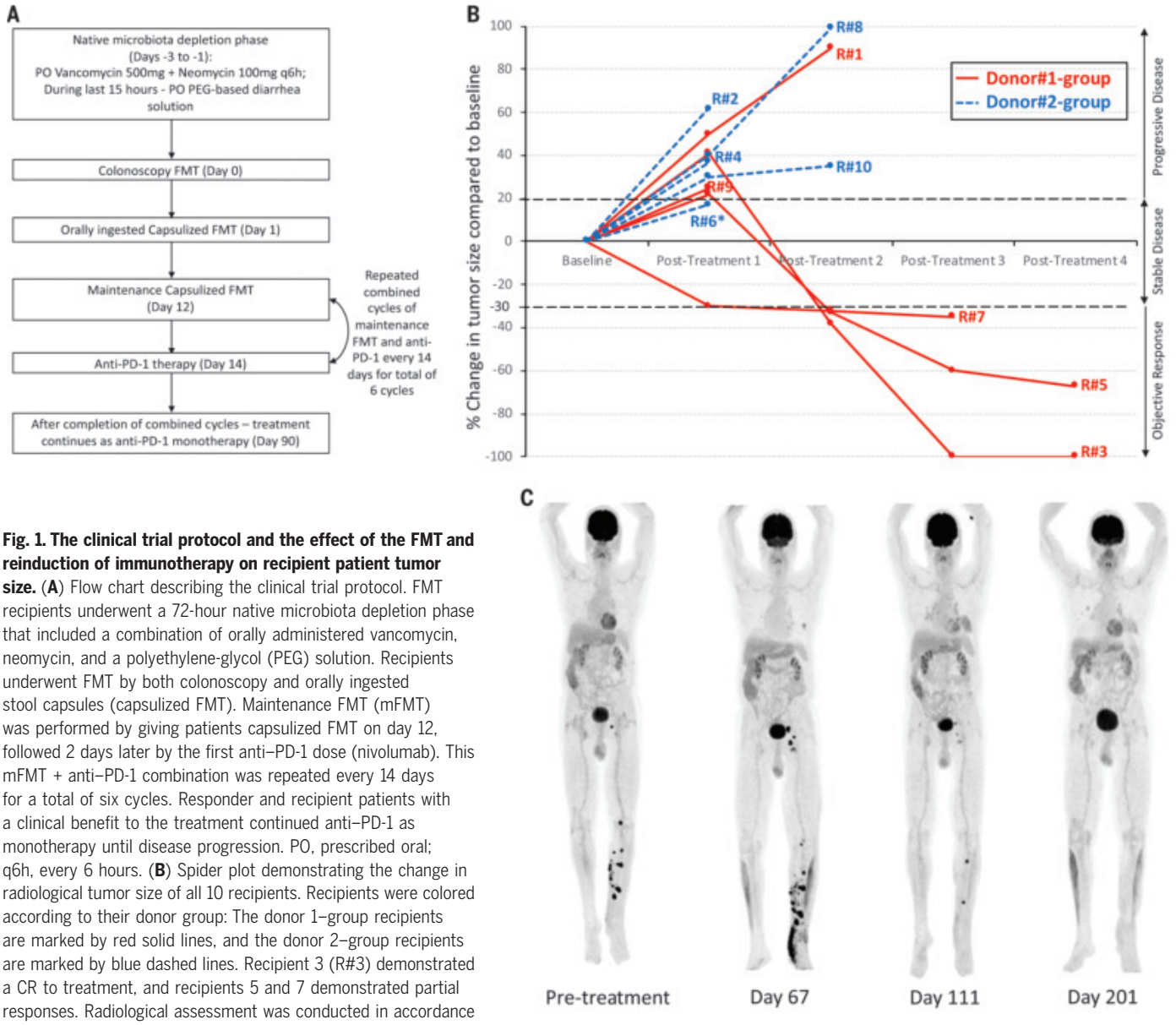

Fig. 1. The clinical trial protocol and the effect of the FMT and reinduction of immunotherapy on recipient patient tumor size. (**A**) Flow chart describing the clinical trial protocol. FMT recipients underwent a 72-hour native microbiota depletion phase that included a combination of orally administered vancomycin, neomycin, and a polyethylene-glycol (PEG) solution. Recipients underwent FMT by both colonoscopy and orally ingested stool capsules (capsulized FMT). Maintenance FMT (mFMT) was performed by giving patients capsulized FMT on day 12, followed 2 days later by the first anti–PD-1 dose (nivolumab). This mFMT + anti–PD-1 combination was repeated every 14 days for a total of six cycles. Responder and recipient patients with a clinical benefit to the treatment continued anti–PD-1 as monotherapy until disease progression. PO, prescribed oral; q6h, every 6 hours. (**B**) Spider plot demonstrating the change in radiological tumor size of all 10 recipients. Recipients were colored according to their donor group: The donor 1–group recipients are marked by red solid lines, and the donor 2–group recipients are marked by blue dashed lines. Recipient 3 (R#3) demonstrated a CR to treatment, and recipients 5 and 7 demonstrated partial responses. Radiological assessment was conducted in accordance with the immune response evaluation criteria in solid tumors (iRECIST) (*7*) and included measurements of target and new target lesions. The asterisk indicates that recipient 6 was excluded from the trial after the first posttreatment imaging study because of unstable metastatic brain disease (hemorrhage into a brain metastasis that was known before inclusion in the trial). (**C**) Recipient 3 PET-CT imaging. The metastatic lesions, represented as black emission areas, were concentrated in the left leg and groin (inguinal). As a result of the treatment, the metastases had initially increased in size and new lesions appeared (day 67). However, a complete resolution of all lesions was demonstrated in consecutive follow-up imaging studies. The initial tumor size increment was likely cased by the substantial increase in $CD8^+$ T cell intratumoral infiltration that was observed in this patient (14 cells/mm^2 pretreatment versus 736 cells/mm^2 on day 70; see below, Fig. 3, E to G), a phenomenon known as pseudoprogression (*8*).

to promote immune tolerance via regulatory T cells (*9*) (figs. S6 and S7). Both donors had previously reported immunotherapy-favorable features (fig. S8 and table S6) such as high relative abundances of *Lachnospiraceae* (both donors), *Veillonellaceae* (donor 1), and *Ruminococcaceae* (donor 2) (fig. S8) (*2*–*4*). Comparison of posttreatment recipient microbiota compositions by their assigned donors demonstrated that the donor 1 group was characterized by a higher relative abundance of taxa like *Bifidobacterium adolescentis* (Fig. 2B), whereas the donor 2 group had a high relative abundance of taxa like *Ruminococcus bromii* (table S7)—both of which have been previously described as immunotherapy favorable (*2*, *3*). The pretreatment microbiota compositions of the three responding patients (recipients 3, 5, and 7) did not differ from the pretreatment microbiota compositions of the rest of the cohort. When the responders' posttreatment compositions were compared with the posttreatment compositions of the other two nonresponders from the donor 1 group (recipients 1 and 9), four taxa differed in a statistically significant manner (fig. S9A). The responders had a higher relative abundance of *Enterococcaceae*, *Enterococcus*, and *Streptococcus australis* and a lower relative abundance of *Veillonella atypica*. However, when the abundance of these specific taxa was assessed in the entire patient cohort (fig. S9B), there were some nonresponders and even pretreatment

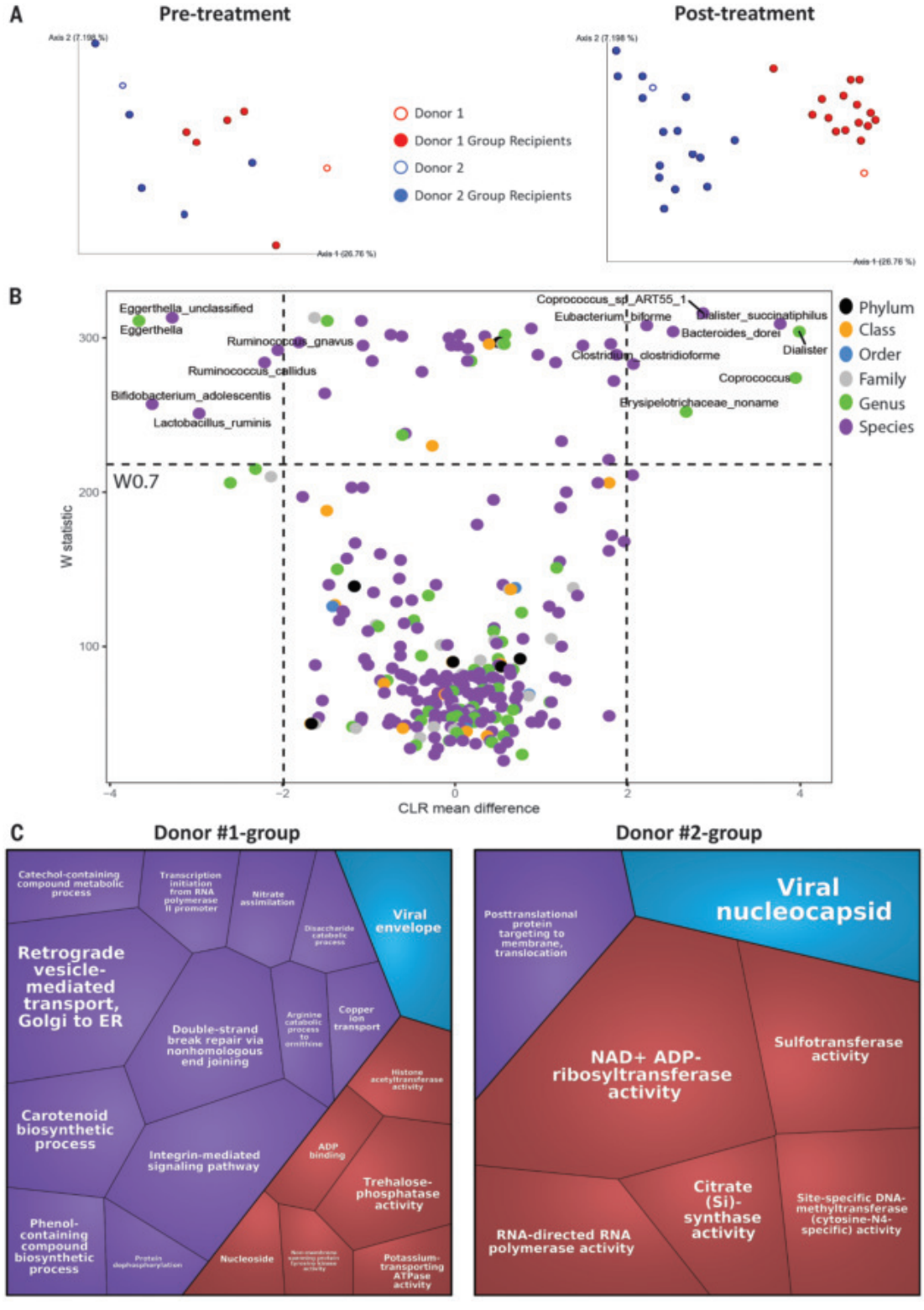

Fig. 2. The effect of FMT on gut microbiota composition in metastatic melanoma recipient patients. (**A**) Principal components analysis (PCA) plots of patient gut microbiota compositions based on stool 16S rRNA gene sequencing dissimilarity test (β-diversity, unweighted UniFrac). The distance between samples on the plot represents their dissimilarity—the greater the distance between two samples, the higher the dissimilarity of their composition. Recipient patients were grouped according to their donors: Those who received FMT implants from donor 1 are colored in red, and those who received implants from donor 2 are colored in blue. The plots demonstrate no difference between the pretreatment recipient compositions of the two donor groups (FDR = 0.45), in contrast to a clear post-treatment donor-based division (FDR = 0.003). (**B**) A volcano plot based on the ANCOM test. The plot compares the relative abundance of specific taxa between the donor 1 group (negative *x* axis) and the donor 2 group (positive *x* axis). Each donor group was composed of posttreatment samples of the relevant recipients and the donor sample. Taxa that differed between the groups with FDR $q \leq 0.05$ are presented above the horizontal dashed line. The center log transformation (CLR) mean difference on the *x* axis is an ANCOM calculation that is used to determine compositional differences in microbial communities. For convenience, only taxa with a mean difference above an absolute value of 2 are labeled with text. The full list of taxa that significantly differed between the two donor groups is detailed in table S7. (**C**) Voronoi treemap plots of microbiota GO gene sets that were enriched among the different donor groups' microbiotas. The abundance of gene sets was compared across donors and posttreatment recipient samples. Gene sets that showed statistically significant differences between the donor 1 group and the donor 2 group and had a $\log_2$ differential abundance >1 (table S8) are plotted. The polygon size represents the scale of the $\log_2$ abundance difference—a bigger polygon represents a more abundant pathway. The GO gene sets are also colored according to their GO category: purple for biological processes, light blue for cellular components, and red for molecular functions. ER, endoplasmic reticulum; ADP, adenosine 5′-diphosphate; ATPase, adenosine triphosphatase; NAD+, oxidized nicotinamide adenine dinucleotide.

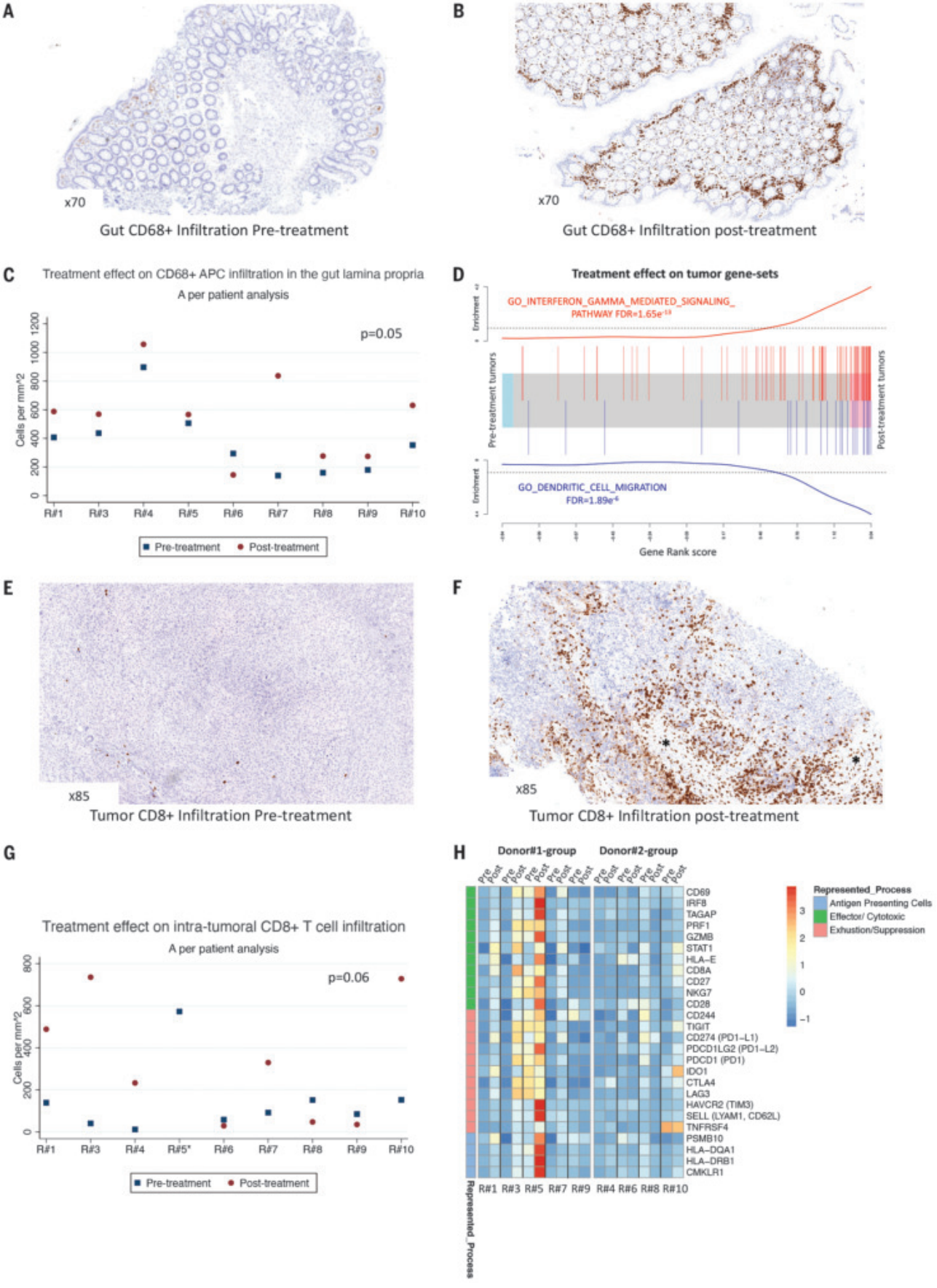
A
x70
Gut CD68+ Infiltration Pre-treatment
B
x70
Gut CD68+ Infiltration post-treatment
C
Treatment effect on CD68+ APC infiltration in the gut lamina propria
A per patient analysis
p=0.05
Cells per mm^2
R#1 R#3 R#4 R#5 R#6 R#7 R#8 R#9 R#10
Pre-treatment
Post-treatment
D
Treatment effect on tumor gene-sets
GO_INTERFERON_GAMMA_MEDIATED_SIGNALING_PATHWAY FDR=1.65e-13
Enrichment
Pre-treatment tumors
Post-treatment tumors
GO_DENDRITIC_CELL_MIGRATION FDR=1.89e-6
Gene Rank score
E
x85
Tumor CD8+ Infiltration Pre-treatment
F
x85
Tumor CD8+ Infiltration post-treatment
G
Treatment effect on intra-tumoral CD8+ T cell infiltration
A per patient analysis
p=0.06
Cells per mm^2
R#1 R#3 R#4 R#5* R#6 R#7 R#8 R#9 R#10
Pre-treatment
Post-treatment
H
Donor#1-group
Donor#2-group
Pre Post
CD69
IRF8
TAGAP
PRF1
GZMB
STAT1
HLA-E
CD8A
CD27
NKG7
CD28
CD244
TIGIT
CD274 (PD1-L1)
PDCD1LG2 (PD1-L2)
PDCD1 (PD1)
IDO1
CTLA4
LAG3
HAVCR2 (TIM3)
SELL (LYAM1, CD62L)
TNFRSF4
PSMB10
HLA-DQA1
HLA-DRB1
CMKLR1
R#1 R#3 R#5 R#7 R#9 R#4 R#6 R#8 R#10
Represented_Process
Represented_Process
Antigen Presenting Cells
Effector/ Cytotoxic
Exhustion/Suppression
3
2
1
0
−1

Fig. 3. The effect of FMT and reinduction of immunotherapy on immune activity in the gut and in the tumor microenvironment of metastatic melanoma recipient patients. (**A**) IHC staining of CD68, representing APCs, conducted on pretreatment sigmoid colon biopsies of recipient 7. (**B**) IHC staining of $CD68^+$ cells conducted on the posttreatment (day 31) sigmoid colon biopsy of recipient 7, which demonstrates a clear increase in $CD68^+$ cell infiltration in the gut lamina propria. This infiltration was especially prominent in the subepithelial area, which is physically closer to the gut. (**C**) An image analysis algorithm was used to quantify the number of $CD68^+$ APCs within the gut lamina propria of each recipient patient. A posttreatment increment in $CD68^+$ cell infiltration was demonstrated in most recipients ($P = 0.05$). (**D**) A barcode plot of gene set enrichment among tumor samples. Each bar represents a single gene out of the entire gene set. The plot demonstrates the up-regulation of APC- and T cell–related gene sets among posttreatment tumor samples. The full list of enriched gene sets is detailed in table S12. (**E**) IHC staining of CD8, representing cytotoxic T cells, conducted on pretreatment tumor metastasis (subcutaneous, left leg) of recipient 3. (**F**) IHC staining of $CD8^+$ T cells conducted on posttreatment biopsy from another subcutaneous metastasis in the left leg of recipient 3, demonstrating a clear increase in intratumoral $CD8^+$ T cell infiltration and immune-induced tumor necrosis (marked by asterisks). (**G**) An image analysis algorithm was used to quantify the number of $CD8^+$-stained T cells within viable tumor tissue for each remote tumor metastasis biopsy. Posttreatment tumor biopsies were preferably taken from the same metastasis used for the pretreatment biopsy or from another metastasis at the same organ. Five recipient patients had increased their intratumoral $CD8^+$ T cell infiltration in posttreatment biopsies ($P = 0.06$). The asterisk indicates that recipient 5 achieved a near-pathological CR (<1% viable tumor), and hence their posttreatment $CD8^+$ infiltration could not be accurately assessed. (**H**) Heatmap of tumor immune gene expression. The heatmap illustrates expression dynamics before and after treatment across three representative immune processes—antitumoral effector activity, suppression-exhaustion activity, and APCs activity-abundance. Only members of the donor 1 group demonstrated a posttreatment up-regulation of effector T cell response. Recipient 10 demonstrated a posttreatment up-regulation of the immune checkpoints IDO-1 and TIGIT without an effector response. Scale represents the *z*-score of gene counts.

samples with similar dynamics. Hence, no clear association between those taxa and clinical response to therapy was established. Functional metabolic data were based on annotation of genes to the MetaCyc database (direct measurements of metabolite levels were not conducted). The functional metabolic data demonstrated that the donor 1 group up-regulated the lactose and galactose degradation I pathway [log-fold change (logFC) = 1; FDR = 0.015], whereas the donor 2 group up-regulated the formaldehyde assimilation II (logFC = 2.2; FDR = 3.93×10^{-6}), the formaldehyde oxidation I (logFC = 2.4; FDR = 0.001), and the creatinine degradation I (logFC = 1.4; FDR = 0.014) pathways. Metagenomics GO gene sets that significantly differed between the microbiota of the two donor groups are illustrated in Fig. 2C (table S8). Comparison between the posttreatment microbiota composition of the responding patients (recipients 3, 5, and 7) and the other two nonresponding patients (recipients 1 and 9) among the donor 1 group showed no significant functional or metabolic differences.

Gut sample analysis of all available FMT-recipient patients demonstrated a posttreatment up-regulation of gene sets that were related to the presentation of peptides by antigen-presenting cells (APCs) via major histocompatibility complex (MHC) class I and interleukin-1–mediated signaling (FDR = 0.014 and 0.038, respectively; table S9). Analysis per donor group demonstrated that the donor 1–group recipients up-regulated additional gene sets related to APC activity, innate immunity, and interleukin-12 (table S10). By contrast, the donor 2–group recipients did not up-regulate any immune-related gene sets (table S11). Per-patient analysis demonstrated an increased lamina propria infiltration of $CD68^+$ cells, representing APCs, from an overall pretreatment median of 353 to 569 cells/mm^2 posttreatment ($P = 0.05$; Fig. 3, A to C, and fig. S10). The $CD68^+$ infiltration was concentrated in the subepithelial area, where the proximity to the gut lumen is the highest. All available recipients increased the posttreatment $CD68^+$ infiltration except for recipient 6 (donor 2 group, nonresponder patient). Notably, gut sample analysis did not demonstrate a statistically significant increase in T cell infiltration in the gut lamina propria (fig. S11) or T cell–related gene set enrichment.

Tumor sample analysis of all available recipients demonstrated posttreatment up-regulation of multiple immune-related gene sets (Fig. 3D and table S12), such as interferon-γ–mediated signaling pathway (FDR = 1.65×10^{-13}), T cell activation (FDR = 3.27×10^{-12}), MHC class II protein complex (FDR = 9.31×10^{-13}), dendritic cell differentiation (FDR = 5.15×10^{-9}), and T helper 1–type immune response (FDR = 1.06×10^{-6}). Although these immune-related gene sets remained enriched in the donor 1 group–only analysis (table S13), no immune-related gene sets were statistically significantly enriched among tumor samples of the donor 2 group (table S14). Per-patient analysis demonstrated increased posttreatment intratumoral $CD8^+$ T cell infiltration among five patients (recipients 1, 3, 4, 7, and 10) with an overall pretreatment median of 89 cells/mm^2 versus 282 cells/mm^2 posttreatment ($P = 0.06$; Fig. 3, E to G, and fig. S12). Recipient 5 achieved a near-pathological CR, as posttreatment viable tumor tissue composed <1% of the entire biopsy, and recipients 3 and 7 achieved partial pathological response (Table 1). Assessment of commonly investigated genes related to intratumoral immune activity demonstrated that the posttreatment tumors of recipients 1, 3, 5, and 7 up-regulated effector-related genes with some reciprocal exhaustion responses (Fig. 3H). Recipient 10, however, up-regulated exhaustion-related genes without an effector response.

This study demonstrates that the combination of FMT from a CR donor and reinduction of anti–PD-1 therapy in refractory metastatic melanoma patients is safe, feasible, and potentially effective. FMT is considered a common treatment for recurrent *Clostridioides difficile* colitis, with a well-established safety profile (*10*), and its safety has been demonstrated even in immunocompromised patients (*11*). Nevertheless, the lack of FMT-related complications in this study among immunocompetent metastatic patients treated with repeated FMTs was reassuring. Notably, the combination of FMT and reinduction of anti–PD-1 therapy appeared safe and resulted in some objective clinical responses. Out of 10 anti–PD-1 refractory recipients, three demonstrated clinical responses, including one CR. A similar trial of FMT and anti–PD-1 reinduction in refractory melanoma patients has reported preliminary results of one objective partial response and one stable disease among the first three patients (*12*). Because the FMT-recipient patients were not treatment naïve, there is a possibility that these clinical outcomes are caused by delayed responses to previous anti–PD-1 treatments. However, this possibility is unlikely, as Ribas *et al.* have reported that delayed response rates in metastatic melanoma patients who continued anti–PD-1 therapy beyond RECIST-confirmed disease progression were <8% (*13*). Similarly, Betof Warner *et al.* have reported that response rates of metastatic melanoma patients who were reinduced with anti–PD-1 monotherapy were 5 out of 34 (<15%) (*14*). These results were possibly an overestimation because three of five responders in that study had an elapsed previous-to-reinduction dose time of at least 12 months (*14*). Such a prolonged time period might enable the reemergence of

immunotherapy-susceptible tumor clones. In our study, the median previous-to-reinduction dose time was only 113 days among the entire cohort and 119 days among the three responders. Moreover, the inclusion criterion of our trial was disease progression on previous anti–PD-1 lines based on iRECIST. According to RECIST 1.1, partial responses or CRs may be deemed unconfirmed pending follow-up, but the classification of progressive disease is always considered final (*15*). However, immunotherapies might sometimes lead to pseudoprogression (*8*), as seen in recipients 3 and 5. iRECIST was designed to distinguish between unconfirmed and confirmed disease progression (*7*) (table S5). Hence, it is possible that the use of iRECIST in those previous publications would have resulted in even lower postfailure response rates.

This higher-than-expected clinical response rate can be explained by the correlative immunological data. Tumor-infiltrating dendritic cells (DCs) have a crucial role in trafficking T cells into tumors (*16*, *17*). Multiple papers from mouse-model studies have demonstrated that microbiota modulation promoted the infiltration of DCs into remote tumors, which resulted in the activation of both T helper 1 cells via interleukin-12 (*4*, *18*) and cytotoxic $CD8^+$ T cells (*19*–*21*). The same findings were demonstrated in our human FMT trial. Because the donors' microbiotas were transplanted into the recipients' guts, it is plausible to assume that the immune activation cascade started in the gut. The donor 1–group recipients demonstrated increased posttreatment gut infiltration and activity of APCs. Geva-Zatorsky *et al.* have assessed the immune response to colonization of different commensal gut microbes and demonstrated that the local effect of microbes in the gut was mostly on the innate immunity cells (*22*), which could later migrate into the lymphatic system (*23*). Notably, some of the donor 2–group recipients also increased their posttreatment gut APC infiltration, although as a group, their RNA-seq findings were not statistically significant. Overall, the recipients who increased their posttreatment intratumoral

Table 1. Clinical characteristics of patients receiving FMT and reinduction of anti–PD-1 treatment. The time from previous anti–PD-1 treatment dose to the first trial dose was calculated from the most recent anti–PD-1 treatment dose to the day of the first anti–PD-1 treatment in the clinical trial. The percentage of viable tumor was calculated as the percentage of viable tumor out of the entire tumor tissue which was examined in a hematoxylin and eosin (H&E) slide of the tumor biopsy (see materials and methods). Clinical responses were based on the iRECIST (*7*). Response category "None" represents iRECIST-confirmed progressive disease. Recipient 2 did not consent to undergo repeated tumor and gut biopsies, and hence, the percentage of viable tumor is presented as not available (N/A). Additional clinical data per donor and recipient can be found in the supplementary materials (tables S1 and S2, respectively). D, dabrafenib; T, trametinib; Nivo, nivolumab; Pembro, pembrolizumab; Ipi, ipilimumab; T-VEC, talimogene laherparepvec; TIL, adoptive cell therapy composed of tumor-infiltrating lymphocytes.

FMT donor group	Recipient	Previous treatment lines (in chronological order)	Best response during all previous anti–PD-1 lines	Time from previous anti–PD-1 dose to first trial dose (days)	Percentage of viable tumor during the current trial		Clinical response in the current trial
					Pretreatment	Posttreatment	
Donor 1	1	D+T; Nivo; D+T reinduction; Ipi+Nivo	None	57	100	95	None
Donor 1	3	Pembro	None	66	100	30	Complete
Donor 1	5	Ipi+Nivo	Partial	119	100	<1	Partial
Donor 1	7	Pembro; D+T	Complete	204	80	30	Partial
Donor 1	9	Nivo (adjuvant); Ipi; Carboplatin + Paclitaxel	None	209	80	90	None
Donor 2	2	Pembro; Ipi; Pembro reinduction	Stable disease	114	N/A	N/A	None
Donor 2	4	Nivo (adjuvant)	None	112	85	90	None
Donor 2	6	Ipi; Pembro; D+T; Nivo; T-VEC + Nivo; TIL; D+T reinduction; Palbociclib; Carboplatin + Pacliataxel	Partial	322	100	85	None
Donor 2	8	Ipi+Nivo	Mixed	42	90	100	None
Donor 2	10	Ipi+Nivo	Stable disease	57	100	90	None

$CD8^+$ T cell infiltration also increased their APC gut infiltration. It is unlikely that the increment in $CD8^+$ T cell infiltration was caused by the mere anti–PD-1 administration, because Chen *et al.* have used pre- and on-treatment tumor biopsies to demonstrate that nonresponding patients undergoing anti–PD-1 therapy did not increase their intratumoral $CD8^+$ infiltration (*24*). However, microbiota-driven gut APC activation would not necessarily yield enhanced intratumoral $CD8^+$ activity. Impaired antigen presentation machinery within the tumor cells themselves is a well-known anti–PD-1 resistance mechanism that usually results in lack of intratumoral $CD8^+$ T cell infiltration (*25*). The tumor from recipient 9 demonstrated such an antigen presentation impairment (fig. S13). Moreover, even the presence of high intratumoral infiltration of $CD8^+$ T cells sometimes fails to translate into a clinical response. Tumors with high $CD8^+$ T cell infiltration can be refractory if the T cell infiltration is ineffective, for example as a result of $CD8^+$ T cell exhaustion after exposure to additional immune checkpoints (*26*). Recipient 10 had overexpression of these molecules, such as IDO-1 (Fig. 3H). Recipient 1, who demonstrated increased intratumoral $CD8^+$ T cell activity, had an initial regression in some metastases but eventually progressed as a result of an unknown cause. These tumor characteristics of different patients emphasize the wide context of clinical responses to immunotherapy and that beneficial microbiota composition is not the only factor in treatment response.

The microbiota composition of the two donors and the posttreatment recipients from both donor groups were characterized by high relative abundances of taxa that were previously associated with response to immunotherapy. Yet, the three responding recipients were solely part of the donor 1 group. The reason for this dissonance is unclear. However, this study was statistically powered to assess safety and was not designed to compare efficiency between donors. Lack of clinical responders among the donor 2 group does not necessarily implicate that clinical responses could not be observed in a larger cohort. Moreover, our inability to pinpoint specific response-inducer microbiota characteristics echoes the inconsistency among previous observational studies (*6*). As the characteristics of optimal microbiota compositions of donors and recipients remain elusive, the design and implementation of future microbiome modulation clinical trials must be carefully considered. Numerous considerations must be taken into account when contemplating strategies to modulate gut microbes, including diet (*27*). Studies in preclinical models incorporating microbiota into germ-free mice avatars may yield insight into both microbe and host factors. Nonetheless, in light of the decades-based safety profile of FMTs (*10*), promising results in preclinical models (*2*–*4*, *18*, *19*, *21*), and findings that suggest treatment effectiveness in our current clinical trial, clinical institutions should not be deterred by the lack of sufficient mechanistic knowledge to examine the clinical potential of FMTs in the setting of well-designed and supervised human trials. This is especially true for refractory patients, in whom the risk-to-benefit ratio of FMTs appears favorable.

One limitation of this clinical trial arises from the use of antibiotics as part of the pre-FMT preparation. Antibiotic preparation was adopted because it has enhanced the FMT ability to modulate microbiota composition in reported murine models (*28*). The vancomycin-neomycin protocol has been reported as an effective pre-FMT protocol in humans (*29*). Because all of our recipients underwent the exact same pre-FMT protocol, we believe that the use of antibiotics did not affect the observed immune and clinical outcomes. However, this possibility cannot be ruled out in the current study design.

FMT from CR donors and reinduction of anti–PD-1 therapy in refractory metastatic melanoma patients was demonstrated to be safe and feasible. In some patients, this treatment increased the intratumoral immune activity, which was translated into objective clinical responses. These findings support the concept of overcoming resistance to immunotherapy by modulating the gut microbiota.

REFERENCES AND NOTES

1. P. A. Ascierto *et al.*, *JAMA Oncol.* **5**, 187–194 (2019).
2. V. Gopalakrishnan *et al.*, *Science* **359**, 97–103 (2017).
3. V. Matson *et al.*, *Science* **359**, 104–108 (2018).
4. B. Routy *et al.*, *Science* **359**, 91–97 (2017).
5. Y. Belkaid, T. W. Hand, *Cell* **157**, 121–141 (2014).
6. V. Gopalakrishnan, B. A. Helmink, C. N. Spencer, A. Reuben, J. A. Wargo, *Cancer Cell* **33**, 570–580 (2018).
7. L. Seymour *et al.*, *Lancet Oncol.* **18**, e143–e152 (2017).
8. E. Borcoman *et al.*, *Ann. Oncol.* **30**, 385–396 (2019).
9. R. Verma *et al.*, *Sci. Immunol.* **3**, eaat6975 (2018).
10. U. Iqbal, H. Anwar, M. A. Karim, *Eur. J. Gastroenterol. Hepatol.* **30**, 730–734 (2018).
11. S. C. Lin, C. D. Alonso, A. C. Moss, *Transpl. Infect. Dis.* **20**, e12967 (2018).
12. G. Trinchieri, *Cancer Res.* **80**, IA28 (2020).
13. A. Ribas, J. M. Kirkwood, K. T. Flaherty, *Lancet Oncol.* **19**, e219 (2018).
14. A. Betof Warner *et al.*, *J. Clin. Oncol.* **38**, 1655–1663 (2020).
15. E. A. Eisenhauer *et al.*, *Eur. J. Cancer* **45**, 228–247 (2009).
16. S. Spranger, D. Dai, B. Horton, T. F. Gajewski, *Cancer Cell* **31**, 711–723.e4 (2017).
17. S. Spranger, T. F. Gajewski, *OncoImmunology* **5**, e1086862 (2016).
18. M. Vétizou *et al.*, *Science* **350**, 1079–1084 (2015).
19. A. Sivan *et al.*, *Science* **350**, 1084–1089 (2015).
20. T. Tanoue *et al.*, *Nature* **565**, 600–605 (2019).
21. M. Uribe-Herranz *et al.*, *JCI Insight* **3**, e94952 (2018).
22. N. Geva-Zatorsky *et al.*, *Cell* **168**, 928–943.e11 (2017).
23. Z. Zhang *et al.*, *Immunity* **44**, 330–342 (2016).
24. P. L. Chen *et al.*, *Cancer Discov.* **6**, 827–837 (2016).
25. M. Sade-Feldman *et al.*, *Nat. Commun.* **8**, 1136 (2017).
26. J. A. Trujillo, R. F. Sweis, R. Bao, J. J. Luke, *Cancer Immunol. Res.* **6**, 990–1000 (2018).
27. J. L. McQuade, C. R. Daniel, B. A. Helmink, J. A. Wargo, *Lancet Oncol.* **20**, e77–e91 (2019).
28. S. K. Ji *et al.*, *Front. Microbiol.* **8**, 1208 (2017).
29. J. Ni *et al.*, *Sci. Transl. Med.* **9**, eaah6888 (2017).

ACKNOWLEDGMENTS

This study was conducted in honor of the memory of Allen S. Berg. We wish to thank the Lemelbaum family for its support, O. Mazuz for assisting in trial coordination, M. Davies for his thoughtful insights, A. Lipsky for assisting in the statistical design of the clinical trial, M. Stern for performing most of the tumor biopsies, N. Nissan for assisting in acquiring radiological data, Y. Glick for assisting with the RNA-seq analysis, G. Smollan for assisting in the donor screening process, M. Shaharabany and A. Nachmani for their technical support in the use of the Aperio scanner, N. Keidar and N. Orbach-Zingboim for designing the suggested diet, D. Binyamin for assisting in the 16*S* rRNA gene sequencing analysis, and the patients and their families. **Funding:** This trial was funded only by the Ella Lemelbaum Institute for Immuno-Oncology internal funds. E.N.B. was supported by the Allen Berg Fund for Excellence in Immuno-Oncology Research, Young Researcher Scholarship. G.M. was supported by the Henry and Susan Samueli Foundation Grant for Integrative Immuno-Oncology. **Author contributions:** Conceptualization: B.B., G.M., and E.N.B.; Formal analysis and software: E.N.B., N.B., K.A., M.A., M.A.W.K., and N.J.A.; Funding acquisition: G.M. and J.S.; Investigation: E.N.B., R.O., S.B.-S., O.Z., J.M., D.D.-N., D.R., K.A., L.A., C.A., G.B.-B., L.K., T.B.-N., S.R., A.L., Y.S.-S., Y.E., H.H., N.A., and R.S.-F.; Methodology: E.N.B., B.B., I.Y., R.O., L.K., T.B.-N., R.M., O.K., L.K., A.L., and I.B.; Project administration: E.N.B. and R.O.; Resources: G.M., O.K., I.Y., I.B., and J.S.; Supervision: G.M., B.B., J.S., I.B., I.Y., O.K., and J.A.W.; Visualization: E.N.B., S.R., N.J.A., K.A., N.B., and M.A.W.K.; Writing – original draft: E.N.B.; Writing – review and editing: E.N.B., B.B., I.Y., G.M., M.A., N.J.A., R.M., J.S., and J.A.W. **Competing interests:** I.Y. is a medical adviser for Mybiotix Ltd. G.B.-B. received honoraria and travel support from MSD, Roche, BMS, Novartis, and Medison. Y.S.-S. received honoraria from MSD, Roche, BMS, and Novartis. N.A. received honoraria from MSD, Roche, BMS, Novartis, and Medison. R.S.-F. received honoraria from MSD and BMS. J.S. received honoraria from MSD, Roche, BMS, and Novartis; serves on the advisory boards of MSD, BMS, and Novartis; owns shares of 4c BioMed; and is partially employed by 4cBiomed. J.A.W. is an inventor on a U.S. patent application (PCT/US17/53.717) submitted by the University of Texas MD Anderson Cancer Center that covers methods to enhance immune checkpoint blockade responses by modulating the microbiome; reports compensation for speaker's bureau and honoraria from Imedex, Dava Oncology, Omniprex, Illumina, Gilead, PeerView, Physician Education Resource, MedImmune, Exelixis, and Bristol-Myers Squibb; serves as a consultant and/or advisory board member for Roche/Genentech, Novartis, AstraZeneca, GlaxoSmithKline, Bristol-Myers Squibb, Merck, Biothera Pharmaceuticals, and Microbiome DX; and receives research support from GlaxoSmithKline, Roche/Genentech, Bristol-Myers Squibb, and Novartis. G.M. received honoraria from MSD, Roche, BMS, and Novartis; received research grants from Novartis and BMS (not related to this study); serves on the advisory board of MSD, NucleAI, and Biond Biologics; holds IP and shares of Kitov and 4cBiomed; and is partially employed by 4cBiomed. The rest of the authors declare no competing interests. **Data and materials availability:** Microbiome 16*S* rRNA and metagenomics sequencing data have been deposited in the National Center for Biotechnology Information (NCBI) Sequence Read Archive (SRA) under BioProject ID PRJNA678737. The human gut and tumor RNA-seq data have been deposited at the NCBI Gene Expression Omnibus (GEO) under BioProject ID GSE162436.

SUPPLEMENTARY MATERIALS

science.sciencemag.org/content/371/6529/602/suppl/DC1
Materials and Methods
Supplementary Text
Figs. S1 to S13
Tables S1 to S15
References (*30*–*64*)
MDAR Reproducibility Checklist

6 March 2020; accepted 1 December 2020
Published online 10 December 2020
10.1126/science.abb5920

CATALYSIS

A hydrophobic FeMn@Si catalyst increases olefins from syngas by suppressing C1 by-products

Yanfei Xu[1], Xiangyang Li[2], Junhu Gao[2], Jie Wang[1], Guangyuan Ma[1], Xiaodong Wen[2,3], Yong Yang[2,3], Yongwang Li[2,3], Mingyue Ding[1]*

Although considerable efforts have been made in the selective conversion of syngas [carbon monoxide (CO) and hydrogen] to olefins through Fischer-Tropsch synthesis (FTS), ~50% of the converted CO is transformed into the undesired one-carbon molecule (C1) by-products [carbon dioxide (CO_2) and methane (CH_4)]. In this study, a core-shell FeMn@Si catalyst with excellent hydrophobicity was designed to hinder the formation of CO_2 and CH_4. The hydrophobic shell protected the iron carbide core from oxidation by water generated during FTS and shortened the retention of water on the catalyst surface, restraining the side reactions related to water. Furthermore, the electron transfer from manganese to iron atoms boosted olefin production and inhibited CH_4 formation. The multifunctional catalyst could suppress the total selectivity of CO_2 and CH_4 to less than 22.5% with an olefin yield of up to 36.6% at a CO conversion of 56.1%.

Olefins are feedstocks for many high-value-added chemical products and are usually produced from petroleum (*1*), so there is increasing interest in alternative production routes from nonpetroleum carbon resources (*2*), including syngas (a mixture of CO and H_2) that can be derived from biomass, coal, and natural gas (*3*, *4*). Recently, many breakthroughs have been made in the conversion of syngas to olefins. Bao and colleagues (*5*, *6*) reported the concept of oxide-zeolite (OX-ZEO), separating CO activation and C–C coupling on different active sites. At 400°C, $ZnCrO_x$/SAPO and MnO_x/SAPO exhibited a high selectivity of 80% for light olefins (C_2 to C_4) with CO conversion of ~17 and ~8%, respectively. Later, Wang and colleagues (*7*) prepared a $ZnZrO_x$/SAPO catalyst that had 70% selectivity for light olefins with ~10% CO conversion at 400°C. Although greater olefin selectivity in hydrocarbons was obtained through the OX-ZEO pathway, a lower catalytic activity and olefin yield were exhibited even at a very high reaction temperature.

Alternatively, another route, called Fischer-Tropsch to olefins (FTO), was developed for selectively converting syngas to olefins with a relatively high activity. Zhong *et al.* (*8*) reported that 61% selectivity for light olefins could be obtained over CoMn oxides with ~32% CO conversion. After de Jong and colleagues (*9*) found excellent selectivity of light olefins over iron-based catalysts for Fischer-Tropsch synthesis (FTS), research on Fe active metal ramped up (*10*–*12*). Liu *et al.* (*13*) prepared Mn-modified Fe_3O_4 nanoparticles, which exhibited 60% selectivity for light olefins with ~42% CO conversion. Our previous work (*14*) indicated that a core-shell Fe_3O_4@MnO_2 catalyst presented a greater olefin selectivity of 79% with ~68% CO conversion.

The olefin selectivity reported above refers to the hydrocarbon products and does not include the CO_2 fraction. However, during the conversion process of syngas, the water-gas shift (WGS) reaction is inevitable given the coexistence of CO and H_2O under high reaction temperatures, which results in a high CO_2 selectivity (between 40 and 50%) when converting CO (*5*–*9*, *14*, *15*). Moreover, ~10 to 20% selectivity of by-product CH_4 is generally presented in the FTS reaction, especially for the iron-based catalysts (*9*, *10*, *13*, *16*). Thus, during the syngas-to-olefin reaction, >45% of the converted CO is transformed into the undesired one-carbon molecule (C1) by-products (CO_2 and CH_4) either through the OX-ZEO process (*5*) or the FTO path (*8*, *9*), as depicted in Fig. 1A. Recently, some work has been done to try to address this issue (*17*, *18*), but the total selectivity of C1 products was still very high and the olefin yield was very low. Notably, Wang *et al.* (*19*) and Xie *et al.* (*20*) reported the suppression of C1 products by a specific iron carbide phase and by cobalt promoted with Mn/Na/S, respectively. However, these catalysts could only run at relatively low CO conversion levels (<20%), implying poor olefin yield.

We present a core-shell FeMn@Si catalyst with excellent hydrophobicity that hindered the WGS reaction, which enhanced the C–C coupling reaction and inhibited the formation of CO_2 and CH_4. The chain growth probability was increased to 0.73 (fig. S1), and the selectivity for undesired C1 by-products was suppressed to 22.1% (Fig. 1A). Moreover, the multifunctional catalyst exhibited an olefin selectivity of 83.3% (including 68.2% of α-olefins) and an olefins/paraffins molar ratio of 5.0 in the C_{2+} hydrocarbons (Fig. 1B). Reaction conditions, such as reaction temperature, space velocity, and pressure, were tuned to modify the catalytic performance (figs. S2 to S4). Under the optimum reaction conditions of 320°C, 3.0 MPa, 4000 $ml \cdot h^{-1} \cdot g^{-1}$, $H_2/CO = 2$, the yield of olefins reached as high as 36.6% at a CO conversion of 56.1% in a single run (table S1).

The stability of catalysts is another crucial index to advance industrial applications. In this study, the CO conversion and product distribution remained stable with time on stream (Fig. 1C). The selectivity of undesired C1 by-products was suppressed to ~23% and the olefin selectivity in total products remained at ~65% during the 100-hour stability test. All of the above catalytic tests suggested that our catalyst worked well for efficiently converting syngas to olefins while successfully suppressing the formation of undesired CO_2 and CH_4.

We used several characterization methods to study the origin of the low C1 selectivity and high olefin yield. An unpromoted Fe_2O_3@SiO_2 catalyst was used to investigate the formation path and inhibition mechanism of CO_2 during iron-based FTS reaction. An appropriate amount of Mn promoter was then added to enhance the C-C coupling reaction, which suppressed the CH_4 selectivity and boosted olefin production while maintaining low CO_2 selectivity. The core-shell Fe_2O_3@SiO_2 (Fe@Si) was prepared using the modified Stöber method with nanorod-shaped Fe_2O_3 (figs. S5 and S6). Transmission electron microscopy (TEM) images directly confirmed that the nanorod-shaped Fe_2O_3 was encapsulated by a homogeneous SiO_2 shell (Fig. 2A and fig. S7). As shown in the Fourier transform infrared (FTIR) spectra (Fig. 2C), the absorption bands at 465 and 542 cm^{-1} were assigned to the vibration of Fe–O bonds in the Fe_2O_3 core (*21*), and the bands at 471, 800, and 1095 cm^{-1} to the vibration of Si–O–Si bonds in the SiO_2 shell. Additionally, an absorption band appeared at 950 cm^{-1}, corresponding to the stretching vibration of Si–OH (*22*). The OH stretch of isolated silanol groups at 3740 cm^{-1} on Fe@Si was detected in the diffuse reflectance infrared Fourier transform spectroscopy (DRIFTS) (fig. S8), providing the possibility to introduce hydrophobic $-CH_3$ groups through the silanization reaction (fig. S9).

The obtained Fe@Si was rendered hydrophobic (Fe@Si-c) by further organic modification with chlorotrimethylsilane (TMCS). This modification had no obvious influence on the morphology, phase composition, or pore structure of Fe@Si (figs. S10 to S12). TEM images of Fe@Si-c showed that the nanorod-shaped Fe_2O_3 was also well encapsulated by the amorphous SiO_2 shell (Fig. 2B). FTIR and DRIFTS revealed new absorption bands at ~2925 cm^{-1} for Fe@Si-c compared with Fe@Si (Fig. 2C and fig. S8), which were attributed

[1]School of Power and Mechanical Engineering, Wuhan University, Wuhan 430072, China. [2]Synfuels China Co., Ltd., Beijing 101407, China. [3]State Key Laboratory of Coal Conversion, Institute of Coal Chemistry, Chinese Academy of Sciences, Taiyuan 030001, China.
*Corresponding author. Email: dingmy@whu.edu.cn (M.D.)

to the vibration of introduced $-CH_3$ groups (*22*). The water-droplet contact angle tests were also conducted to characterize the hydrophobicity of Fe@Si and Fe@Si-c. Fe@Si exhibited a contact angle of 40.2°, implying a hydrophilic surface (Fig. 2E). After the hydrophobic modification, the contact angle increased to 137.6° over the Fe@Si-c surface, indicating that hydrophilic Fe@Si had been completely converted to the hydrophobic surface of Fe@Si-c through TMCS modification. Although Fe@Si was well dispersed in water, it was difficult to infiltrate the hydrophobic surface of Fe@Si-c with water, and it formed a long-lasting separate phase (Fig. 2F). The water vapor adsorption and desorption tests also confirmed that the hydrophobic modification hindered the adsorption of water molecules (fig. S13).

The hydrophobic shell coated on iron species played a critical role in tuning the active iron phases during FTS. Compared with fresh Fe@Si, new absorption bands at 578 and 700 cm^{-1} were detected in the FTIR spectra of spent Fe@Si (Fig. 2D) and were related to the vibration of the Fe–O bond in the Fe_3O_4 phase (*23*); bands attributed to the vibration of the Fe–O bond in the Fe_2O_3 phase disappeared. Furthermore, both Fe_3O_4 and iron carbides were detected in the x-ray diffraction (XRD) pattern of spent Fe@Si (Fig. 3A), which was consistent with the Fe_2O_3 phase in traditional iron-based catalysts being converted into a mixture of iron oxides and carbides with reaction time on stream (*4*, *24*, *25*).

For Fe@Si-c, no absorption bands related to the vibration of Fe–O bonds in Fe_2O_3 and Fe_3O_4 were seen in the FTIR spectra after reaction (Fig. 2D), implying that iron oxides disappeared during FTS. Only iron carbides were detected in the XRD pattern of spent Fe@Si-c (Fig. 3A), demonstrating that iron oxides were completely converted to carbides during FTS. We also used Mössbauer spectra to determine the content of the iron phases. The spent Fe@Si consisted of 60.7% Fe_3O_4 and 39.3% iron carbides (χ-Fe_5C_2 and θ-Fe_3C), whereas the spent Fe@Si-c consisted only of iron carbides (Fig. 3, B and C, and table S2), directly confirming that the hydrophobic shell could effectively tune iron phases during reaction.

To study the phase transformation in more detail, we synthesized iron carbides by introducing a carburization procedure (320°C, 0.1 MPa, 4000 $ml \cdot h^{-1} \cdot g^{-1}$, H_2/CO = 1, 5 hours) and compared phase composition of catalysts during FTS. After carburization, the Fe_2O_3 phase in both Fe@Si and Fe@Si-c was completely transformed into iron carbides (Fig. 3D, fig. S14, and table S3). During the subsequent FTS reaction, iron carbides inside Fe@Si were converted into a mixture of iron carbides and Fe_3O_4 phases, whereas Fe@Si-c was only composed of iron carbides (Fig. 3D, fig. S15, and table S4). Given that the only difference between Fe@Si and Fe@Si-c was their water-droplet contact angle, the different phase evolution processes on the two catalysts could be attributed to the hydrophobicity of the catalyst surface. As the FTS reaction proceeded, water was produced and the surrounding ambient became more oxidizing. As a result, iron carbides were partially converted into Fe_3O_4 by water oxidation (*26*–*28*), leading to the coexistence of iron oxides and carbides in Fe@Si. The hydrophobic surface on Fe@Si-c would facilitate rapid water desorption and inhibit its entry into the catalyst. Thus, although the FTS reaction produced water, its restricted entry inhibited the conversion of iron carbides back to oxides.

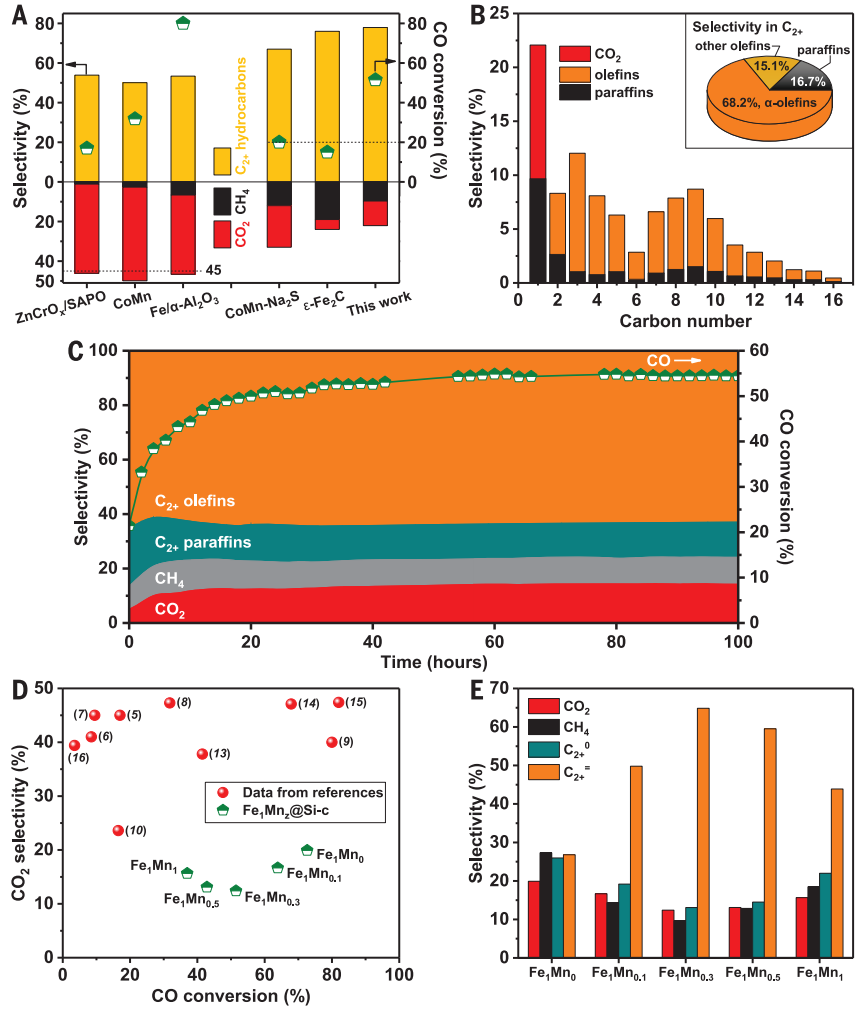

Fig. 1. Catalytic performance for syngas to olefins. (**A**) Product distribution (including CO_2) of FeMn@Si-c in comparison with previous work (*5*, *8*, *9*, *19*, *20*). (**B**) Detailed product distribution (including CO_2) and the selectivity of olefins in C_{2+} hydrocarbons (inset) over FeMn@Si-c. (**C**) A stability test of FeMn@Si-c. (**D**) CO conversion and CO_2 selectivity and (**E**) product distribution (including CO_2) over Fe_1Mn_2@Si-c with different Mn/Fe ratios. Reaction conditions: 320°C, 2.0 MPa, 4000 $ml \cdot h^{-1} \cdot g^{-1}$, H_2/CO = 2.

It is generally accepted that CO_2 formation on iron-based FTS catalysts consists of primary CO_2 and secondary CO_2 (*19*, *29*–*32*). In the CO_2 selectivity–CO conversion curve, the extrapolated CO_2 selectivity toward the axis intercept was ascribed to the primary CO_2 ($CO^* + O^* \rightarrow 1\ CO_2$, where the asterisk means chemisorbed). The increasing CO_2 selectivity above the axis intercept was assigned to the secondary CO_2, which was related to the readsorption of water and its subsequent WGS reaction with CO. The slope of the curve reflected the rate of secondary CO_2 formation stemming from the WGS reaction. The CO_2 selectivity–CO conversion curve (Fig. 4A) was obtained by adjusting the flow rate at a constant H_2/CO ratio. Fe@Si exhibited a primary CO_2 selectivity of ~10%, whereas Fe@Si-c was free of primary CO_2. Because Fe@Si was composed of a mixture of Fe_3O_4 and iron carbides, whereas Fe@Si-c only consisted of iron carbides during reaction (Fig. 3 and fig. S16), we

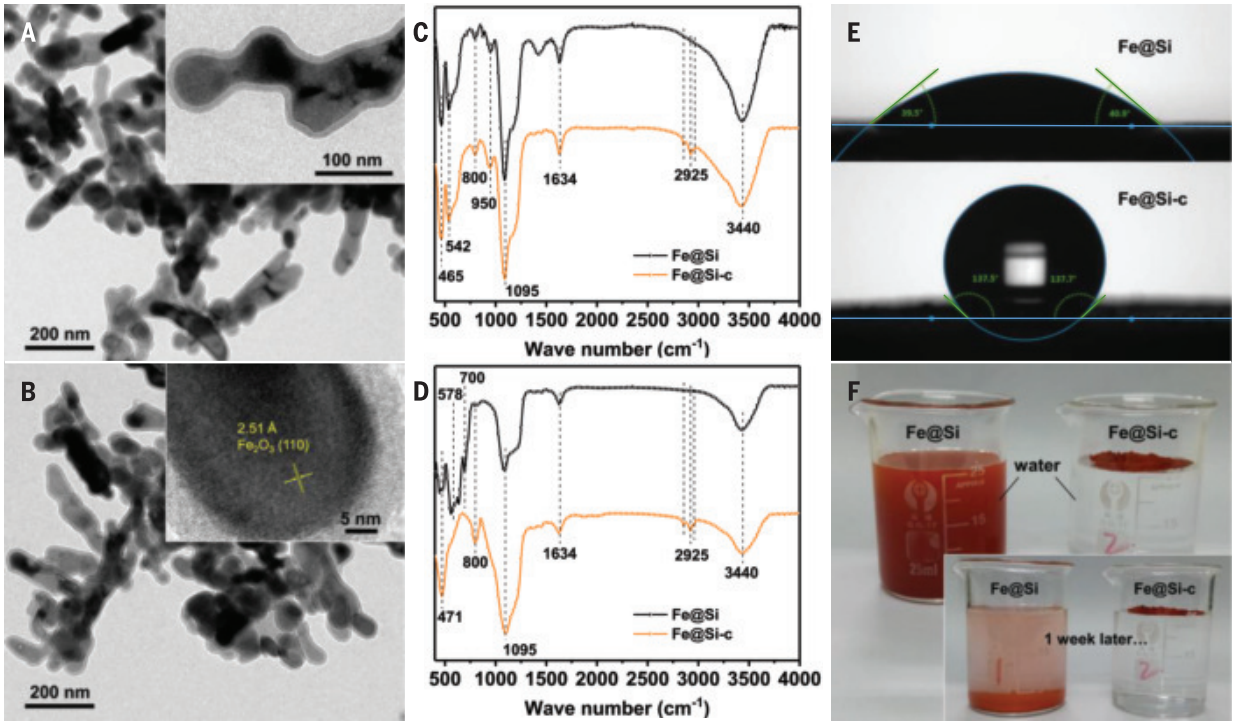

Fig. 2. Structural characterization of the Fe@Si and Fe@Si-c catalysts. (**A** and **B**) TEM images of Fe@Si (A) and Fe@Si-c (B). (**C** and **D**) FTIR spectra of the fresh (C) and spent (D) catalysts. (**E**) Water-droplet contact angle tests. (**F**) Photographs of catalysts dispersed in water, initially and 1 week later.

attributed primary CO_2 formation to the Fe_3O_4 presented in the Fe@Si catalyst, consistent with the previous report (*19*).

The slope of the curve obtained over Fe@Si was 1.81 times that obtained over Fe@Si-c (Fig. 4A), suggesting that Fe@Si favored the formation of secondary CO_2. However, the hydrophobic shell coated on Fe@Si-c facilitated the timely desorption of water and prevented the readsorption of water, reducing the local water partial pressure in the vicinity of iron species and inhibiting the WGS reaction. Also, the Fe_3O_4 phase is the most active phase for the WGS reaction in the iron-based FTS catalysts (*19*, *29*, *33*, *34*) and would form more by-product CO_2 from CO (figs. S17 and S18 and table S5). The hydrophobic shell coated on Fe@Si-c inhibited the reoxygenation of iron carbides toward Fe_3O_4, further inhibiting the WGS reaction. A >40% reduction in CO_2 emission was achieved at a medium CO conversion level (~41%) (Fig. 4B).

To certify the above conclusions, the Fe@Si-c catalysts with different hydrophobic abilities were prepared by changing the TMCS coverage. As shown in fig. S19, the increase in the TMCS exposure increased the water contact angle from 40.2° for Fe@Si to 125.9° for Fe@Si-$c_{0.5}$ (0.5 ml per gram of catalyst) and to 137.6° for Fe@Si-$c_{2.0}$, implying gradually enhanced hydrophobicity. Moreover, the slope of curve obtained over Fe@Si-$c_{0.5}$ was 1.26 times that obtained over Fe@Si-$c_{2.0}$ (fig. S20), further confirming that the enhancement of catalyst hydrophobicity could suppress the WGS reaction by inhibiting the readsorption of water. For TMCS exposures >2.0 ml/g, the water contact angle and the slope of the curve tended to remain stable (figs. S19 and S20), suggesting that excessive addition of TMCS had no obvious effect on the catalyst hydrophobicity and the suppression of the WGS reaction. Fe@Si-$c_{2.0}$ was chosen as the appropriate catalyst for the work that follows unless otherwise noted.

We tuned the H_2/CO ratio in syngas to modify the CO_2 selectivity of Fe@Si-c. As shown in fig. S21A, upon increasing the H_2/CO ratio in syngas from 1 to 4, CO conversion gradually increased from 55.5 to 80.2%, accompanied by a decrease in CO_2 selectivity from 35.0 to 15.0%, demonstrating that a higher H_2/CO ratio increased the amount of H_2 in the system and suppressed the WGS reaction. However, the selectivity of CH_4 (the other undesired C1 byproduct) in hydrocarbons increased from 14.1 to 47.6% because of enhanced hydrogenation (fig. S21B).

The formation path and inhibition mechanism of CO_2, on the basis of the above results, were illustrated in fig. S22. During the FTS reaction, the adsorbed H_2* and CO* on the surface of iron species reacted to form surface CH_x species, and further C–C coupling, dehydrogenation, and hydrogenation reactions would produce various olefins and paraffins. The chemisorbed O* formed by CO dissociation could be removed by reacting with coadsorbed H* and CO* to form H_2O and CO_2, respectively, as oxygen carriers through primary FTS steps. Readsorption of H_2O on the surface of iron species and reaction with CO* would form secondary CO_2 through the WGS reaction. Phase transformation of iron oxides to iron carbides would remove O* from the iron oxides and form primary CO_2. During reaction, Fe@Si-c consisted only of iron carbides, which were free of primary CO_2. The inhibited adsorption of H_2O and the absence of Fe_3O_4 further suppressed the WGS reaction, so the CO_2 selectivity over the Fe@Si-c catalyst during FTS was obviously reduced. Inhibition of the WGS reaction on Fe@Si-c would decrease the amount of H_2 produced and suppress over-hydrogenation reaction, promoting olefins over CH_4 (fig. S23). The olefin selectivity in hydrocarbons increased from 11.1% of Fe@Si to 65.3% of Fe@Si-c.

Mn as a promoter is widely used to boost olefin formation in FTS. We prepared and characterized the Mn-modified catalysts (figs. S24 to S26). Fe@Si-c with moderate addition of Mn (Mn/Fe ratio ≤ 0.3) still suppressed water adsorption and inhibited the oxidation of iron carbides during reaction. However, as the Mn/Fe ratio exceeded 0.3, both Fe_3O_4 and iron carbide phases were detected in the spent Fe_1Mn_z@Si-c catalyst (figs. S27 and S28 and table S6), because excessive Mn hindered the effective contact between the hydrophobic shell and iron carbide core (fig. S29) and led to partial oxidation.

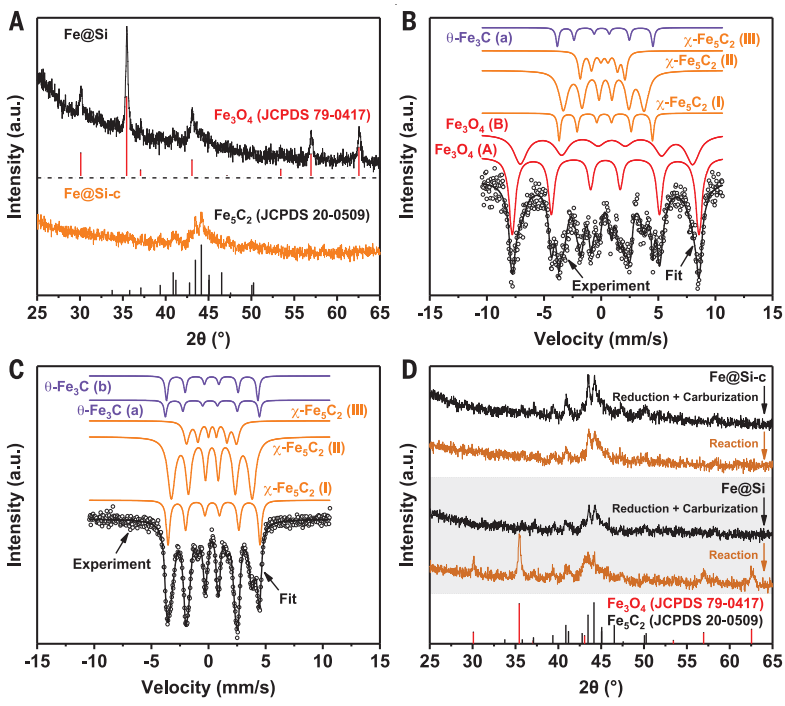

Fig. 3. Comparison of phase composition. (**A**) XRD patterns of the spent catalysts. (**B** and **C**) Mössbauer spectra of the spent Fe@Si (B) and Fe@Si-c (C). (**D**) XRD patterns of the catalysts after reduction and carburization and subsequent reaction. Reaction conditions: 320°C, 2.0 MPa, H_2/CO = 1. a.u., arbitrary units.

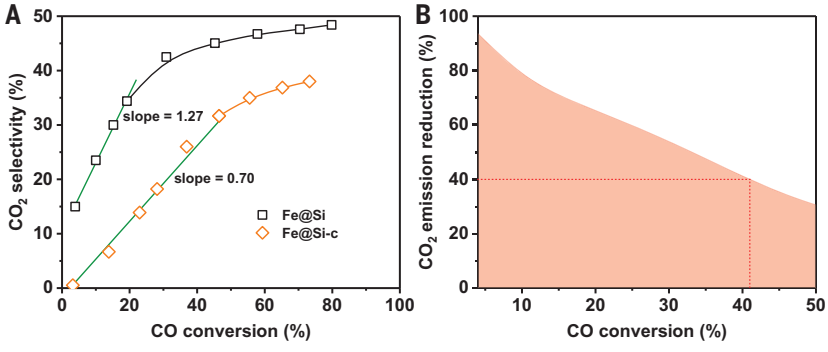

Fig. 4. Effect of hydrophobic modification on the performance of catalysts. (**A**) CO_2 selectivity–CO conversion curve. Reaction conditions: 320°C, 2.0 MPa, H_2/CO = 1. (**B**) CO_2 emission reduction of Fe@Si-c in comparison with Fe@Si. A >40% reduction in CO_2 emission was achieved at a medium CO conversion level (~41%).

The catalytic performance of Fe_1Mn_z@Si-c catalysts was shown in Fig. 1, D and E. The CO_2 selectivity obtained over all the Fe_1Mn_z@Si-c catalysts was suppressed to a low level (<20%) (Fig. 1D and fig. S30), much lower than the reported data under all the CO conversion levels in the previous references (*5–10*, *13–16*), suggesting that the WGS reaction was still inhibited after the addition of Mn. Notably, an inverse volcanic curve between CO_2 selectivity and CO conversion was observed over the Fe_1Mn_z@Si-c catalysts. CO_2 selectivity gradually decreased with the increase of Mn content and reached the minimum value of 12.4% with 51.5% CO conversion over $Fe_1Mn_{0.3}$@Si-c. More importantly, moderate addition of Mn promoted the formation of olefins and suppressed that of CH_4. The olefin selectivity in total products increased with the increasing Mn content and reached the maximum value of 64.9% over $Fe_1Mn_{0.3}$@Si-c (Fig. 1E), which we attributed to the enhanced electron transfer from Mn to Fe atoms (fig. S31). This process facilitated the dissociated adsorption of CO and weakened hydrogenation in favor of the C–C coupling reaction and olefin production (*14*). Further increase of Mn content and formation of Fe_3O_4 during FTS hindered the effective contact between the hydrophobic shell and the iron species core (fig. S29), which unproductively enhanced the WGS reaction and promoted the formation of C1 by-products (Fig. 1E and fig. S32).

REFERENCES AND NOTES

1. H. M. Torres Galvis, K. P. de Jong, *ACS Catal.* **3**, 2130–2149 (2013).
2. W. Zhou *et al.*, *Chem. Soc. Rev.* **48**, 3193–3228 (2019).
3. Q. H. Zhang, J. C. Kang, Y. Wang, *ChemCatChem* **2**, 1030–1058 (2010).
4. J. Bao, G. H. Yang, Y. Yoneyama, N. Tsubaki, *ACS Catal.* **9**, 3026–3053 (2019).
5. F. Jiao *et al.*, *Science* **351**, 1065–1068 (2016).
6. Y. F. Zhu *et al.*, *ACS Catal.* **7**, 2800–2804 (2017).
7. K. Cheng *et al.*, *Angew. Chem. Int. Ed.* **55**, 4725–4728 (2016).
8. L. Zhong *et al.*, *Nature* **538**, 84–87 (2016).
9. H. M. Torres Galvis *et al.*, *Science* **335**, 835–838 (2012).
10. J. Z. Lu *et al.*, *ACS Catal.* **4**, 613–621 (2014).
11. P. Zhai *et al.*, *Angew. Chem. Int. Ed.* **55**, 9902–9907 (2016).
12. X. Chen, D. Deng, X. Pan, Y. Hu, X. Bao, *Chem. Commun.* **51**, 217–220 (2015).
13. Y. Liu, J. F. Chen, J. Bao, Y. Zhang, *ACS Catal.* **5**, 3905–3909 (2015).
14. J. Wang *et al.*, *ACS Appl. Mater. Interfaces* **10**, 43578–43587 (2018).
15. V. P. Santos *et al.*, *Nat. Commun.* **6**, 6451 (2015).
16. O. Zhuo *et al.*, *Chem. Sci.* **10**, 6083–6090 (2019).
17. E. Rytter *et al.*, *Catal. Today* **299**, 20–27 (2018).
18. X. F. Yu *et al.*, *Appl. Catal. B* **232**, 420–428 (2018).
19. P. Wang *et al.*, *Sci. Adv.* **4**, eaau2947 (2018).
20. J. Xie *et al.*, *Nat. Commun.* **10**, 167 (2019).
21. S. M. Rodulfo-Baechler *et al.*, *Mater. Lett.* **58**, 2447–2450 (2004).
22. L. H. Shi, D. B. Li, B. Hou, Y. H. Sun, *Chin. J. Catal.* **28**, 999–1002 (2007).
23. Y.-S. Li, J. S. Church, A. L. Woodhead, *J. Magn. Magn. Mater.* **324**, 1543–1550 (2012).
24. E. de Smit, B. M. Weckhuysen, *Chem. Soc. Rev.* **37**, 2758–2781 (2008).
25. M. Y. Ding *et al.*, *Appl. Energy* **160**, 982–989 (2015).
26. C. N. Satterfield, R. T. Hanlon, S. E. Tung, Z. M. Zou, G. C. Papaefthymiou, *Ind. Eng. Chem. Prod. Res. Dev.* **25**, 407–414 (1986).
27. D. B. Bukur, B. Todic, N. Elbashir, *Catal. Today* **275**, 66–75 (2016).
28. J. H. Liu *et al.*, *Ind. Eng. Chem. Res.* **57**, 9120–9126 (2018).
29. Y. Cheng *et al.*, *Appl. Catal. B* **204**, 475–485 (2017).
30. S. Krishnamoorthy, A. Li, E. Iglesia, *Catal. Lett.* **80**, 77–86 (2002).
31. S. Li, S. Krishnamoorthy, A. Li, G. D. Meitzner, E. Iglesia, *J. Catal.* **206**, 202–217 (2002).
32. M. Ojeda *et al.*, *J. Catal.* **272**, 287–297 (2010).
33. C. Pirola, C. L. Bianchi, A. Di Michele, S. Vitali, V. Ragaini, *Catal. Commun.* **10**, 823–827 (2009).
34. G. P. van der Laan, A. A. C. M. Beenackers, *Appl. Catal. A Gen.* **193**, 39–53 (2000).

ACKNOWLEDGMENTS

Funding: This work was supported by the National Natural Science Foundation of China (51861145102 and 21978225), National Key Research and Development Plan of China (2018YFE0125200), Guangdong Provincial Science and Technology Project (2019A050510031), Science and Technology program of Shenzhen (JCYJ20180302153928437), and Fundamental Research Fund for the Central Universities (2042019kf0221). **Author contributions:** Y.X. performed the catalyst preparation, characterization, and catalytic tests. X.L. and J.G. provided helpful characterization and analysis. J.W. and G.M. participated in the catalytic tests. X.W., Y.Y., and Y.L. provided helpful discussion. M.D. and Y.X. designed the study, analyzed the data, and wrote the paper. All authors approved the final version of the manuscript. **Competing interests:** A Chinese patent application held by Wuhan University that covers the preparation of catalysts is pending. **Data and materials availability:** All data are available in the manuscript or the supplementary materials.

SUPPLEMENTARY MATERIALS

science.sciencemag.org/content/371/6529/610/suppl/DC1
Materials and Methods
Figs. S1 to S32
Tables S1 to S6
References (*35–39*)

18 February 2020; accepted 18 December 2020
10.1126/science.abb3649

QUANTUM SYSTEMS

A quantum-logic gate between distant quantum-network modules

Severin Daiss[1]*†, Stefan Langenfeld[1]†, Stephan Welte[1], Emanuele Distante[1,2], Philip Thomas[1], Lukas Hartung[1], Olivier Morin[1], Gerhard Rempe[1]

The big challenge in quantum computing is to realize scalable multi-qubit systems with cross-talk–free addressability and efficient coupling of arbitrarily selected qubits. Quantum networks promise a solution by integrating smaller qubit modules to a larger computing cluster. Such a distributed architecture, however, requires the capability to execute quantum-logic gates between distant qubits. Here we experimentally realize such a gate over a distance of 60 meters. We employ an ancillary photon that we successively reflect from two remote qubit modules, followed by a heralding photon detection, which triggers a final qubit rotation. We use the gate for remote entanglement creation of all four Bell states. Our nonlocal quantum-logic gate could be extended both to multiple qubits and many modules for a tailor-made multi-qubit computing register.

Quantum computers promise the capability to solve problems that cannot be dealt with by classical machines (*1*). Despite recent progress with local qubit arrays (*2*–*4*), foreseeable implementations of quantum computers are limited in the number of individually controllable and mutually coupleable qubits held in one device because of residual cross-talk, coupling constraints, and restricted space, to mention just three challenges (*5*). One solution for scaling up the computational power is to embed the qubits into a nonlocal quantum network that, in essence, forms a large quantum machine (*6*). This enables a modular approach to quantum computing, in that small and spatially separated processing modules with accessible qubits can be arbitrarily connected with quantum links to carry out more complex joint calculations (*5*, *7*).

First elementary and fully coherent quantum networks with distant qubits have already demonstrated their ability to transfer quantum states or to create entanglement between distant quantum nodes (*8*–*10*). This has been achieved with optical fibers that can carry photonic qubits, typically between different parts of a building or between nearby buildings. Combined with the small size of the modules containing the qubits, this is a key prerequisite for a distributed quantum computer with a potentially huge number of individually addressable qubits. For example, our modules are not much larger than a few cubic centimeters and can hold multiple independent atomic qubits (*11*). Together with shared laser systems and single-atom reservoirs for uninterrupted operation (*12*), the number of connected modules and qubits can be straightforwardly scaled up. Replacing our free-space optics modules with miniaturized cavity technology (*13*) could increase this number even further.

A mandatory step to extend state-of-the-art networks to a distributed quantum computing architecture is the ability to perform nonlocal two-qubit gates between arbitrary network modules. Toward this goal, gate teleportation has been proposed (*14*). This technique constitutes a generalization of teleportation and allows the construction of a quantum computer using previously shared entanglement, local operations, and classical communication (*15*). The general working principle has first been demonstrated with photonic systems based on linear optical quantum computing (*16*, *17*) and, more recently, in isolated setups with material qubits like superconductors in a single cryostat (*18*) and ions in a single Paul trap (*19*).

Here we realize a nonlocal, universal quantum gate between two distant and completely independent quantum modules using a radically different and conceptually simple approach. Our scheme relies on a single photon as a flying ancilla qubit that we reflect

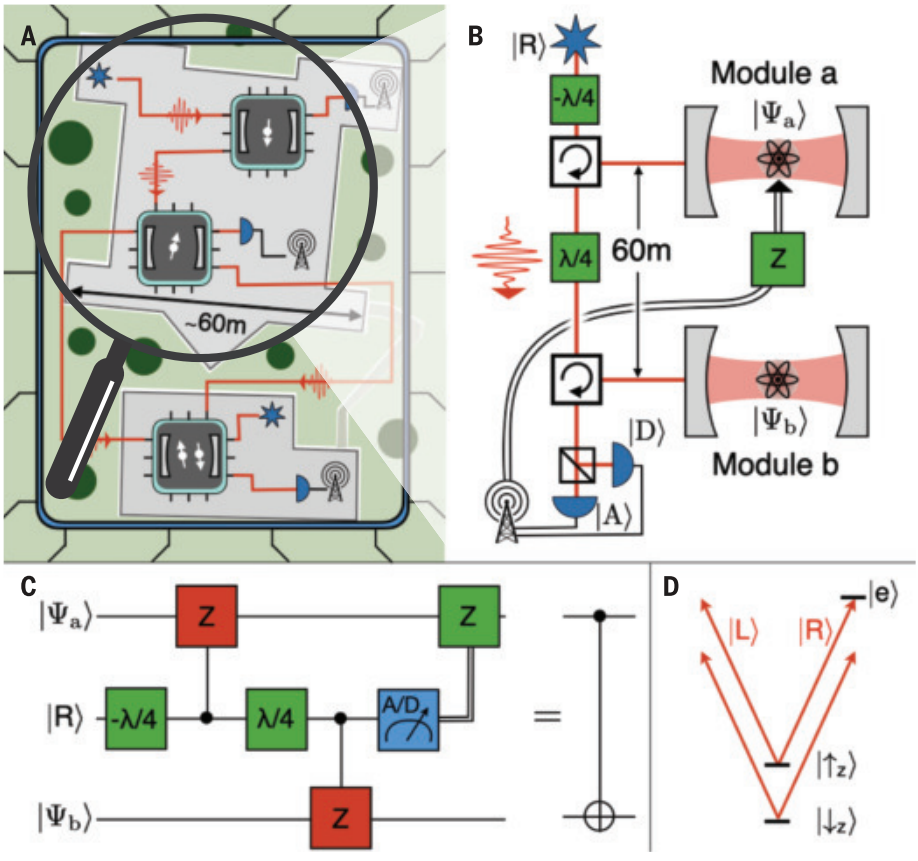

Fig. 1. A quantum-logic gate between two distant qubit modules in a network. (**A**) An elementary computing cluster formed by distributed qubit modules linked with optical fibers (red lines). The modules are connected to light sources (blue stars) and single-photon detectors (blue half disks), which feed classical communication channels (black antennas). (**B**) Enlarged view of our two qubit modules. They consist of an atom-cavity system each and are linked with an optical fiber and circulators. An ancilla photon is sent from a light source via the two modules to a polarization detector. The measurement result is communicated through a classical channel (double black line) to the first module for a conditional state rotation. (**C**) The quantum circuit diagram of our protocol, which realizes the nonlocal quantum gate between the states $|\Psi_a\rangle$ and $|\Psi_b\rangle$ of the atomic qubits. (**D**) The relevant level scheme of the atomic species used, ^{87}Rb.

[1]Max-Planck-Institut für Quantenoptik, Hans-Kopfermann-Straße 1, 85748 Garching, Germany. [2]ICFO-Institut de Ciencies Fotoniques, The Barcelona Institute of Science and Technology, Mediterranean Technology Park, 08860 Castelldefels (Barcelona), Spain.
*Corresponding author. Email: severin.daiss@mpq.mpg.de
†These authors contributed equally to this work.

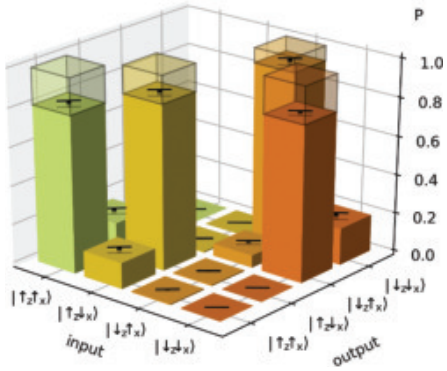

Fig. 2. Truth table of the nonlocal protocol. The diagram shows the probability P of measuring a certain gate output state for the different input states $|\uparrow_z\uparrow_x\rangle$, $|\uparrow_z\downarrow_x\rangle$, $|\downarrow_z\uparrow_x\rangle$, and $|\downarrow_z\downarrow_x\rangle$. In this basis, our protocol acts as a CNOT gate. Errors are given as black ranges and indicate the standard deviations in our measurement. The expected output states for an ideal CNOT gate are shown as light shaded bars.

successively from two distant network modules (*20*, *21*). They are connected by a 60-m fiber link, and each contains a stationary qubit. The photon reflections establish two passive and, in principle, deterministic local gates between the photon and the qubits in the modules (*8*). Combined with a final measurement of the photon and feedback on the stationary qubit, our protocol implements a heralded, nonlocal quantum controlled-NOT (CNOT) gate. It has the advantage that the network modules are always ready for a gate operation and that a typically fragile entangled state does not need to be prepared and held available but is generated by the photon mediating the gate. The scheme is related to a local photon-photon gate protocol that was recently realized with the role of material and light qubits interchanged (*22*). The gate operation can be readily incorporated in a larger modularized quantum computer that is distributed over several buildings (Fig. 1A).

Our setup is schematically shown in Fig. 1B. It comprises two modules in separate laboratories each made up of a single ^{87}Rb atom trapped at the center of an optical cavity with a finesse of 60,000. We use a light source to send photons to the modules, and single-photon detectors register successful photon transmissions through the system. The resonators are single-sided, and light interacting with them leaves predominantly through the incoming channel and is reflected. Two ground states of each atom, $|\uparrow_z\rangle = |5^2S_{1/2}, F = 2, m_F = 2\rangle$ and $|\downarrow_z\rangle = |5^2S_{1/2}, F = 1, m_F = 1\rangle$, serve as the qubit basis. We use a pair of Raman lasers to perform qubit rotations between them. The cavities are tuned to be resonant with the atomic transition $|\uparrow_z\rangle \leftrightarrow |e\rangle = |5^2P_{3/2}, F = 3, m_F = 3\rangle$ (Fig. 1D). Both systems are in the strong coupling regime; thus, the coherent atom-light interactions in the resonator modes have higher rates than the respective decays of the intracavity fields and the atomic excitations (*23*). Owing to tailored light shifts on the energy levels of the atom, right-circular polarization $|R\rangle$ couples to an atomic transition, whereas left-circular polarization $|L\rangle$ does not. For an atom in $|\uparrow_z\rangle$ and coupling light in $|R\rangle$, this leads to a shift in the resonance frequency of the atom-cavity system (*8*). In this situation, an impinging photon resonant with the empty resonators cannot enter the cavities and is directly reflected. Only for an atom in the noncoupling state $|\downarrow_z\rangle$ or for left-circularly polarized light $|L\rangle$, the photon enters the resonator before leaving again through the incoupling mirror. In this process, it acquires a relative π phase shift compared to directly reflected light, constituting a quantum Z gate between the photonic and the stationary qubit (*8*). For an incoming linear polarization $|A\rangle = 1/\sqrt{2}(i|R\rangle + |L\rangle)$, this relative phase shift between $|R\rangle$ and $|L\rangle$ flips the polarization to an orthogonal state $|D\rangle = 1/(\sqrt{2}i)(i|R\rangle - |L\rangle)$ if the atom is in a coupling state $|\uparrow_z\rangle$. As the polarization remains unchanged for an atom in $|\downarrow_z\rangle$, the reflection can entangle the photonic qubit to the atomic state, and it thus forms the basic building block of our nonlocal quantum gate.

The circuit diagram for our protocol is shown in Fig. 1C. We start with a right circular polarized photon $|R\rangle$ with a duration of 1 μs (full width at half maximum) and use a wave plate to convert it to the linear polarization $|A\rangle$. In practice, we approximate the single photon by a weak coherent laser pulse with an average photon number of $\bar{n} = 0.07 \pm 0.01$. We tune it to be resonant with the empty resonators and reflect it from the first cavity, thereby entangling the photon polarization and the atomic spin. The light is subsequently sent through a quarter wave plate and a 60-m-long optical single-mode fiber to the other module located 21 m away. Passing a circulator, the photon is reflected from the second system, resulting in an atom-atom-photon entangled state. Finally, the light is sent to a polarization-detection setup measuring in the linear basis of $|A\rangle/|D\rangle$. The detection of the photon acts as a herald of a successful gate operation and triggers a rotation of the state of the first qubit conditioned on the measurement outcome. The resulting overall protocol realizes a nonlocal quantum gate. In the basis of $|\uparrow_z\rangle/|\downarrow_z\rangle$ for the first atom and in the superposition basis of $|\uparrow_x\rangle = \frac{1}{\sqrt{2}}(|\uparrow_z\rangle + |\downarrow_z\rangle)$ and $|\downarrow_x\rangle = \frac{1}{\sqrt{2}}(|\uparrow_z\rangle - |\downarrow_z\rangle)$ for the second atom, this gate acts as a CNOT

$$\begin{aligned} |\uparrow_z\uparrow_x\rangle &\rightarrow |\uparrow_z\uparrow_x\rangle \\ |\uparrow_z\downarrow_x\rangle &\rightarrow |\uparrow_z\downarrow_x\rangle \\ |\downarrow_z\uparrow_x\rangle &\rightarrow |\downarrow_z\downarrow_x\rangle \\ |\downarrow_z\downarrow_x\rangle &\rightarrow |\downarrow_z\uparrow_x\rangle \end{aligned} \quad (1)$$

Here we adopt a common notation for the two distant qubits with the first (second) state belonging to the qubit in the first (second) module. A detailed derivation of our gate protocol and the corresponding truth table are given in the supplementary materials (*23*).

We probe our gate with all combinations of $|\uparrow_z\rangle/|\downarrow_z\rangle$ for the first and $|\uparrow_x\rangle/|\downarrow_x\rangle$ for the second qubit as input states and measure the resulting atomic states in the z and x bases, respectively. For each input combination, we register about 500 heralding clicks. This truth table of our operation is given in Fig. 2. We achieve a fidelity of (85.1±0.8)% with the populations expected for an ideal quantum CNOT gate.

To rule out possible nonzero phases in the unitary underlying the truth table [for a more detailed discussion, see supplementary materials (*23*)] and to confirm the quantum nature of our nonlocal gate, we furthermore use it to entangle the two qubits. For this purpose, we initialize each atom either in $|\uparrow_x\rangle$ or $|\downarrow_x\rangle$, execute our protocol, and perform a full state tomography on the resulting two-qubit state by measuring both atoms in random combinations of detection bases (*24*). Depending on the initial state, we generate all four maximally entangled Bell states. For each of them, we collect about 3000 heralding photon detections. The results of this measurement are displayed in Table 1 and Fig. 3. The table gives the final fidelities with the ideal Bell states, and the figure displays the real parts of the reconstructed density matrices for each input state. The imaginary residues are given in the supplementary materials (*23*). We achieve an average overlap fidelity with the ideal Bell states of (76.6±1.0)%.

The whole protocol is performed at a rate of 1 kHz. The gate itself takes 22 μs, limited by the time needed for single-qubit rotations. Although in our implementation, this is still slow compared to state-of-the-art quantum computers, the gate serves as a special connecting gate and might not need to run with the same high repetition rate and speed.

The success probability of detecting the heralding photon is relatively small, 0.006, with a major limitation coming from our use of a weak coherent laser pulse with a vacuum contribution of 93%. Furthermore, the efficiency is lowered by the cavity reflectivities (60% and 55%); the link between the two systems, including optical elements, a fiber coupling, photon loss in the fiber, and a circulator transmission (52% in total); and the

Table 1. Bell-state generation results. List of input and output states of the generation of the Bell states with our nonlocal CNOT gate protocol up to a global phase. The last column gives the measured fidelities with the expected final state.

Input state	Output state	Fidelity
$\|\uparrow_x\uparrow_x\rangle$	$\frac{1}{\sqrt{2}}(\|\uparrow_z\uparrow_x\rangle + \|\downarrow_z\downarrow_x\rangle) = \|\Phi^+\rangle$	$(78.8 \pm 2.0)\%$
$\|\uparrow_x\downarrow_x\rangle$	$\frac{1}{\sqrt{2}}(\|\uparrow_z\downarrow_x\rangle + \|\downarrow_z\uparrow_x\rangle) = \|\Psi^+\rangle$	$(75.1 \pm 2.0)\%$
$\|\downarrow_x\uparrow_x\rangle$	$\frac{1}{\sqrt{2}}(\|\uparrow_z\uparrow_x\rangle - \|\downarrow_z\downarrow_x\rangle) = \|\Phi^-\rangle$	$(76.8 \pm 2.0)\%$
$\|\downarrow_x\downarrow_x\rangle$	$\frac{1}{\sqrt{2}}(\|\uparrow_z\downarrow_x\rangle - \|\downarrow_z\uparrow_x\rangle) = \|\Psi^-\rangle$	$(75.8 \pm 2.0)\%$

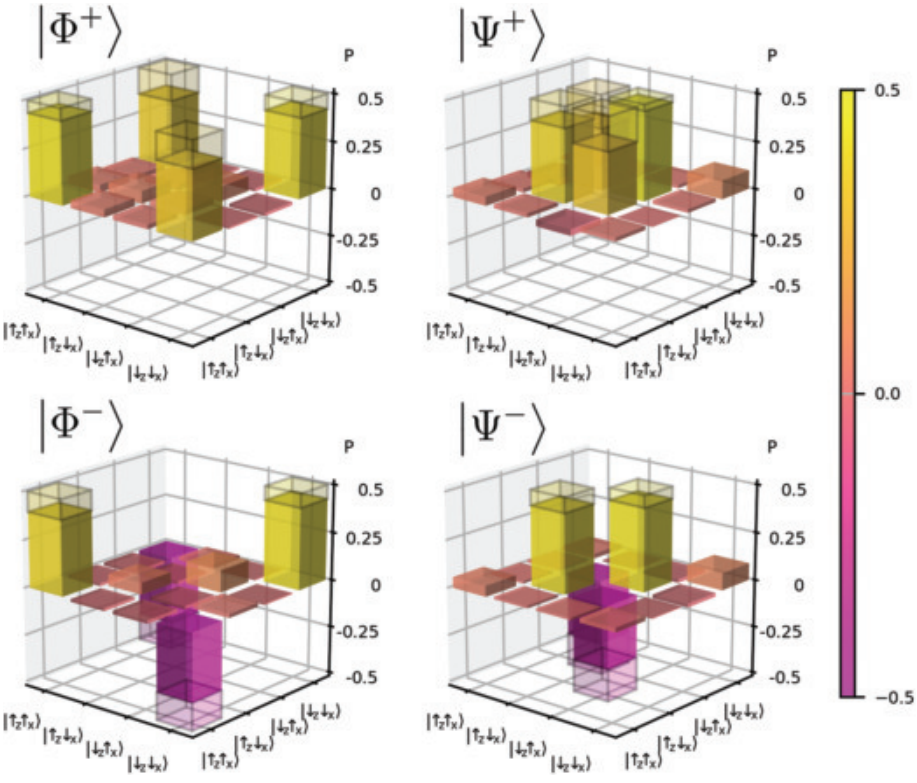

Fig. 3. Density matrices for the produced Bell states. The real part of the reconstructed density matrices is shown. The ideal values are indicated as shaded bars in the plots.

Table 2. Effects of experimental imperfections. List of major experimental imperfections in our implementation and their effective fidelity reduction on Bell-state production and truth table measurements derived from a separate simulation. Errors are estimated from the fluctuations of the experimental parameters.

Imperfection	Effect on truth table	Effect on Bell states
Weak coherent states and losses	$(2.3^{+0.3}_{-0.3})\%$	$(3.8^{+0.5}_{-0.4})\%$
State-preparation and measurement	$(2.9^{+1.0}_{-1.0})\%$	$(2.7^{+1.0}_{-1.0})\%$
Polarization effects	$(2.2^{+0.3}_{-0.5})\%$	$(2.7^{+0.4}_{-0.6})\%$
Mode matching	$(2.0^{+1.6}_{-1.2})\%$	$(2.4^{+2.5}_{-1.5})\%$
Atom-cavity detunings and lock widths	$(1.4^{+1.3}_{-0.7})\%$	$(1.9^{+2.8}_{-1.0})\%$
Atomic decoherence	$(0.11^{+0.09}_{-0.03})\%$	$(3.2^{+0.3}_{-0.2})\%$

detection efficiency after the second module, again including a circulator transmission (50% in total). The only intrinsic limitation to the success probability is the photon transmission in the 60-m fiber link (95% for a wavelength of 780 nm).

The fidelity of our nonlocal quantum gate is currently limited by various experimental imperfections. We have identified the major effects and performed simulations to estimate their reduction of fidelity, both for the truth table and for the generation of entanglement. The results are listed in Table 2. These imperfections are not intrinsic to the protocol and are expected to be improved in future implementations.

One of the main contributions stems from our use of a weak coherent laser pulse that has a residual probability of a two-photon state impinging on either cavity. Such a contribution changes the relative π phase in the atom-light state between a coupling and a noncoupling atom to a full 2π phase, thereby nullifying the effect caused by the atom. The resulting infidelity can be readily overcome by using a single photon, for example, derived from a well-controlled atom-cavity system (*8*), as an ancilla between the modules.

Additional limitations come from our state preparation and measurement, the finite coherence times of the atoms, the transversal mode matching between fibers and cavities, the frequency stability of both resonators, and the matching of polarizations between the different modules and the detection setup. Some of these effects have a smaller impact on the fidelity of the truth table, for two reasons. First, in this measurement, the qubit in the first module is prepared in an energy eigenstate and second, additional polarization effects and higher photon numbers do not affect the fidelity with a noncoupling atom in $|\downarrow_z\rangle$. Smaller errors in both measurements in the subpercent range arise from dark counts of the detectors and the parameters of our cavities. A more detailed discussion of the imperfections is given in the supplementary materials (*23*). Overall, we expect to reduce these sources of error with measures such as using single photons, implementing faster single-qubit rotations, and better long-term stability of the relevant frequencies and polarizations.

In summary, we have demonstrated a nonlocal quantum gate between two separated qubit modules connected with a 60-m optical fiber. Although we implement this gate using single atoms coupled to an optical cavity, the general principle can be transferred to different platforms such as quantum dots (*25*) or impurity-vacancies in diamond (*26*). We use weak coherent states to approximate a single photon, but better sources such as atom-cavity systems could greatly improve both the efficiency and the fidelity of our implementation.

Arguably most fascinating, however, would be to extend our experiment to more than two modules and more than one qubit per module, including local two-qubit gates (*27*). This could facilitate in a controlled way a single-photon entangled multi-qubit array (*28*), or a quantum repeater chain (*29*).

REFERENCES AND NOTES

1. R. P. Feynman, *Int. J. Theor. Phys.* **21**, 467–488 (1982).
2. H. Levine *et al.*, *Phys. Rev. Lett.* **123**, 170503 (2019).
3. F. Arute *et al.*, *Nature* **574**, 505–510 (2019).
4. K. Wright *et al.*, *Nat. Commun.* **10**, 5464 (2019).
5. T. D. Ladd *et al.*, *Nature* **464**, 45–53 (2010).
6. C. Monroe *et al.*, *Phys. Rev. A* **89**, 022317 (2014).
7. H. J. Kimble, *Nature* **453**, 1023–1030 (2008).
8. A. Reiserer, G. Rempe, *Rev. Mod. Phys.* **87**, 1379–1418 (2015).
9. S. Pirandola, J. Eisert, C. Weedbrook, A. Furusawa, S. L. Braunstein, *Nat. Photonics* **9**, 641–652 (2015).
10. S. Wehner, D. Elkouss, R. Hanson, *Science* **362**, eaam9288 (2018).
11. S. Langenfeld, O. Morin, M. Körber, G. Rempe, *npj Quantum Inf.* **6**, 86 (2020).
12. M. Endres *et al.*, *Science* **354**, 1024–1027 (2016).
13. J. D. Thompson *et al.*, *Science* **340**, 1202–1205 (2013).
14. D. Gottesman, I. L. Chuang, *Nature* **402**, 390–393 (1999).
15. J. Eisert, K. Jacobs, P. Papadopoulos, M. B. Plenio, *Phys. Rev. A* **62**, 052317 (2000).
16. Y.-F. Huang, X.-F. Ren, Y.-S. Zhang, L.-M. Duan, G.-C. Guo, *Phys. Rev. Lett.* **93**, 240501 (2004).
17. W.-B. Gao *et al.*, *Proc. Natl. Acad. Sci. U.S.A.* **107**, 20869–20874 (2010).
18. K. S. Chou *et al.*, *Nature* **561**, 368–373 (2018).
19. Y. Wan *et al.*, *Science* **364**, 875–878 (2019).
20. L.-M. Duan, B. Wang, H. J. Kimble, *Phys. Rev. A* **72**, 032333 (2005).
21. X.-M. Lin, Z.-W. Zhou, M.-Y. Ye, Y.-F. Xiao, G.-C. Guo, *Phys. Rev. A* **73**, 012323 (2006).
22. B. Hacker, S. Welte, G. Rempe, S. Ritter, *Nature* **536**, 193–196 (2016).
23. Materials and methods are available as supplementary materials.
24. J. B. Altepeter, D. F. V. James, P. G. Kwiat, "Qubit Quantum State Tomography" in *Quantum State Estimation* (vol. 649 of Lecture Notes in Physics), M. Paris, J. Řeháček, Eds. (Springer, 2004).
25. P. Lodahl, S. Mahmoodian, S. Stobbe, *Rev. Mod. Phys.* **87**, 347–400 (2015).
26. M. K. Bhaskar *et al.*, *Nature* **580**, 60–64 (2020).
27. S. Welte, B. Hacker, S. Daiss, S. Ritter, G. Rempe, *Phys. Rev. X* **8**, 011018 (2018).
28. I. Cohen, K. Mølmer, *Phys. Rev. A* **98**, 030302 (2018).
29. M. Uphoff, M. Brekenfeld, G. Rempe, S. Ritter, *Appl. Phys. B* **122**, 46 (2016).
30. S. Daiss *et al.*, Data of "A quantum-logic gate between distant quantum-network modules," Zenodo (2020). http://doi.org/10.5281/zenodo.4284323.

ACKNOWLEDGMENTS

We thank B. Hacker, M. Körber, and T. Nadolny for contributions during the early stage of the experiments. **Funding:** This work was supported by the Bundesministerium für Bildung und Forschung via the Verbund Q.Link.X (16KIS0870), by the Deutsche Forschungsgemeinschaft under Germany's Excellence Strategy–EXC-2111–390814868, and by the European Union's Horizon 2020 research and innovation programme via the project Quantum Internet Alliance (QIA, GA no. 820445). E.D. acknowledges support by the Cellex-ICFO-MPQ postdoctoral fellowship program. **Author contributions:** All authors contributed to the experiment, the analysis of the results, and the writing of the manuscript. **Competing interests:** The authors declare that there are no competing financial interests. **Data and materials availability:** The data underlying the figures can be found at Zenodo (*30*). All other data needed to evaluate the conclusions in the paper are present in the paper or the supplementary materials.

SUPPLEMENTARY MATERIALS

science.sciencemag.org/content/371/6529/614/suppl/DC1
Supplementary Text
Fig. S1
Table S1
References (*31*–*33*)

13 August 2020; accepted 20 November 2020
10.1126/science.abe3150

QUANTUM MATERIALS

Programmable hyperbolic polaritons in van der Waals semiconductors

A. J. Sternbach[1]*†, S. H. Chae[2]†, S. Latini[3], A. A. Rikhter[4], Y. Shao[1], B. Li[2], D. Rhodes[2]‡, B. Kim[2], P. J. Schuck[2], X. Xu[5], X.-Y. Zhu[6], R. D. Averitt[4], J. Hone[2], M. M. Fogler[4], A. Rubio[3,7], D. N. Basov[1]

Collective electronic modes or lattice vibrations usually prohibit propagation of electromagnetic radiation through the bulk of common materials over a frequency range associated with these oscillations. However, this textbook tenet does not necessarily apply to layered crystals. Highly anisotropic materials often display nonintuitive optical properties and can permit propagation of subdiffractional waveguide modes, with hyperbolic dispersion, throughout their bulk. Here, we report on the observation of optically induced electronic hyperbolicity in the layered transition metal dichalcogenide tungsten diselenide (WSe_2). We used photoexcitation to inject electron-hole pairs in WSe_2 and then visualized, by transient nanoimaging, the hyperbolic rays that traveled along conical trajectories inside of the crystal. We establish here the signatures of programmable hyperbolic electrodynamics and assess the role of quantum transitions of excitons within the Rydberg series in the observed polaritonic response.

Van der Waals (vdW) semiconductors of the MX_2 series (where M = W or Mo and X = Se or S) and their heterostructures are paragons of programmable electronic, lattice, and excitonic properties (*1*, *2*). The extreme anisotropy commonplace in vdW crystals can give rise to nonintuitive optical properties. Chief among them is the formation of hyperbolic wave packets with subdiffractional wavelength that travel as conical rays through the bulk of a medium, similar to electromagnetic wave propagation in ionized plasmas (*3*). Hyperbolic rays provide a viable platform for controlling the flow of nanophotonic energy, a heralded goal with far-reaching potential for nanotechnology (*4*, *5*) and strong light-matter interactions (*6*, *7*).

Central to the implementation of programmable hyperbolicity is the notion of polaritons (*6*, *8*–*20*), hybrids of light and matter that enable subdiffractional confinement of hyperbolic waveguide modes. A plethora of physical processes can give rise to hyperbolic polaritons, in which photons are coupled to dipole active resonances such as phonons (*4*, *8*, *10*, *13*–*20*), intersubband transitions in quantum wells (*19*, *21*), plasmons (*6*, *19*, *20*, *22*), excitons (*19*, *23*), or Cooper pairs (*6*, *19*) within highly anisotropic matter. In this work, we demonstrate propagating hyperbolic polaritons rooted in photo-induced electron-hole pairs. These on-demand hyperbolic rays can be turned on and off within MX_2 semiconductors, emerging on the subpicosecond time scale and encompassing a broad spectral bandwidth in the infrared range.

Hyperbolic waveguide modes in layered crystals exist in the frequency range where the in-plane $\varepsilon_1^{ab}(\omega)$ and out-of-plane $\varepsilon_1^{c}(\omega)$ components of the dielectric tensor satisfy $\varepsilon_1^{ab}(\omega) \cdot \varepsilon_1^{c}(\omega) < 0$ (*24*–*26*). Here, we fulfilled this imperative condition for hyperbolicity by generating electron-hole pairs in WSe_2 with photoexcitation (Fig. 1A). The photo-induced pairs altered the in-plane polarizability driving $\varepsilon_1^{ab}(\omega) < 0$ while $\varepsilon_1^{c}(\omega) > 0$ was preserved. Our density functional theory calculations (Fig. 1B and supplementary note S6) corroborate the anisotropic electronic structure of WSe_2. The dielectric response obtained after photoexcitation using the standard Mott-Wannier (MW) model (*27*–*29*) (supplementary notes S2 and S6) attests to a broadband hyperbolic region of the electromagnetic spectrum (Fig. 1, C and D) with the experimentally attainable bound carrier density n_x ~1 to 3 × 10^{19} cm^{-3}. Thus, the condition $\varepsilon_1^{ab}(\omega) \cdot \varepsilon_1^{c}(\omega) < 0$ can be satisfied for $\omega \lesssim$ 1100 cm^{-1} in WSe_2 (Fig. 1C). The character of the mid-infrared optical constants dictates subdiffractional transport of electrogenic radiation following conical trajectories (Fig. 1A), in agreement with our experimental data (Fig. 1D).

We begin with the electrodynamics of WSe_2 investigated with time-resolved nano-Fourier-transform infrared spectroscopy (FTIR) (*9*, *30*, *31*). In the steady state, the obtained nano-FTIR spectra validated that WSe_2 retains dielectric-like properties (both ε_1^{ab} and ε_1^{c}) within the frequency window of our FTIR probe (supplementary note S3). We agitated WSe_2 with pump photons with energy E of ~12,180 cm^{-1}

[1]Department of Physics, Columbia University, New York, NY 10027, USA. [2]Department of Mechanical Engineering, Columbia University, New York, NY 10027, USA. [3]Max Planck Institute for the Structure and Dynamics of Matter, 22761 Hamburg, Germany. [4]Department of Physics, University of California–San Diego, La Jolla, CA 92093, USA. [5]Department of Physics, University of Washington, Seattle, WA 98195, USA. [6]Department of Chemistry, Columbia University, New York, NY 10027, USA. [7]Center for Computational Quantum Physics (CCQ), Flatiron Institute, New York, NY 10010, USA.
***Corresponding author. Email: as5049@columbia.edu**
†These authors contributed equally to this work.
‡Present address: Materials Science and Engineering, University of Wisconsin–Madison, Madison, WI 53706, USA.

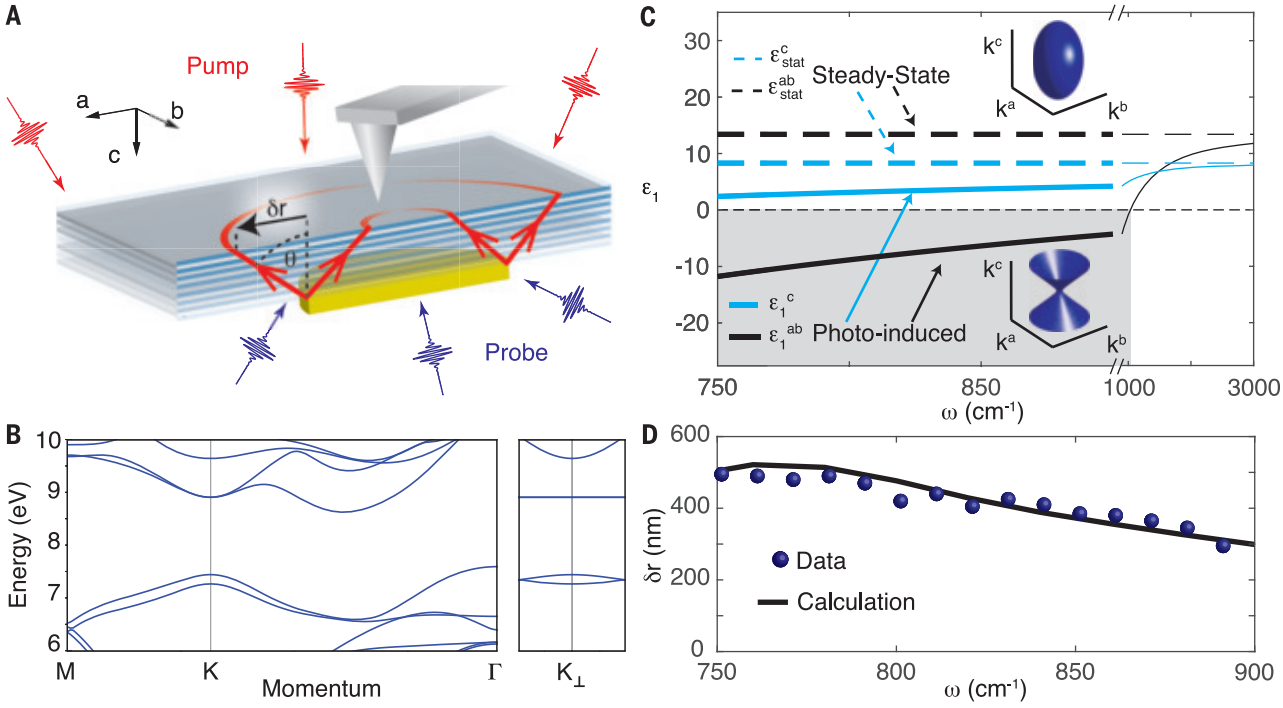

Fig. 1. Transient hyperbolic polariton experiment. (**A**) The layered vdW crystal, WSe_2, is interrogated with a mid-infrared probe (blue pulses) after photoexcitation with optical pump radiation (red pulses). Gold antennae are patterned beneath the sample to launch hyperbolic polaritons, which travel along conical trajectories with angle θ from the surface normal. The hyperbolic rays reach the crystal surface at a lateral distance δ*r* from the edge of the gold disk and are scattered to the detector by the sharp apex of an AFM probe. (**B**) Density functional theory calculations (see supplementary note S6) reveal dispersive bands in the a-b plane and flat bands perpendicular to the planes of WSe_2 at the *K* point of the Brillion zone, $K_\perp$. (**C** and **D**) Optical response of WSe_2 with $n_x = 2.1 \times 10^{19}$ cm^{-3} and γ = 33 meV. (C) Principal values of the dielectric tensor under steady-state (dashed lines) and photoexcited (solid lines) conditions. Within the gray-shaded region, the isofrequency surface is driven from an ellipse to a hyperboloid on demand by photoexcitation (insets). (D) The coordinate δ*r*, defined in (A), plotted as a function of probe frequency ω. The dispersive trends extracted from experimental data (fig. S5B) are shown as blue dots. The dispersion of δ*r* calculated from the model dielectric functions in (C) is shown as a black line.

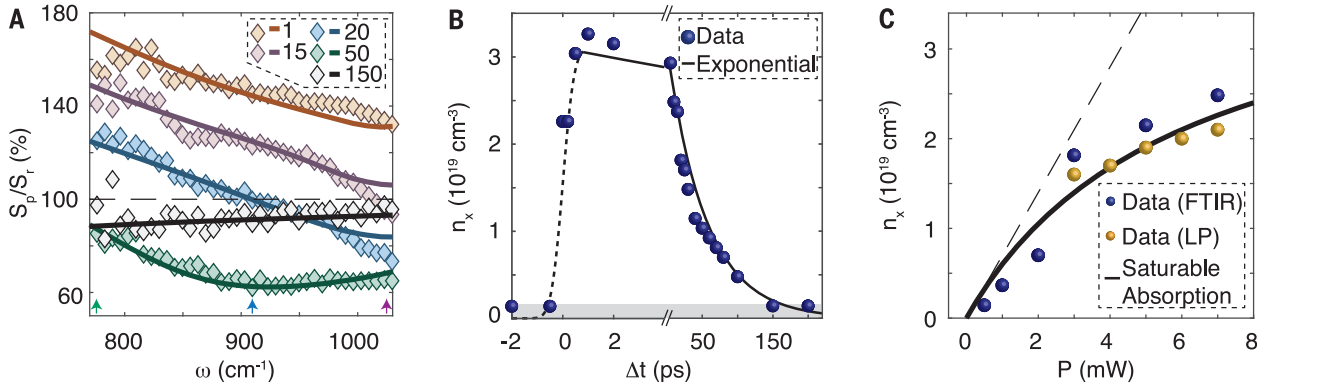

Fig. 2. FTIR results. (**A**) Representative series of normalized near-field amplitude spectra, S_p/S_r (see supplementary note S4). The data (diamonds) are color coded according to the time delay Δ*t* indicated in units of picoseconds in the legend. The color-coded solid lines (legend) were calculated as described in the main text with n_x (B) and γ (fig. S2E). The arrows approximately indicate the frequency where ε_1^{ab} crosses zero (fig. S3A). (**B**) The trend of n_x versus Δ*t* (dots) is overlaid on an exponential fit with a time constant of 55 ps (black line). The dashed black line is a guide to the eye, and the gray-shaded region approximately indicates the noise floor. (**C**) The trend of n_x is shown against the photoexcitation power *P* at Δ*t* = 2 ps. Results extracted from FTIR measurements (blue dots) are compared with the results of a hyperbolic line profile (LP) analysis discussed in Fig. 3F (yellow dots; see table S1).

(=1.51 eV), which is red detuned from the optical gap (supplementary note S4). The analysis of the near-field amplitude spectra *S*(ω) uncovers zero-crossing in the corresponding trend of $\varepsilon_1^{ab}(\omega)$ at frequencies with approximate locations marked with arrows in Fig. 2A and fig. S2. In our analysis, we computed the dielectric response in the photoexcited state by solving the MW equation (supplementary notes S2 and S6; Eq. 2). Spectra of *S*(ω) were then calculated with the lightning rod formalism (*32*). Excellent agreement between the theoretical traces and our data is evident in Fig. 2A. A by-product of the same analysis is a precise extraction of n_x and its dynamics (see fig. S2 for dynamics of the scattering rate, γ). The density, n_x, decays with a nearly exponential rate (Fig. 2B). At a fixed time delay, n_x increases with increasing photoexcitation power. Further, the data are consistent with the characteristic sublinear trend of saturable

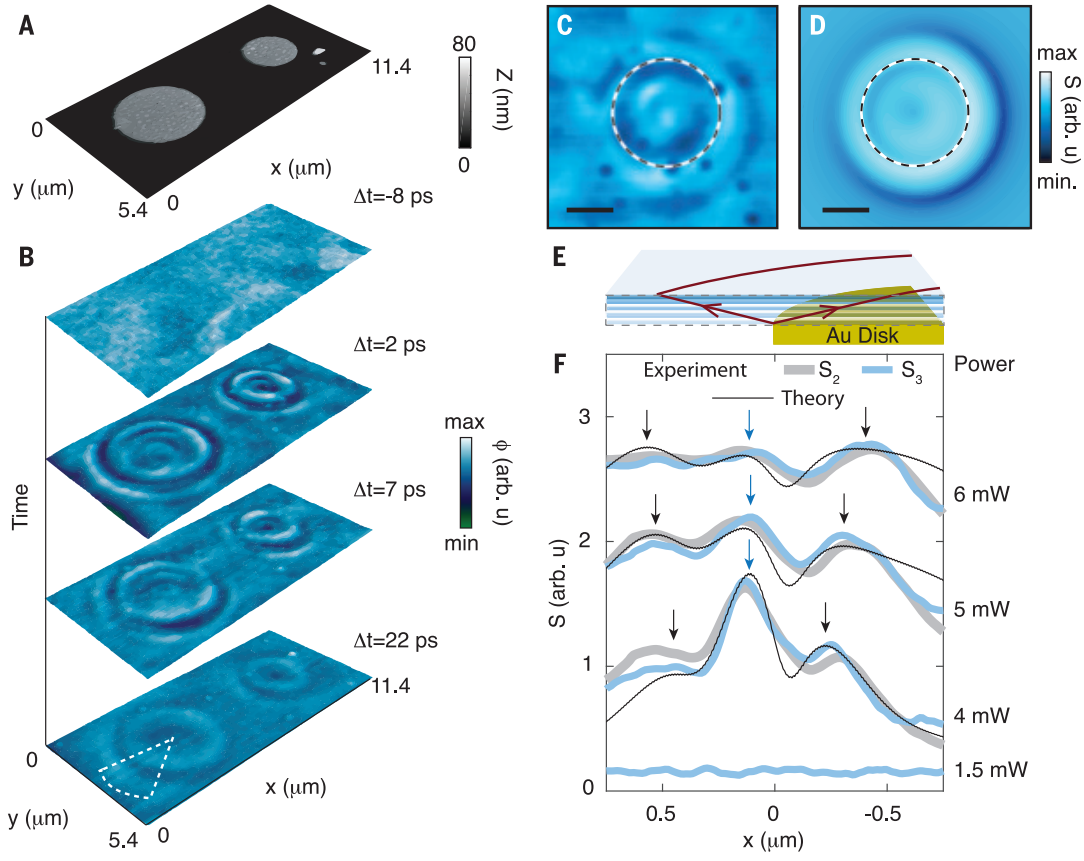

Fig. 3. Switchable transient hyperbolic polaritons revealed by nano-imaging. (**A**) Topographic image showing two gold antennas. (**B**) A 440-nm-thick WSe_2 slab was transferred on top of the antennas. Images of nano-optical phase (ϕ) contrast measured at ω = 910 cm^{-1} after photoexcitation with a 5-mW pump beam for a series of Δt are shown. (**C**) Near-field amplitude from the same data set shown in (B) at Δt = 2 ps. (**D**) Near-field amplitude calculated with n_x = 1.9 × 10^{19} cm^{-3}, γ = 30 meV, C = 1.2, and d_{diff} = 170 nm using the MW model (see supplementary notes S5 and S6). The scale bars are 1 μm in length and the edge of the gold disks beneath the crystal are indicated with dashed lines in (C) and (D). (**E**) Schematic of hyperbolic polaritons launching. (**F**) One-dimensional line profiles of S measured at the second (gray) and third (light blue) harmonics of the tip-tapping frequency. The data were recorded on a 450-nm-thick flake with a probe frequency of ω = 770 cm^{-1} at Δt = 2 ps for a series of applied pump powers. The line profiles were averaged over a 40° arc located approximately at the white dashed lines at Δt = 22 ps in (B). The solid black lines are theoretical calculations (see supplementary note S5). The arrows indicate the positions where maxima are observed in our calculations. The curves in (F) are vertically offset. The horizontal axis is relative to the edge of the disk [see (E) and supplementary note S5].

absorption (Fig. 2C and supplementary note S2). The totality of data in Fig. 2 establishes the zero-crossing character of ε_1^{ab}, which is transiently driven in WSe_2, a precondition for photo-induced hyperbolicity.

To visualize hyperbolic wave packets that propagate through the bulk of WSe_2, we patterned several optical antennas on an SiO_2 substrate (Fig. 3A), and exfoliated WSe_2 crystals on top of the antenna array. In Fig. 3B, we display representative transient images collected using narrowband mid-infrared probe pulses (supplementary note S1) at varying time delays after photoexcitation (Δt). In the steady state (Δt < 0), nearly featureless images (Fig. 3B and fig. S4) attest to the opaque character of WSe_2 for nano-infrared visualization of buried antennas. Photoexcitation prompts the appearance of images in the form of concentric "hot rings" of enhanced nano-infrared contrast surrounding the edges of gold disks. The hot rings are evident in images of both near-field amplitude and phase φ (Figs. 3, B and C) and are consistent with the notion of conical propagation of hyperbolic polaritons introduced in Fig. 1. Our theoretical calculations predict the appearance of hot rings in a material in which photo-induced dielectric response is described by the MW model (Fig. 3D). The hyperbolic hot rings were observed for tens of picoseconds after photoexcitation (Fig. 3B), in agreement with the dynamics of n_x (Fig. 2, A and B). Therefore, our experiment described in Fig. 3 demonstrates real-space signatures of switchable transient hyperbolic polaritons.

We then demonstrated that the directional propagation of hyperbolic polaritons in WSe_2 is programmable by varying the photoexcitation density. We considered the line profiles of S with representative data displayed in Fig. 3F. The lowest photoexcitation power of P = 1.5 mW was insufficient to drive ε_1^{ab} below zero, and nearly featureless line profiles were correspondingly observed. Data obtained with increasing pump power revealed maxima inside and outside of the gold disk's edge. The lateral distance between these maxima and the edge of the antennae, δr (Fig. 1A), increased systematically with increasing photoexcitation power. In addition to these two humps, a central peak can also be observed in Fig. 3F, the magnitude of which is dependent on P.

Our modeling provides a quantitative account of the observed line forms (supplementary note S5). The slope of polaritonic trajectories |tanθ| is given by the following equation (*3*):

$$\frac{dr}{dz} = |\tan\theta| = i\sqrt{\varepsilon^{ab}}/\sqrt{\varepsilon^{c}} \qquad (1)$$

Hyperbolic rays reach the top surface of WSe_2 at the coordinate δr (Fig. 1A). If the hyperbolic medium is homogeneous, then $\delta r = d|\tan\theta|$, where d is the sample thickness and θ is the angle from the surface normal. However, our transient hyperbolic medium is not uniform. In our experimental geometry, the gold antenna also acted as a mirror for pump radiation, further enhancing the photoexcitation density within the limelight of the reflected pump beam. Thus, the slope of the conical trajectory (Eq. 1) may vary along the pathway of the polaritonic rays.

The best fits to the experimental amplitude profiles were obtained with a monotonic increase of the adjustable parameter n_x with increasing power. The extracted trend of $n_x(P)$ is in good agreement with our nano-FTIR measurements (Fig. 2C and table S1). The central peak is linked to the heterogeneous carrier distribution in our model, which disappears with increasing power consistent with the trend of saturable absorption (Fig. 2C and supplementary note S5). These data demonstrate

that the directional propagation of hyperbolic polaritons can be dynamically controlled by manipulating the photoexcitation density.

Next, we elaborate on the physics of photoexcitation of MX_2 semiconductors with the pump beam red detuned from the optical gap. At modest excitation densities below the Mott threshold for exciton melting, n_{mott} (*33*, *34*), optically generated electron-hole pairs form Coulomb-bound excitons (*2*, *35*). Because all data shown in Figures 1 to 3 were collected below n_{mott} (supplementary note S4), we conclude that excitons dominate the photo-induced hyperbolic dynamics. Below n_{mott}, quantum transitions (QTs) between different states within the excitonic Rydberg series are known to produce long-lived spectral weight at mid-infrared frequencies in MX_2 semiconductors (*27*, *28*). For sufficiently large exciton densities, Rydberg polaritons may be formed in which transitions of excitons between states with differing quantum number couple to photons.

The Rydberg polariton scenario naturally accounts for the requisite anisotropy and the hyperbolic response of WSe_2 (Fig. 3). The spectral weight of QTs is proportional to the bound carrier density, n_x (*27*, *28*). The eigenenergy E and wave function ψ of the bound states are obtained from a solution of the MW model as follows:

$$\left\{-\frac{1}{2}\nabla^2-\frac{1}{(r^2-\kappa z^2)^{1/2}}\right\}\psi=E\psi \qquad (2)$$

where the single parameter $\kappa=1-\varepsilon^{ab}_{stat}m^{ab}/\varepsilon^{c}_{stat}m^{c}$, which absorbs the static permittivity and effective mass, governs anisotropy of the excitonic dielectric response (*29*). Given the strong anisotropy ($\kappa \cong 0.8$) of WSe_2, the MW model predicts that a hyperbolic response can be realized throughout a broad range of the infrared frequencies, which is consistent with our data. Thus, Rydberg polaritons provide a tunable platform for enabling on-demand hyperbolicity and for routing strongly confined "nanolight" at mid-infrared frequencies.

The observed hyperbolic polaritons manifest in programmable waveguiding and confinement of radiation on subdiffractional length scales. Unlike hyperbolic phonon-polaritons (*8*, *13*–*20*, *36*), in which the propagation direction is set by the rigid atomic arrangement of the crystal lattice, the directional flow of hyperbolic Rydberg polaritons stemming from electronic processes can be tuned by simply varying the optical excitation density (Fig. 3F). Here, we have demonstrated in operando tunability at the extreme: switching hyperbolicity on and off at will with subpicosecond optical excitation. Tunable hyperbolicity within the MX_2 species offers an encouraging modus operandi for control over the directional propagation of nanolight.

REFERENCES AND NOTES

1. K. S. Novoselov, A. Mishchenko, A. Carvalho, A. H. Castro Neto, *Science* **353**, aac9439 (2016).
2. G. Wang *et al.*, *Rev. Mod. Phys.* **90**, 021001 (2018).
3. R. K. Fisher, R. W. Gould, *Phys. Lett. A* **31**, 235–236 (1970).
4. J. Taboada-Gutiérrez *et al.*, *Nat. Mater.* **19**, 964–968 (2020).
5. K. Chaudhary *et al.*, *Sci. Adv.* **5**, eaau7171 (2019).
6. T. Low *et al.*, *Nat. Mater.* **16**, 182–194 (2017).
7. K.-D. Park *et al.*, *Sci. Adv.* **5**, eaav5931 (2019).
8. S. Dai *et al.*, *Science* **343**, 1125–1129 (2014).
9. M. A. Huber *et al.*, *Nat. Nanotechnol.* **12**, 207–211 (2017).
10. W. Ma *et al.*, *Nature* **562**, 557–562 (2018).
11. M. Mrejen, L. Yadgarov, A. Levanon, H. Suchowski, *Sci. Adv.* **5**, eaat9618 (2019).
12. F. Hu *et al.*, *Nat. Photonics* **11**, 356–360 (2017).
13. P. Li *et al.*, *Science* **359**, 892–896 (2018).
14. M. Chen *et al.*, *Nat. Mater.* **19**, 1372 (2020).
15. G. Hu *et al.*, *Nature* **582**, 209–213 (2020).
16. J. Duan *et al.*, *Nano Lett.* **20**, 5323–5329 (2020).
17. Z. Zheng *et al.*, *Adv. Mater.* **30**, e1705318 (2018).
18. Z. Zheng *et al.*, *Sci. Adv.* **5**, eaav8690 (2019).
19. D. N. Basov, A. Asenjo-Garcia, P. J. Schuck, X.-Y. Zhu, A. Rubio, *Nanophotonics* **10**, 549–577 (2020).
20. J. D. Caldwell *et al.*, *Nat. Rev. Mater.* **4**, 552–567 (2019).
21. A. J. Hoffman *et al.*, *J. Appl. Phys.* **105**, 122411 (2009).
22. G. Hu, A. Krasnok, Y. Mazor, C.-W. Qiu, A. Alù, *Nano Lett.* **20**, 3217–3224 (2020).
23. I. Epstein *et al.*, *2D Materials* **7**, 035031 (2020).
24. P. Li *et al.*, *Nat. Commun.* **6**, 7507 (2015).
25. Z. Jacob *et al.*, *Appl. Phys. B* **100**, 215–218 (2010).
26. H. N. S. Krishnamoorthy, Z. Jacob, E. Narimanov, I. Kretzschmar, V. M. Menon, *Science* **336**, 205–209 (2012).
27. P. Merkl *et al.*, *Nat. Commun.* **11**, 2167 (2020).
28. C. Poellmann *et al.*, *Nat. Mater.* **14**, 889–893 (2015).
29. T. G. Pedersen, S. Latini, K. S. Thygesen, H. Mera, B. K. Nikolić, *New J. Phys.* **18**, 073043 (2016).
30. M. Eisele *et al.*, *Nat. Photonics* **8**, 841–845 (2014).
31. M. Wagner *et al.*, *Nano Lett.* **14**, 894–900 (2014).
32. A. S. McLeod *et al.*, *Phys. Rev. B* **90**, 085136 (2014).
33. A. Chernikov, C. Ruppert, H. M. Hill, A. F. Rigosi, T. F. Heinz, *Nat. Photonics* **9**, 466–470 (2015).
34. A. J. Sternbach *et al.*, *Nat. Commun.* **11**, 3567 (2020).
35. J. Wang *et al.*, *Sci. Adv.* **5**, eaax0145 (2019).
36. T. G. Folland *et al.*, *Nat. Commun.* **9**, 4371 (2018).

ACKNOWLEDGMENTS

Funding: This work is supported as part of Programmable Quantum Materials, an Energy Frontier Research Center funded by the U.S. Department of Energy (DOE), Office of Science, Basic Energy Sciences (BES), under award no. DE-SC0019443. D.N.B. is a Moore Investigator in Quantum Materials EPIQS no. 9455. The development of pump-probe nanoscale optics at Columbia is supported by Vannevar Bush Faculty Fellowship no. N00014-19-1-2630. We acknowledge support from the European Research Council (ERC-2015-AdG694097) and the Cluster of Excellence "Advanced Imaging of Matter" (AIM). Support by the Flatiron Institute, a division of the Simons Foundation, is acknowledged. S.L. acknowledges support from the Alexander von Humboldt foundation. S.H.C. and J.H. were supported by the National Research Foundation of Korea through the Global Research Laboratory (GRL) program (2016K1A1A2912707). Synthesis of WSe2 was supported by the NSF MRSEC Program through Columbia in the Center for Precision-Assembled Quantum Materials (DMR-2011738). We acknowledge workshops and conferences at the Max Planck Institute - New York City Center for Non-Equilibrium Quantum Phenomena for providing forum for discussions. **Author contributions:** A.J.S. and D.N.B. conceived the study. S.H.C. performed sample fabrication supervised by B.L., D.R., B.K., and J.H. A.J.S. and S.H.C. performed the experiments with assistance from Y.S. S.L. computed the parameters of the Mott-Wannier model with supervision from A.R. A.A.R. performed electrostatic simulations with assistance from A.J.S. and supervision from M.F. P.J.S., X.X., X.-Y.Z., and R.D.A., who also helped to interpret the results. D.N.B. coordinated and supervised the work. A.J.S. and D.N.B. wrote the manuscript with the input of all coauthors. **Competing interests:** The authors declare no competing financial interests. **Data and materials availability:** All data needed to evaluate the conclusions in the study are present in the main text or the supplementary materials.

SUPPLEMENTARY MATERIALS

science.sciencemag.org/content/371/6529/617/suppl/DC1
Materials and Methods
Figs. S1 to S6
Tables S1 to S2
References (*37*–*44*)
MDAR Reproducibility Checklist

24 September 2020; accepted 22 December 2020
10.1126/science.abe9163

ORGANIC CHEMISTRY

Electrophotocatalytic diamination of vicinal C–H bonds

Tao Shen and Tristan H. Lambert*

The conversion of unactivated carbon-hydrogen (C–H) bonds to carbon–nitrogen (C–N) bonds is a highly valued transformation. Existing strategies typically accomplish such reactions at only a single C–H site because the first derivatization diminishes the reactivity of surrounding C–H bonds. Here, we show that alkylated arenes can undergo vicinal C–H diamination reactions to form 1,2-diamine derivatives through an electrophotocatalytic strategy, using acetonitrile as both solvent and nitrogen source. The reaction is catalyzed by a trisaminocyclopropenium (TAC) ion, which undergoes anodic oxidation to furnish a stable radical dication while the cathodic reaction reduces protons to molecular hydrogen. Irradiation of the TAC radical dication (wavelength of maximum absorption of 450 to 550 nanometers) with a white-light compact fluorescent light generates a strongly oxidizing photoexcited intermediate. Depending on the electrolyte used, either 3,4-dihydroimidazole or aziridine products are obtained.

Chemical reactions that convert ubiquitous but relatively inert carbon-hydrogen (C–H) bonds to valuable carbon–nitrogen (C–N) bonds can greatly accelerate the construction of complex molecules, particularly those relevant to the biomedical enterprise (*1*). Accordingly, a variety of C–H amination reactions have been devised, ranging from classic transformations such as the Hofmann-Löffler-Freytag reaction to modern methods that involve transition metal or photoredox catalysis (*2*, *3*). Despite the power and scope of these advances, the vast majority of such methods

Department of Chemistry and Chemical Biology, Cornell University, Ithaca, NY 14850, USA.
*Corresponding author. Email: tristan.lambert@cornell.edu

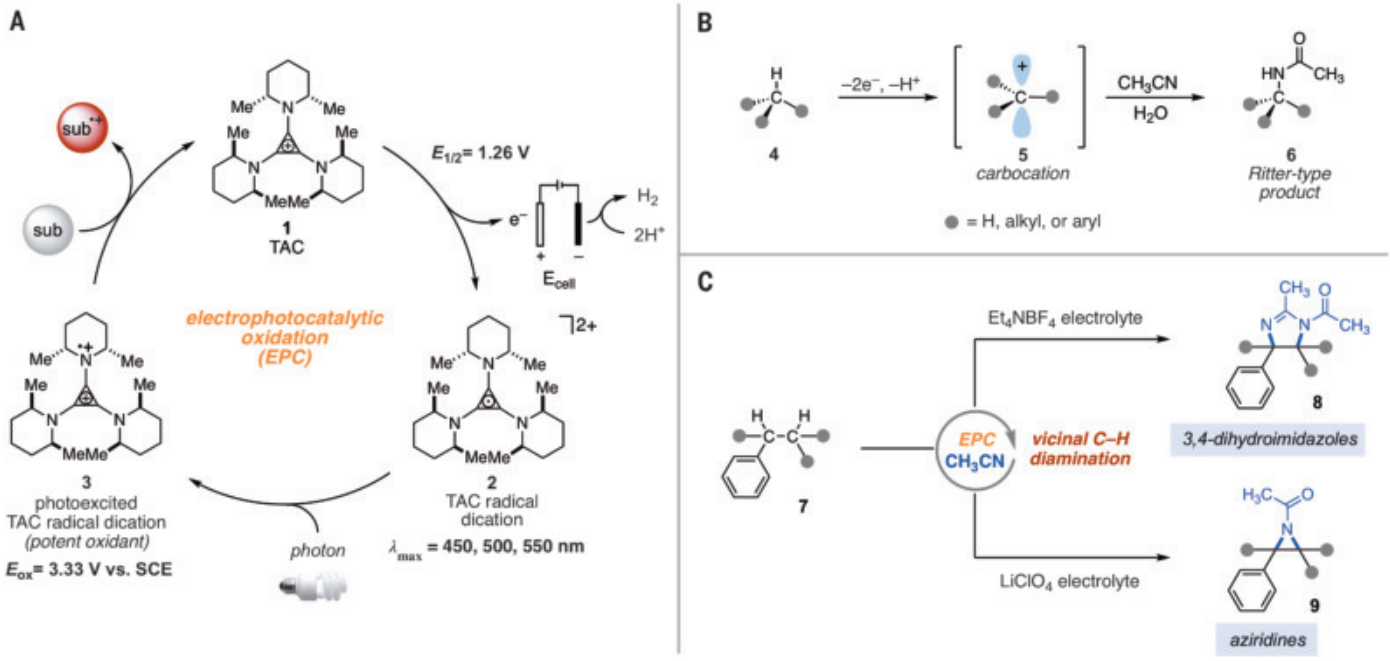

Fig. 1. Electrophotocatalytic amination of C–H Bonds. (**A**) Generic electrophotocatalytic cycle with trisaminocyclopropenium (TAC) **1**. (**B**) Ritter-type C–H amination reaction. (**C**) Electrophotocatalytic vicinal C–H diamination reactions reported in this work. Sub, substrate; sub_{ox}, oxidized substrate; Me, methyl; Et, ethyl; Ac, acetyl; E_{ox}, oxidation potential; λ_{max}, wavelength of maximum absorption.

result in the transformation of only single C–H bonds, whereas many synthetic campaigns require the installation of numerous C–N linkages. Thus, the development of chemical reactions that produce multiple C–H bond activation events concurrently promise great value to the field of chemical synthesis. However, one of the major challenges to developing such reactions is that the installation of heterofunctionality tends to deactivate surrounding bonds toward the typical mechanistic modes of C–H activation. Accordingly, few reaction technologies have been reported that accomplish this type of multipotent functionalization on proximal C–H bonds (*4*).

We recently reported a strategy for potent oxidation chemistry that combined the energy of light and electricity within a single catalyst, a process termed electrophotocatalysis (EPC) (*5*–*7*). This strategy involved electrochemical oxidation of the trisaminocyclopropenium (TAC) ion **1** under a relatively mild electrochemical potential and concomitant visible light irradiation to excite the resulting radical dication intermediate **2** (Fig. 1A). The photoexcited radical dication **3** is an extremely potent oxidant, which we demonstrated could promote challenging reactions such as the oxidative functionalization of benzene and other electron-poor arenes or the regioselective C–H functionalization of ethers. We speculated that the oxidizing power of **1** might also enable other C–H bond activation manifolds. In particular, we hypothesized that under the right conditions, the electrophotocatalytic (*8*–*13*) approach might lead to the generation of carbocation intermediates, which would enable the Ritter-type functionalization of C–H bonds without the need for an external chemical oxidant. Ritter-type reactions involve the generation of a carbocation **5** with subsequent trapping by a nitrile (usually as solvent), which leads to the formation of nitrilium ion intermediates and, after hydrolysis, amide products **6** (Fig. 1B) (*14*, *15*). If the carbocation is generated from the corresponding C–H bond, Ritter-type processes provide an avenue to achieve C–H amination, and several methods have been developed that accomplish this type of transformation (*16*–*18*). We speculated that the strongly oxidizing yet selective conditions offered by TAC EPC might enable a sequence of multiple Ritter-type C–H functionalization reactions, in which the initially formed acetamide group facilitated a second amination reaction at an adjacent (vicinal) position. If feasible, such a process could enable the regioselective amination of two C–H bonds by using simply visible light, a mild electrochemical potential, and a common solvent (acetonitrile) as the nitrogen source rather than potentially explosive nitrene precursors. Here, we report the realization of this electrophotocatalytic diamination of vicinal C–H bonds to furnish either dihydroimidazoles **8** or aziridines **9**, depending on the electrolyte used (Fig. 1C).

After extensive screening of reaction conditions—including the cell potential, electrolyte, acid additive, and reaction time—we identified reaction conditions that enabled the efficient conversion of a variety of benzylic hydrocarbons to the corresponding *N*-acyl-4,5-dihydroimidazole adducts (Fig. 2; optimization with phenylcyclopentane is provided in table S1). The reaction setup involved visible light irradiation with a white compact fluorescent light (CFL) of a solution of the substrate, 8 mol % TAC **1**, and tetraethylammonium tetrafluoroborate (Et_4NBF_4) in 5:1 acetonitrile: trifluoroacetic acid (TFA) solution within a divided electrolytic cell (carbon felt anode and platinum plate cathode) under controlled potential [2.4 V, anode potential (E_{anode}) = 1.3 V versus Ag/AgCl]. The TAC catalyst and the substrate were contained within the anodic chamber, which was where the C–H diamination chemistry occurred. The electrochemical reaction was balanced by the cathodic reduction of protons to molecular hydrogen, providing an effectively traceless redox by-product. Using these conditions, a variety of benzylic hydrocarbons were found to undergo vicinal C–H diamination. No more than trace amounts of such products could be detected without the catalyst **1** or in the absence of irradiation. In addition, no traditional oxidants were found to promote this transformation, including $K_2S_2O_8$, oxone, *tert*-butyl hydrogen peroxide (TBHP), MnO_2, $Mn(OAc)_3$, $HClO_4$, phenyliodine(III) diacetate (PIDA), ceric ammonium nitrate (CAN), or O_2.

Using this procedure, isopropylbenzene (cumene) was converted to adduct **10** in 72% yield (Fig. 2). Halogen substitution on the aryl ring was also tolerated (**11** to **14**), as was a protected anilino nitrogen (**15**) and a bromomethyl substituent (**16**). On the other hand, 4-isopropylbiphenyl did not lead to any of the diaminated product **17**; instead, the reaction

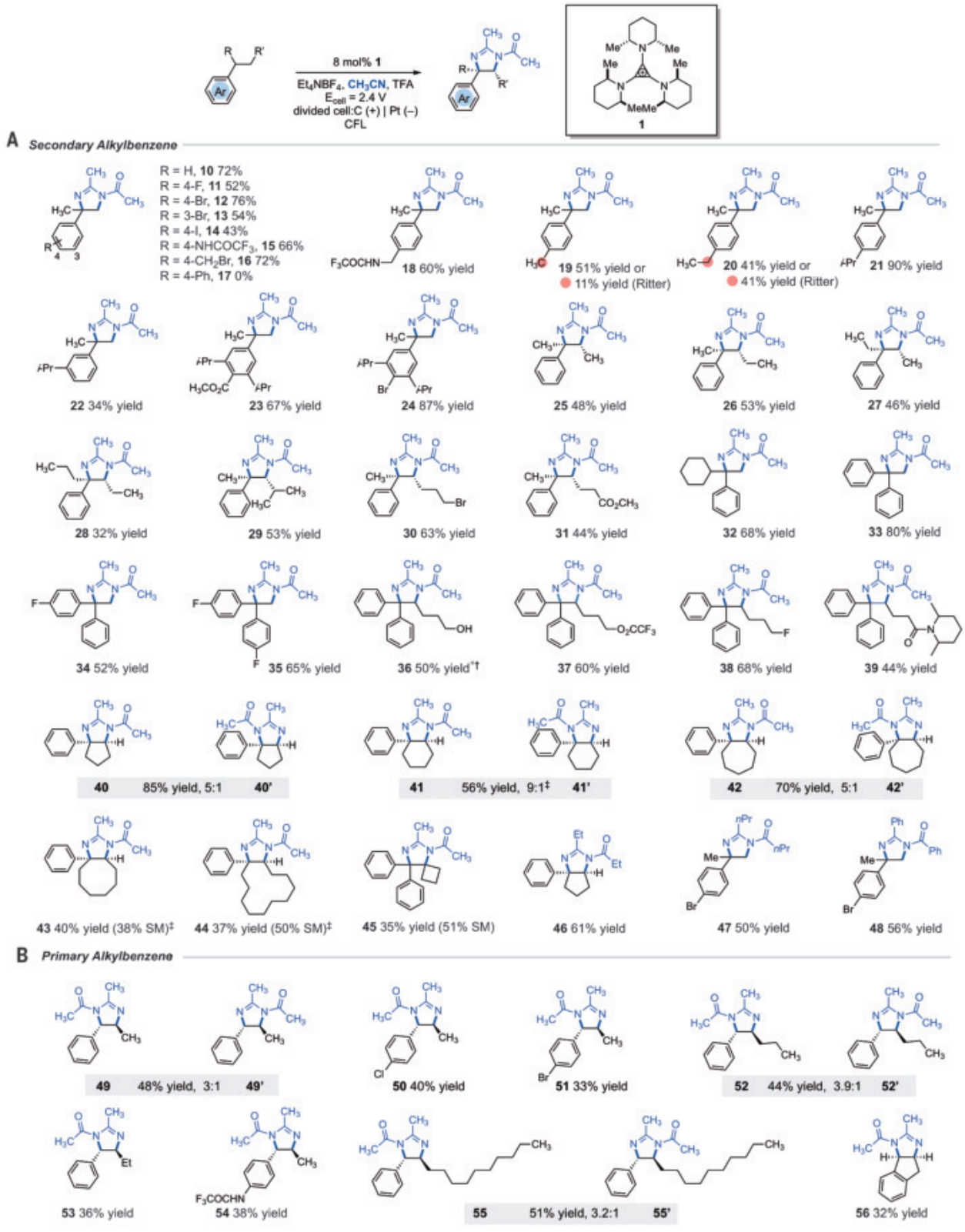

Fig. 2. Substrate scope of electrophotocatalytic vicinal C–H diamination. All yields are of isolated products. Products were obtained as racemic mixtures; wedge and dash depictions indicate relative stereochemical relationships. (**A**) Diamination of secondary alkylbenzenes. (**B**) Diamination of primary alkylbenzenes. Experimental details are provided in thesupplementary materials. An asterisk indicates run at 2.2 V; a dagger symbol (†) indicates work-up with $NaHCO_3$ (aq) and CH_3OH; and a double dagger dymbol (‡) indicates nBu_4NPF_6 instead of Et_4NBF_4. SM, starting materials. Compound **36** was deacylated upon workup.

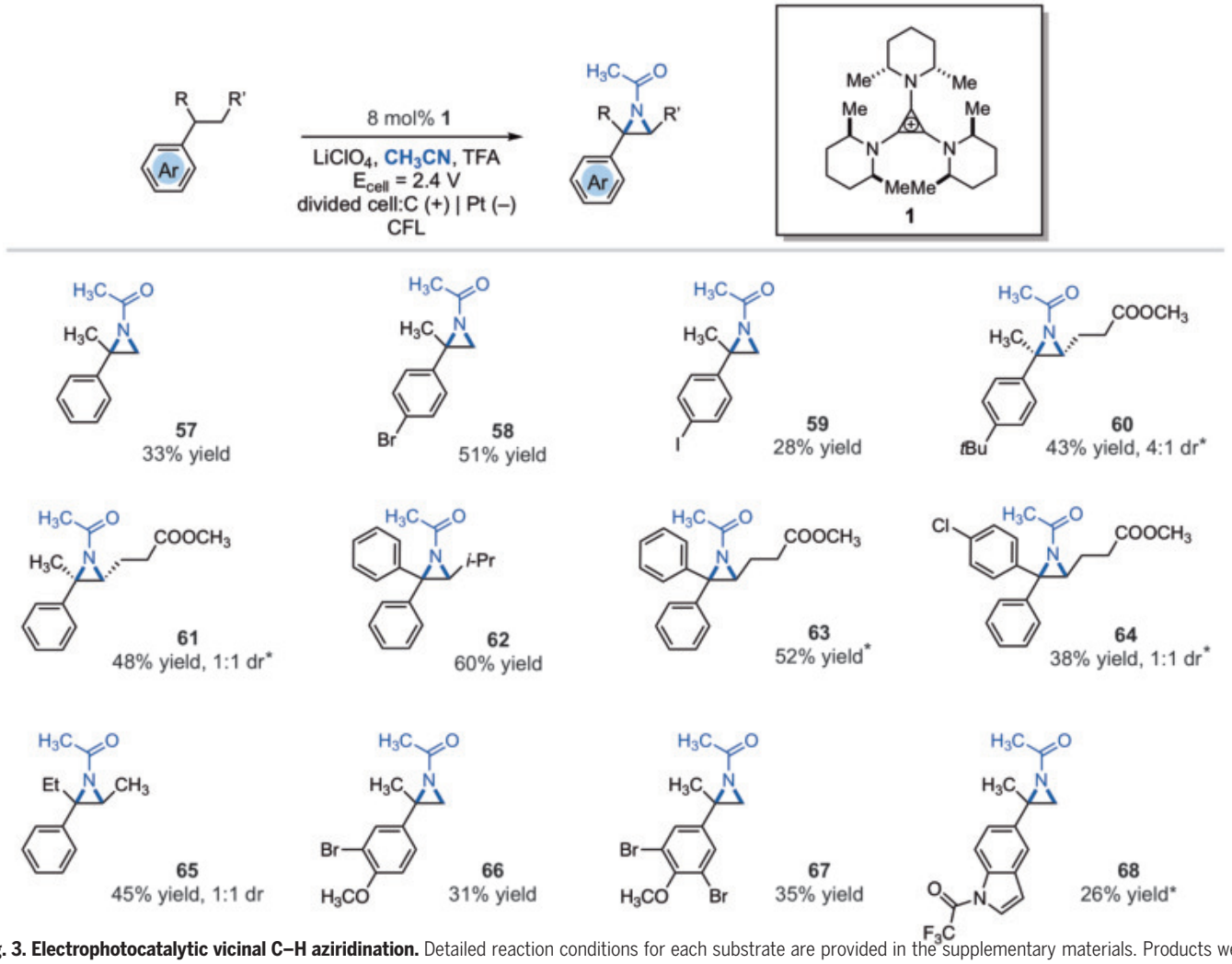

Fig. 3. Electrophotocatalytic vicinal C–H aziridination. Detailed reaction conditions for each substrate are provided in the supplementary materials. Products were obtained as racemic mixtures; wedge and dash depictions indicate relative stereochemical relationships. An asterisk indicates run at 2.2 V. *i*-Pr, isopropyl.

mixture turned black, and an unidentified mixture of products was generated. Despite the strongly oxidizing conditions, a benzylic trifluoroacetamide group was reasonably well tolerated (**18**). When 4-methylisopropylbenzene (*p*-cymene) was used, a 51% yield of the diaminated product **19** was generated, along with an 11% yield of the product arising from Ritter reaction of the benzylic methyl group. This alternative process was even more competitive with 4-ethylisopropylbenzene, with which a 41% yield of the diaminated adduct **20** was accompanied by 41% of the ethyl-functionalized product. By contrast, 1,4-diisopropylbenzene underwent efficient conversion to adduct **21** in which only one of the isopropyl groups was diaminated. The isomeric 1,3-diisopropylbenzene also furnished adduct **22**, although the efficiency was notably lower in this case. In the reactions to form **21** and **22**, we only observed products resulting from functionalization of one of the benzylic carbons. Similarly, methyl 2,4,6-triisopropylbenzoate and 2,4,6-triisopropylbromobenzene were functionalized exclusively on the 4-isopropyl group to furnish **23** and **24**, respectively, in good to high yields.

We also examined the site selectivity for amination of the nonbenzylic carbon (**25** to **32**). In all cases, functionalization of methylene carbons occurred in preference to methyl carbons, even when the presence of a sterically demanding group (**29**) or electron-withdrawing groups (**30** and **31**) might have modified the outcome. By contrast, a substrate probing the competition between a methyl and a methine carbon led exclusively to adduct **32** in which the methyl was functionalized preferentially.

Because α,α-diaryl amines are a valuable substructure in biomedically relevant compounds, we also investigated this transformation on gem-diaryl substrates. We found that 1,1-diphenylethane reacted efficiently to furnish compound **33** in 80% yield. Fluorine substituents on one (**34**) or both (**35**) rings was tolerated, albeit with a slight decrease in yield. Meanwhile, the compatibility of alcohol, ester, alkyl fluoride, and amide substituents enabled the synthesis of the more highly functionalized adducts **36** to **39**.

We also investigated the capacity of this reaction to functionalize ring systems. Reaction of phenylcyclopentane led to the bicyclic compound in 85% yield, formed as a 5:1 mixture of *N*-acyl isomers (**40** and **40′**). Similarly, the six- and seven-membered ring products **41** and **42**, respectively, were also produced as regioisomeric mixtures, whereas eight-membered and 12-membered ring products **43** and **44**, respectively, were produced as single isomers. Some of the yields for cyclic substrates were improved by the use of tetrabutylammonium phosphate ($TBAPF_6$) as the electrolyte. The spiro compound **45** was also accessible, demonstrating functionalization of a C–H bond in a strained ring. Furthermore, in addition to acetonitrile, other nitriles could also be used in this reaction, giving rise to diaminated products **46** to **48** derived from propionitrile, butyl nitrite, or benzonitrile as the nitrogen source.

We also evaluated the diamination process with unbranched benzylic substrates.

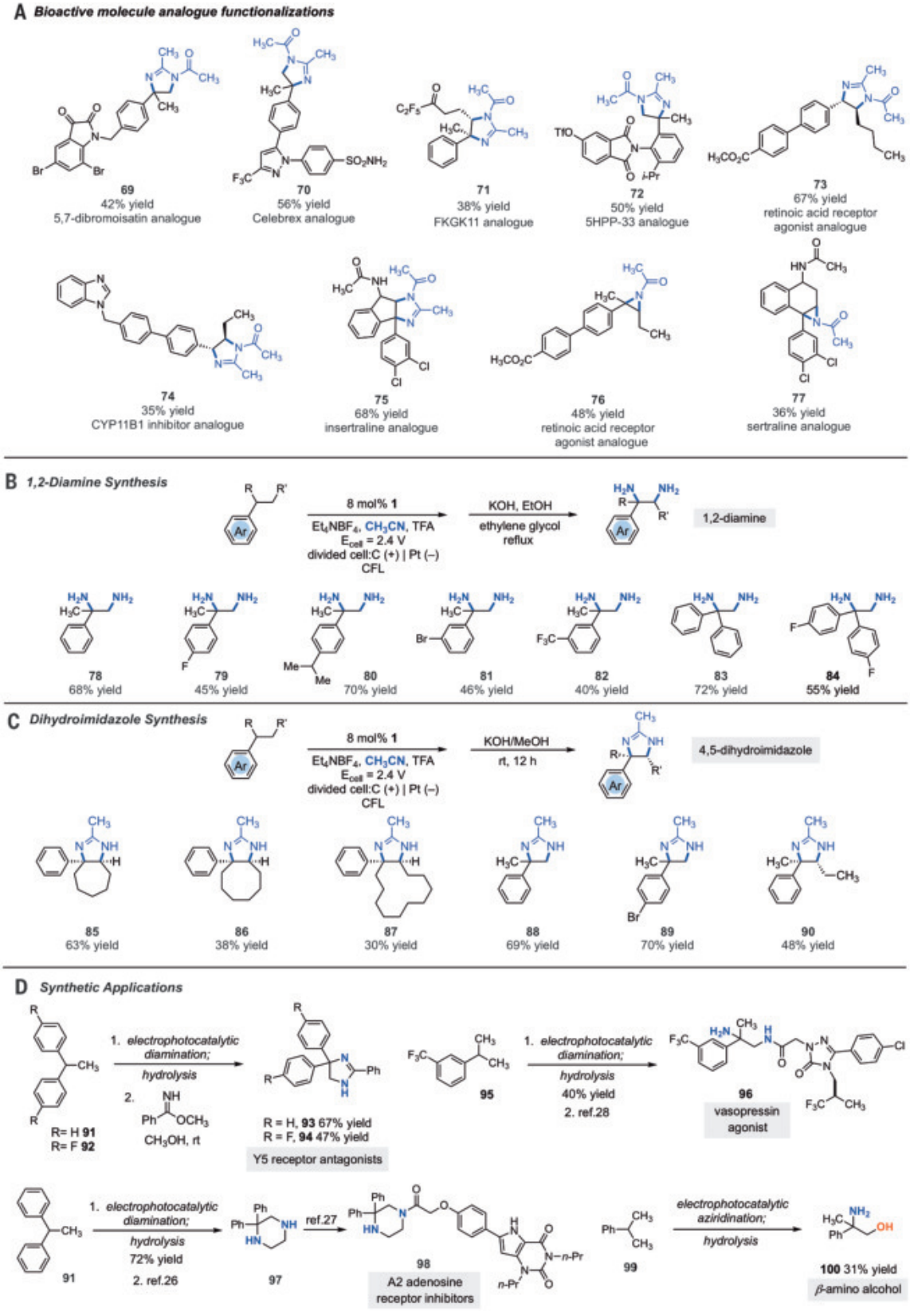

Fig. 4. Synthetic applications of electrophotocatalytic vicinal C–H diamination. (**A**) Bioactive compound analogs prepared by means of electrophotocatalytic vicinal C–H diamination or aziridination. (**B**) 1,2-Diamine synthesis. (**C**) Dihydroimidazole synthesis. (**D**) Bioactive compound synthesis. Detailed reaction conditions are provided in the supplementary materials. Products were obtained as racemic mixtures; wedge and dash depictions indicate relative stereochemical relationships. Products **80** and **81** were isolated as bis tosylate salts. Ph, phenyl; Tf, trifluoromethanesulfonate.

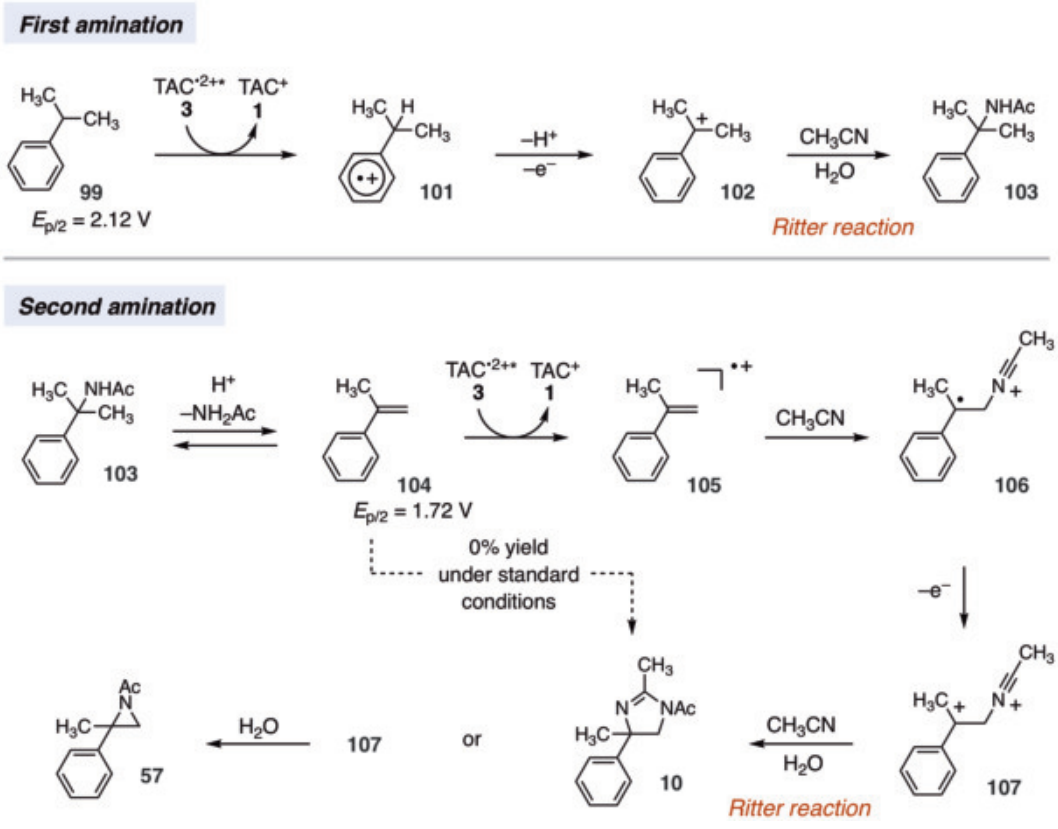

Fig. 5. Mechanistic rationale for electrophotocatalytic vicinal C–H diamination. Voltages were measured in a 5:1 mixture of CH_3CN and TFA to mimic the reaction conditions and are relative to SCE.

Both *n*-propylbenzene and halogenated *n*-propylbenzenes reacted with CH_3CN to deliver products **49** to **51** in moderate yields. For *n*-propylbenzene, two isomers (**49** and **49′**) were obtained in a 3:1 ratio; the major product had the opposite acyl group regioselectivity to that observed with the branched substrates. Similar regioselectivity was also observed when longer alkyl chain substrates such as *n*-butylbenzene (**52** and **52′**) and *n*-dodecylbenzene (**55** and **55′**) were used. Additionally, cyclic indane could be functionalized to furnish adduct **56** in 32% yield.

During the course of our studies, we discovered that changing the electrolyte from Et_4NBF_4 to $LiClO_4$ resulted in an alternative vicinal C–H difunctionalization product: *N*-acyl aziridines (Fig. 3). Thus, cumene and halogenated derivatives gave rise to aziridines **57** to **59** in low to modest yields, along with nearly equal yields of the diaminated products. Other oxidants we tried did not deliver any of the aziridine or diamination products (tables S3 and S4). With substrates bearing a pendant carboxyl substituent, the aziridine products **60** and **61** were the major ones. Product yields were somewhat higher with *gem*-diaryl substrates (**62** to **64**). Reaction of 3-phenylpentane led to the formation of aziridine **65** in modest yield as a 1:1 mixture of diastereomers. In general, substrates bearing electron-rich aryl rings did not participate well in this process; however, we were able to prepare adducts **66** to **68** in modest yields. The reason for the formation of aziridines when changing the electrolyte to a perchlorate salt is not obvious, but presumably, the counterions (supplied by the electrolyte) affect the stability of a key cationic intermediate. We speculate that the perchlorate salts lead to collapse of this intermediate to form an aziridine ring before a second solvolysis step can occur, as happens with tetrafluoroborate counterions (more complete mechanistic discussion is available in the supplementary materials).

Because late-stage C–H functionalization processes offer powerful tools for the diversification of medicinal compound libraries, we decided to test this difunctionalization chemistry on several molecules that are close analogs of known biologically active molecules (Fig. 4A). Thus, we found that a dibromoisatin derivative could be diaminated to produce compound **69** in 42% yield. Isatin derivatives have been investigated for a number of medicinal properties, including antitumor and antiviral activities (*19*). We also found that the celecoxib (Celebrex) analog **70** could be produced in 56% yield under standard conditions. FKGK11 is a group VIA calcium-independent phospholipase A2 inhibitor (*20*), and we found that the methylated derivative analog **71** could be accessed in 38% yield. Meanwhile, an analog of thalidomide 5HPP-33, which has shown antiproliferative activity against nine cancer cell lines in vitro (*21*), was converted to **72** in 50% yield after protection of the phenolic hydroxyl group as a triflate group. We also found that a retinoic acid receptor agonist and a CYP11B1 inhibitor (*22*, *23*), both of which possessed a biaryl moiety, were amenable to the diamination procedure to furnish analogs **73** and **74**, respectively. Successful synthesis of the insertraline analog **75** proceeded in 68% yield despite the presence of a potentially sensitive benzylic C–N group. In addition to the diamination products, we also found that the aziridination procedure was operable in a more complex setting, allowing direct access to products **76** and **77**.

Because of the importance of 1,2-diamines for pharmaceutical synthesis, ligands for catalysis, and other applications, it would be highly appealing to synthesize these structures directly from abundant sources. We found that a small modification to our electrophotocatalytic procedure led to the isolation of free 1,2-diamines in good yields (Fig. 4B). Following the diamination procedure described above, treating the crude reaction mixture with KOH, ethanol, and ethylene glycol and heating to reflux furnished the diamine products **78** to **84** (**80** and **81** were isolated as their bistoluenesulfonic acid salts). Cumene (**99**, < $0.03 per milliliter), a petroleum-derived feedstock of the Hock reaction for industrial phenol production, could be efficiently converted into valuable 2-phenylpropane-1,2-diamine **78** ($569 per gram) with this route (*24*). Alternatively, by using similar hydrolysis conditions but at room temperature, the free dihydroimidazole adducts **85** to **90** could be

obtained (Fig. 4C). To further demonstrate the synthetic potential of this method for the generation of valuable compounds, we executed several short synthetic sequences (Fig. 4D). The Y5 receptor antagonists **93** and **94** were prepared in high yield by the electrophotocatalytic diamination of diarylethanes **91** and **92**, followed by hydrolysis and amidine formation (*25*). Alternatively, diamination and hydrolysis of **91**, conversion to piperazine **97**, and acylation afforded the A2 adenosine receptor inhibitor **98** (*26*, *27*). Meanwhile, trifluoromethyl compound **95** was engaged in a similar sequence to synthesize the vasopressin agonist **96** in short order (*28*). Last, cumene (**99**) could also be directly transformed into the important β-amino alcohol **100** ($357 per gram) (*24*) by means of a simple two-step process of aziridination and hydrolysis.

Regarding the mechanism, we believe that the reaction begins with Ritter-type amination of the substrate's benzylic C–H bond in a process that accords with known electrochemical Ritter-type reactions (Fig. 5) (*29*, *30*). In this case, the TAC photoexcited radical dication **3** effects single-electron oxidation of the substrate **99** [half-peak potential ($E_p/2$) = 2.12 V versus saturated calomel electrode (SCE) in 5:1 CH_3CN:TFA] to produce radical cation **101**, after which deprotonation and a second oxidation (presumably by TAC radical dication **2**) reveals the cation **102**. Solvolysis of **102** then furnishes the Ritter adduct **103**. Acetamide **103** converts to the dihydroimidazole product **10** when subjected to the standard reaction conditions. The pathway for the second C–H bond amination is less certain. One likely possibility is that the initially formed Ritter product **103** undergoes a reversible, acid-catalyzed elimination reaction to produce α-methylstyrene **104** (*31*). Single-electron oxidation of α-methylstyrene **104** ($E_p/2$ = 1.72 V versus SCE in 5:1 CH_3CN:TFA) (*32*) with subsequent solvent trapping (*33*) and oxidation events would then lead to the dihydroimidazole product **10** or the aziridine **57**, depending on the electrolyte. We have been able to detect trace amounts of styrenic products in these reactions (fig. S12), and we have indirectly implicated the formation of **104** under related conditions (supplementary materials). However, α-methylstyrene **104** did not furnish any diaminated products when subjected to the standard conditions and instead led to only polymeric material. We speculate that only small steady-state quantities of this intermediate are generated under the reaction conditions, allowing the diamination to occur without the dimerization or oligomerization self-reactions to which styrenes are prone. If so, the conditions are remarkable in that they are potent enough to enable the oxidative functionalization of unactivated C–H bonds while still allowing for the selective reaction of a notoriously sensitive intermediate. A more in-depth mechanistic discussion can be found in the supplementary materials.

The compatibility of the diamination with a reasonable diversity of functionality lends some degree of optimism that this reaction could be of practical utility. Meanwhile, the power of combining light and electrical energy within the operation of a single catalyst has been further shown to hold value for advancing synthetic capabilities.

REFERENCES AND NOTES

1. M. F. Richter *et al.*, *Nature* **545**, 299–304 (2017).
2. H. M. Davies, J. R. Manning, *Nature* **451**, 417–424 (2008).
3. Y. Park, Y. Kim, S. Chang, *Chem. Rev.* **117**, 9247–9301 (2017).
4. A. F. Prusinowski, R. K. Twumasi, E. A. Wappes, D. A. Nagib, *J. Am. Chem. Soc.* **142**, 5429–5438 (2020).
5. H. Huang *et al.*, *Angew. Chem. Int. Ed.* **58**, 13318–13322 (2019).
6. H. Huang, T. H. Lambert, *Angew. Chem. Int. Ed.* **59**, 658–662 (2020).
7. H. Huang, Z. M. Strater, T. H. Lambert, *J. Am. Chem. Soc.* **142**, 1698–1703 (2020).
8. J. C. Moutet, G. Reverdy, *J. Chem. Soc. Chem. Commun.* **0**, 654–655 (1982).
9. R. Scheffold, R. Orlinski, *J. Am. Chem. Soc.* **105**, 7200–7202 (1983).
10. F. Wang, S. S. Stahl, *Angew. Chem. Int. Ed.* **58**, 6385–6390 (2019).
11. H. Yan, Z. W. Hou, H. C. Xu, *Angew. Chem. Int. Ed.* **58**, 4592–4595 (2019).
12. L. Zhang *et al.*, *Nat. Catal.* **2**, 266–373 (2019).
13. W. Zhang, K. L. Carpenter, S. Lin, *Angew. Chem. Int. Ed.* **59**, 409–417 (2020).
14. J. J. Ritter, P. P. Minieri, *J. Am. Chem. Soc.* **70**, 4045–4048 (1948).
15. J. J. Ritter, J. Kalish, *J. Am. Chem. Soc.* **70**, 4048–4050 (1948).
16. Q. Michaudel, D. Thevenet, P. S. Baran, *J. Am. Chem. Soc.* **134**, 2547–2550 (2012).
17. K. Kiyokawa, K. Takemoto, S. Minakata, *Chem. Commun.* **52**, 13082–13085 (2016).
18. T. Duhamel, M. D. Martinez, I. K. Sideri, K. Muniz, *ACS Catal.* **9**, 7741–7745 (2019).
19. G. Krishnegowda *et al.*, *Bioorg. Med. Chem.* **19**, 6006–6014 (2011).
20. C. Baskakis *et al.*, *J. Med. Chem.* **51**, 8027–8037 (2008).
21. Y. Hashimoto, *Bioorg. Med. Chem.* **10**, 461–479 (2002).
22. B. W. Lund *et al.*, *J. Med. Chem.* **48**, 7517–7519 (2005).
23. U. E. Hille, C. Zimmer, C. A. Vock, R. W. Hartmann, *ACS Med. Chem. Lett.* **2**, 2–6 (2011).
24. Prices are from the following vendors: cumene (Sigma-Aldrich, 1 liter); 2-phenylpropane-1,2-diamine (SKU, 1 g); and 2-amino-2-phenyl-propan-1-ol (SKU, 1 g).
25. N. Sato *et al.*, *Bioorg. Med. Chem. Lett.* **19**, 1670–1674 (2009).
26. L. Guandalini *et al.*, *Bioorg. Med. Chem. Lett.* **25**, 1700–1704 (2015).
27. B. Vidal Juan *et al.*, *PCT Int. Appl.* WO/2003/000694 (2003).
28. C. Fuerstner *et al.*, *PCT Int. Appl.* WO/2012/028644 (2012).
29. J. Y. Becker, L. R. Byrd, L. L. Miller, Y.-H. So, *J. Am. Chem. Soc.* **97**, 853–856 (1975).
30. J. Y. Becker, L. R. Byrd, L. L. Miller, *J. Am. Chem. Soc.* **96**, 4718–4719 (1974).
31. C. Metallinos, S. Nerdinger, V. Snieckus, *Org. Lett.* **1**, 1183–1186 (1999).
32. H. G. Roth, N. A. Romero, D. A. Nicewicz, *Synlett* **27**, 714–723 (2016).
33. H. J. P. de Lijser, D. R. Arnold, *J. Org. Chem.* **62**, 8432–8438 (1997).

ACKNOWLEDGMENTS

Funding: Research reported in this publication was supported by the National Institutes of Health under R35 GM127135. **Author contributions:** T.H.L. conceived of and directed the project and prepared the manuscript. T.H.L. and T.S. designed the experiments. T.S. performed the experiments. **Competing interests:** The authors declare no conflicts of interest. **Data and materials availability:** Data are available in the supplementary materials.

SUPPLEMENTARY MATERIALS

science.sciencemag.org/content/371/6529/620/suppl/DC1
Materials and Methods
Figs. S1 to S20
Tables S1 to S5
References (*34*–*44*)
^{1}H and ^{13}C NMR spectra

19 October 2020; accepted 6 January 2021
10.1126/science.abf2798

SURFACE CHEMISTRY

Solvent molecules form surface redox mediators in situ and cocatalyze O_2 reduction on Pd

Jason S. Adams[1], Ashwin Chemburkar[2], Pranjali Priyadarshini[1], Tomas Ricciardulli[1], Yubing Lu[3], Vineet Maliekkal[2], Abinaya Sampath[1], Stuart Winikoff[2], Ayman M. Karim[3], Matthew Neurock[2]*, David W. Flaherty[1]*

Solvent molecules influence the reactions of molecular hydrogen and oxygen on palladium nanoparticles. Organic solvents activate to form reactive surface intermediates that mediate oxygen reduction through pathways distinct from reactions in pure water. Kinetic measurements and ab initio quantum chemical calculations indicate that methanol and water cocatalyze oxygen reduction by facilitating proton-electron transfer reactions. Methanol generates hydroxymethyl intermediates on palladium surfaces that efficiently transfer protons and electrons to oxygen to form hydrogen peroxide and formaldehyde. Formaldehyde subsequently oxidizes hydrogen to regenerate hydroxymethyl. Water, on the other hand, heterolytically oxidizes hydrogen to produce hydronium ions and electrons that reduce oxygen. These findings suggest that reactions of solvent molecules at solid-liquid interfaces can generate redox mediators in situ and provide opportunities to substantially increase rates and selectivities for catalytic reactions.

Solvents influence catalytic reactions by stabilizing reactive intermediates, opening low-barrier reaction pathways, or altering the solubility of reagents (*1*–*3*), which can increase reaction rates and product selectivities by orders of magnitude (*2*–*4*). The direct catalytic participation of solvents is better recognized in homogeneous catalysis (*3*–*5*) than in thermal catalysis at solid-liquid interfaces (*2*), where changes in reaction rates in distinct solvents are often attributed to differences in solubilities or mass

transfer rates (*6*, *7*). Solvents can, however, influence surface chemistry by binding to active sites (*8*), stabilizing surface intermediates (*3*, *9*), or cocatalyzing steps like proton transfer (*10*–*14*). Here, we describe how solvents can also spontaneously form surface-bound redox mediators and control the phase of catalytic metal nanoparticles (NPs).

We discovered these phenomena in our efforts to develop a molecular understanding of how H_2O_2 forms from H_2 and O_2 over Pd NPs (*15*) in the presence of solvent molecules. Most studies have proposed that oxygen reduction occurs through homolytic reactions between chemisorbed oxygen and hydrogen species (*16*–*19*), suggesting that solvents merely affect the solubilities of H_2 and O_2 (*20*). However, H_2O_2 formation requires protic solvents (*21*), and rates of oxygen reduction depend on the pH of the solution (*21*, *22*), which indicates that H_2O_2 forms through solvent-assisted proton-transfer steps (*21*). Yields of H_2O_2 are greater in alcohols and their aqueous mixtures than they are in water, and such improvements are often attributed to the adsorption of alcohols onto the unselective sites of NP surfaces (*8*, *23*).

Through a combination of kinetic isotope effect (KIE) measurements and density functional theory (DFT) simulations, we demonstrate that methanol was activated on Pd to form chemisorbed hydroxymethyl intermediates (CH_2O–H*) that directly transferred electrons and protons to adsorbed oxygen species. The resulting formaldehyde molecules subsequently regenerated hydroxymethyl intermediates through heterolytic oxidation of chemisorbed H atoms. The coupled reactions of this surface redox mediator (CH_2O–H*) resembled cycles that involve electrochemical redox mediators (*24*) and biological coenzymes (*25*), but this mediator underwent redox cycles while maintaining covalent bonds to a catalytic surface. By contrast, liquid-phase water molecules heterolytically oxidized hydrogen to generate electrons within the metal surface and transferred protons to bound oxygen intermediates.

Thus, methanol provided pathways inaccessible to water because hydroxymethyl readily transferred both protons and electrons, whereas water and surface hydroxyls (e.g., O–H*) only transferred protons effectively. Operando x-ray absorption spectroscopy (XAS) showed that methanol-derived intermediates also changed the free energy of NP surfaces and stabilized subsurface hydrogen, which favored β-PdH_x formation. Compared with metallic Pd, the electronic structure of the β-PdH_x surface provided lower-barrier paths for proton-electron transfer (PET) processes while obstructing O-O dissociation paths that inevitably formed H_2O.

We compared transient H_2O_2 formation rates for Pd NPs on SiO_2 in methanol, water, and aqueous methanol (70 vol % CH_3OH) in the absence of mass-transfer constraints (Fig. 1A). Selectivities for the conversion of H_2 to H_2O_2 reached constant values after 6 hours and were 29% for aqueous methanol, 22% for water, and 14% for methanol. Rates of H_2O_2 formation decreased over time in organic solutions but were constant in water. The quantity of supported Pd remained constant (table S1), so these changes show that methanol-derived surface intermediates accumulate on Pd (supplementary text, section S1). Oxidative treatments (e.g., 50 mM H_2O_2 or 800 kPa O_2 at 278 K) remove these species and restore the initial H_2O_2 formation rates (fig. S6, A and B). Moreover, the H_2O_2 formation rates and selectivities changed nonmonotonically with increasing methanol volume fractions, which indicates that methanol-derived intermediates change the rates of the elementary steps that reduce oxygen.

In situ infrared spectra revealed the accumulation of surface species that contained methyl and methylene functions [e.g., ν(CH_3) at 2960

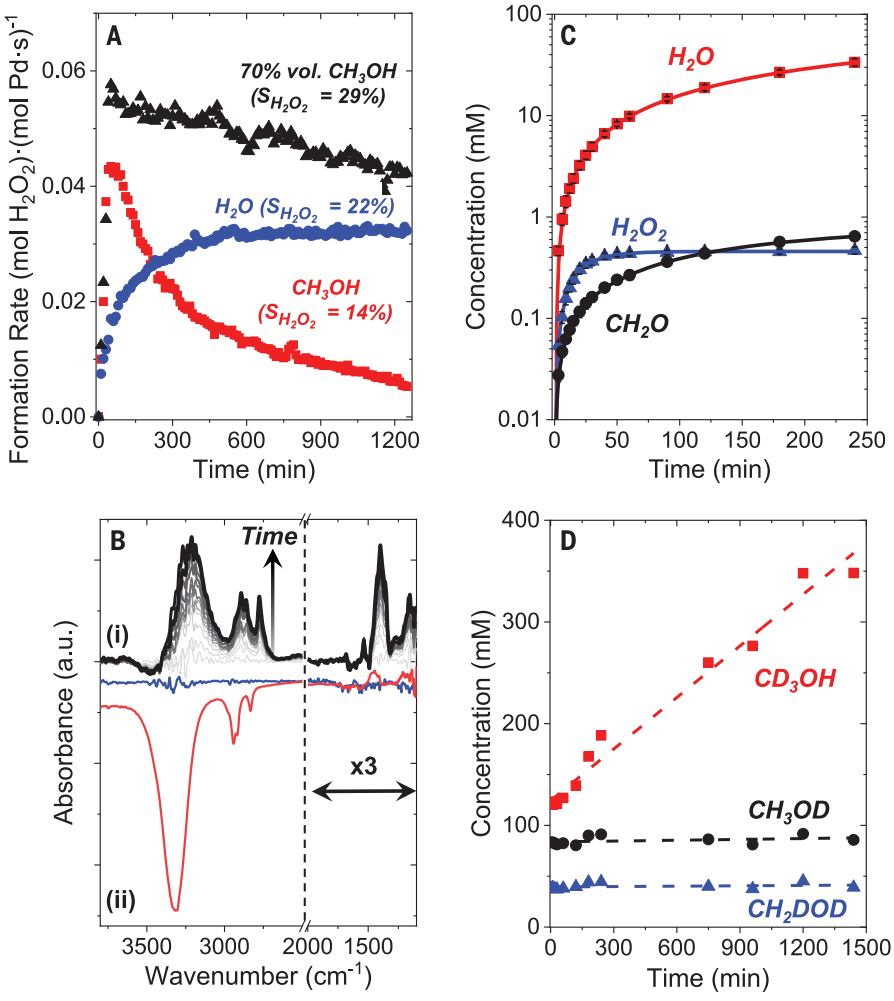

Fig. 1. Reactions of methanol couple with H_2O_2 and H_2O formation on Pd. (**A**) H_2O_2 formation rates as a function of time in methanol (red squares), water (blue circles), and aqueous solutions with 70 vol % CH_3OH (black triangles) from a fixed-bed reactor (60 kPa H_2 and 60 kPa O_2 at 278 K). (**B**) In situ infrared spectra of (i) accumulating methanol-derived intermediates on Pd/SiO_2 over the course of 8 hours (50 kPa H_2 and 50 kPa O_2 at 298 K) and (ii) the difference between steady-state spectra of species on Pd-SiO_2 (blue line) and SiO_2 (red line) under O_2-rich (101 kPa O_2) and reaction conditions (50 kPa H_2 and 50 kPa O_2) at 293 K. a.u., arbitrary units. (**C**) Concentrations of H_2O_2, H_2O, and CH_2O formed over time during direct synthesis in CH_3OH (4.8 kPa H_2 and 4.8 kPa O_2 at 298 K). (**D**) Changes in the concentration of specific methanol isotopologs, determined by ^{1}H NMR, as functions of time during direct synthesis in initially perdeuterated methanol (CD_3OD) (4.8 kPa H_2 and 4.8 kPa O_2 at 298 K). CD_3OD contained detectable H-atom impurities.

[1]Department of Chemical and Biomolecular Engineering, University of Illinois Urbana-Champaign, Champaign, IL 61801, USA. [2]Department of Chemical Engineering and Materials Science, University of Minnesota, Minneapolis, MN 55455, USA. [3]Department of Chemical Engineering, Virginia Polytechnic Institute and State University, Blacksburg, VA 24061, USA.
*Corresponding author. Email: dwflhrty@illinois.edu (D.W.F.); mneurock@umn.edu (M.N.)

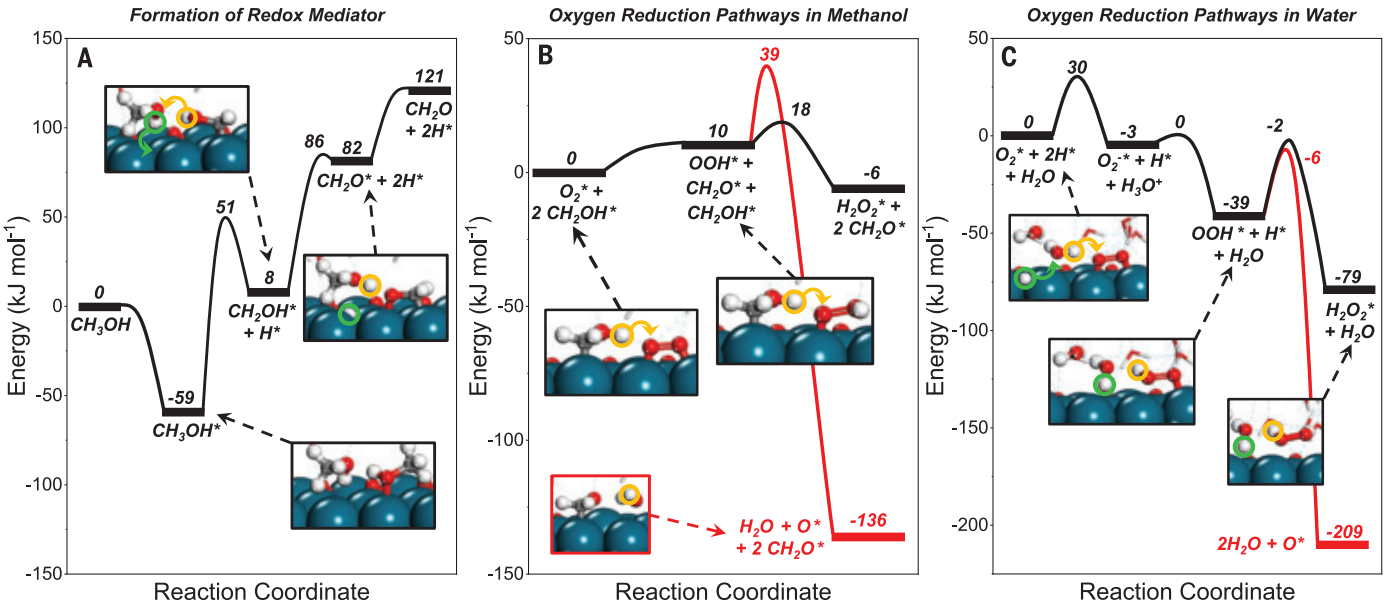

Fig. 2. Reaction energetics in methanol and water. (**A** to **C**) DFT-derived reaction energy diagrams for the formation of the redox mediator by adsorption and reaction of methanol or formaldehyde (A) and the catalytic formation of H_2O_2 and H_2O in methanol (B) and in water (C) on Pd(111)-based surfaces. The modeled Pd(111) slab contains adsorbed O* [1/3 monolayer (ML)] and subsurface H* (1/3 ML in water or 2/3 ML in methanol) to represent the state of Pd NPs at reaction conditions determined by operando EXAFS. The green circles show the hydrogen atom that is oxidized into a proton, and the yellow circles show the proton that is transferred in the heterolytic mechanism. The transition states of each reaction are shown in movies S1 to S5.

to 2855 cm^{-1} and $\delta(CH_3)$ at 1390 cm^{-1}; $\nu(CH_2)$ at 2780 cm^{-1} and $\delta(CH_2)$ at 1536 cm^{-1}], hydroxyl groups [ν(OH) at 3200 cm^{-1}], and carbon-oxygen bonds [ν(C-O) at 1150 cm^{-1}] during catalysis (Fig. 1B). The appearance of these features suggested the formation of surface methanol (CH_3OH*), methoxy (CH_3O*), and hydroxymethyl (CH_2OH*) species. Under O_2-rich conditions, the hydroxyl and methyl features attenuated while peaks at 1450 and 1150 cm^{-1} grew, which indicated the formation of η^2-formaldehyde on Pd (*26*). Notably, the dehydrogenation of these methanol-derived intermediates was completely reversible when H_2 was introduced (fig. S7). Collectively, these observations demonstrate that a mixture of methanol-derived species formed on the surface, which readily hydrogenated and dehydrogenated under reaction conditions. These intermediates blocked a fraction of surface sites but also influenced H_2O_2 formation through more-complex processes.

To better understand the role of methanol and methanol-derived intermediates in O_2 reduction pathways, we compared reaction rates obtained with different isotopologs of methanol and hydrogen in low-pressure semibatch reactors. Formation rates of H_2O_2 and H_2O were slower in CH_3OD than in CH_3OH by factors of 1.8 ± 0.2 and 1.2 ± 0.2, respectively (Table 1). These comparisons indicated that the –OH or –OD groups of methanol reacted with O_2 in the kinetically relevant steps that reduced O_2. We then compared rates in CH_3OH and CD_3OH, which exhibited normal KIEs of 2.9 ± 0.2 for H_2O_2 and 3.0 ± 1.3 for H_2O, suggesting that C–H bonds in methanol cleaved before O_2 reduction. Methanol, however, was not a stoichiometric reductant for O_2 because the sum of the formation rates of H_2O_2 and H_2O was initially 20 times as great as that for CH_2O and increased to become 90-fold greater after 4 hours (Fig. 1C and supplementary text, section S2) [$90 \geq (r_{H_2O_2} + r_{H_2O})/r_{CH_2O} \geq 20$].

These comparisons demonstrated that H_2-derived species participated in the reaction, which was further supported by rates that were greater with H_2 than with D_2 (KIEs of 5.8 ± 0.9 for H_2O_2 and 1.9 ± 0.2 for H_2O; Table 1). We then examined how the methanol-derived surface species formed and reacted by measuring isotopic scrambling between the solvent and H_2 by conducting reactions in CD_3OD (4.8 kPa H_2 and 4.8 kPa O_2 at 295 K) through ^1H nuclear magnetic resonance (NMR) measurements (Fig. 1D). The –OD and –OH functions underwent rapid exchange, whereas the solvent methyl groups retained their original isotope labels, which showed that the Pd surface cleaved C–H and C–D bonds irreversibly before releasing CH_2O under these conditions. Together, these observations suggest that methanol and H_2 reacted with the Pd surface to form a complex that mediated O_2 reduction, and these methanol-derived complexes turned over ~90 times, on average.

These results were not consistent with homolytic reactions between chemisorbed H* or D* atoms and O_2* species (*16*–*18*) (supplementary text, section S5) nor with heterolytic reaction mechanisms that reduced O_2 through PET pathways mediated by liquid-phase methanol (*24*, *25*) (supplementary text, section S6). First, reactions of O_2* with chemisorbed H* atoms cannot explain the kinetic effects of isotope substitutions in methanol (Table 1). Second, a mechanism in which liquid-phase methanol serves as the primary hydrogen donor did not explain the decrease in rates when using D_2. Furthermore, neither mechanism explained the differences in rates between H_2 consumption and CH_2O and H_2O_2 formation. All of the observations, however, were consistent with the formation of H_2O_2 and H_2O by reactions that involve a methanol-derived surface redox mediator that transferred protons and electrons to O_2* and OOH* intermediates (supplementary text, section S7).

We examined this possibility by carrying out DFT calculations on a model Pd(111) surface (representative of dominant facets on Pd NPs; fig. S1) with coadsorbed H*- and O*-atom coverages that were consistent with operando extended x-ray absorption fine structure (EXAFS) measurements (see below) and established adlayer structures (supplementary text, sections S3 and S4) (*27*). Ab initio molecular dynamics simulations were performed with liquid methanol on these covered Pd surfaces to generate the lowest-energy hydrogen-bonding networks over the catalysts and the adsorbates. We

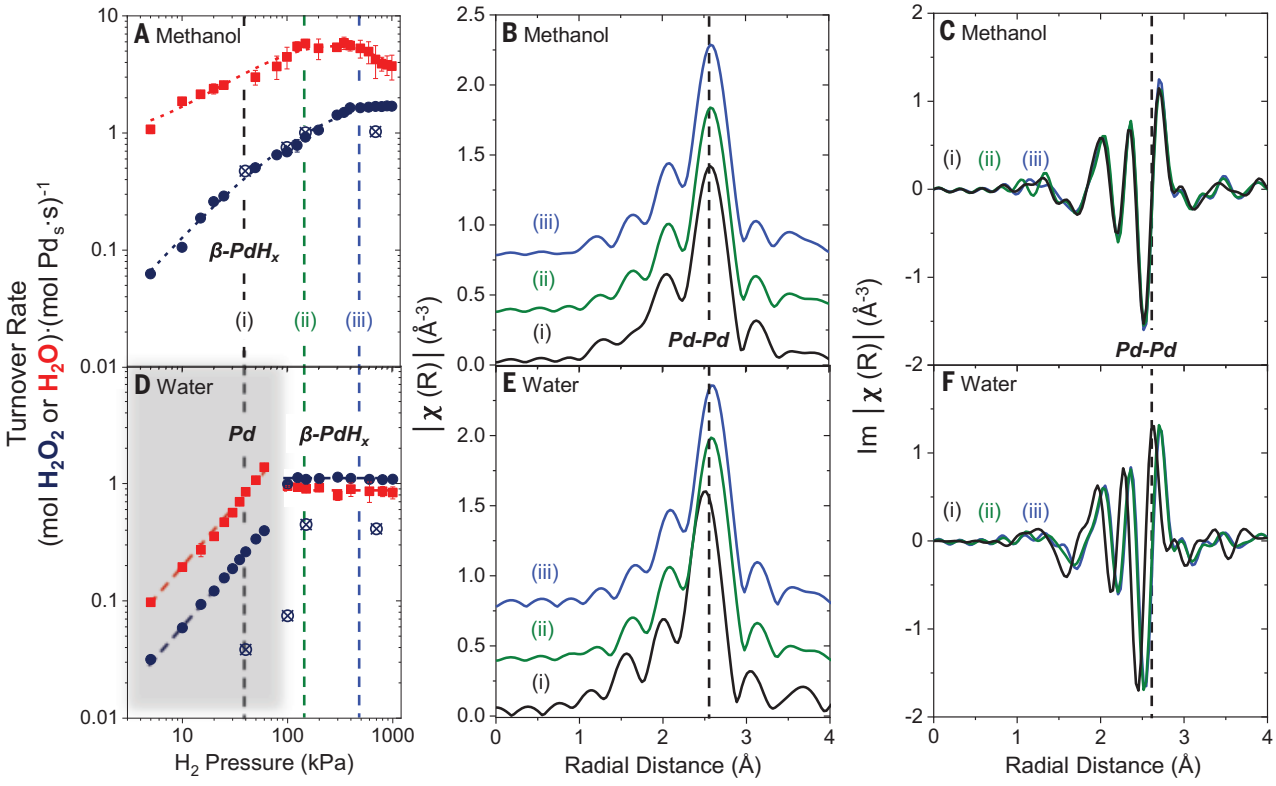

Fig. 3. Effects of H_2 and O_2 on Pd catalytic rates and NP phase. (**A** to **F**) Formation rates of H_2O_2 (blue circles) and H_2O (red squares) in methanol (A) and water (D) as a function of H_2 pressure (5 to 1000 kPa H_2 and 60 kPa O_2 at 278 K). Pd K-edge EXAFS magnitude of the Fourier transformed k^2-weighted $\chi(k)$ data (k = 2.7 to 13 Å^{-1}) [(B) and (E)] and imaginary χ(R) data [(C) and (F)] from operando EXAFS measurements in both methanol and water [60 kPa O_2 and (i) 40 kPa H_2, (ii) 150 kPa H_2, or (iii) 800 kPa H_2 at 293 K]. Additional rate measurements and x-ray absorbance data and analysis are presented in the supplementary text, section S4.

calculated intrinsic activation barriers ($\Delta E_{int}^{\ddagger}$) and reaction energies (ΔE_{rxn}) for multiple forms of heterolytic reactions and the commonly proposed homolytic surface reactions (supplementary text, section S8, and figs. S36 and S37).

Among all these pathways, the mechanism involving PET from a covalently bound hydroxymethyl (CH_2OH*) species to dioxygen intermediates (O_2* and OOH*) had the lowest barriers ($\Delta E_{int}^{\ddagger}$ = 8 to 10 kJ mol^{-1}) (Fig. 2B). Analogous heterolytic reaction pathways mediated by liquid-phase methanol gave higher activation barriers ($\Delta E_{int}^{\ddagger} \geq$ 30 kJ mol^{-1}) (fig. S40), and homolytic reactions between chemisorbed H* atoms and dioxygen showed the highest barriers ($\Delta E_{int}^{\ddagger} \geq$ 44 kJ mol^{-1}) (fig. S40). Moreover, DFT calculations predicted KIEs for this pathway (i.e., $k_{CH_2OH}/k_{CH_2OD} > 1$ and $k_{CH_2OH}/k_{CD_2OH} > 1$; tables S11 and S12 and supplementary text, section S9) similar to experimental values (Table 1). The differences between $\Delta E_{int}^{\ddagger}$ for these competing pathways reflected the different acidities (i.e., deprotonation energies) of the reactive hydrogen within the CH_2OH*, CH_3OH, and H* intermediates (table S8). These calculations indicated that CH_2OH* more effectively mediated PET than CH_3OH or surface H* atoms because the organic fragment and Pd NP form an enol-like surface complex that efficiently promotes resonance-stabilized electron transfer to the metal with facile proton transfer to chemisorbed dioxygen intermediates.

Energetic calculations for reactions involving the hydroxymethyl redox mediator explained the slower formation rate of CH_2O compared with H_2O_2 and H_2O. To initiate the redox cycle, adsorbed methanol (CH_3OH*) must overcome a large initial barrier ($\Delta E_{int}^{\ddagger}$ = 110 kJ mol^{-1}) (Fig. 2A) to form CH_2OH*, although reactions with OH* and O_2* likely provide lower-energy pathways to activate C–H bonds (*28*). Subsequent dehydrogenation of CH_2OH* to CH_2O* on Pd was unfavorable at these conditions ($\Delta E_{int}^{\ddagger}$ = 78 kJ mol^{-1}, ΔE_{rxn} = 74 kJ mol^{-1}) (Fig. 2A). Coupled oxygen reduction and hydroxymethyl oxidation, however, provided much lower barriers ($\Delta E_{int}^{\ddagger}$ = 8 to 29 kJ mol^{-1}) and more favorable thermodynamics (Fig. 2B) by generating CH_2O* together with H_2O_2* or H_2O*. Once formed, CH_2O* readily regenerated CH_2OH* by a solvent-assisted reaction of H* with CH_2O* ($\Delta E_{int}^{\ddagger}$ = 4 kJ mol^{-1}) (Fig. 2A) or escaped the surface but at lower rates (ΔE_{rxn} = 39 kJ mol^{-1}) (Fig. 2A). Thus, CH_2OH* formed from irreversible C–H rupture of CH_3OH* (Fig. 1D) or hydrogenation of CH_2O*. This mediator (CH_2OH*) rarely reduced further to form methanol because the barrier to do so exceeded that for CH_2OH* oxidation by 33 kJ mol^{-1}.

We measured steady-state H_2O_2 and H_2O formation rates (Fig. 3A) to determine whether the proposed mechanism predicted catalytic behavior over a wide range of H_2 and O_2 pressures (5 to 1000 kPa H_2 and 5 to 1000 kPa O_2 at 295 K). In methanol, we measured rates after the catalyst stabilized after >20 hours on stream. During that period, we estimated that methanol-derived intermediates accumulated to cover >90% of the exposed surface of Pd NPs on the basis of the decrease in H_2 conversion (Fig. 1, A and B). Analysis of operando EXAFS spectra showed that these NPs were β-PdH$_x$ at all conditions for steady-state rate measurements (Fig. 3, B and C; fig. S23, A to D; and table S5). The metallic Pd phase only formed when the O_2-to-H_2 molar ratio was ≥10 (e.g., 10 kPa H_2 and 100 kPa O_2 or 60 kPa H_2 and 1000 kPa O_2). This phase change coincided with an increase in the Pd-O coordination number ($N_{Pd\text{-}O}$ = 0 to 0.7) as the molar ratio of O_2 to H_2 (table S5 and

supplementary text, section S4) increased, which suggests a greater coverage of oxygen-derived species. Similarly, a feature corresponding to Pd-C coordination grew over the course of 12 hours on stream, which signified the accumulation of organic intermediates (fig. S25, A and D) consistent with in situ infrared spectroscopy (Fig. 1B). Last, operando H_2O_2 formation rates matched the steady-state rates measured in the trickle-bed reactor (Fig. 3A).

H_2O_2 formation rates depended weakly on O_2 pressure between 10 and 600 kPa, which implies that oxygen intermediates (OH*, O_2*, or OOH*; fig. S30A) nearly saturated active sites exposed among the methanol-derived adlayer. H_2O_2 formation rates increased linearly with H_2 pressure (5 to 60 kPa H_2) before approaching constant values above 400 kPa H_2 (Fig. 3A). Across these conditions, dissociative adsorption of H_2 was highly reversible and approached quasi-equilibrium at the highest H_2 pressures, as shown by H_2-D_2 scrambling rates (30 to 1000 kPa H_2 and D_2 and 60 kPa O_2; fig. S29A).

These rate measurements agreed with the proposed mechanism, indicating that H_2O_2 formed during kinetically relevant PET from CH_2OH* to OOH* (eqs. S7.46 to S7.49); the alternative mechanisms proposed were not able to reproduce the results fully. The apparent dependence of rates on H_2 pressure changed between the lowest and highest pressures examined, which indicates that the prevailing surface intermediates differed across this range of conditions. For example, a combination of O*, O_2*, and CH_2O* occupied most sites at the lowest H_2 pressures, but at the highest H_2 pressures, OH*, OOH*, and CH_2OH* became more prevalent.

Computational results showed that water formed through similar PET steps, but this process involved irreversible O–O bond rupture to produce both H_2O and O* (*29*), which reduced to water (Fig. 2B). These calculations agreed with studies showing that mixtures of H_2, $^{16}O_2$, and $^{18}O_2$ reactants only formed $H^{16}O^{16}OH$ and $H^{18}O^{18}OH$, which indicated that O* and OH* did not regenerate O–O bonds (*30*). Although OOH* and H_2O_2* readily formed on a single atom of Pd, their subsequent reduction to form water required larger ensembles of Pd atoms. Thus, high coverages of oxygen-derived and CH_xO* intermediates likely blocked sites and disproportionately increased barriers to form H_2O over those for H_2O_2. The measured KIEs, rates, and operando XAS, together with DFT-derived reaction coordinates, provide compelling evidence that surface-bound hydroxymethyl redox mediators react with oxygen to form H_2O_2 and H_2O in methanol (Fig. 4A).

In the absence of methanol and the derived surface intermediates, water facilitates distinct heterolytic paths to form H_2O_2. We measured oxygen reduction rates in different isotopologs of water and hydrogen (Table 1). In hydrogenated and deuterated water, H_2O_2 formation rates remained constant ($k_{H_2O}/k_{D_2O} = 0.95 \pm 0.10$), whereas H_2O formation rates exhibited a normal KIE ($k_{H_2O}/k_{D_2O} = 1.5 \pm 0.3$). These results imply that H_2O forms by kinetically relevant proton transfer, but other processes limit rates for H_2O_2 production. Reactions with either D_2 or H_2

Table 1. Kinetic isotope effects. Effects of isotopic substitution on rate constants for the formation of H_2O_2 and H_2O on silica-supported Pd catalysts in 80 cm^3 of CH_3OH, CD_3OH, CH_3OD, H_2O, or D_2O (4.8 kPa H_2 or D_2 and 4.8 kPa O_2 at 298 K). Transient reaction profiles are discussed in more detail in supplementary text, section S2.

k_H/k_D	Methanol			Water	
	CH_3OH/CH_3OD	H_2/D_2	CH_3OH/CD_3OH	H_2O/D_2O	H_2/D_2
$H_2 + O_2 \rightarrow H_2O_2$	1.8 ± 0.2	5.8 ± 0.9	2.9 ± 0.4	1.0 ± 0.1	2.7 ± 0.4
$H_2 + H_2O_2 \rightarrow 2H_2O$	1.7 ± 0.1	2.5 ± 0.3	4.1 ± 1.5	1.5 ± 0.3	5.7 ± 0.6
$H_2 + ½O_2 \rightarrow H_2O$	1.2 ± 0.2	1.9 ± 0.2	3.0 ± 1.3	1.0 ± 0.1	2.7 ± 0.4

Table 2. Barriers in aqueous and organic cosolvents. Apparent activation enthalpies measured for H_2O_2 and H_2O formation and comparable energy barriers calculated by DFT on Pd(111) containing adsorbed O* (1/3 ML). Reactions in organic cosolvents (entries 1 to 3) were calculated using a 2/3 ML of subsurface H*. Reaction in water at different H_2 pressures were calculated using a 0/3 (entry 4), 1/3 (entry 5), or 2/3 (entry 6) ML of subsurface H*. All measurements were performed on silica-supported Pd catalysts (60 kPa O_2 at 278 to 298 K). The calculations of apparent barriers are discussed in supplementary text, section S13.

Solvent and reaction conditions	$\Delta H^{\ddagger}_{H_2O_2}$ (kJ mol^{-1})	$\Delta E^{\ddagger}_{H_2O_2,DFT}$ (kJ mol^{-1})	$\Delta H^{\ddagger}_{H_2O}$ (kJ mol^{-1})	$\Delta E^{\ddagger}_{H_2O,DFT}$ (kJ mol^{-1})
Methanol (60 kPa H_2; β-PdH_x–SiO_2)	13 ± 1	18	80 ± 5	39
70 vol % methanol (60 kPa H_2; β-PdH_x–SiO_2)	10 ± 1	18	29 ± 3	39
0.5 M aqueous formalin (60 kPa H_2; β-PdH_x–SiO_2)	5 ± 1	18	24 ± 2	39
Water (40 kPa H_2; Pd^0–SiO_2)	19 ± 2	39	11 ± 1	21
Water (60 kPa H_2; α-PdH_x–SiO_2)	8 ± 1	37	13 ± 1	33
Water (200 kPa H_2; β-PdH_x–SiO_2)	7 ± 1	33	18 ± 2	38

gave normal KIEs for both H_2O_2 ($k_{H_2}/k_{D_2} = 2.7 \pm 0.4$) and H_2O ($k_{H_2}/k_{D_2} = 5.7 \pm 0.6$) formation, which confirms the kinetically relevant steps that form both products involve H_2-derived species. Measured rates of H_2-D_2 scrambling (fig. S29B) showed that dissociative H_2 adsorption was effectively irreversible at low H_2 pressures (30 to 60 kPa H_2 and D_2 and 60 kPa O_2) but approached quasi-equilibrium at the highest H_2 pressures (>200 kPa H_2 and D_2 and 60 kPa O_2). These observations in water could explain multiple plausible mechanisms for the formation of H_2O_2, including kinetically relevant H_2 adsorption (*31*), homolytic reactions between hydrogen and dioxygen intermediates (supplementary text, section S5), or heterolytic hydrogen oxidation and electron transfer (supplementary text, section S6) (*21*).

We examined these paths computationally in explicit liquid water over Pd(111) with surface O* (1/3 monolayer) and subsurface H* (1/3 monolayer) to create a model representative of the state of Pd NPs during catalysis, as determined by EXAFS (supplementary text, section S4). The dissociative adsorption of H_2 had a negligible barrier ($\Delta E^{\ddagger}_{int} \leq 2$ kJ mol^{-1}) and was highly reversible ($\Delta E_{rxn} = -14$ kJ mol^{-1}) (fig. S18), which demonstrates that this step did not determine rates of O_2 reduction. Among the remaining options, the PET mechanism ($H^* + H_2O + O_2^* \rightarrow * + H_3O^+ + O_2^{-}*$; $\Delta E^{\ddagger}_{int} = 30$ kJ mol^{-1}) resulted in a lower intrinsic activation energy than the competing homolytic ($H^* + O_2^* \rightarrow OOH^* + *$; $\Delta E^{\ddagger}_{int} = 52$ kJ mol^{-1}) or hydroxyl-mediated ($OH^* + O_2^* \rightarrow OOH^* + O^*$; $\Delta E^{\ddagger}_{int} = 85$ kJ mol^{-1}) paths (fig. S40).

Simulations of this PET reaction showed that water molecules first heterolytically oxidized H* atoms and activated dioxygen intermediates by kinetically relevant electron transfer ($\Delta E^{\ddagger}_{int} = 30$ kJ mol^{-1}) through the Pd surface (fig. S41 and supplementary text, section S10). Subsequently, H_3O^+ spontaneously transferred protons to anionic dioxygen intermediates (e.g., $H_3O^+ + O_2^{-}* \rightarrow OOH^*$; $\Delta E^{\ddagger}_{int} = 1$ to 3 kJ mol^{-1}). Both O_2* and OOH* were reduced by kinetically relevant electron transfer followed by facile proton transfer, which agreed with the measured KIE ($k_{H_2O}/k_{D_2O} \sim 1$). DFT also predicted a negligible change between D_2O and H_2O and a normal KIE between D_2 and H_2 reactants (table S13 and supplementary text, section S9). Moreover, these findings matched KIEs reported for electrochemical oxygen reduction on Pd and Pt that found electron transfer determined oxygen reduction rates (*32*). One distinction between oxygen reduction in water versus methanol is that the OH* intermediate formed in water is much less acidic than the CH_2OH* intermediate formed in methanol and cannot actively mediate oxygen reduction (table S8).

Rate expressions derived from the proposed PET mechanism matched measured H_2O_2 and H_2O formation rates at steady state (supplementary text, section S6). These rates increased linearly with O_2 pressure (5 to 25 kPa O_2), exhibited a discontinuous change, and remained constant at greater O_2 pressures (100 to 800 kPa O_2; fig. S30B). These results indicate that O_2-derived species (O*, OH*, O_2*, and OOH*) bind to available active sites at low pressures and became the predominant reactive intermediates at the highest pressures (>100 kPa O_2). Among these species, we observed dioxygen intermediates on Au NPs (active for surface-enhanced Raman scattering) within higher concentrations of H_2O_2, whereas Pd surfaces stabilized low coverages of O_2* and OOH* relative to other oxygenates (supplementary text, section S14).

We also observed that H_2O_2 and H_2O formation rates first increased proportionally to H_2 pressure (5 to 60 kPa H_2), increased sharply, and finally reached a constant value for all higher H_2 pressures (125 to 1000 kPa H_2; Fig. 3D). The functional dependence of rates on reactant pressures agreed with the derived rate expressions for the PET mechanism (eqs. S6.70 to S6.75). This discontinuous increase in rates occurred when molar ratios of H_2 to O_2 exceeded 2, which coincided with a twofold increase in H_2O_2 selectivity and a marked increase in the reversibility of dissociative H_2 adsorption. Thus, we hypothesized that these differences resulted from a change in the phase of the Pd NPs.

We used operando EXAFS to examine the structure of Pd NPs over a similar range of reactant pressures (8 to 1000 kPa H_2 and 60 to 1000 kPa O_2). These data (Fig. 3, E and F; fig. S24, A to D; and table S4) showed that silica-supported Pd NPs remained metallic at lower H_2-to-O_2 ratios (40 to 100 kPa H_2 and 60 kPa O_2 at 295 K) but transformed into β-PdH_x when the reactant ratio increased (150 to 1000 kPa H_2 and 60 kPa O_2 at 295 K; Fig. 3, E and F). Similarly, at 60 kPa H_2, β-PdH_x was observed at 8 kPa O_2, whereas metallic Pd formed between 60 to 1000 kPa O_2 (fig. S24, A to D). These results were consistent with previous in situ XAS measurements of Pd NPs supported on TiO_2, in which a Pd–to–β-PdH_x phase transition occurred at molar ratios of H_2 to O_2 greater than 2 in water (*33*).

The different phases formed by Pd NPs in water and methanol suggest that organic surface species stabilize the formation of β-PdH_x. DFT calculations supported these inferences and showed that subsurface H* atoms were more stable in Pd(111) when CH_2OH* rather than O* covered the surface (fig. S42 and supplementary text, section S11). Further, operando XAS showed Pd-O coordination in water (tables S4 and S5); however, we observed substantially less Pd-O coordination in methanol. Moreover, the presence of organic intermediates on the surface (Fig. 1, A and B) explained why methanol readily formed β-PdH_x. Notably, β-PdH_x gave greater H_2O_2 selectivities (55%; Fig. 3E) than metallic Pd (25%), which likely stemmed from the increase in the d-band filling of β-PdH_x over Pd (fig. S43 and table S14), consistent with the decreased experimental work function (table S16) (*34*).

DFT results showed a small decrease in the O_2 reduction barriers over PdH_x versus Pd for reactions in methanol (11 kJ mol^{-1}) and water (6 kJ mol^{-1}), resulting in apparent barriers of 18 kJ mol^{-1} and 33 kJ mol^{-1}, respectively, and a small increase in the H_2O formation barriers in methanol (11 kJ mol^{-1}) and water (17 kJ mol^{-1}) (tables S9, S10, S17, and S18, and supplementary text, sections S8 and S12). These trends resembled those measured experimentally over metallic Pd (40 kPa H_2 and 60 kPa O_2), α-PdH_x (60 kPa H_2 and 60 kPa O_2), and β-PdH_x (200 kPa H_2 and 60 kPa O_2) in water (Table 2). These energy differences were small and near the error limits of DFT, but the trends were consistent with experimentally observed differences in the electronic structure of Pd and β-PdH_x (*35*). Thus, both theory and experiment suggest that β-PdH_x is more selective for H_2O_2 formation than metallic Pd for both PET mechanisms.

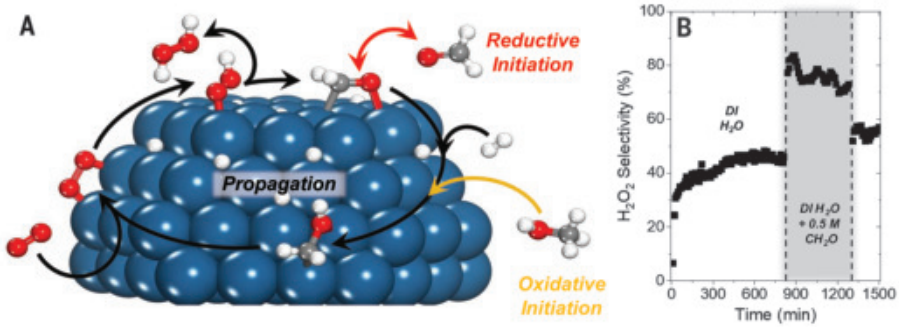

Fig. 4. Catalytic O_2 reduction with surface redox mediators. (**A**) Hydroxymethyl (CH_2OH*) forms either by oxidative initiation of methanol or the reductive initiation of formaldehyde, after which CH_2OH* acts as a redox mediator for reactions of O_2 and H_2 to form H_2O_2 and water. (**B**) Steady-state H_2O_2 selectivities increased when formaldehyde (0.5 M CH_2O) is added to deionized (DI) H_2O (200 kPa H_2 and 60 kPa O_2 at 278 K).

Despite the differences in barriers on Pd and β-PdH_x, H_2O_2 selectivities were lower in methanol (6 to 31%) than in water (25 to 55%) for H_2 pressures between 10 and 1000 kPa, even though methanol stabilized β-PdH_x at each reaction condition. Notably, the calculated and experimentally measured barriers for H_2O formation were higher in methanol than in water (Table 2), which did not explain these selectivity differences. These results suggested that the entropic penalties related to solvent reorganization favor the formation of H_2O over H_2O_2 in methanol (supplementary text, section S13).

We measured steady-state H_2O_2 and H_2O formation rates in aqueous solutions of either methanol or formaldehyde. H_2O_2 rates and selectivities first increased with the volumetric fraction of methanol and reached a maximum in a solution of 70% methanol in water (fig. S46), in agreement with analogous studies (*20*). Activation enthalpy measurements in this 70% methanol–water mixture showed similar trends to methanol, where reaction barriers increased and entropy barriers decreased relative to pure water (Table 2 and table S19). For this mixture, we proposed that hydroxymethyl intermediates reduce oxygen species, but solution-phase water molecules solvate these transition state structures. Such interactions would increase the activation excess Gibbs free energy to form H_2O in pure methanol relative to aqueous methanol and improve the H_2O_2 selectivity in the mixed solution (supplementary text, section S13).

We then hypothesized that H_2O_2 rates and selectivities would increase on a Pd surface covered by organic redox mediators (i.e., CH_2OH*) and that deactivation rates would decrease if the solution contained a greater fraction of water. To test this proposal, we conducted reactions in an aqueous formaldehyde solution (0.5 M CH_2O) and pure water. Compared with water, H_2O_2 formation rates were twofold greater and selectivities increased from 22 to 54% in aqueous formaldehyde (fig. S47A). Moreover, the H_2O_2 selectivity increased to 80% at higher H_2 pressures (200 kPa H_2; Fig. 4B and fig. S47, B and C), whereas the selectivity in pure water is only 40 to 55%.

These greater H_2O_2 selectivities suggest that CH_2O molecules bind to Pd and react to form redox mediators (Fig. 4) that result in lower-barrier oxygen reduction pathways. For 100 mM CH_2O, H_2O_2 formation rates were greater in H_2O than in D_2O solvent ($k_{H_2O}/k_{D_2O} = 1.6 \pm 0.2$) (fig. S15), which differed from the observation in pure water but resembled the effect of using selectively deuterated methanol as a solvent (Table 1). These measurements indicated that CH_2O molecules adsorbed onto Pd and partially hydrogenated to form CH_2OH* intermediates (Fig. 2A) that exchanged deuterons with D_2O to generate CH_2OD* in situ. Differences between the apparent activation enthalpies to form H_2O_2 and H_2O were similar between the 0.5 M CH_2O and 70% methanol solutions ($\Delta H^{\ddagger}_{H_2O} - \Delta H^{\ddagger}_{H_2O_2} = 18$ kJ mol^{-1}). H_2O_2 selectivities, however, were much greater in aqueous formaldehyde (54 versus 29%) because of changes in apparent activation entropies that favor H_2O_2 formation over H_2O (table S20). Presumably, the greater fraction of water in the solution affected transition-state solvation and contributed to changes in the activation excess free energies of reaction.

We examined other carbonyl species, such as 1,4-benzoquinone (BQ), that provided additional resonance stabilization to aid both proton and electron transfer. Exposure to low concentrations of BQ (1 to 4 mM) increased H_2O_2 selectivity (65 to 90%; fig. S50) at similar rates when the reaction was then run in pure water (200 kPa H_2 and 60 kPa O_2 at 278 K). These improvements lasted for ~1 hour before the catalyst eventually returned to its initial state (~8 hours; fig. S50). We carried out DFT calculations (fig. S51) and found that 1,4-hydroquinone presented low barriers for PET steps to reduce O_2* (15 kJ mol^{-1}) and OOH* (3 kJ mol^{-1}).

Taken together, these findings demonstrate that redox mediators can form spontaneously by reactions of solvents or other organic molecules on metal NPs and cocatalyze reduction reactions (Fig. 4A). These surface redox mediators have three characteristic features. First, the metal-bound hydroxyalkyl intermediate provides a resonance-stabilized complex with a highly acidic proton and enol-like motif, which enable low-barrier PET steps. Second, the resulting carbonyl moiety preferentially reacts with surface H atoms to regenerate the mediator. Third, strong metal-carbon bonds secure the mediator to the surface and permit multiple redox cycles before desorption. These species present facile reaction pathways and modify the surface energies that influence the structure and phase of NPs. These insights present opportunities to decouple the benefits (greater selectivities and rates) and drawbacks (rapid deactivation and environmental waste) of organic solvents.

REFERENCES AND NOTES

1. T. Welton, C. Reichardt, *Solvents and Solvent Effects in Organic Chemistry* (Wiley, ed. 4, 2010).
2. C. Sievers *et al.*, *ACS Catal.* **6**, 8286–8307 (2016).
3. P. J. Dyson, P. G. Jessop, *Catal. Sci. Technol.* **6**, 3302–3316 (2016).
4. M. A. Mellmer *et al.*, *Nat. Catal.* **1**, 199–207 (2018).
5. C. A. Thomas, R. J. Bonilla, Y. Huang, P. G. Jessop, *Can. J. Chem.* **79**, 719–724 (2001).
6. C. W. Kohlpaintner, R. W. Fischer, B. Cornils, *Appl. Catal. A* **221**, 219–225 (2001).
7. R. Burch, P. R. Ellis, *Appl. Catal. B* **42**, 203–211 (2003).
8. V. Paunovic, V. V. Ordomsky, V. L. Sushkevich, J. C. Schouten, T. A. Nijhuis, *ChemCatChem* **7**, 1161–1176 (2015).
9. D. T. Bregante, D. W. Flaherty, *ACS Catal.* **9**, 10951–10962 (2019).
10. J. Shangguan, Y. H. C. Chin, *ACS Catal.* **9**, 1763–1778 (2019).
11. B. N. Zope, D. D. Hibbitts, M. Neurock, R. J. Davis, *Science* **330**, 74–78 (2010).
12. K. B. Sravan Kumar, T. N. Whittaker, C. Peterson, L. C. Grabow, B. D. Chandler, *J. Am. Chem. Soc.* **142**, 5760–5772 (2020).
13. D. D. Hibbitts, B. T. Loveless, M. Neurock, E. Iglesia, *Angew. Chem. Int. Ed.* **52**, 12273–12278 (2013).
14. B. S. Akpa *et al.*, *J. Catal.* **289**, 30–41 (2012).
15. D. W. Flaherty, *ACS Catal.* **8**, 1520–1527 (2018).
16. Y. Voloshin, R. Halder, A. Lawal, *Catal. Today* **125**, 40–47 (2007).
17. D. C. Ford, A. U. Nilekar, Y. Xu, M. Mavrikakis, *Surf. Sci.* **604**, 1565–1575 (2010).
18. R. Todorovic, R. J. Meyer, *Catal. Today* **160**, 242–248 (2011).
19. X. Song *et al.*, *J. Phys. Chem. C* **123**, 26324–26337 (2019).
20. D. A. Crole, S. J. Freakley, J. K. Edwards, G. J. Hutchings, *Proc. R. Soc. A* **472**, 20160156 (2016).
21. N. M. Wilson, D. W. Flaherty, *J. Am. Chem. Soc.* **138**, 574–586 (2016).
22. Q. S. Liu, J. H. Lunsford, *Appl. Catal. A* **314**, 94–100 (2006).
23. Y. F. Han, J. H. Lunsford, *J. Catal.* **230**, 313–316 (2005).
24. J. B. Gerken, S. S. Stahl, *ACS Cent. Sci.* **1**, 234–243 (2015).
25. S. Y. Reece, D. G. Nocera, *Annu. Rev. Biochem.* **78**, 673–699 (2009).
26. E. Jeroro, J. M. Vohs, *J. Am. Chem. Soc.* **130**, 10199–10207 (2008).
27. D. O. Demchenko, G. M. Sacha, M. Salmeron, L.-W. Wang, *Surf. Sci.* **602**, 2552–2557 (2008).
28. D. D. Hibbitts, M. Neurock, *J. Catal.* **299**, 261–271 (2013).
29. A. Plauck, E. E. Stangland, J. A. Dumesic, M. Mavrikakis, *Proc. Natl. Acad. Sci. U.S.A.* **113**, E1973–E1982 (2016).
30. D. Dissanayake, J. H. Lunsford, *J. Catal.* **214**, 113–120 (2003).
31. W. Tu *et al.*, *J. Catal.* **377**, 494–506 (2019).
32. E. C. M. Tse, J. A. Varnell, T. T. H. Hoang, A. A. Gewirth, *J. Phys. Chem. Lett.* **7**, 3542–3547 (2016).
33. M. Selinsek *et al.*, *ACS Catal.* **8**, 2546–2557 (2018).
34. R. Duś, R. Nowakowski, E. Nowicka, *J. Alloys Compd.* **404–406**, 284–287 (2005).
35. R. J. Davis, S. M. Landry, J. A. Horsley, M. Boudart, *Phys. Rev. B* **39**, 10580–10583 (1989).

ACKNOWLEDGMENTS

We acknowledge the contributions of J. Mabon and G. Kulkarni. This work was carried out in part at the Frederick Seitz Materials Research Laboratory Central Research Facilities and the School of Chemical Sciences Microanalysis Laboratory at the University of Illinois. **Funding:** We acknowledge generous funding to support this work provided by the Energy & Biosciences Institute through the EBI-Shell program, support from the National Science Foundation (CBET-1511819 and CCI-1740656), and computational support from the Minnesota Supercomputing Institute. J.S.A. acknowledges the National Science Foundation Graduate Research Fellowship program (DGE-1144245). A.M.K. and Y.L. acknowledge funding from the National Science Foundation Chemistry Division (CHE-1507370). Use of the Stanford Synchrotron Radiation Light Source (beamline 9-3, user proposal 4938) was supported by the U.S. Department of Energy, Office of Basic Energy Sciences under contract no. DE-AC02-76SF00515. M.N. acknowledges helpful discussions with S. Stahl, M. Mahanthappa, and I. Tonks. **Author contributions:** J.S.A., D.W.F., M.N., and A.M.K. designed the experiments and conceived the study. J.S.A. performed kinetic and spectroscopic experiments. A.C., V.M., and S.W. performed computational calculations. P.P., Y.L., and A.M.K. assisted with XAS measurements. T.R. and P.P. assisted with FTIR measurements, and A.S. performed Raman experiments. The original manuscript drafts were written by J.S.A. and D.W.F., and the final draft was edited by M.N. and A.M.K. **Competing interests:** None declared. **Data and materials availability:** There are no restrictions on materials. All data needed to evaluate the conclusions in the paper are present in the paper or the supplementary materials.

SUPPLEMENTARY MATERIALS

science.sciencemag.org/content/371/6529/626/suppl/DC1
Materials and Methods
Supplementary Text
Figs. S1 to S52
Tables S1 to S21
Movies S1 to S5

7 April 2020; accepted 29 December 2020
10.1126/science.abc1339

CLIMATE CHANGE

Exposure to climate change drives stability or collapse of desert mammal and bird communities

E. A. Riddell[1,2], K. J. Iknayan[3,4], L. Hargrove[5], S. Tremor[5], J. L. Patton[1], R. Ramirez[6], B. O. Wolf[6], S. R. Beissinger[1,3]*

High exposure to warming from climate change is expected to threaten biodiversity by pushing many species toward extinction. Such exposure is often assessed for all taxa at a location from climate projections, yet species have diverse strategies for buffering against temperature extremes. We compared changes in species occupancy and site-level richness of small mammal and bird communities in protected areas of the Mojave Desert using surveys spanning a century. Small mammal communities remained remarkably stable, whereas birds declined markedly in response to warming and drying. Simulations of heat flux identified different exposure to warming for birds and mammals, which we attribute to microhabitat use. Estimates from climate projections are unlikely to accurately reflect species' exposure without accounting for the effects of microhabitat buffering on heat flux.

With one of six species threatened by future warming (*1*), conserving biodiversity depends on identifying the factors that make a species vulnerable to climate change. Exposure, sensitivity, and adaptive capacity are fundamental components of climate vulnerability (*2*), but it is the magnitude of exposure—determined by the degree of change at a given site and by behavioral buffering from microhabitat use—that establishes whether organisms experience the direct effects of climate change (*3*). Despite diverse strategies used by animals to reduce exposure to lethal temperatures and desiccation (*4*, *5*), species inhabiting a site are typically assumed to experience similar magnitudes and rates of exposure (*6*–*9*). However, comparisons of exposure among taxa at the same sites—especially where climate change has pushed organisms toward their physiological limits—are lacking and are rarely connected to long-term community responses.

To assess the impact of exposure on communities, we compared the responses of small mammals and birds of the Mojave Desert to warming and drying by resurveying sites originally visited by Joseph Grinnell and colleagues in the early 20th century (*10*). Our comparison leveraged the recently documented collapse of the Mojave bird community (*11*, *12*) to evaluate how exposure affects vulnerability across taxa. Multiday surveys were conducted for 34 small mammal species at 90 sites and 135 bird species at 61 sites located primarily on protected lands (Fig. 1A) (see supplementary materials). We used a dynamic multispecies occupancy model to estimate occupancy probabilities for species in each era, accounting for differences in detection between time periods. The model also evaluated the influence of climate change as well as other causes of turnover, such as habitat change from fire and grazing (*11*). We then estimated the degree of exposure for birds and mammals using a heat flux model that simulates thermoregulatory costs on the basis of behavioral strategies, morphology, thermal properties, and microhabitat conditions (see supplementary materials). We expected that small mammals would mirror the collapse of the Mojave bird community (*11*) because they are endotherms, occupy similar trophic levels (*13*), have comparable life history traits and ecological strategies (*13*), and have exhibited similar sensitivities to warming, including elevational and latitudinal range shifts (*14*–*17*). Alternatively, small mammals may buffer their exposure to climate change by accessing cool fossorial microhabitats. In that case, biotic interactions, such as competition, should influence changes in community assembly of desert mammals (*18*, *19*).

Over the past century, occupancy of small mammals remained stable while birds severely declined (Fig. 1B and fig. S1). The mean occupancy probability of small mammals during the historical time period [μ = 0.26; 95% credible interval (CRI), 0.24 to 0.29] was indistinguishable from the value derived from modern surveys (μ = 0.26; 95% CRI, 0.24 to 0.29). Occupancy of 3 (9%) mammal species decreased, 27 (79%) did not change, and 4 (12%) increased (Fig. 1B and table S1). In contrast, bird community occupancy declined over the past century from 0.24 (95% CRI, 0.17 to 0.32) to 0.11 (95% CRI, 0.07 to 0.15). Of 135 bird species, occupancy of 39 (29%) decreased, 95 (70%) did not change, and 1 (<1%) increased (*11*).

Species richness was characterized by stability over the past century for the small mammal community but collapse for the bird community. Richness declined significantly at 55 of 61 sites for birds (90.1%) versus only 3 of 90 sites for mammals (3.3%) (Fig. 1C). Sites supported an average of 8.79 mammal species (95% CRI, 8.18 to 9.72) in historical surveys compared to 8.92 species (95% CRI, 8.47 to 9.73) in modern surveys. However, the stability of mammal species richness conceals moderate species turnover at survey sites (Fig. 1D). There was an average gain of 2.02 mammal species (95% CRI, 1.50 to 2.60) colonizing per site and an average loss of 1.89 species (95% CRI, 1.58 to 2.30) extirpated per site. Thus, a 23% gain in species per site was offset by a 22% loss relative to historical species richness. In contrast, site-level richness for birds collapsed by 42% (−17.9 species per site; 95% CRI, −15.5 to −20.5; Fig. 1C). For birds, colonization rarely occurred, resulting in species loss without replacement at surveyed sites (Fig. 1D). Moreover, the mean probability of persistence was much lower for birds (μ = 0.43; 95% CRI 0.31 to 0.55) than for mammals (Fig. 1E; μ = 0.79; 95% CRI, 0.70 to 0.86).

Warming and drying over the past century was not associated with persistence or colonization in small mammals, but drove bird turnover. Only 1 of 34 mammal species (3%) responded to precipitation change and none to temperature change (table S2). Likewise, habitat degradation from fire and grazing was not associated with persistence and colonization in small mammals (table S3). Instead, long-term turnover in the composition of the small mammal community reflected a combination of putative interspecific interactions, habitat requirements, and stochastic processes (fig. S3). For desert birds, however, a reduction in precipitation drove the community collapse over the past century, as persistence was positively associated with precipitation for 35 (26%) of 135 bird species (*11*). The effect was compelling at sites that both warmed and dried (*12*), which suggests that desert birds are particularly vulnerable to increased water requirements for evaporative cooling.

Exposure to climate change differed markedly between bird and small mammal communities, despite widespread warming (Fig. 2A). However, differences were apparent only upon simulating exposure with downscaled microhabitat conditions, which we accomplished using high-resolution climate models incorporating behavioral buffering. Differences were especially evident in the amount of water required for evaporative cooling to maintain homeothermy ("cooling costs"), a critical aspect of survival for desert birds and mammals (*20*–*22*). Cooling costs were higher in birds than in mammals by a factor of 3.3 across a representative landscape, and climate change

[1]Museum of Vertebrate Zoology, University of California, Berkeley, CA 94720, USA. [2]Department of Ecology, Evolution, and Organismal Biology, Iowa State University, Ames, IA 50010, USA. [3]Department of Environmental Science, Policy, and Management, University of California, Berkeley, CA 94720, USA. [4]San Francisco Estuary Institute, Richmond, CA 94804, USA. [5]Department of Birds and Mammals, San Diego Natural History Museum, San Diego, CA 92101, USA. [6]Department of Biology, University of New Mexico, Albuquerque, NM 87131, USA.
*Corresponding author. Email: beis@berkeley.edu

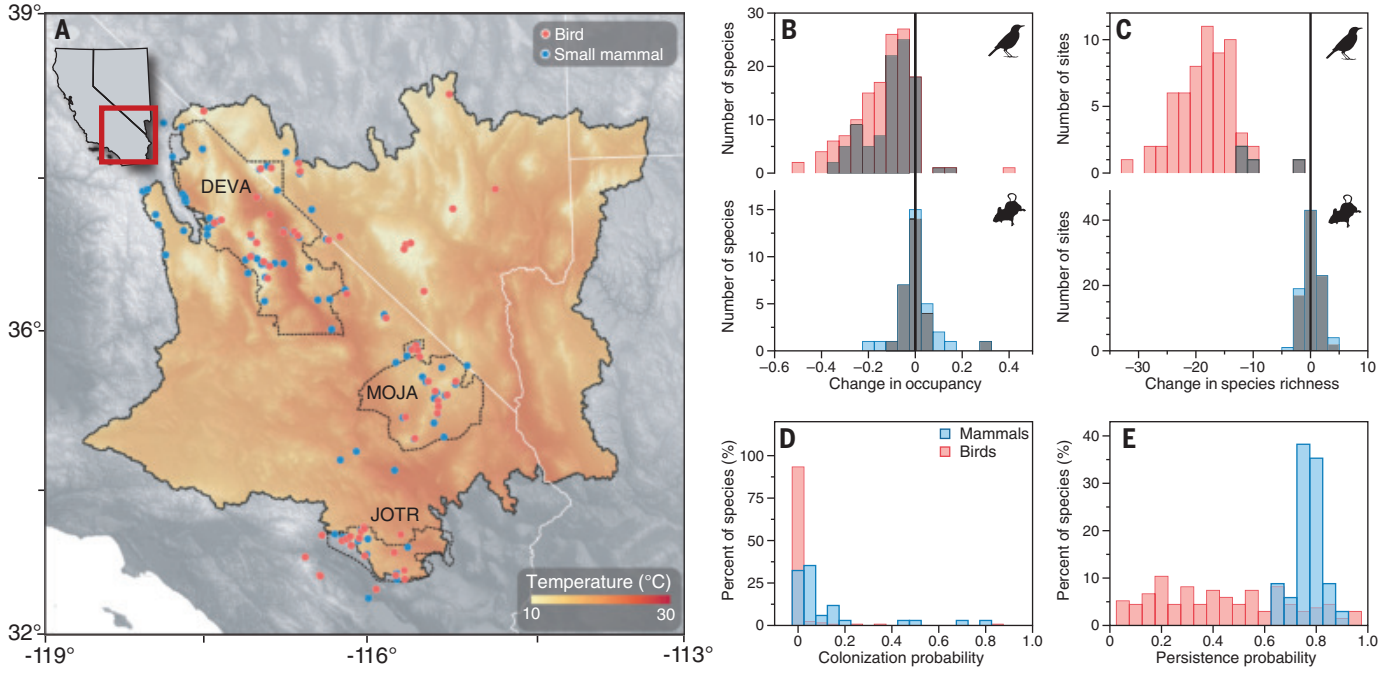

Fig. 1. The simultaneous collapse of bird communities and stability of small mammal communities over the past century in the Mojave Desert. (**A**) Survey sites for birds (red) and small mammals (blue) within the Mojave Desert, with average annual temperature from 1970 to 2000 (Worldclim v.2.1) and park boundaries for Death Valley National Park (DEVA), Mojave National Preserve (MOJA), and Joshua Tree National Park (JOTR). (**B** and **C**) Change (modern – historical) in occupancy and species richness at survey sites. Species and sites in gray did not change over the past century, whereas birds (red) and mammals (blue) changed significantly. (**D** and **E**) Colonization and persistence probabilities.

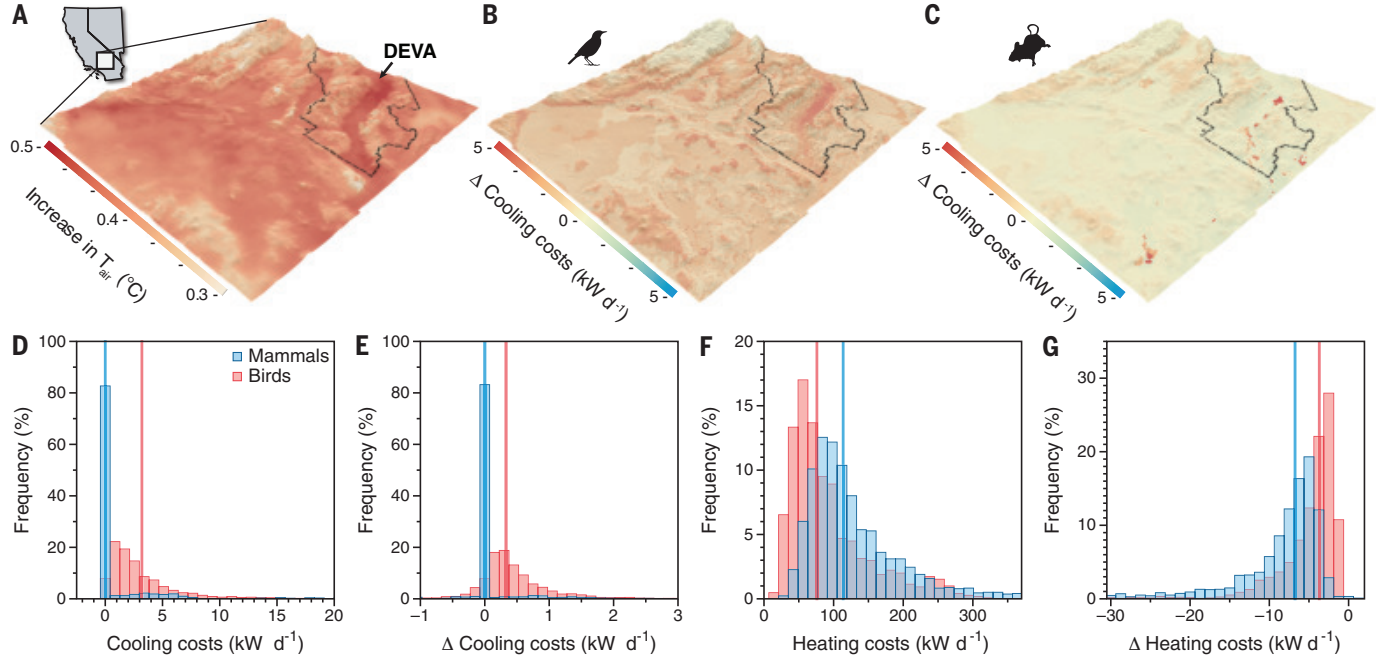

Fig. 2. Small mammals and birds differ in exposure over the past century. (**A**) Increase in average spring air temperature (see supplementary materials) for a landscape representative of climatic extremes. Dotted black line shows DEVA boundary; arrow points to Death Valley. (**B** and **C**) Average daily change in evaporative cooling required for homeothermy ("cooling costs") for birds (B) and mammals (C) assuming 50% cover in locations with vegetation. (**D**) Birds exhibited higher cooling costs than mammals at survey sites (Mann-Whitney U test; $W = 1018$, $P < 0.001$). (**E**) Changes in cooling costs at survey sites were higher for birds than for mammals ($W = 1076$, $P < 0.001$). (**F** and **G**) Relative to birds, mammals experienced higher heating costs ($W = 309$, $P < 0.001$) (F) and a greater reduction in heating costs due to climate change ($W = 936$, $P < 0.001$) (G) at survey sites. Vertical lines indicate medians for birds (red) and mammals (blue).

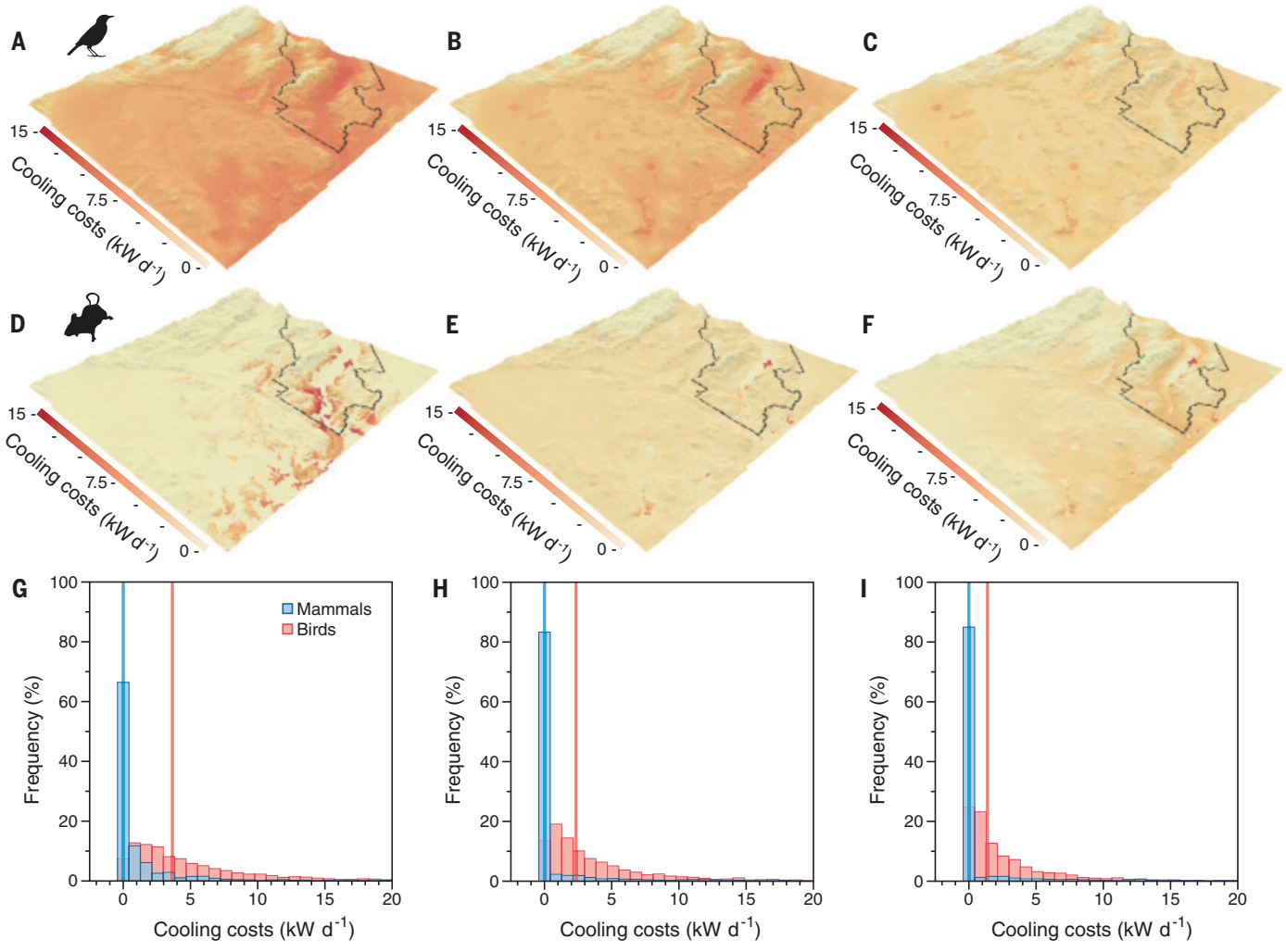

Fig. 3. Small mammals are more buffered from future climate change than birds. (**A** to **F**) Water requirements for evaporative cooling costs in a Mojave Desert landscape representative of climatic extremes for birds [(A) to (C)] and mammals [(D) to (F)] under a moderate warming scenario (RCP 6.0) and shaded 0% [(A) and (D)], 50% [(B) and (E)], and 100% [(C) and (F)] by vegetation. Dashed black line is DEVA boundary. (**G** to **I**) Cooling costs at survey sites were always higher for birds than for small mammals under warming scenario RCP 6.0 and shaded 0% (Mann-Whitney U test; $W = 1084$, $P < 0.001$) (G), 50% ($W = 1018$, $P < 0.001$) (H), and 100% ($W = 996$, $P < 0.001$) (I) by vegetation. Vertical lines indicate medians for birds (red) and mammals (blue).

increased these costs by 58.5% for birds but only 17.4% for mammals (Fig. 2, B and C). Similarly, relative to mammals, birds experienced higher cooling costs and increases in cooling costs at survey sites (Fig. 2, D and E). In fact, more than 80% of small mammals experienced low to no change in cooling costs (Fig. 2E). Metabolic heat production was similarly reduced for birds and mammals over the past century (Fig. 2, F and G). Restrictions on activity from hot temperatures were also similar for birds and mammals (fig. S4) and do not explain the contrasting community dynamics, unlike the proposed mechanism underlying population declines in some ectotherms (*23*). Despite small geographic differences between bird and mammal survey sites (Fig. 1A), climatic conditions were nearly identical between the two sets over the past century (fig. S5 and table S4).

Projections of exposure to future climate change indicate that birds will experience higher thermoregulatory costs than small mammals. Cooling costs are projected to be greater for birds than for mammals by a factor of 3.8 across a representative Mojave landscape by 2080 (Fig. 3). In general, microhabitat use produces lower physiological exposure for small mammals (Fig. 3, A to F), except for isolated locations where shallow soil depths constrain burrowing. At survey sites, birds are projected to experience greater cooling costs than small mammals, and both nocturnal and diurnal small mammals can avoid thermoregulatory cooling costs in underground burrows, even without vegetation cover (Fig. 3, G to I, and fig. S6).

Adaptations to desert life may contribute to divergent responses of birds and small mammals over the past century, but microhabitat buffering likely played a more influential role. Desert rodents are well known for dietary, physiological, and behavioral adaptations that reduce reliance on free water from their environment (*24*). However, not all rodents are well adapted to desert life. *Neotoma lepida* requires preformed water from vegetation and lacks a well-developed ability to concentrate urine (*25*). Yet this species exhibited high persistence and colonization probabilities (figs. S1 and S2), which suggests that microhabitat use offsets physiological sensitivity to warming by reducing exposure. Mammal species exhibited stable occupancy regardless of specialization to desert habitats (fig. S7) and changes were not concentrated in any family (table S1). Diurnal mammals, which have immediate, unrestricted access to cool microhabitats below ground, experienced similar, although more variable, exposure to warming than their nocturnal

counterparts (fig. S6). Among birds, desert specialists and habitat generalists declined similarly (*11*), which suggests that desert adaptation was not a buffer from climate change.

The impending threat of climate change to global biodiversity underscores the need to rapidly evaluate climate vulnerability (*2*), which is often done by assuming that changes in conditions estimated from climate projections reflect exposure for all taxa at a site (*6*–*9*). In contrast, we have demonstrated that sympatric mammals and birds with comparable physiological and ecological requirements experienced fundamentally different exposures to warming due to microhabitat buffering, which enabled stability or drove collapse of their respective communities. Moreover, among Mojave birds, species-specific exposure was strongly related to species declines (*12*). Thus, each species likely experiences different magnitudes of exposure that may affect population persistence through physiological requirements. Modeling approaches that combine physiology and behavior are needed to predict how exposure differences affect species' persistence in the face of a rapidly changing climate.

REFERENCES AND NOTES

1. M. C. Urban, *Science* **348**, 571–573 (2015).
2. S. E. Williams, L. P. Shoo, J. L. Isaac, A. A. Hoffmann, G. Langham, *PLOS Biol.* **6**, 2621–2626 (2008).
3. T. P. Dawson, S. T. Jackson, J. I. House, I. C. Prentice, G. M. Mace, *Science* **332**, 53–58 (2011).
4. B. R. Scheffers, D. P. Edwards, A. Diesmos, S. E. Williams, T. A. Evans, *Glob. Change Biol.* **20**, 495–503 (2014).
5. M. Kearney, R. Shine, W. P. Porter, *Proc. Natl. Acad. Sci. U.S.A.* **106**, 3835–3840 (2009).
6. M. T. Burrows *et al*., *Science* **334**, 652–655 (2011).
7. S. R. Loarie *et al*., *Nature* **462**, 1052–1055 (2009).
8. R. Warren, J. Price, E. Graham, N. Forstenhaeusler, J. VanDerWal, *Science* **360**, 791–795 (2018).
9. C. H. Trisos, C. Merow, A. L. Pigot, *Nature* **580**, 496–501 (2020).
10. J. Grinnell, *Pop. Sci. Mon.* **77**, 163–169 (1910).
11. K. J. Iknayan, S. R. Beissinger, *Proc. Natl. Acad. Sci. U.S.A.* **115**, 8597–8602 (2018).
12. E. A. Riddell, K. J. Iknayan, B. O. Wolf, B. Sinervo, S. R. Beissinger, *Proc. Natl. Acad. Sci. U.S.A.* **116**, 21609–21615 (2019).
13. R. S. C. Cooke, F. Eigenbrod, A. E. Bates, *Nat. Commun.* **10**, 2279 (2019).
14. K. C. Rowe *et al*., *Proc. R. Soc. London Ser. B* **282**, 20141857 (2015).
15. R. J. Rowe, J. A. Finarelli, E. A. Rickart, *Glob. Change Biol.* **16**, 2930–2943 (2010).
16. C. Moritz *et al*., *Science* **322**, 261–264 (2008).
17. M. W. Tingley, W. B. Monahan, S. R. Beissinger, C. Moritz, *Proc. Natl. Acad. Sci. U.S.A.* **106** (suppl. 2), 19637–19643 (2009).
18. J. H. Brown, B. J. Fox, D. A. Kelt, *Am. Nat.* **156**, 314–321 (2000).
19. A. E. Cahill *et al*., *Proc. R. Soc. B* **280**, 20121890 (2013).
20. O. Levy, T. Dayan, W. P. Porter, N. Kronfeld-Schor, *Am. Nat.* **188**, 205–218 (2016).
21. S. R. Conradie, S. M. Woodborne, S. J. Cunningham, A. E. McKechnie, *Proc. Natl. Acad. Sci. U.S.A.* **116**, 14065–14070 (2019).
22. T. P. Albright *et al*., *Proc. Natl. Acad. Sci. U.S.A.* **114**, 2283–2288 (2017).
23. B. Sinervo *et al*., *Science* **328**, 894–899 (2010).
24. K. A. Nagy, *Aust. J. Zool.* **42**, 55–63 (1994).
25. F. A. Smith, I. W. Murray, L. E. Harding, H. M. Lease, J. Martin, *J. Mammal.* **95**, 1128–1143 (2014).
26. E. A. Riddell *et al*., Code and data for "Exposure to climate change drives the stability or collapse of desert mammal and bird communities". Zenodo (2020), doi:10.5281/zenodo.4421498.

ACKNOWLEDGMENTS

Thanks to P. Unitt, H. Thomas, C. Patton, and many volunteers for field assistance, and. M. Kearney, O. Levy, and P. Unitt for helpful reviews. All experiments and field sampling were approved by the Institute for Animal Care and Use Committees at the University of New Mexico (16-200518-MC) and University of California, Berkeley (R317-0815). **Funding:** Supported by NSF grants DEB-1457742, -1457521, -1457524, and -1911334. Any opinions, findings, and conclusions or recommendation expressed in this material are those of the authors and do not necessarily reflect the views of NSF. **Author contributions:** S.R.B., E.A.R., K.J.I., J.L.P., L.H., and B.O.W. conceived of the study; all authors collected data; E.A.R. and K.J.I. analyzed data and performed modeling; and E.A.R., K.J.I., and S.R.B. wrote the manuscript. **Competing interests:** The authors declare no competing interests. **Data and materials availability:** Additional data and code not in the supplementary materials are found at Zenodo (*26*).

SUPPLEMENTARY MATERIALS

science.sciencemag.org/content/371/6529/633/suppl/DC1
Materials and Methods
Supplementary Text
Figs. S1 to S15
Tables S1 to S7
References (*27*–*89*)

23 June 2020; accepted 5 January 2021
10.1126/science.abd4605

SOLAR CELLS

Reconfiguring the band-edge states of photovoltaic perovskites by conjugated organic cations

Jingjing Xue[1]*, Rui Wang[1]*, Xihan Chen[2]*, Canglang Yao[3], Xiaoyun Jin[4], Kai-Li Wang[5], Wenchao Huang[6], Tianyi Huang[1], Yepin Zhao[1], Yaxin Zhai[2], Dong Meng[1], Shaun Tan[1], Ruzhang Liu[4], Zhao-Kui Wang[5], Chenhui Zhu[7], Kai Zhu[2], Matthew C. Beard[2]†, Yanfa Yan[3]†, Yang Yang[1]†

The band edges of metal-halide perovskites with a general chemical structure of ABX_3 (A, usually a monovalent organic cation; B, a divalent cation; and X, a halide anion) are constructed mainly of the orbitals from B and X sites. Hence, the structural and compositional varieties of the inorganic B–X framework are primarily responsible for regulating their electronic properties, whereas A-site cations are thought to only help stabilize the lattice and not to directly contribute to near-edge states. We report a π-conjugation–induced extension of electronic states of A-site cations that affects perovskite frontier orbitals. The π-conjugated pyrene-containing A-site cations electronically contribute to the surface band edges and influence the carrier dynamics, with a properly tailored intercalation distance between layers of the inorganic framework. The ethylammonium pyrene increased hole mobilities, improved power conversion efficiencies relative to that of a reference perovskite, and enhanced device stability.

The band-edge electronic structure of hybrid metal-halide perovskites (ABX_3, where A is usually a monovalent organic cation, B is a divalent cation, and X is a halide anion) develops from the orbitals of B and X sites (*1*) and can be tuned through the compositional and structural flexibility of the B–X framework (*2*–*12*). By contrast, the A-site cations are generally not thought to directly affect electronic structure near the band edges because their electronic states lie far from the inorganic band edges (*13*). Instead, different A-site cation sizes can induce indirect effects by causing structural deformation of the inorganic B–X framework, such as unit volume variation, octahedral distortion, and dimensional reduction (*14*–*17*). We now show that the electronic states of the A-site cations can be extended and directly contribute to the frontier orbitals of the hybrid perovskite through a combination of a large π-conjugated structure and a tailored intercalation distance between layers of the inorganic framework, which provides additional degrees of electronic tunability to near-edge electronic configuration. The carrier dynamics could be rationally tuned in accordance with the device architecture by modifying the A-site organic structure.

We designed a polycyclic aromatic tail with large π-conjugation that was attached to an ammonium A-site cation. The chemical structures of the as-synthesized organic cations featured different lengths of the tethering alkylammonium group—namely PRA, PRMA, and PREA for pyrene-based ammonium, methylammonium, and ethylammonium, respectively (Fig. 1A; see synthesis details in supplementary text S1). When these organic cations were assembled with the inorganic framework, the extent to which the positively charged ammonium head group intercalated into the octahedral cavity depended on the length of the

[1]Department of Materials Science and Engineering and California NanoSystems Institute, University of California, Los Angeles, CA 90095, USA. [2]National Renewable Energy Laboratory, Golden, CO 80401, USA. [3]Department of Physics and Astronomy and Center for Photovoltaics Innovation and Commercialization, The University of Toledo, Toledo, OH 43606, USA. [4]School of Chemistry and Chemical Engineering, Yangzhou University, Yangzhou 225002, China. [5]Institute of Functional Nano & Soft Materials (FUNSOM), Jiangsu Key Laboratory for Carbon-Based Functional Materials & Devices, Soochow University, Suzhou 215123, China. [6]Department of Materials Science and Engineering, Monash University, Clayton, VIC, 3800, Australia. [7]Advanced Light Source, Lawrence Berkeley National Laboratory, Berkeley, CA 94720, USA.
*These authors contributed equally to this work.
†Corresponding author. Email: matt.beard@nrel.gov (M.C.B.); yanfa.yan@utoledo.edu (Y.Yan); yangy@ucla.edu (Y.Yang)

bridging alkyl chain. Electron delocalization in the large conjugated pyrene structure lowered the frontier orbital separation of the organic molecule and enabled orbital overlap with the inorganic moiety (*18*).

The alkyl chain length affected the electronic interaction between the two moieties. Ultraviolet photoemission spectroscopy of PRMA and PREA cations assembled onto the surface of the Pb–I framework of a formamidinium-based perovskite thin film (Fig. 1B) revealed additional electronic states near the tail of the valence band (the Fermi energy has been aligned for better comparison). However, a perovskite thin film with the PRA moieties attached

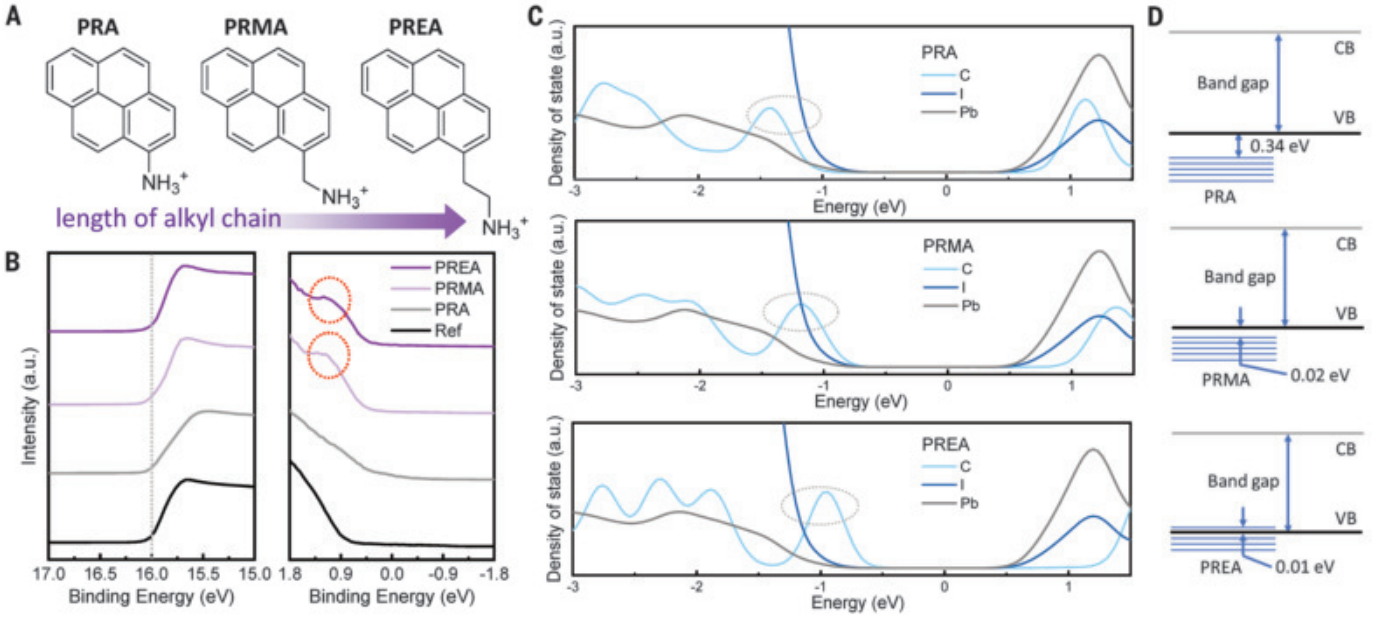

Fig. 1. Surface band-edge structures with the electronic contribution from conjugated A-site cations. (**A**) Chemical structures of three different organic ammoniums featuring different lengths of tethering alkylammonium. (**B**) Ultraviolet photoemission spectroscopy results. The vertical dashed line indicates the aligned Fermi energy; dashed circles indicate the additional electronic states. a.u., arbitrary units. (**C** and **D**) Calculated partial density of states (C) and band diagrams (D) of perovskites with PRA, PRMA, and PREA. Dashed ovals indicate the electronic states near the surface band edges. CB, conduction band; VB, valence band.

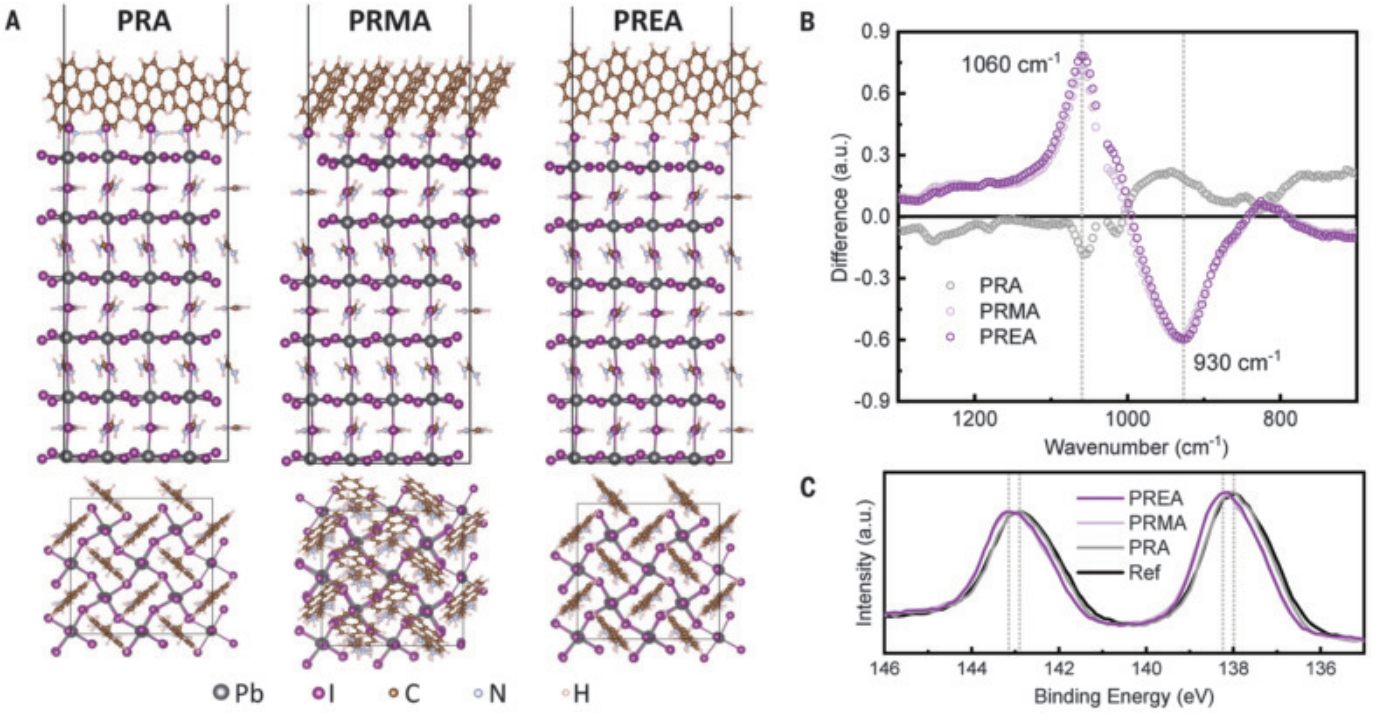

Fig. 2. Interaction modes between the conjugated ammoniums and the perovskite framework. (**A**) Side view (top) and top view (bottom) of intercalation configuration modeled by density functional theory (DFT) for PRA, PRMA, and PREA. (**B**) Difference ATR spectra of perovskite with PRA, PRMA, and PREA with respect to the reference sample. (**C**) XPS data for Pb 4f 7/2 and Pb 4f 5/2 core-level spectra for perovskite with PRA, PRMA, and PREA.

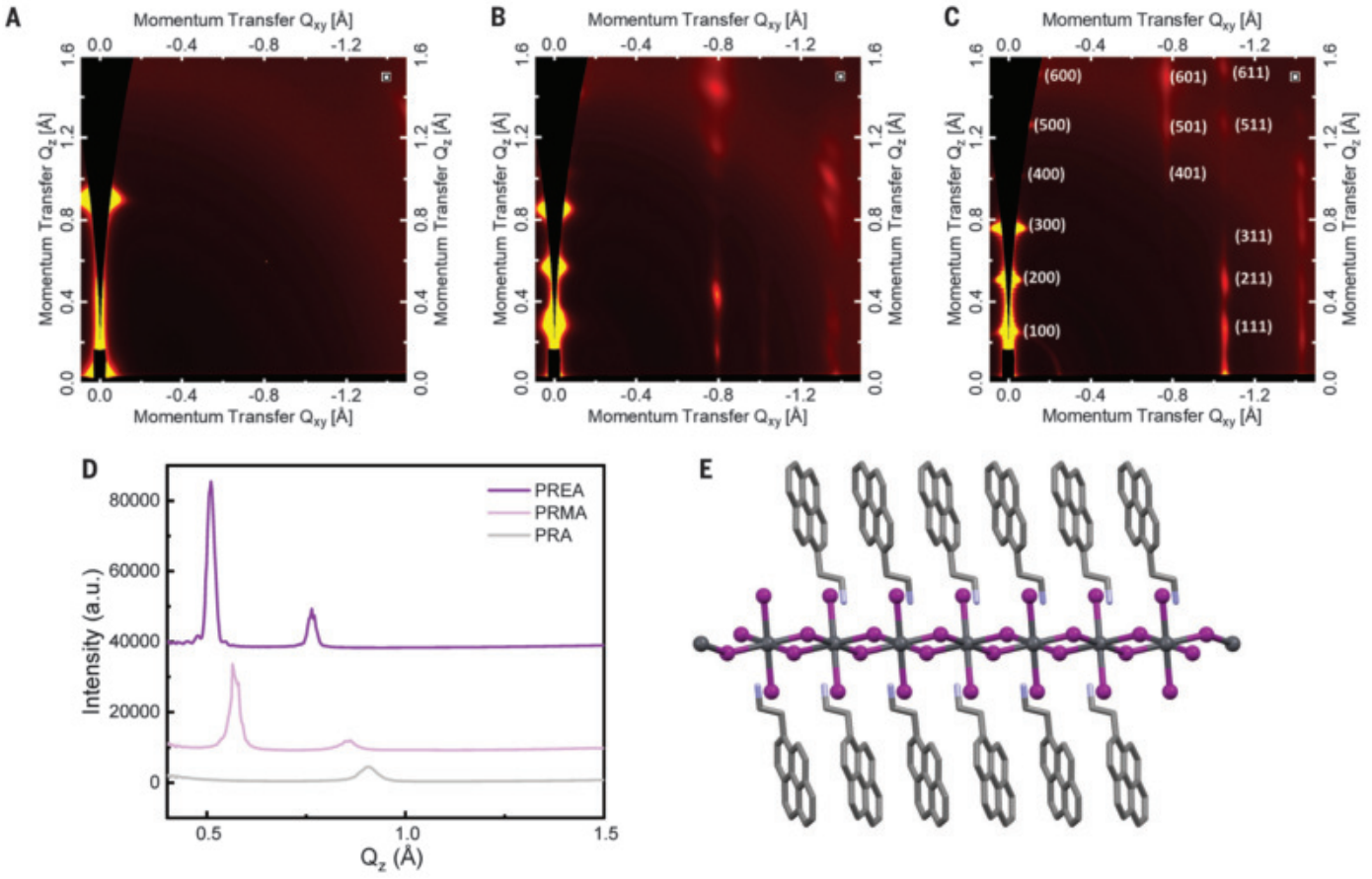

Fig. 3. Intercalation configuration of the conjugated ammoniums. (**A** to **C**) GIWAXS patterns of perovskite thin films when PbI_2 is stoichiometrically mixed with (A) PRA, (B) PRMA, and (C) PREA salt, respectively, to form a 2D perovskite phase. (**D**) Out-of-plane GIWAXS profiles for PRA-, PRMA-, and PREA-based samples. (**E**) Crystal structure of a 2D $PREA_2PbI_4$ perovskite single crystal.

exhibited similar band-tail characteristics to that of the reference, indicating a lack of electronic contribution from PRA to the surface band edges.

First-principles calculations of the partial density of states revealed electronic states near the surface band edges (Fig. 1C). As the alkyl chain of the ammonium group became longer, the electronic states from the organic components at the valence band were pushed to a higher energy level. The electronic states from PRA were as much as 0.34 eV below the valence band maximum (VBM), but PRMA and PREA had electronic states near the VBM. The distribution of the electronic states of the organic ammonium cations with respect to the inorganic band structure (Fig. 1D) showed that the orbitals of PRMA and PREA greatly overlapped with the inorganic VBM, with the highest unoccupied orbitals only 0.02 eV below and 0.01 eV above the VBM, respectively. Thus, the band structure of PRA resembled that of the reference film, with the VBM consisting of I 5p and Pb 6s orbitals. However, for PRMA and PREA, the VBM had contributions from the orbitals of both inorganic and organic components. The participation of PRMA and PREA in the surface band-edge construction was also observed in all-inorganic $CsPbI_2Br$ perovskite (supplementary text S2), indicating the generality of this concept.

The discrepancy in the surface band-edge configuration originated from different chemical interaction modes between the inorganic framework and the ammonium cations with different alkyl chain lengths; theoretical modeling of the assembly of these organic ammoniums on the surface of the Pb–I framework is shown in Fig. 2A. We used time-of-flight secondary-ion mass spectrometry and grazing-angle polarization-dependent infrared reflection-absorption spectroscopy to verify the vertical assembly of the ammonium cations on the surface (supplementary text S2 and S3). Both PRMA and PREA could anchor into the octahedral cavity through electrostatic interactions between the ammonium cations and the PbI_6^{2-} octahedra. However, PRMA, which has a shorter alkyl chain length between the ammonium head and the pyrene tail, exhibited a distorted intercalation configuration because of the structural rigidity and pronounced steric hindrance induced by the pyrene ring.

The elongated alkyl chain in PREA enabled more flexibility with less steric hindrance and displayed almost vertical intercalation of PREA into the inorganic layers. The conjugated tails of PREA were stacked nearly perpendicular to the plane of the inorganic layer. With a reduction in the length of the tethering alkylammonium group, the orientation of PRMA tilted away from the vertical direction by ~30°, which disrupted the π-π stacking and reduced the electronic delocalization. By contrast, PRA, which lacked a flexible alkyl chain, failed to relieve the steric hindrance of the pyrene group when anchoring into the Pb–I framework. Its binding mode to the inorganic surface would be more accurately described as adsorption rather than anchoring, as also evidenced by the vertically oriented pyrene tail in PRA stacking. With a shallow interaction depth, the steric hindrance from the large pyrene tail no longer affects the intercalation configuration, enabling a molecular orientation driven by the surface energy and π-π stacking.

We used attenuated total reflection–Fourier transform infrared (ATR-FTIR) spectroscopy to investigate the chemical binding between

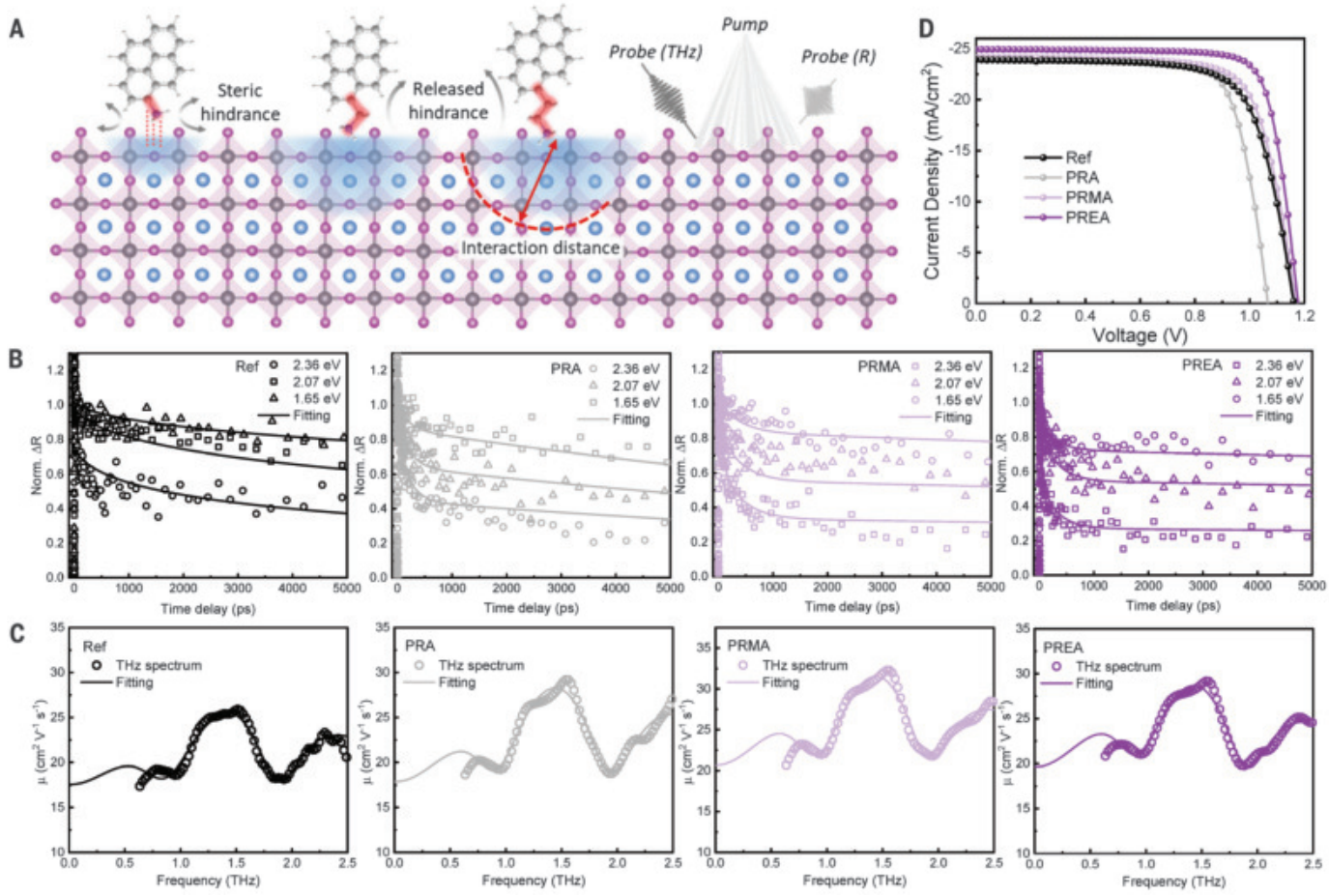

Fig. 4. Investigations on the change of carrier dynamics and photovoltaic response. (**A**) Schematic illustration of the influence of intercalation configuration and the interaction distance revealed by the combination of TRS and TRTS. R, reflection; THz, terahertz. (**B**) Surface-carrier kinetics pumped at 2.36, 2.07, and 1.65 eV probed by TRS and fitted with a diffusion model and (**C**) TRTS spectra at 5-ps time delay and fitted with a Drude-Smith model for the reference sample and perovskite with PRA, PRMA, and PREA. (**D**) Current density–voltage curves of the as-fabricated perovskite solar cells, showing the influence of the changed band-edge configurations, and thus the carrier dynamics, on photovoltaic performance.

the organic cations and the Pb-I framework. Difference ATR-FTIR spectra of perovskite films with PRA, PRMA, and PREA with respect to the reference film are shown in Fig. 2B. Distinctive vibration features from the reference and PRA samples were observed in PRMA and PREA samples between 900 to 1100 cm^{-1}. Both PRMA and PREA showed substantially reduced absorption near 930 cm^{-1} and increased absorption near 1060 cm^{-1}, which we attributed to the change of the out-of-plane N–H wagging and C–N stretching modes, respectively. The absence of distinctive vibration features in PRA samples indicated a different binding mode with a weak interaction. High-resolution x-ray photoemission spectroscopy (XPS) of the Pb 4f orbital for the perovskite film with different ammonium cations (Fig. 2C) showed two main peaks at ~138 and ~143 eV, corresponding to the Pb 4f 7/2 and Pb 4f 5/2 orbitals, respectively (*19*). The peaks from Pb 4f shifted to higher binding energies in the film with PRMA and PREA, whereas the spectra of PRA samples remained almost identical to that of the reference sample. This difference suggested a stronger interaction between PRMA or PREA and Pb, as well as a more profound influence on the bonding character of Pb in the inorganic framework, compared with that in the case of PRA.

The dense and periodic insertion of the pyrene-based ammoniums into the Pb–I framework was further evaluated by grazing-incident wide-angle x-ray scattering (GIWAXS) and the growth of two-dimensional (2D) perovskite single crystals. The GIWAXS patterns of perovskite thin films generated by stoichiometrically mixing PbI_2 and PRA, PRMA, or PREA salt to form a 2D perovskite phase are shown in Fig. 3, A to C, respectively. Both PRMA- and PREA-based perovskite samples exhibited out-of-plane diffraction patterns of {100} planes, indicating the formation of 2D perovskite phases, but this diffraction feature was absent for PRA, confirming that it failed to anchor into the Pb–I framework. The PREA-based 2D perovskite showed much higher crystallinity and preferred out-of-plane crystallographic orientation than PRMA perovskites (Fig. 3D), further verifying the distorted intercalation configuration of PRMA. Single crystals of PREA-based 2D perovskite showed the periodic stacking mode of the pyrene-based ammonium cations, and the pyrene rings had an edge-on packing with the Pb–I framework (Fig. 3E; see details of the crystal structures and the growth of single crystals in supplementary text S4).

The reconfiguration of the surface band-edge electronic structures involving A-site organic cations and the alkylammonium-controlled intercalation distance were also reflected in the change of surface carrier dynamics, which were probed by transient reflection spectroscopy (TRS) and time-resolved terahertz spectroscopy (TRTS) (*20*, *21*). By modeling the measured surface carrier kinetics with a defined surface interaction distance (see the modeling details in supplementary text S5), we could determine the binding configuration

because the electronic interaction distance was related to the binding character between the organic ammonium cations and the inorganic moieties (Fig. 4A). The surface carrier kinetics probed by transient optical reflection for the cases of reference, PRA, PRMA, and PREA (Fig. 4B) revealed a ~33% increase in the interaction distance for PRMA or PREA relative to that for PRA (the absolute values may be longer than expected in the model, owing to the effects of film roughness). This increase in the interaction distance was consistent with the interaction mode between the organic ammonium cations and the perovskite lattice, where PRMA and PREA inserted into the lattice, unlike PRA.

The photoinduced electron and hole carrier mobilities are extracted by combining TRS and TRTS results. The surface photogenerated carrier transport was measured with the reflected optical probe (*22*) and provided information on the ambipolar diffusion coefficient (D_{ab}) (*23*, *24*), whereas the terahertz probe pulse was sensitive to the sum of the electron and hole mobilities $\sum\mu = \mu_e + \mu_h$ (*20*). By using the Einstein relation to determine the ambipolar mobility (μ_{ab}) from D_{ab} and combining it with $\sum\mu$, the individual mobilities of electrons μ_e and holes μ_h can be derived because $1/\mu_{ab} = (1/\mu_e) + (1/\mu_h)$. The sum of the dc mobility (μ_{dc}) was extracted by using a Drude-Smith model from transient terahertz spectra at 5-ps delay for reference, PRA, PRMA, and PREA (Fig. 4C; see modeling details in supplementary text S5). The best-fit parameters and the calculated carrier mobilities are summarized in table S1. Because the orbitals of the organic ammonium cations mainly interacted with the valence band of the inorganic lattice, the hole mobility was most substantially affected. The largest increase in hole mobility was observed for PREA; electron mobilities remained almost invariant across all samples.

The enhancement in hole mobility benefited the carrier collection in perovskite photovoltaic devices, as reflected by an increase in the short-circuit current (J_{sc}) and fill factor (FF). The power conversion efficiency (PCE) of the as-fabricated perovskite solar cells with PREA exhibits the largest enhancement, from 20.1 to 23.0% (Fig. 4D). A smaller enhancement of hole mobility, and thus J_{sc} and FF, was observed for PRMA, which we attributed to the distorted intercalation of the ammonium cations generating energy disorder in the lattice. However, PRA actually led to a decrease in PCE because of a reduced open-circuit voltage that resulted from an unmatched energy level with the hole-transporting layer (supplementary text S3). Thus, rational control of the intercalation distance regulated by the tethering alkyl ammonium enabled electronic contribution of A-site cations to the near-edge band structure and, in turn, modified the carrier kinetics within devices. The insertion of the ammonium head into the framework, and thus the exposure of the hydrophobic polycyclic aromatic tail, further increased the stability of the devices. After 2000 hours of exposure to continuous light under open-circuit conditions, the device with PREA maintained more than 85% of its original PCE, whereas the reference device degraded to only 60% of its initial PCE (supplementary text S6).

REFERENCES AND NOTES

1. W. J. Yin, T. Shi, Y. Yan, *Appl. Phys. Lett.* **104**, 063903 (2014).
2. J. S. Manser, J. A. Christians, P. V. Kamat, *Chem. Rev.* **116**, 12956–13008 (2016).
3. W. Nie *et al.*, *Science* **347**, 522–525 (2015).
4. B. Saparov, D. B. Mitzi, *Chem. Rev.* **116**, 4558–4596 (2016).
5. J. W. Lee, H. S. Kim, N. G. Park, *Acc. Chem. Res.* **49**, 311–319 (2016).
6. B. Chen, P. N. Rudd, S. Yang, Y. Yuan, J. Huang, *Chem. Soc. Rev.* **48**, 3842–3867 (2019).
7. D. Bi *et al.*, *Nat. Energy* **1**, 16142 (2016).
8. H. Zhang, M. K. Nazeeruddin, W. C. H. Choy, *Adv. Mater.* **31**, e1805702 (2019).
9. R. Wang *et al.*, *Adv. Funct. Mater.* **29**, 1808843 (2019).
10. Y. Gao *et al.*, *Nat. Chem.* **11**, 1151–1157 (2019).
11. H. Min *et al.*, *Science* **366**, 749–753 (2019).
12. R. Wang *et al.*, *Science* **366**, 1509–1513 (2019).
13. W. J. Yin, J. H. Yang, J. Kang, Y. Yan, S. H. Wei, *J. Mater. Chem. A* **3**, 8926–8942 (2015).
14. J.-W. Lee *et al.*, *Nat. Commun.* **9**, 3021 (2018).
15. H. Tsai *et al.*, *Nature* **536**, 312–316 (2016).
16. G. Grancini *et al.*, *Nat. Commun.* **8**, 15684 (2017).
17. G. Grancini, M. K. Nazeeruddin, *Nat. Rev. Mater.* **4**, 4–22 (2019).
18. P. A. J. de Paula, *Physical Chemistry for the Life Sciences* (Oxford Univ. Press, 2006).
19. L. Wang *et al.*, *Science* **363**, 265–270 (2019).
20. Y. Zhai *et al.*, *ACS Energy Lett.* **5**, 47–55 (2020).
21. J. Tong *et al.*, *Science* **364**, 475–479 (2019).
22. W. Chu, Q. Zheng, O. V. Prezhdo, J. Zhao, W. A. Saidi, *Sci. Adv.* **6**, eaaw7453 (2020).
23. Y. Yang *et al.*, *Nat. Energy* **2**, 16207 (2017).
24. X. Chen, K. Wang, M. C. Beard, *Phys. Chem. Chem. Phys.* **21**, 16399–16407 (2019).

ACKNOWLEDGMENTS

Funding: This material is based on work supported by the U.S. Department of Energy's (DOE) Office of Energy Efficiency and Renewable Energy (EERE) under Solar Energy Technologies Office award DE-EE0008751. Work performed at the National Renewable Energy Laboratory and University of Toledo was supported as part of the Center for Hybrid Organic Inorganic Semiconductors for Energy (CHOISE), an Energy Frontier Research Center funded by the DOE Office of Basic Energy Sciences, under contract DE-AC36-08GO28308, with Alliance for Sustainable Energy, LLC, the Manager and Operator of the National Renewable Energy Laboratory. The views expressed in the article do not necessarily represent the views of the DOE or the U.S. government. All theoretical works were performed on National Renewable Energy Laboratory's Eagle Computing System and National Energy Research Scientific Computing Center. The work at the Yangzhou University was financially supported by the Priority Academic Program Development of Jiangsu Higher Education Institutions. Z.-K.W. acknowledges the Natural Science Foundation of China (91733301). This project was also supported by the Collaborative Innovation Center of Suzhou Nano Science and Technology. Part of the GIWAXS measurement was performed in beamline 7.3.3 at the Advanced Light Source, Lawrence Berkeley National Laboratory. The Australian Synchrotron, part of ANSTO, is also acknowledged for the GIWAXS characterizations. **Author contributions:** J.X. and R.W. conceived the idea, designed and conducted the experiments, and prepared the manuscript under the supervision of Y.Yang. X.C. designed and carried out the spectroscopy investigations and assisted with manuscript preparation under the supervision of M.C.B. Y.Zhai assisted with the spectroscopy measurement. C.Y. performed the DFT calculations under the supervision of Y.Yan. X.J., R.L., and J.X. designed and synthesized the materials. J.X., R.W., and D.M. synthesized and analyzed the single crystals. K.-L.W. assisted with the characterization of single crystals under the supervision of Z.-K.W. T.H., S.T., and Y.Zhao assisted with the thin-film characterizations. C.Z., W.H., and R.W. performed the GIWAXS measurement. K.Z. contributed helpful discussion during the project. All authors discussed the results and commented on the manuscript. **Competing interests:** The authors declare no competing interests. **Data and materials availability:** All data are available in the main text or the supplementary materials. Crystallographic parameters for the structure of $PREA_2PbI_4$ are archived at the Cambridge Crystallographic Data Centre (www.ccdc.cam.ac.uk/) under reference number CCDC 2045757.

SUPPLEMENTARY MATERIALS

science.sciencemag.org/content/371/6529/636/suppl/DC1
Materials and Methods
Supplementary Text S1 to S6
Figs. S1 to S22
Tables S1 to S3
References (*25*–*32*)

23 June 2020; resubmitted 4 December 2020
Accepted 5 January 2021
10.1126/science.abd4860

NGS Cancer Panels

Oxford Gene Technology (OGT) has expanded its SureSeq range of NGS panels to facilitate the interrogation of genes involved in breast and ovarian cancer and myeloid disorders. The two new panels include a comprehensive 70-gene myeloid panel and a 7-gene breast and ovarian cancer panel that incorporates copy number variation (CNV) detection. Facilitated by OGT's expert bait design and complimentary Interpret NGS analysis software, the SureSeq Pan-Myeloid panel includes genes such as *CEBPA*, *JAK2*, *CALR*, and *MPL*, as well as covering regions containing hard-to-detect structural variants such as *FLT3*-ITDs and *KMT2A*-PTDs. The SureSeq Breast Cancer + CNV panel targets *BRCA1*, *BRCA2*, *ATM*, *TP53*, *CHEK2*, *PALB2*, and *PTEN*, and can detect CNVs ranging from single exons to full gene deletions and duplications in these genes as well. For customers interested in a larger breast or ovarian cancer panel, OGT offers customization through the SureSeq myPanel range of preoptimized panel content, which can be added to the Breast Cancer + CNV Panel.

Oxford Gene Technology
For info: +44-(0)-1865-856800
www.ogt.com/ngs_products

HiFi Sequencing

PacBio's Sequel IIe System offers increased computational capacity and on-instrument data processing for streamlined production of highly accurate long reads—known as HiFi reads. Optimized for HiFi reads, Sequel IIe eliminates the need for postprocessing of sequence data by users and delivers a 70% reduction in overall secondary analysis time, depending on the application. It also reduces file-transfer and data-storage needs by as much as 90%. The instrument includes powerful new analysis tools, complete workflow integration on the Amazon Web Services cloud, and a new genome-assembly application for generating reference-quality de novo assemblies from HiFi reads.

PacBio
For info: 877-920-7222
www.pacb.com

High Molecular Weight DNA Extraction

Monarch HMW DNA Extraction Kits provide rapid, reliable extraction of high molecular weight (HMW) DNA from biological samples. These kits utilize an optimized process that combines gentle cell lysis with a tunable fragment-length generation, followed by precipitation of the extracted DNA onto the surface of large glass beads. DNA size ranges from 50 kb to 250 kb for the standard protocol and into the Mb range for certain sample types when the lowest agitation speeds are used. Purified DNA is recovered in high yield with excellent purity—including nearly complete removal of RNA—and is ready for use in downstream applications, including long-read sequencing.

New England BioLabs
For info: 800-NEB-LABS (800-632-5227)
www.neb.com

cDNA Library Preparation

KAPA HyperPrep Kits offer a streamlined complementary DNA (cDNA) library preparation protocol that combines several enzymatic steps and eliminates bead cleanups to significantly reduce library preparation time and improve consistency. Their novel, single-tube chemistry further improves library construction efficiency, particularly for challenging samples such as formalin-fixed, paraffin-embedded tissue and cell-free DNA. The kits offer a complete library preparation solution with KAPA Adapters and KAPA HyperPure Beads. RNA-sequencing (RNA-seq) is becoming the gold standard for transcriptomics research, which provides valuable insights into different gene-expression levels due to environmental conditions, therapeutic intervention, developmental stage, or tumor state and progression. Some researchers have found RNA-seq difficult to adopt due to the wide variety of workflows and challenges in cDNA library preparation. Roche's KAPA RNA HyperPrep Kits cover multiple different RNA-seq workflows, including ribosomal depletion and messenger RNA capture.

Roche Sequencing
For info: 800-262-4911
sequencing.roche.com/en.html

Cas9 Proteins for CRISPR Genome Editing

System Biosciences' products deliver highly controlled CRISPR/Cas9 activity through direct introduction—by transfection, electroporation, or microinjection—of the Cas9 protein. Choose our EGFP-labeled Cas9 Protein (NLS-Cas9-EGFP) for easy visualization and screening of cells that have had Cas9 successfully introduced. Or choose our unlabeled option, Purified Cas9 Protein (NLS-Cas9-NLS), which is tagged with two nuclear localization signals (NLS) for efficient targeting to the nucleus. Highly concentrated and ready-to-use, purified Cas9 protein acts immediately upon entering the nucleus and is rapidly cleared, leading to fewer off-target events than delivery by messenger RNA or DNA. Both NLS-Cas9-EGFP and NLS-Cas9-NLS are available bundled into complete kits with a T7 guide RNA cloning and production vector for your convenience.

System Biosciences
For info: 888-266-5066
systembio.com

SARS-CoV-2 Real-Time RT-PCR Assay

The PerkinElmer SARS-CoV-2 Real-Time RT-PCR assay is CE-IVD (in vitro diagnostic) marked and intended for qualitative detection of nucleic acid from the SARS-CoV-2 virus in human oropharyngeal swab, nasopharyngeal swab, and saliva specimens from individuals suspected of having COVID-19 or from asymptomatic carriers. The assay target two specific genomic regions of SARS-CoV-2: the nucleocapsid (N) gene and ORF1ab; so mutations in spike protein, as seen in the B.1.1.7 and B.1.351 coronavirus lineages, do not impact the safety and effectiveness of PerkinElmer's assays. This test is also for qualitative detection of nucleic acid from the SARS-CoV-2 virus in pooled specimens containing up to five individual specimens (nasopharyngeal swabs and saliva) on the chemagic 360 instrument, where each specimen is collected under observation or by a health care provider using individual vials containing transport media. Pooling is desirable because it allows labs to reduce costs and increase throughput, but it requires a sensitive assay. Automation solutions are available delivering plug-and-play pooling prior to viral RNA isolation.

PerkinElmer
For info: 800-762-4000
www.perkinelmer.com

Electronically submit your new product description or product literature information! Go to www.sciencemag.org/about/new-products-section for more information.

Newly offered instrumentation, apparatus, and laboratory materials of interest to researchers in all disciplines in academic, industrial, and governmental organizations are featured in this space. Emphasis is given to purpose, chief characteristics, and availability of products and materials. Endorsement by *Science* or AAAS of any products or materials mentioned is not implied. Additional information may be obtained from the manufacturer or supplier.

Who's the top employer for 2020?

Science Careers' annual survey reveals the top companies in biotech & pharma voted on by *Science* readers.

Read the article and employer profiles at sciencecareers.org/topemployers

Science 2020
TOP EMPLOYER

CityU
香港城市大學
City University of Hong Kong

48th World University
4th World's top 50 Universities under age 50
1st World's Most International Universities
1st Engineering/Technology/Computer Sciences in Hong Kong
2nd Business School in Asia

Worldwide Search for Talent

City University of Hong Kong is a dynamic, fast-growing university that is pursuing excellence in research and professional education. As a publicly funded institution, the University is committed to nurturing and developing students' talents and creating applicable knowledge to support social and economic advancement. The University has nine Colleges/Schools. As part of its pursuit of excellence, the University aims to recruit **outstanding scholars** from all over the world in various disciplines, including **business, creative media, data science, energy and environment, engineering, humanities and social sciences, law, science, veterinary medicine and life sciences.**

The University welcomes applications and nominations for all faculty positions of Chair Professor, Professor, Associate Professor and Assistant Professor. The remuneration package will be highly competitive, commensurate with qualifications and experience. Interested parties are invited to submit an online application with current curriculum vitae to apply for current openings at http://go.cityu.hk/hrojobus or by email to "hrojob@cityu.edu.hk".

City University of Hong Kong is an equal opportunity employer and we are committed to the principle of diversity. Personal data provided by applicants will be used for recruitment and other employment-related purposes.

Worldwide recognition ranking 48th, and 4th among top 50 universities under age 50 (QS survey 2021); 1st in the World's Most International Universities (THE survey 2020); 1st in Engineering/Technology/Computer Sciences in Hong Kong (ARWU survey 2016); and 2nd Business School in Asia-Pacific region (UT Dallas survey 2017).

ScienceCareers online @sciencecareers.org

ScienceCareers
FROM THE JOURNAL SCIENCE AAAS

Confused about your next career move?

Download Free Career Advice Booklets!

ScienceCareers.org/booklets

ICYS Research Fellow at ICYS, NIMS, Japan

The International Center for Young Scientists (ICYS) of the National Institute for Materials Science (NIMS) invites applications for ICYS Research Fellow positions. ICYS will offer you the freedom to conduct independent and self-directed research in various areas of materials science with full access to NIMS advanced research facilities.

The common language at ICYS is English. Clerical and technical support in English will be given by the ICYS staff. An annual salary of approximately 5.35 million yen is guaranteed, which may be increased to a maximum of ~5.88 million yen depending on the performance of the Research Fellow*. In addition, a research grant of 2 million yen per year will be provided to each Research Fellow. The initial contract term is two years, which may be extended for another year depending on one's performance.

All applicants must have obtained a PhD degree within the last ten years. Applicants should submit an **application form** including a research proposal during the ICYS term, **CV Header**, **CV** with a list of publications and patents, **a list of DOI of journal publications**, and **PDF files of three significant publications**, to the ICYS Recruitment Desk by **March 31, 2021 JST**. The format for the **application form** and **CV header** can be downloaded from **our website**. The selection will be made on the basis of originality and quality of the research proposal as well as the research achievements. Please visit our website for more details.

* Approximately 23% of annual salary will be deducted as social insurance premium, residence tax and income tax.

ICYS Recruitment Desk
National Institute for Materials Science
www.nims.go.jp/icys/recruitment/

School of Medicine Columbia

UNIVERSITY OF SOUTH CAROLINA
NON-TENURE TRACK RESEARCH ASSISTANT PROFESSOR

The Department of Pathology, Microbiology and Immunology at the University of South Carolina's School of Medicine invites applications for a non-tenure track **Research Assistant Professor**. This position will be part of the phase-2 Center of Biomedical Research Excellence (COBRE) focusing on Dietary Supplements and Inflammation (CDSI). The successful candidate will study effects of plant products and environmental pollutants on autoimmune and inflammatory diseases including cancer addressing the epigenetic mechanisms and microbial dysbiosis underlying immune dysregulation.

Candidates must have a PhD in any area of Biomedical Sciences. Preference will be given to candidates who have experience in -omics technology. Salary commensurate with experience. Please apply to the position by following this link **https://uscjobs.sc.edu/postings/93296**.

The University of South Carolina does not discriminate in educational or employment opportunities on the basis of race, sex, gender, gender identity, transgender status, age, color, religion, national origin, disability, sexual orientation, genetics, protected veteran status, pregnancy, childbirth or related medical conditions.

TEXAS A&M UNIVERSITY Biology

Head, Department of Biology Texas A&M University

A national search is underway to identify outstanding candidates for **Head of the Department of Biology** at Texas A&M University, the fourth largest university in the nation with more than 50,000 students, a multibillion-dollar endowment ranked fourth among public universities and a top 20 research enterprise.

The Department of Biology currently has 40 tenured/tenure-track faculty, 14 academic professional track faculty, 39 staff, 1600 undergraduate majors and 90 graduate students. Further information about the Department, its faculty and its facilities can be found at **https://www.bio.tamu.edu**.

We seek candidates who have an internationally recognized research program, demonstrated experience and commitment to undergraduate and graduate teaching and scholarship, a broad perspective of biology disciplines, and proven leadership skills. The Head reports to the Dean of the College of Science and is responsible for the Department's administrative, budgetary and personnel matters. The Head will be responsible for implementing our strategic plan (**https://www.bio.tamu.edu/strategic-plan/**) to raise five cutting-edge research areas within the biological sciences at Texas A&M University to preeminence. The Head will also promote high standards for continued growth, excellence and innovation in undergraduate and graduate education. The position requires a Ph.D. in Biology or related field and a record of scholarship and teaching consistent with the level of professor at a major research university.

Interested applicants should submit a detailed CV and statements of research accomplishments, teaching perspective and administrative philosophy online at **http://apply.interfolio.com/82061**. Review of applications will begin **February 1** and continue until the position is filled. Any questions regarding this position may be directed to the Chair of the Search Committee, Dr. Paul Hardin at **headsearch@biol.tamu.edu**.

Bryan-College Station, home to Texas A&M University, is a vibrant, dynamic, and rapidly growing community that offers cultural diversity, arts and entertainment, job opportunities, and overall quality of life. Located in the heart of the Houston-Dallas-Austin triangle, the region offers the modern amenities of a big city with a warm, small-town charm, and the community's low cost of living is advantageous to the student and general populations, making it an ideal place to live.

Texas A&M University is committed to enriching the learning and working environment for all visitors, students, faculty, and staff by promoting a culture that embraces inclusion, diversity, equity, and accountability. Diverse perspectives, talents, and identities are vital to accomplishing our mission and living our core values.

Equal Opportunity/Affirmative Action/Veterans/Disability Employer committed to diversity.

ScienceCareers online @sciencecareers.org

By **Nawar Naseer** *and* **Katherine Strelau**

Tracing contacts, finding ourselves

In March 2020, we shut down our Ph.D. experiments and prepared for an indefinite period of working from home. As we threw away our cell cultures and wound down our animal colonies, we imagined the manuscripts we would finally draft, the papers we would read, and the bioinformatic skills we would learn. However, our plans went astray a few days later when we received an email from our program director with a subject line that read: "Interested in an 'at home' public health project to help fight COVID-19?" The email set us down a path we never imagined—one that taught us how the soft skills we've learned in graduate school can serve us in the real world. We also learned the hard way that in order to take care of others, we must first take care of ourselves.

Our program director asked us to lead a contact tracing team, charged with tracking down people who'd tested positive for COVID-19 in our city and anyone they may have come in contact with. At first we hesitated, unsure we were qualified. We were both pursuing certificates in public health alongside our microbiology doctorate degrees, but we didn't have any real-world experience in public health or epidemiology. We were comfortable in a tissue culture hood; what did we know about contact tracing?

We signed up anyway, itching to do something, *anything*, to help in a time of crisis. Knowing we would need an army of people to serve as contact tracers, we drafted a volunteer application form and emailed it to everyone at our university working in public health, social work, and medicine. Over the next 5 days, we screened and interviewed more than 100 candidates, ultimately taking on 60 volunteers.

Then we built our operation from scratch. We dug into the literature about contact tracing to identify best practices, reached out to contact tracing teams across the nation for guidance, and prepared instructional presentations for the volunteers. Skills we'd gained through our Ph.D. training proved surprisingly useful, such as the ability to research and digest large amounts of information and communicate it to others. Contact tracing was nothing like our Ph.D. projects, but in some ways, we felt prepared to take it on.

Within 3 weeks, our team started to make phone calls to people who may have come in contact with an infected individual and our roles shifted toward providing guidance and support. Every day, new scenarios arose that we hadn't anticipated, keeping us on our toes.

Our most emotionally challenging day came on the same April day the United States surpassed 1 million confirmed COVID-19 cases. One of our volunteers called a contact, only to learn they had already passed away from the virus. It was a dark reminder of what we were up against and the importance of moving quickly.

"Skills we'd gained through our Ph.D. training proved surprisingly useful."

The sense of urgency left little time for anything else. We ate meals quickly so we could keep up with the onslaught of video calls. We gave up rejuvenating activities, such as yoga classes and relaxing baths. Our sleep suffered and our mental health plummeted. As weeks turned into months, it became increasingly difficult to think clearly, and we started to make mistakes. One of us even had a panic attack during a meeting.

Eventually, we realized we'd forgotten about our own well-being; we needed to keep ourselves emotionally and physically healthy to help others. So we started to reclaim our weekends, taking turns being on call so the other person could unplug. We were still stressed at times, but as our well-being improved, we found it easier to focus on the critical work we were doing.

After 4 months, our labs began to reopen and we needed to resume our bench science, so we handed our duties over to others. We were devastated to walk away from the work, but also immensely grateful for what we learned from the experience. We're not sure where we'll head next in our careers—whether toward research or the front lines of public health—but we now know we can pivot away from bench science if we choose to. Our doctoral training has equipped us with skills transferable to just about anything, as long as we remember to take care of ourselves. ■

Nawar Naseer and Katherine Strelau are Ph.D. candidates at the University of Pennsylvania. Send your career story to SciCareerEditor@aaas.org.

ILLUSTRATION: ROBERT NEUBECKER

Pushing the Boundaries of Knowledge

As AAAS's first multidisciplinary, open access journal, *Science Advances* publishes research that reflects the selectivity of high impact, innovative research you expect from the *Science* family of journals, published in an open access format to serve a vast and growing global audience. Check out the latest findings or learn how to submit your research: **ScienceAdvances.org**

Science Advances
AAAS

GOLD OPEN ACCESS, DIGITAL, AND FREE TO ALL READERS

Immune Cells Research CRO

Advancing All Things Immunology

Lymphoid Cells

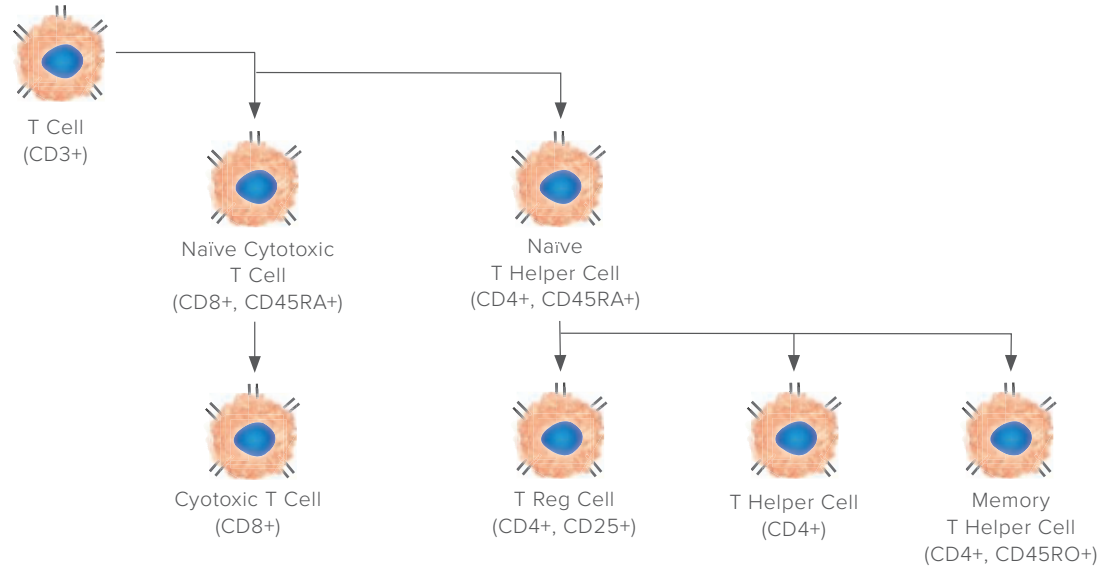

Myeloid Cells

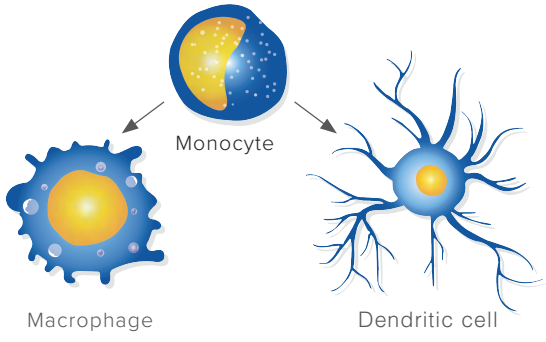

CAR-T Cells

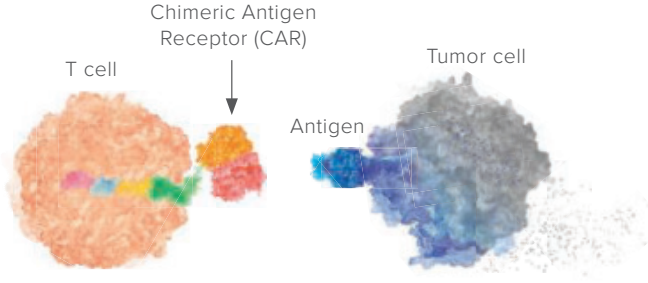

ProMab Biotechnologies offers many different products and services to advance immuno-oncology research. With a wide offering of high quality human primary cells or engineered CAR-T cells, ProMab can help be your supplier or establish a proof-of-concept for your immune cell research.

Custom Research Solutions

- Isolated Human Primary Cell Subsets
- CAR-T / NK Cells Generation
- Engineered Stable Cell Lines With Exogenous Protein Expression (+/-)
- Custom Cell Based Assays
- Antibody Development
- Protein Expression
- Technology Licensing

All products are for research only

Discover more | www.promab.com

ProMab Biotechnologies, Inc.
2600 Hilltop Dr, Building B, Richmond, CA 94806
1.866.339.0871 | info@promab.com

SCAN ME